# THE MECHANISM OF MEMBRANE FISSION AT THE RECYCLING ENDOSOME OF *C. ELEGANS*

A Dissertation

by

LAUREN KUSTIGIAN

Submitted to the Office of Graduate and Professional Studies of
Texas A&M University
in partial fulfillment of the requirements for the degree of

DOCTOR OF PHILOSOPHY

| | |
|---|---|
| Chair of Committee, | Hays Rye |
| Committee Members, | Steve Lockless |
| | Jean-Philippe Pellois |
| | Dorothy Shippen |
| Head of Department, | Dorothy Shippen |

May 2019

Major Subject: Biochemistry

# ABSTRACT

Membrane fission, or the controlled pinching off of vesicles and tubules from intracellular organelles and the plasma membrane, is the first step in vesicle trafficking in eukaryotic cells. The mechanoenzyme dynamin-1 was the first protein identified to catalyze membrane fission and remains one of the best understood fission reactions. However the diversity of membrane fission mechanisms has increased over the past two decades. The focus of this research is identifying the mediator of membrane fission at the basolateral recycling endosome, a pathway well characterized in the model organism *C. elegans*. Fission at the basolateral recycling endosome returns proteins back to the plasma membrane and requires the activities of at least two interacting proteins, amphiphysin 1 (AMPH-1) and receptor mediated endocytosis-1 (RME-1). In order to address the roles of these two proteins, fission reactions were measured by Burst Analysis Spectroscopy (BAS). This single particle fluorescence-based method was developed as a novel approach to quantitatively study membrane fission reactions and validated using the ENTH domain of epsin, a well-characterized membrane fission protein. Using this technique we identified AMPH-1 as the mediator of membrane fission. This fission activity was stimulated in the presence of GTP, an unexpected result because AMPH-1 has no known nucleotide binding domain. Additionally the

GTP-stimulated fission activity of AMPH-1 is dependent on the amphipathic helices, and is regulated by RME-1.  Therefore we propose that mechanism of membrane fission at the basolateral recycling endosome is through the insertion of the amphipathic helices of AMPH-1.

# DEDICATION

This dissertation is dedicated to my family.

# CONTRIBUTORS AND FUNDING SOURCES

This work was supervised by a dissertation committee consisting of Professors Hays Rye, Jean-Philippe Pellois and Dorothy Shippen of the Department of Biochemistry and Biophysics and Professor Steve Lockless of the Department of Biology.

The data for Chapter III was generated by Arielle Brooks and processed by Daniel Shoup.

The data for Chapter IV was in part provided by Xue Gong.

The data for Apendix C was obtained by collaborators Dakota Brock, and Mengjui Jiang, Kristin Graham, Ting-Yi Wang, Kristina Najjar, and Alfredo Erazo-Oliveras.

All other work for the dissertation was completed independently by the student.

This work was made possible by N.I.H. under R01-GM114405.

# NOMENCLATURE

| | |
|---|---|
| TC | Transport Carriers |
| ER | Endoplasmic Reticulum |
| ERGIC | ER-Golgi intermediate compartment |
| MVB | Multivesicular bodies |
| CME | Clathrin mediated endocytosis |
| Sar1 | Secretion-associated Ras-related 1 |
| ADP | Adenosine diphosphate |
| ATP | Adenosine triphosphate |
| Arf1 | ADP-ribosylation factor 1 |
| ENTH | Epsin N-terminal homology |
| BAR | Bin-Amphiphysin-RVS |
| COPI | Coat protein I |
| COPII | Coat protein II |
| GTP | Guanosine triphosphate |
| GDP | Guanosine diphosphate |
| Atg18 | autophagy-related protein 18 |
| M2 | Matrix protein 2 |
| $L_o$ | Liquid ordered state |
| $L_d$ | Liquid disordered state |

| | |
|---|---|
| PC/PtdChl | Phosphatidylcholine |
| eGFP | Enhanced green fluorescent protein |
| TfnR | Transferrin receptor |
| GED | GTPase effector domain |
| Cryo-EM | Cryogenic electron microscopy |
| PH | Pleckstatin homology |
| $PI(4,5)P_2$ | Phosphoinositide 4, 5 bisphosphate |
| ESCRT | Endosomal Sorting Complexes Required for Transport |
| Vps4 | Vacuolar protein sorting-associated protein 4 |
| GUVs | Giant unilamellar vesicles |
| LUVs | Large unilamellar vesicles |
| HIV | Human Immunodeficiency Virus |
| BFA | Brefeldin A |
| PLA2 | Phospholipase A2 |
| BARS | Brefeldin A ADP-ribosylated substrate |
| LPAAT | lysophosphatidic acid transferase |
| FDS | Friction-driven scission |
| ERC | Endocytic recycling complex |
| TRE | Tubular recycling endosome |
| ARE | Apical recycling endosome |
| BRE | Basolateral recycling endosome |
| AEE | Apical early endosome |

| | |
|---|---|
| BEE | Basolateral recycling endosome |
| MDCK | Madin-Darby canine Kidney |
| RME-1 | Receptor mediated endocytosis 1 |
| hTAC | human IL2-receptor alpha chain |
| EH | Eps15 homology |
| AMPH-1 | Amphiphysin 1 |
| EHD | EH domain |
| Bin1 | Myc box-dependent-interacting protein 1 |
| SH3 | Src homology |
| RVS161/167 | Reduced Viability upon Starvation 161 and 167 |
| TEM | transmission electron microscopy |
| PS/PtdSer | Phosphatidylserine |
| PA | Phosphatidic acid |
| PE/PtdEth | Phosphatidylethanolamine |
| BAS | Burst analysis spectroscopy |
| cBAS | Concatenated BAS |
| MC-BAS | MultiColor BAS |
| SPAD | Single photon counting avalanche photodiodes |
| PtdIns | Phosphatidylinositol |
| TopFluor PE | 1-palmitoyl-2-(dipyrrometheneboron difluoride)undecanoyl-sn-glycero-3-phosphoethanolamine |

| | |
|---|---|
| IPTG | Isopropyl β-D-thiogalactose |
| DTT | Dithiothreitol |
| FCS | Fluorescence Correlation Spectroscopy |
| TEV | Tobacco etch virus |
| GST | Glutathione S-transferase |
| BSA | Bovine serum albumin |
| CPP | Cell-penetrating peptides |
| TAT | HIV-1 Trans-Activator of Transcription |
| dfTAT | dimeric fluorescent TAT |

# TABLE OF CONTENTS

Page

# LIST OF FIGURES

# CHAPTER I

# INTRODUCTION

Membrane fission is the controlled pinching off of vesicles and tubules from intracellular organelles and the plasma membrane. Release of membrane carriers from a parental membrane is an essential step in the trafficking of many kinds of essential material between distinct compartments in eukaryotic cells. While these membrane enclosed carriers or “transport carriers” (TC) were identified almost 50 years ago [1], the mechanisms by which fission reactions occur is still an active area of study. Well characterized trafficking pathways have provided key insights into the spatially and temporally defined sequence of events that culminates in membrane fission. However, a universal mechanism of membrane fission remains elusive, if one exists at all. Currently, numerous proteins which function in fission pathways have been identified *in vivo*, but their precise role in membrane fission has not been elucidated.

## Membrane trafficking pathways

The survival of eukaryotic cells requires the uptake of nutrients and the removal of waste products, as well as the ability to sense and respond to their environment. To accomplish these tasks, cells secrete proteins, sterols, fluid, and small molecules, often called ‘cargo’, and take up extracellular material through two processes known as exocytosis and endocytosis, respectively [2-4]. Both endocytosis and exocytosis are highly regulated processes involving the transfer of cargo between several organelles. These pathways use membrane enclosed vesicles or tubules, hereafter referred to as TCs to transfer cargo

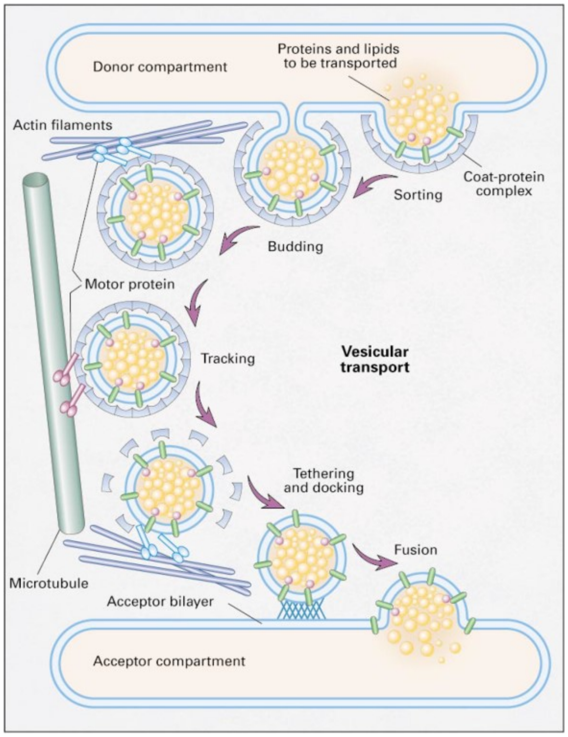

**Figure I.1. Vesicular transport. Cargo is recruited to the site of membrane fission. Prior to the membrane fission event the parental membrane is sculpted, and a bud is formed. After the fission event the TC is trafficked to the acceptor membrane where the TC is docked. The TC merges with the acceptor membrane through membrane fusion. Reprinted from "Genetic defects of intracellular-membrane transport" by Olkkonen, V.M. and E. Ikonen, 2000. *N Engl J Med* 343(15) p. 1095-104, Copyright 2000 with permission from the Massachusetts Medical Society [5].**

without exposing luminal material to the cytosolic environment. This transfer of cargo between organelles in TCs is generally referred to as membrane trafficking. Membrane trafficking can be broken down into three steps: (1) the release of the TC from the parental membrane through a process known as fission, (2) the transfer of the vesicle to the receiving organelle, and (3) the merging of the vesicle into the receiving organelle through a process known as fusion (Figure I.1).

There are two well characterized pathways in which cargo is trafficked through the cell: the secretory and endocytic pathways (Figure I.2). The secretory pathway was originally characterized as the pathway in which secreted proteins, were folded, and processed, giving this pathway its name [1]. It has been estimated that a third of the proteins made by the cell traffic through this pathway [6]. The secretory pathway originates in the endoplasmic reticulum (ER) where proteins are folded, and post translationally modified [7]. The ER is also the site where sterol, small molecules, and lipids are synthesized. Cargo is trafficked from the ER to the ER-Golgi intermediate compartment (ERGIC), which acts in sorting cargo either returning it to the ER, or trafficking it to the Golgi apparatus [8]. Cargo enters the Golgi apparatus through the cis-Golgi cisterna where it can continue to traffic through the cisterna, or can return back to the ER through a retrograde trafficking pathway [8]. Cargo trafficked through the Golgi apparatus undergoes modifications, e.g. protein and lipid glycosylation. At the trans-Golgi the cargo can be constitutively exocytosed, or can be stored in secretion vesicles, until a stimulus causes their release. Constitutively exocytosed cargo includes proteins that are important for the makeup of the extracellular matrix, such as collagen, while cargo stored in the secretion vesicles includes insulin, and neurotransmitters [9-11]. Alternatively, lipids and integral membrane proteins, such as cell surface receptors are trafficked to the plasma membrane, either directly or through the endocytic recycling complex [12], described in more detail in a later section [10, 13]. The secretion pathway transports cargo from the ER, through the Golgi apparatus, to its final destination of the plasma membrane, endosomes, lysosomes, or extracellular space.

Cell surface receptors containing endocytic signal sequences or modifications, such as phosphorylation and ubiquitination, as well as extracellular cargo, are transported from the plasma membrane to the early or “sorting” endosome [14]. The lumen of the early endosome is slightly acidic, in many cases causing ligands to dissociate from their receptors. The early endosome acts as a point of divergence in which the endocytosed cargo can be degraded, or recycled back to the plasma membrane. As the early endosome matures, to the late endosome it becomes more acidic [15]. Late endosomes can also become multivesicular bodies (MVB), which are distinct due to their intraluminal vesicles [16]. Cargo in the late endosomes and the MVBs is degraded when these organelles fuse with the lysosome, or is secreted into the extracellular space in vesicles known as exosomes. By contrast, recycled cargo is directed back to the plasma membrane through either a fast pathway, in which cargo leaves the early endosome to fuse with the plasma membrane, or through a slow pathway, in which cargo is trafficked to the ERC, prior to being trafficked to the plasma membrane [17].

Regardless of destination, the initiation of all trafficking requires a membrane fission event, in which a vesicle is first released from a donor membrane. Membrane fission appears to require at least three steps: the accumulation of cargo, the shaping of the membrane, and finally the release of the vesicle from a donor membrane. This process is highly regulated, requiring numerous proteins [18]. Several fission pathways have been characterized, and while each organelle uses a unique set of proteins to induce fission, there appear to be several common features of all fission reactions, and it has been proposed that the rearrangement of lipids in the bilayer required for fission are similar for all membrane fission mechanisms [19].

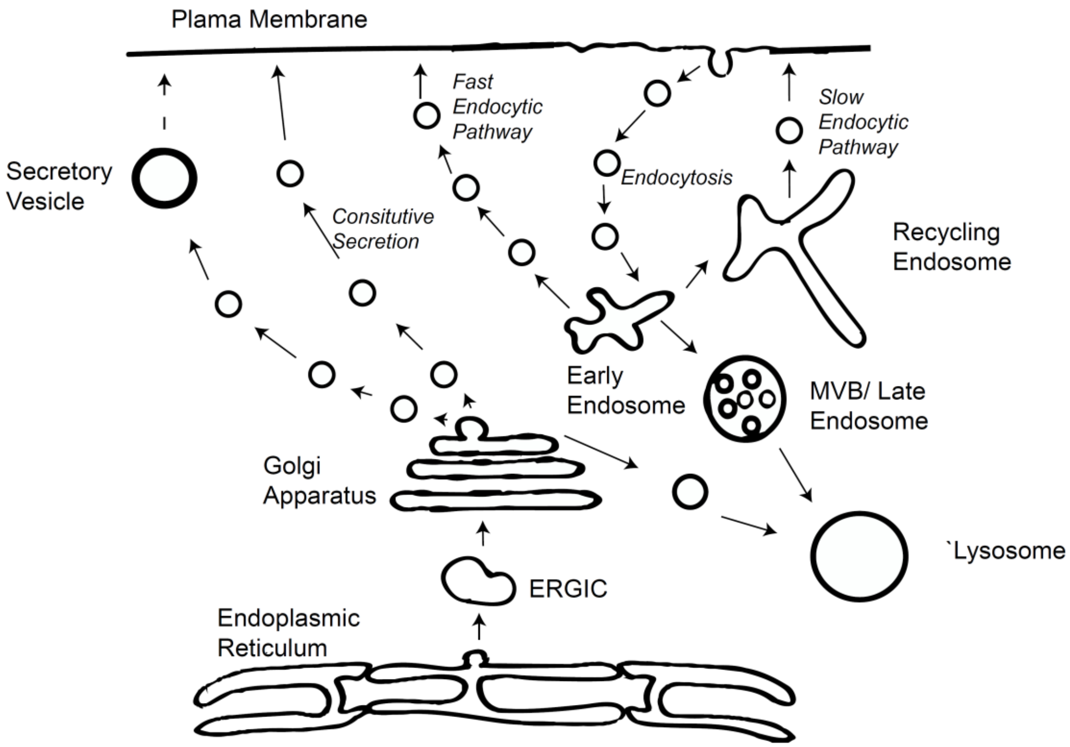

**Figure I.2 Membrane trafficking pathways. The secretory pathway begins at the ER, and transports cargo through the ERGIC, and the Golgi apparatus. The cargo can be transported to the lysosome, the plasma membrane or secreted. The endocytic pathway takes up cargo from the extracellular space and the plasma membrane. The cargo is transported to the early endosome, where it can be marked for degradation by trafficking through the MVBs and late endosome before enter the lysosome. Cargo can also be recycled through the fast recycling pathway where cargo is transported from the early endosome to the plasma membrane, or through the slow recycling pathway which goes to the recycling endosome before trafficking to the plasma membrane. (Reprinted with modifications from [20])**

## Lipid rearrangement in membrane fission

Biologically relevant membrane fission is proposed to go through a conserved mechanism, which prevents the leaking of luminal content into the cytoplasm (Figure I.3). Biological membranes are semi-rigid structures, which spontaneously adopt a planar shape [21, 22]. Consequently for fission to occur, the membrane must be molded to create areas of high curvature. Remodeling starts with the formation of a shallow invagination, or bud. This area constricts further to form a neck which has a narrow diameter. These two events are mediated by different proteins, described in more detail below, that are able to overcome the rigidity of the membrane, and repulsive electrostatic forces of the lipids [23, 24]. At shorter distances, 10 nm or less in diameter, these remodeling mechanisms also must overcome the highly favorable hydration of lipid head groups by water [24]. It has been proposed that as the diameter of the neck decreases to approximately 3.7 nm, lipid tilting will create packing defects allowing the inner monolayers to spontaneously merge [25, 26]. The merger of the inner monolayers results in the hemi-fission intermediate. Once the hemi-fission intermediate is formed, constriction no longer plays any role in separating the vesicle from the parent membrane; rather the so called stalk intermediate must be ruptured in another way, either by elongating the neck, membrane tension or membrane destabilization [27]. It has thus been proposed that all membrane fission mechanisms must initially constrict the membrane and merge the inner leaflets of the bilayer to create the hemi-fission intermediate, after which the outer leaflets of the membrane must then be separated.

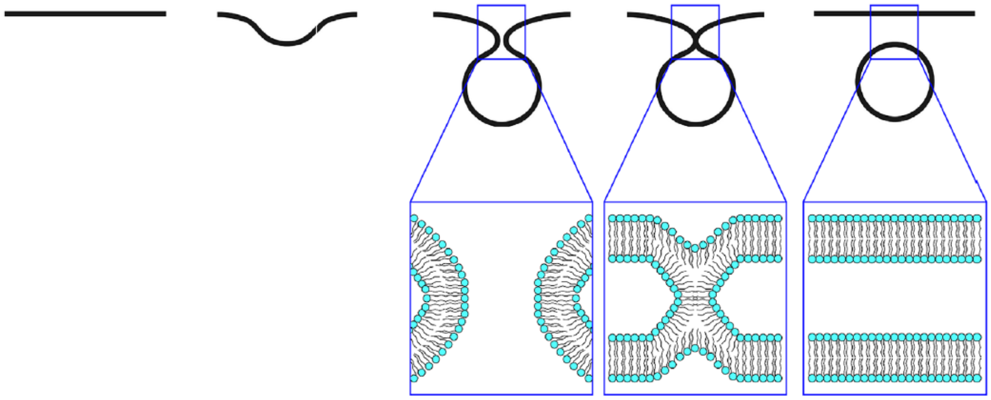

**Figure I.3. Lipid rearrangement in conserved membrane fission. Lipid bilayers tend to adopt a planar geometry. As membrane curvature is generated a bud is formed, and at high membrane curvature a neck is formed. The bilayers are merged to form a single bilayer, which is known as the hemifission intermediate. Membrane fission breaks this intermediate allowing the vesicle to be released from the donor membrane. Reprinted with permission from "Crowd-Sourcing of Membrane Fission: How crowding of non-specialized membrane-bound proteins contributes to cellular membrane fission" by Manni, M.M., J. Derganc, and A. Copic, 2017. *Bioessays,* 39(12), Copyright 2017 by Wiley Periodicals [28].**

## Mechanisms of membrane curvature and membrane fission

A fission reaction can be broken down into two individual stages: (1) the rearrangement of lipids in the bilayer to generate membrane curvature, and (2) the release of the vesicle [29]. While the two stages of membrane fission are fairly distinct *in vivo*, the imposition of membrane curvature and the fission of a membrane bilayer share a number of important features in common, and these commonalities will be outline in more detail in the sections below.

### *Shallow insertions into the bilayer*

The insertion of amphipathic helices or hydrophobic loops into a lipid bilayer can generate membrane curvature [23, 30]. These shallow insertions are thought to act as wedges, causing lipid tilting and expansion of one leaflet of the bilayer in relation to the other (Figure I.4). The insertion of several of these protein motifs into the bilayer in close proximity results in membrane curvature [30, 31]. Many proteins found in membrane fission pathways contain amphipathic helices, including proteins involved in clathrin mediated endocytosis (CME), such as amphiphysin and epsin, and the small G-proteins Secretion associated Ras related 1 (Sar1) and ADP-ribosylation factor (Arf1), which act in the fission reactions at the ER and Golgi apparatus, respectively [32-34]. Hydrophobic loops are found on a variety of membrane-binding proteins, including syndapin and dynamin, which act in CME, and synaptotagmin, a protein involved with membrane fusion [35] [36]. By expanding the surface area of one leaflet of a bilayer compared to the other through insertion of hydrophobic segments, both amphipathic helices and loops can thus create curvature.

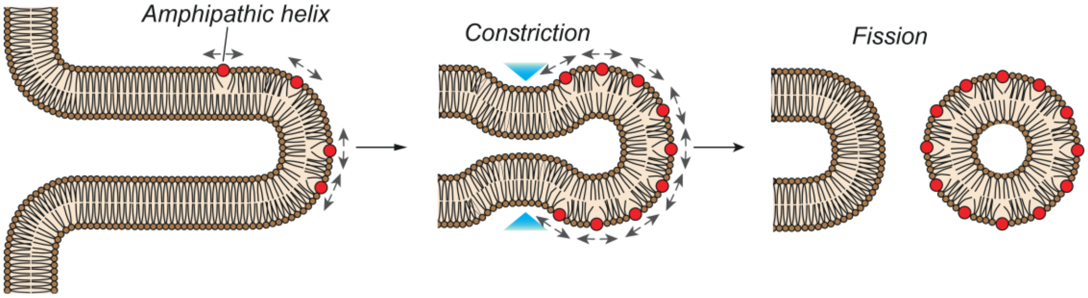

**Figure I.4 Membrane fission through shallow insertions into the bilayer. Proteins with amphipathic helices or hydrophobic loops can insert into the outer leaflet of the lipid bilayer. These insertions can cause membrane curvature, and membrane fission by destabilizing the lipid bilayer. (Reprinted with permission from [37])**

Insertion of amphipathic helices can also lead to membrane fission, though a more extreme version of the same process that generates membrane curvature [34, 38, 39] (Figure I.4). It has been proposed that the local concentration of a surface-bound protein determines whether proteins with amphipathic helices generate curvature or induce fission [32, 37, 40]. However numerous other observations indicate that while protein concentration does affect the fission activity, it is not the only determinant. For example the sequence of an amphipathic helix has been shown affect the proteins ability to cause membrane fission. A single mutation made in the hydrophobic face of the amphipathic helix of the ENTH domain of Epsin, resulted in changes in the fission activity of this domain, that cannot be attributed to changes in the binding of the protein to membrane [34]. Additionally, length of the amphipathic helix plays a role in fission activity, as increasing the length of the amphipathic helix of endophilin, an N-Bin-Amphiphysin-RVS (N-BAR) protein (see below) resulted in a 30% increase in the number of small vesicles observed [40]. Finally, the depth of helix insertion affects the fission activity of amphipathic helix containing proteins. This was observed using specific lipid compositions that promote either tubulation or vesicle formation by the N-BAR protein amphiphysin. Lipid compositions that primarily display tubule formation permit much deeper penetration of the amphipathic helix into the bilayer than lipid compositions that produce vesicles [41]. Furthermore using modified versions of endophilin, it has been shown that deep insertions of an amphipathic helices lead to tubulation, while shallow insertions lead to vesiculation on the same bilayer composition [42]. In the most general terms, the amphipathic helices of proteins like amphiphysin and endophilin are thus important for binding to membranes and helping induce membrane curvature, which can be used to destabilize the bilayer and thereby facilitate fission.

Numerous fission reactions appear to employ variants of this mechanism *in vivo*. Release of COPII coated vesicles from the ER has been attributed to the small amphipathic helix containing GTPase, Sar1 [43, 44]. The fission of yeast (*Saccharomyces cerevisiae*) vacuoles during cell division and osmotic shock is dependent on the insertion of the amphipathic helix of autophagy-related protein 18 (Atg18) [45, 46]. The influenza protein, matrix protein 2 (M2) has been shown to cause fission through its amphipathic helices to release the virus into the extracellular space [47, 48]. Epsin, which is involved with CME, also has been shown to play a direct role in membrane fission in mammalian cells [40]. The presence of an amphipathic helix alone, however, is insufficient to predict the fission activity of a protein. At the same time, while a number of other membrane binding proteins that possess amphipathic helices show fission activity on model membranes *in vitro*, the physiologic significance of these activities remains unclear.

### *Line tension*

The lipids in a membrane bilayer can segregate into domains based on their physical properties, which can affect membrane curvature [49]. Many biological lipid bilayers are composed of glycerophospholipids, with varying amounts of sphingomyelin and sterols [50], which can form two different fluid states, a more ordered state (the liquid-ordered state or $L_o$), and a more disordered state (the liquid-disordered state or $L_d$) [51]. The $L_o$ state is enriched in saturated glycerophospholipids, sphingomyelin, and cholesterol whereas the $L_d$ state consists primarily of lipids with unsaturated fatty acids [51]. The formation of a phase-separated domain within a planar membrane results in an energy mismatch, or line tension, along the length of the domain's interface [52]. The general thermodynamic drive to minimize this unfavorable line tension energy differential will tend to push the edge as small as possible this energy minimization process can result in budding of the domain away from the planar membrane (Figure I.5). The magnitude of this curvature-inducing effect is a trade-off between the line tension, which favors the budding, and membrane rigidity, which favors a planar membrane [53]. It has been shown that in some cases, this line tension effect can lead to spontaneous fission provided line tension energy is high enough [54, 55].

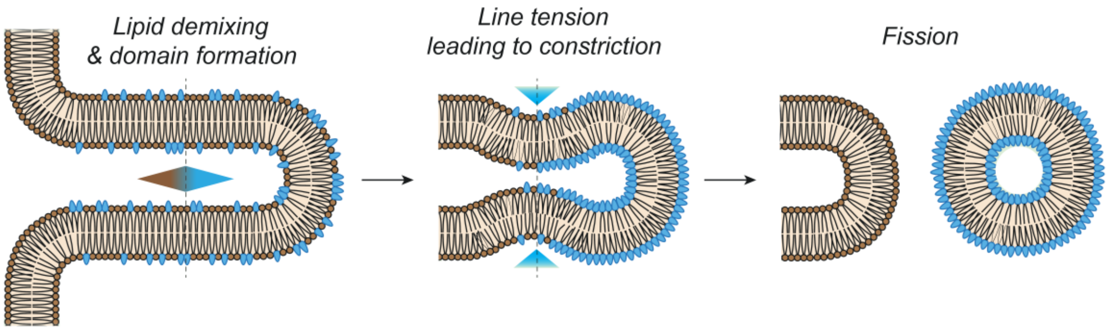

**Figure I.5 Membrane fission caused by line tension. The formation of lipid domains can cause membrane curvature, and membrane fission. (Reprinted with permission from [37])**

Budding of the membrane and fission due to phase separation of the $L_o$ and the $L_d$ domains was first observed using giant unilamellar vesicles (GUVs) [56]. Membrane budding and fission resulting from line tension alone has been observed in a minimal lipid system using a synthetic model membrane [56, 57] [58]. Fission has also been observed on tubulated liposomes in which the phase separation was induced either by a photoactivation or the addition of a protein [57, 58]. Importantly, spontaneous fission observed in these studies depended upon on specific ratios of phosphatidylcholine (PC), cholesterol and sphingolipid in the membranes, [58]. Given these observations, the *in vivo* significance of line tension in driving membrane fission remains unclear. However, viral proteins and toxins are able to creating micro-domains, which have been shown *in vitro* to induce membrane curvature, and could utilize a line tension to mediate membrane fission [59].

### *Protein crowding*

Proteins that bind or are embedded in a membrane have been suggested to cause curvature through protein crowding [30]. This mechanism proposes that collisions between the soluble domains of transmembrane proteins, or proteins bound to the membrane through an amphipathic helix, induce membrane curvature and tubulation through steric pressure (Figure I.6) [60]. This model was initially proposed for membrane binding proteins, such as epsin. Crowding was also suggested as an explanation for how the non-membrane binding protein, enhanced green fluorescent protein (eGFP), which was anchored in the membrane either by the addition of an amphipathic helix, or covalently attaching the protein to the lipid head group could induce membrane curvature [60]. It has also been observed that proteins with intrinsically disordered domains can cause curvature at a lower protein concentration than similarly sized globular proteins [61]. It has been proposed that this observation is the result of the larger hydrodynamic radii of the intrinsically disordered domains, which permits them to act as more efficient crowding agents at the membrane [61, 62].

Protein crowding on membranes may also lead to membrane fission, as suggested by work with the ENTH domain of epsin [63]. A mutation which disrupted the amphipathic helix of the ENTH domain also showed the same fission activity as the wild-type protein. However this amphipathic helix mutation significantly reduced the binding affinity of the ENTH domain for the membrane. Therefore, five-fold higher concentration of the mutant protein was required to achieve a protein binding level similar to the wild-type protein [63]. Membrane fission has also been observed with proteins with large intrinsically disordered segments, such as epsin or amphiphysin. It has been suggested that the large hydrodynamic radius provided by these domains, is important for causing curvature and destabilization of a membrane [64]. While biological membranes are inherently crowded environments there is little *in vivo* evidence to support that this mechanism is relevant at active sites of membrane fission in a living cell [65].

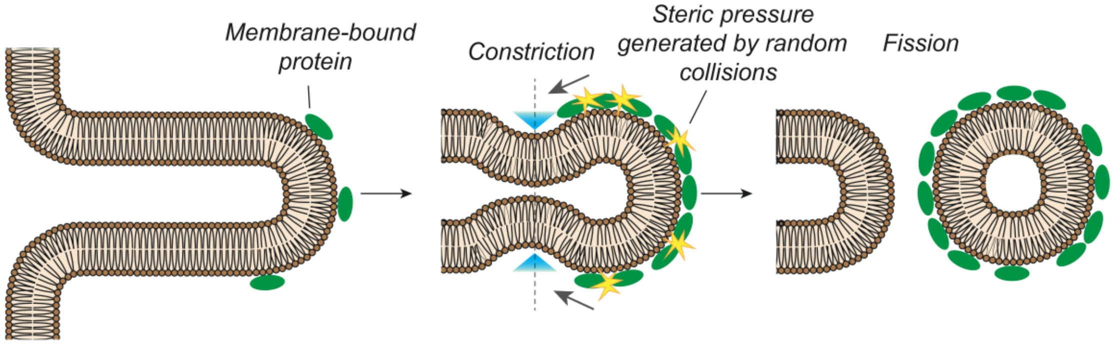

**Figure I.6 Membrane fission by protein crowding. Proteins that bind to lipid bilayers can cause steric pressure resulting in membrane fission. (Reprinted with permission from [37]).**

### *Dynamin*

Dynamin is protein that is essential for clathrin-mediated endocytosis. Dynamin was originally characterized as a microtubule binding ATPase, believed to have activity similar to kinesin, or dynein [66]. Later work showed that dynamin is actually a membrane binding protein, not a microtubule binding protein, and hydrolyzed GTP not ATP [67, 68]. The observation that dynamin plays a role in membrane remodeling was further supported by the amino acid sequence similarity between the mammalian dynamin-1 and the mutant protein associated with the *Drosophila melanogaster shibire* phenotype [69] [70]. The *D. melanogaster shibire* involves a temperature-sensitive mutant of the *shi* gene, which causes a reversible paralysis at restrictive temperatures [71]. Electron micrographs of garland cells from *shi* flies at non-permissive temperatures show an increase in coated pits with regions of high electron density at the neck of the vesicles, in comparison to the cells harvested at permissive temperatures [72]. Direct evidence of a role of dynamin in endocytosis came from the observations that a mutation in the dynamin GTP binding domain, which inhibited the endocytosis of transferrin receptor (TfnR), a protein which uses CME [73]. It was also shown that dynamin-1 is targeted to clathrin coated pits [74] and interacts with amphiphysin, an N-BAR protein which binds to clathrin [75] [76] [77] [78]. Disruption of the interaction between amphiphysin 1 and dynamin-1 disrupted the localization of dynamin to the site of CME [79].

*In vitro* dynamin can bind to membranes and oligomerize to form tubules in a GTP-independent manner [80]. However, *in vivo* studies show that the dynamin-1 GTP cycle is intricately linked to its function. Importantly, dynamin-1 was found to undergo conformational changes that are linked to nucleotide state on model membranes [81-85]. These conformational shifts have been interpreted to show either (1) an expansion of the helical pitch of the dynamin oligomer [81], (2) a constriction of the membrane tubule [86] [81] [83] [26] [85], or (3) twisting of the oligomerized protein on a on a membrane (Figure I.7) [85]. Upon hydrolysis of GTP to GDP, dynamin-1 dissociates from the membrane [81] [27] [87].

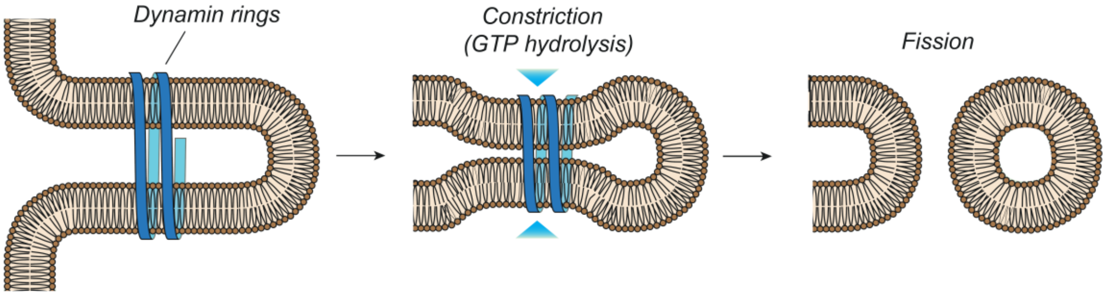

**Figure I.7 Membrane fission mediated by dynamin.Dynamin binds to tubulated membranes. Upon GTP hydrolysis dynamin undergoes a conformational change that causes membrane fission. (Reprinted with permission from [37])**

Two general models have been proposed to explain how dynamin induces fission, both of which attempt to explain the observations noted above through a nucleotide-dependent hydrolysis cycle [88]. The first model is the constrictase/ratchet model (Figure I.8A) [88]. In this model, GTP hydrolysis is directly coupled to a power stroke resulting in the application of a mechanical force on the membrane. In this model, dynamin forms a single turn around the membrane tubule [89]. The dynamin GTP binding domains (G-domains) dimerize between the helical turns of the first and last dynamin [90]. The GTPase effector domain (GED) then stimulates GTP hydrolysis, causing the dimers to slide closer together and constricting the membrane, bringing the membranes together to form the hemi-fission intermediate. Hydrolysis is postulated to cause the G-domain dimers to dissociate, causing an expansion of the helical pitch, which elongate the neck of the hemi-fission intermediate leading to fission. In this model mechanical force is being employed to create large scale conformational changes in the dynamin oligomeric structures which are directly transmitted to the bound membrane. Importantly, the constriction model is consistent with all of the conformational changes outlined above.

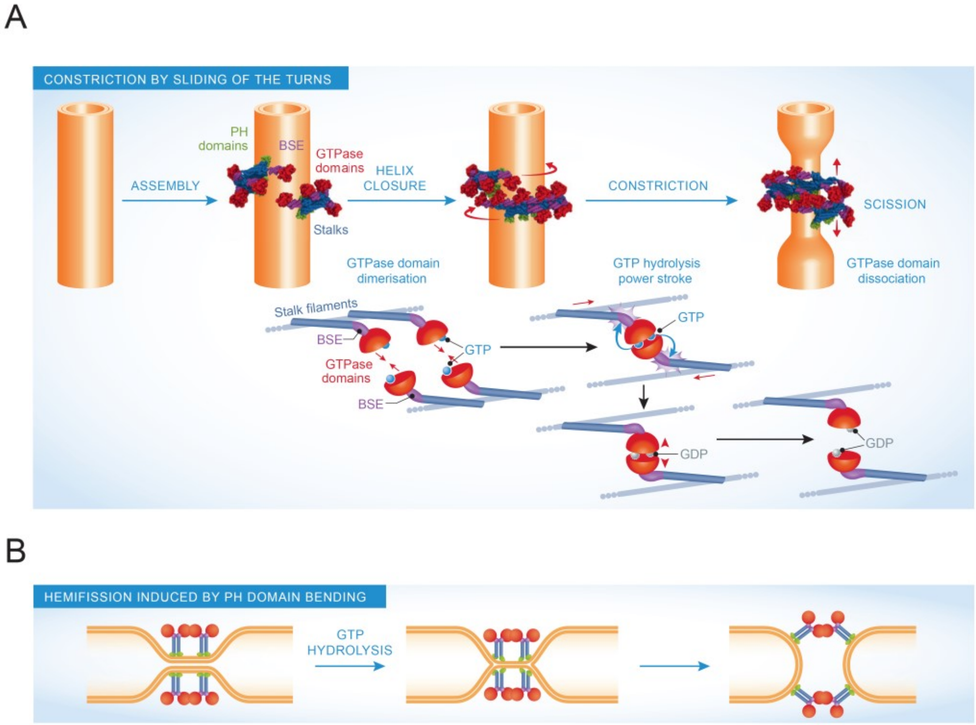

**Figure I.8. Proposed models of membrane fission mediated by dynamin-1.Constrictase/ratchet model of dynamin mediated membrane fission (A). Dynamin binds and oligomerizes around a membrane tubule. The G-domains between the turns of the helix dimerize. GTP hydrolysis causes a sliding of the helix oligomers, and a constriction of the membrane tubule. The G-domains dissociate causing an expansion of the dynamin oligomer resulting in membrane fission. Membrane fission by dynamin dissociation model (B). Dynamin binds to a membrane tubule, and upon GTP hydrolysis the PH domain inserts into the bilayer to constrict the tubule to generate the hemifission intermediate. The hemifission intermediate is stabilized by the dynamin oligomer, and when dynamin dissociates from the membrane, the hemifission intermediate is destabilized which causes membrane fission. (Reprinted with permission [88])**

The second model of dynamin-induced fission requires two stages, where dynamin stabilizes a constricted state of the membrane (Figure I.8B). First, dynamin is proposed to bind to a membrane tubule. Upon GTP hydrolysis it undergoes a rapid conformational change which forms a super-constricted state around the tubule. This super-constricted state causes the membranes to merge and form a hemi-fission intermediate that is stabilized by the dynamin oligomer. Upon $P_i$ dissociation, the dynamin scaffold loosens, destabilizing the hemi-fission intermediate which results in fission. Observations of the structure of dynamin bound to model membranes as well as GTP transition state experiments, have provided support for this model. For example, dynamin can bind to membranes in the absence of GTP, creating a tubule with an inner luminal diameter of 20 nm [83]. The subsequent inclusion of GTP results in a constricting of the membrane to an inner luminal diameter of 7 nm based on cryogenic electron microscopy (cryo-EM) observations [83]. The structure of a dynamin mutant that only slowly hydrolyzes GTP shows a super constricted tubule of an inner luminal diameter of 3.7 nm consistent with the geometric expectations of the hemi-fission intermediate [91]. The observed constriction appears to be due to the “tilting” of the dynamin Pleckstatin Homology (PH) domain into the plane of the membrane bilayer. The PH domain thus appears to act as an anchor to which dynamin binds to phosphoinositide 4, 5 bisphosphate ($PI(4,5)P_2$) and inserts its variable loop into the membrane [92]. Importantly, the insertion of the variable loop into the membrane appears to be essential for dynamin-mediated membrane fission [35] [36]. Structures of dynamin in both the transition state, and the super-constricted state show this tilting of the PH domain, with this domain possibly acting as another type of wedge that stabilizes the membrane [27] [91]. The hydrolysis of GTP to GDP then acts to release the dynamin and destabilize the hemi-fission intermediate, resulting in membrane fission.

Whether either model of dynamin-mediated fission is correct remains unclear as both models are consistent with most know observations. At the same time, it is possible that both or neither model is correct. Both models are in part based on structural information obtained from cryo-EM on long oligomers of dynamin, structures which are not the relevant for dynamin function *in vivo* [89]. Although a unified model of dynamin-mediated vesicle fission has yet to emerge, both models outlined above possess one important commonality: dynamin must undergo a conformational change that is linked to the hydrolysis of GTP. This core idea is referred to hereafter as the “dynamin paradigm”.

### *Scaffolding*

One of the most common mechanisms for the induction of membrane curvature is through a scaffolding mechanism, in which a soluble protein binds directly to the membrane or to membrane bound adaptors and imposes curvature onto the membrane. This mechanism requires that the scaffolding protein must have a semi-rigid structure with an intrinsic curvature [93]. Additionally high local concentration of the scaffolding protein or oligomerization of the protein at the membrane surface is required. Several families of proteins employ this mechanism to generate membrane curvature, with the most well-known scaffolding proteins being the vesicle coat proteins, like coat protein I (COPI) [93], coat protein II (COPII) and clathrin [94]. The subunits of these proteins bind to the membrane through adaptors, and assemble on the membrane to create a semi-rigid coat of oligomerized protein. This coat then molds the membrane into a curvature that matches the shape of the protein oligomer.

Scaffolding also appears to directly used in membrane fission mediated by the “endosomal sorting complexes required for transport” or ESCRT proteins. This fission mechanism, involving numerous proteins that form four ESCRT complexes (ESCRT 0, I, II, III) and an AAA+ ATPase, Vacuolar protein sorting-associated protein 4 (Vps4), that are important for the generation of MVBs and the budding and release of enveloped viruses [16]. This ESCRT-mediated membrane fission pathway is initiated by ESCRT-0, which binds to ubiquitinated cargo and phosphoinositide-3-phosphate [95]. ESCRT-0 recruits ESCRT-1 which complexes with ESCRT-2; this super complex has been shown to generate membrane of buds on giant unilamellar vesicles (GUVs) *in vitro* [96]. The ESCRT-3 complex is then recruited to the site of fission by the ESCRT-1/ESCRT-2 complex. ESCRT-3 polymerizes on the membrane to form spiral disks, helical tubes, or conical funnels, as observed in *in vivo* overexpression studies and *in vitro* (Figure I.9) [16] [97]. The polymerized form of ESCRT-3 has preferred curvature, therefore the spiral form of the ESCRT-3 filaments result in an area of the filament which is over-bent and one that is under-bent, giving the polymer elastic energy [97]. Vps4 is recruited to the site of ESCRT-3 polymerization, and acts in the disassembly of the ESCRT-3 polymer [98] [99]. Recently it was suggested that, along with ESCRT-3, Vps4 generates the force needed to cause membrane fission in an ATP-dependent manner [100]. However, precisely how Vps4 and ESCRT-3 this force is generated remains to be elucidated.

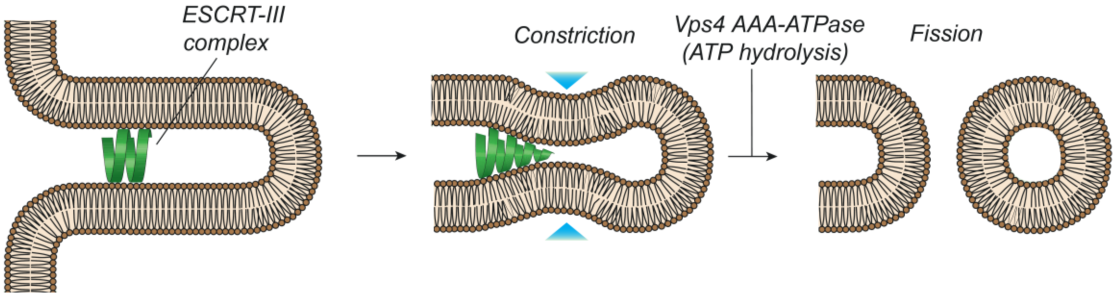

**Figure I.9 Membrane fission mediated by ESCRT-3 and Vps4. ESCRT-3 binds to a leaflet of the lipid bilayer. This complex is able to form spiral oligomers which create membrane curvature. Vps4 dependent disassembly of the ESCRT-3 oligomer results in membrane fission. (Reprinted with permission from [37]).**

The ESCRT proteins facilitate an unusual fission reaction, in that the membrane vesicles they create are released into the lumen of an organelle or extracellular space, rather than the cytoplasm. Thus the topology of the ESCRT-mediated vesicle formation is distinct from other known membrane fission reactions. The ESCRT proteins act in the fission of the limited endosomal membrane which generates MVB [96, 101] [102] [103]. ESCRT-mediate fission is also important for the budding and release of enveloped viruses, such as Human Immunodeficiency Virus (HIV) type 1 and Ebola, into the extracellular space [104, 105] [106]. In the viral budding pathway, the native HIV protein group specific antigen, or Gag, is able to recruit the ESCRT-1 complex, bypassing the need for the ESCRT-0 complex. It should be noted that the role of these complexes are not limited to membrane fission, as the ESCRT proteins also localize to sites of membrane damage, and play a role in resealing both the plasma membrane after cytokinesis and the nuclear envelope [107]. However, ESCRT-mediated membrane fission uses polymerized protein to mold the membrane into a shape conducive to membrane fission though scaffolding.

### *Lipid shape*

Different phospholipids have distinct intrinsic shapes, which can directly impact the potential of a bilayer to be curved. This shape is dependent on both the nature of the head group and the acyl chain [108]. In general lipids are described as being either “cylindrical”, “conical” or “inverse conical.” Membranes made up of a single type of lipid form either bilayers (cylindrical), inverted tubes (conical), or micelles (inverse conical) [108]. The influence of individual lipids and their shapes on membrane curvature in a complex biological is likely unimportant under most circumstances, because the numerous lipid species in a mixture will tend to compensate and cancel one another [108]. However, high local concentrations of a particular lipid species can have a large impact on curvature. Activity of phospholipase A2, an enzyme that cleaves of a fatty acid off of a glycerophospholipid causing the lipid to take on an inverse conical shape, can generate tubules emanating from both the Golgi apparatus, and the endosomes [109] [110].

The biological impact of changes in the lipid composition on membrane curvature has perhaps been most thoroughly characterized at the Golgi apparatus (Figure I.10). Treatment of hepatocytes with the fungal toxin, brefeldin A (BFA), blocks transport of secreted proteins from the Golgi apparatus. BFA treatment also causes large morphological changes to the Golgi apparatus, from stacks to long tubules, while treatment with phospholipase A2 (PLA2) inhibitors reversed the impact of BFA [110, 111]. It has been proposed that an accumulation of lysophospholipid is responsible for the abnormal morphology of the Golgi apparatus upon BFA treatment [110]. At the same time, treatment with a PLA2 antagonist in the absence of BFA induces fragmentation of the Golgi apparatus [110]. In an unrelated study, it was found that fatty acyl coenzyme A is required for membrane fission at the Golgi apparatus [112]. It was later proposed that a protein that bound to Brefeldin A modified ADP-ribose plays an important role in transferring fatty acyl-CoA onto lysophosphatidic acid [113]. This protein is known as Brefeldin A ADP-ribosylated substrate (BARS). While it was originally thought that BARS is a lysophosphatidic acid transferase, it was later discovered that BARS binds and activates lysophosphatidic acid transferases (LPAAT) [114] [115]. Thus fission at the Golgi apparatus, original attributed solely to BARS, was found to be mediated by a complex set of proteins involved in activation of LPAATs [114, 116]. Regulation of Golgi apparatus morphology and membrane fission critically depends on the species of lipid present in the bilayer, which are controlled in part by a delicate balance between LPA2 and LPAAT.

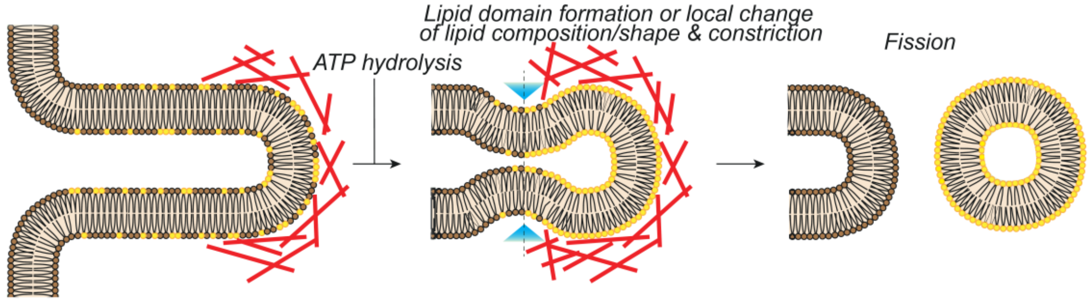

**Figure I.10 Membrane fission mediated by lysophosphatidic acid transferases.The transfer of a fatty acyl-CoA onto lysophosphatidic acid can cause membrane curvature and fission (Reprinted with permission from [37])**

*Cytoskeleton*

The cytoskeleton, which includes actin, microtubules and intermediate filaments act in cell motility, cell division, endocytosis, transport of cargo through the cell and the generate and stabilize membrane shape [117] . The cytoskeleton can also generate membrane curvature through the application of localized forces on cellular membranes to which it is connected. At the plasma membrane, the polymerization of actin can generate pushing forces, causing membrane deformations [118]. Numerous actin filaments must work together to generate the force required to cause these deformations and overcome the rigidity of the membrane [23]. These pushing forces can generate either tubular or sheet-like protrusions, known as filopodia, or lamellipodium, respectively [118, 119]. Like actin, microtubules can be important for the generation of membrane curvature, creating tubules from organelles such as the ER, Golgi apparatus and endosomes; however microtubules do not appear to directly push or pull the membrane of these organelles [120]. Rather, tubular structures are generated by molecular motors from the kinesin and dynein families, which bind to anchor proteins on the organelle and stretch the membrane [120].

In some cases, the cytoskeleton may also play a role in membrane fission. Actin has been shown to localize to the site of many membrane fission events [121]. These include endocytosis, both clathrin dependent and independent, fission at the Golgi apparatus, the recycling endosome, and the ER [122] [123]. At the same time, while actin and tubulin can be observed at the sites of active membrane fission in living cells, they are not sufficient for fission activity and appear to work in concert with other membrane sculpting proteins. However, the nature of this cooperation remains poorly understood. It has been proposed that these cytoskeletal elements counteract membrane tension in order to enhance the fission activity of other proteins [124].

The cytoskeleton is proposed to play a direct role in several membrane fission events. It has been shown that for CME in *S. cerevisiae* deletion of known actin interacting proteins disrupts CME [125]. However, it remains unclear whether actin plays direct a role in the fission event itself or if it acts to overcome turgor pressure at the yeast plasma membrane [121]. A second proposed fission mechanism in which the cytoskeleton plays a direct role is known as friction-driven scission (FDS) (Figure I.11) [126]. In this mechanism membrane curvature proteins bind to the membrane to generate tubules. These membrane curvature proteins generate membrane “fences” which prevent lipid diffusion [126, 127]. Molecular motors bind to the end of the membrane tubule and as they move along the microtubule, generate a pulling force, which mechanically release vesicles. This mechanism has yet to be shown to be relevant *in vivo*, however. Much like the localization of actin to sites of membrane fission, if FDS is biologically relevant it likely works in conjunction with other mechanisms [126].

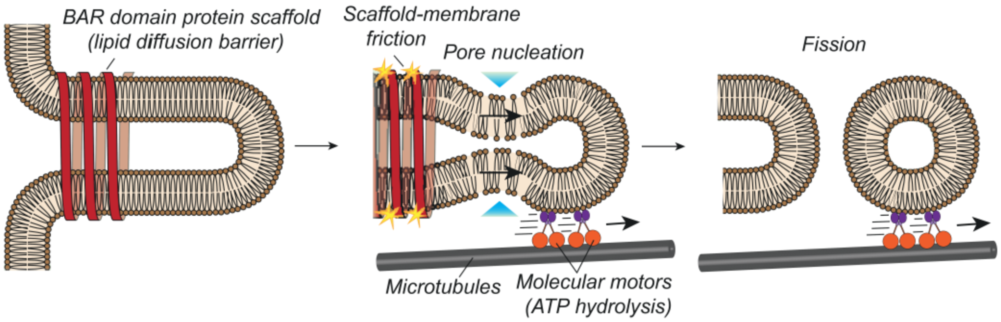

**Figure I.11 Friction driven scission. BAR domain containing proteins will bind to the lipid bilayer. The BAR domains cause membrane curvature and prevent lipid diffusion. Molecular motors will bind to the lipid bilayer and generate pulling forces which lead to membrane fission. (Reprinted with permission from [37])**

### Basolateral recycling endosome

While our understanding of how membrane fission occurs in the cell has improved dramatically over the last couple of decades, this process remains particularly enigmatic at one essential organelle, the tubular recycling endosome (TRE) [128]. Cargo trafficked through the “slow” recycling pathway is transported from the apical and basolateral early endosomes to a series of tubular and vesicular membrane structures found in the perinuclear region of the cell, known as the endocytic recycling complex, ERC. Roughly 35% of all recycled plasma membrane-localized receptors pass through this pathway [129-131]. This material is then transported to the TRE, which is a complex of multiple tubular membrane bound structures that act as a trafficking intermediate between the ERC and the plasma membrane. Several independent membrane fission pathways have been suggested to play a role in traffic between the TRE and the plasma membrane [17, 132]. Disruption of these pathways is associated with diseases such as Charcot-Marie-Tooth disease, autism and cancer progression through aberrant bone morphogenetic protein signaling [133-136]

Recycling endosomes are vital to the maintenance of cell polarity in epithelial cells. In polarized cells like this, there are two subsets of the TREs, which are found near the apical and basolateral plasma membranes (Figure I.12). Consequently, the TREs are named the apical recycling endosomes (ARE) and the basolateral recycling endosomes (BRE) depending on their location.  These two sub-types of recycling endosome are believed to function in a check point process to prevent the missorting of cargo.  Missorting of cargo transported through the ARE and BRE is associated with diseases such as microvillus inclusion disease, familial hypercholesterolemia, congenital sucrase-isomaltase deficiency, and Bartter syndrome [12, 137, 138] [138, 139].  Whether multiple fission pathways exist to help coordinate different sorting and trafficking pathways from the ARE and BRE remain unclear.

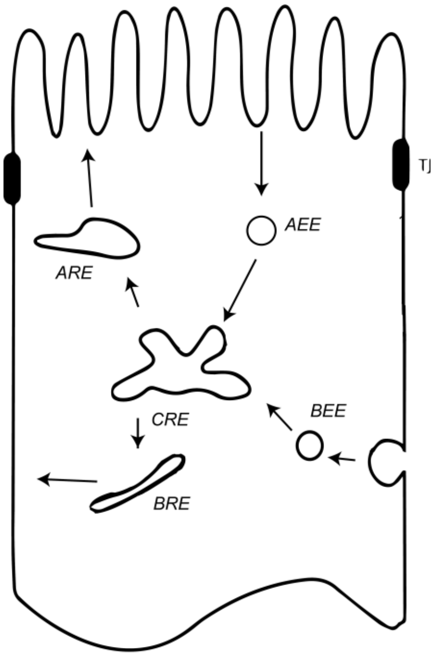

**Figure I.12 Endocytic recycling in polarized epithelial cells. Cargo is endocytosed into the cell and transported to the apical or basolateral early endosome (AEE and BEE). Cargo is transported to a common recycling endosome. It is then transported to either the apical or basolateral recycling endosome (ARE and BRE) after which it is returned to the plasma membrane. (Reprinted with modifications from [140])**

The two primary model systems used to study the ARE and BRE are Madin-Darby canine Kidney cells, MDCK, and *Caenorhabditis elegans* [17, 141]. The genetic analysis of trafficking in *C. elegans* has provided invaluable information about these trafficking pathways in their native cellular environment [142]. Using a genetic screen eight novel genes involved in endocytosis were discovered in worm oocytes [142]. Knockdown of one of these genes, *receptor* *mediated endocytosis 1* (*rme-1*), resulted in large granule filled vacuoles found near the basolateral domain in the intestine of adult worms, a phenotype associated with a block in basolateral recycling [143]. The intestine of *rme-1* knockdown worms of also induced abnormal distributions of two well characterized proteins that traffic through the ERC, human TfnR and human IL2-receptor alpha chain (hTAC) [144]. These proteins accumulate in tubular organelles localized near the basolateral membrane domain but not the apical domain, in *rme-1* mutants strongly suggesting that plays a role in the regulation of fission at the BRE [143].

A functional partner protein of RME-1 was identified in a screen. The Eps15 homology (EH) domain of RME-1 binds to Asp-Pro-Phe sequences and a bioinformatics screen was used to identify 74 proteins with multiple copies of this motif [145]. The candidates were then tested for function in a genetic screen and the N-BAR protein, amphiphysin 1 (AMPH-1) was identified as a possible partner protein for RME-1. RME-1 and AMPH-1 were shown to physically interact through the NPF motif of AMPH-1 *in vitro* [145]. Worms with *amph-1* knockdowns have a similar but weaker phenotype as the *rme*-1 knockdowns. In both phenotypes, known proteins which traffic through the recycling endosome like hTfnR and hTAC accumulate in the BRE, but in *amph*-1 knockdowns both yolk endocytosis and fluid phase recycling is not affected [145]. Additionally, in either *amph-1* knockdown or *amph-1* NPF mutant worms, RME-1 remains cytosolic and does not localizes to the BRE [145]. These results strongly suggest that AMPH-1 plays a role in fission at the recycling endosome and furthermore is required for fission in the RME-1 pathway.

### Receptor mediated endocytosis 1

Receptor mediated endocytosis 1 (RME-1) is a member of a family of proteins known as EH domain proteins for a conserved Eps15 homology domain. This family includes the mammalian Eps15 homology domain 1-4 proteins (EHD1-4), fly (*Drosophila melanogaster*) Past1, and lamprey (*Lampetra fluviatilis*) 1-EHD. The members of this protein family have an N-terminal G-domain, a coil-coil region, and a C-terminal EH domain and are part of the dynamin superfamily (Figure I.13A). Like other members of the dynamin superfamily, these proteins bind and tubulate liposomes made of anionic phospholipids, weakly bind nucleotide tri-and diphosphates, and display a slow rate of hydrolysis, which is increased in the presence of liposomes [145, 146]. Unlike other members of the dynamin superfamily however, the EH domain containing family bind to ATP, rather than GTP [146, 147].

Although RME-1 has been studied *in vivo*, little is known about how this protein acts to remodel membranes. By contrast, the mammalian EHD proteins have been extensively studied, both for structurally and functionally [146, 148, 149]. The high sequence homology between RME-1 and the EHD proteins (greater than 61%) strongly suggest that RME-1 possesses a structure that is very similar to the known EHD structure. The EHD proteins form dimers in solution and appear to be capable of substantial conformational changes, shifting from a closed to an open structure (Figure I.13B-C) [146, 150, 151]. This conformational change is dependent on the N-terminal region, as deletion of this segment appears to lock the dimer in the open conformation independent of bound nucleotide. Surprisingly, however, N-terminal deletion appears to have no impact on function as these mutant EHD proteins are able to bind to liposomes with similar tubular morphologies as the wild type protein, and hydrolyze ATP at a comparable rate. This suggests that the N-terminus acts as a regulator of EHD function [150, 151]. It has been suggested that the EHD proteins exist in a closed conformation in solution and undergo a conformational change to the open state upon binding to membranes. The proposed model for the function of the EHD proteins is that they oligomerize on the membrane in the open state and upon ATP hydrolysis they dissociate from the membrane (Figure I.13D).

The precise role of the RME-1 specifically and the EHD proteins more generally in membrane fission is controversial. *In vivo*, the EHD1 and EHD3 proteins localize to the TREs in non-polarized cells, and EHD2 localizes to caveolae at the plasma membrane [148, 152, 153]. The EHD1 and EHD3 have very high sequence homology (81% identity) but are proposed to have two different functions at the TRE [149]. *In vivo*, EHD1 is proposed to act in membrane fission, whereas EHD3 is been proposed to stabilize the tubular structure of the TREs [148, 149]. Consistent with this result EHD1 has been shown to induce fission of preformed lipid tubules [154]. By contrast, however, on liposomes, the lamprey homolog 1-EHD does not cause fission, but rather appears to regulate the fission activity of dynamin-1 [155]. It was suggested that 1-EHD regulates the length of the dynamin-1 oligomers, preventing dynamin-1 from forming excessively long tubules. Consistent with this model, EHD1 is able to regulate the length of transverse tubules generated by the N-BAR protein, Bin1, in mouse (*Mus musculus*) muscles [156]. EHD2 also appears to act as a regulator at the caveolae to regulate their dynamics [153]. The precise role played by the EHD proteins in membrane fission remains to be fully resolved.

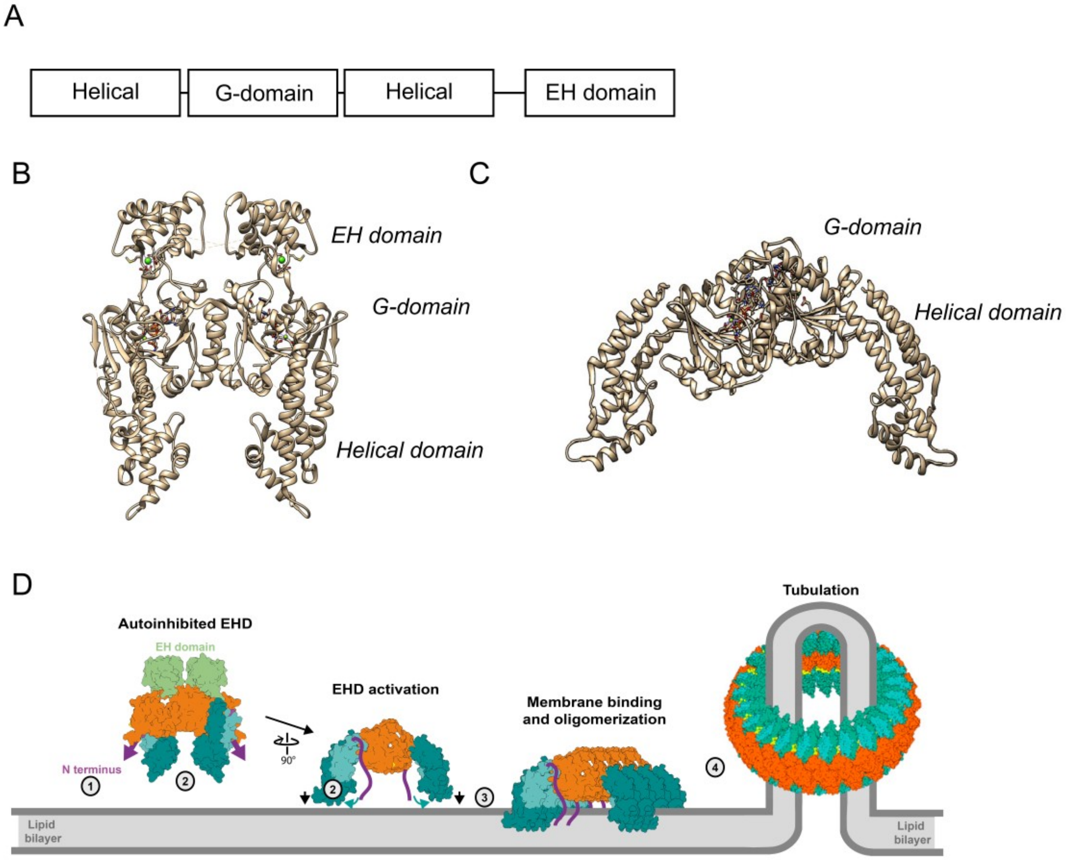

**Figure I.13 EH domain protein structure and activated model.** **Domain architecture of EH domain proteins (A). Structure of AMP-PNP bound EHD2 in the closed conformation (PDB ID 2QPT) (B). Structure of the open conformation of the N-terminus deletion of EHD4 bound to ATPγS (PDB ID 5MTV)(C). Model of EHD membrane binding and activation (D). Membrane insertion of N-termini (1), EHD undergoes a conformational change (2) EHD binds to the membrane and oligomerizes (3), EHD oligomerization generates membrane tubules (4). (Reprinted from [150]).**

## Amphiphysin 1

Amphiphysin 1 or AMPH-1 in *C. elegans*, is member of the N-Bin-Amphiphysin-RVS, or N-BAR, containing protein superfamily [145]. Other members of this superfamily appear to generate and stabilize membrane curvature, through a combination of membrane binding, scaffold assembly and the insertion of an N-terminal amphipathic helix into the membrane [157]. Many of the proteins in this family are involved with both CME, and clathrin independent endocytosis [18, 158-160]. N-BAR proteins also have functions that are not related to endocytosis, rather they are found to stabilize membrane curvature of transverse tubules, and act as regulators of autophagosome formation [161-163]. While it is known that AMPH-1 is involved in basolateral recycling, and can generate membrane curvature on model membranes *in vitro*, little else is known about this protein, however since it is included in this protein family, it is likely that it acts like other N-BAR proteins.

The founding member of the N-BAR protein family, amphiphysin, plays an important role in CME. Amphiphysin was initially identified through its association with synaptic vesicles and its role in CME thus became an area of intense interest [164]. N-BAR proteins contain four different segments an amphipathic helix, a BAR domain, a linker region, and a Src homology domain 3 (SH3) (Figure I.14). The linker region of amphiphysin, a segment of no known structure, contained a clathrin binding sequence. The SH3 domain binds to proteins that contain a proline rich consensus sequence [76] [165]. *In vivo*, it has been observed that binding of the proline rich domain (PRD) of dynamin-1 to the SH3 domain of amphiphysin appears to be required for fission during CME, as disruption of this interaction prevented dynamin-1 from localizing to the neuronal membrane [76, 79]. Based on these observations, it has been suggested that amphiphysin acts to recruit the essential fission protein dynamin-1 [79].

The N-terminal domain of amphiphysin is highly homologous to similar domains in the *S. cerevisiae* proteins Reduced Viability upon Starvation 161 and 167, or Rvs161/167p [166], and to the Myc box-dependent-interacting protein 1, or Bin1, giving this domain the name BAR. *In vitro* experiments have shown that the BAR domain can generate membrane curvature on liposomes and induce formation of narrow tubules with diameters between 20-40 nm [167]. Importantly, the ability of amphiphysin to form tubules was sensitive to the lipid composition of the membranes, where the number of tubules was correlated with the concentration of negatively charged phospholipids in the model membrane [167]. This work suggests that the N-terminus BAR domain was responsible for membrane binding and the generation of membrane curvature *in vitro*.

Additional insight into how the BAR domains generate membrane curvature was revealed by structural studies of the N-terminus of amphiphysin. The BAR domain formed from triple helix coiled-coil, each of which possesses kinks that cause the domain to have a pronounced to curve (Figure I.14B-C). At the same time, the BAR forms dimers, resulting in an overall dimeric BAR domain that displays a crescent, or banana-like structure [32]. The concave face of the BAR domain is highly enriched in basic residues, which bind to anionic phospholipids [32]. It remains unclear whether the dimerized BAR domain forms a rigid or flexible structure. Mutations designed to increase the flexibility of the domain decreased the ability of the BAR domain to bind membranes [168]. Overall, the members of the BAR superfamily appear to be structural homologs, rather than sequential homologs. Consequently, they are further and categorized into subfamilies based on the intrinsic curvature of the BAR domain, as well as other unique structural characteristics.

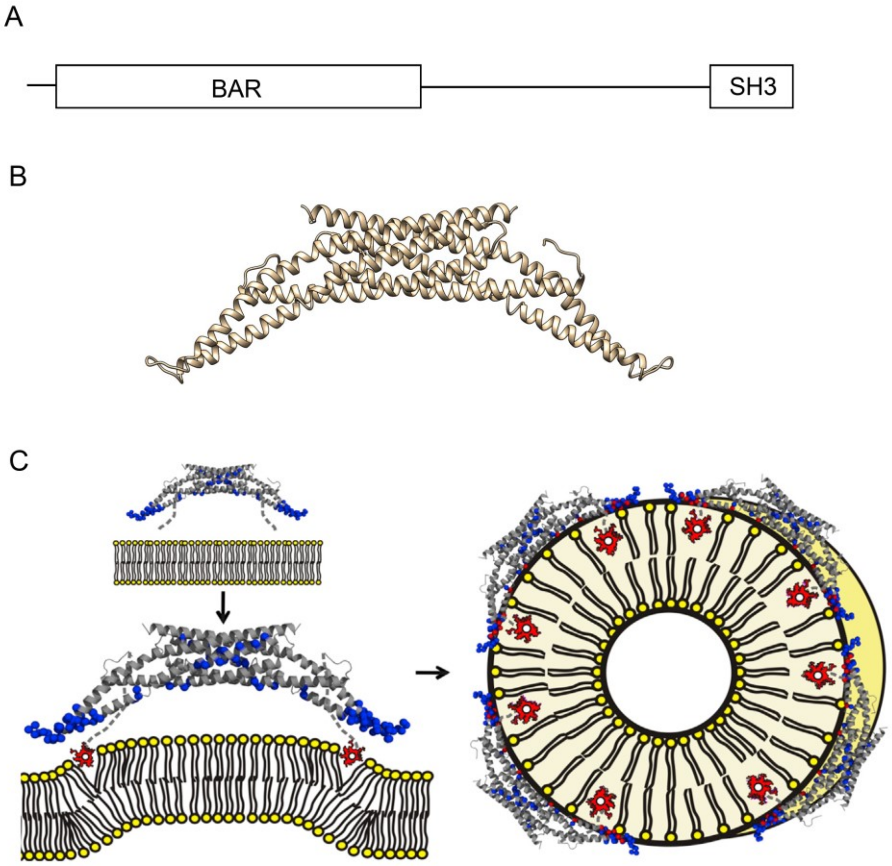

**Figure I.14 N-BAR domain structure and function.**(A**) The domain architecture of AMPH-1. (B) Structure of the BAR domain of amphiphysin. (C) Amphiphysin binds to a lipid bilayer through helix insertion, and oligomerizes to generate membrane tubules. (Reprinted with permission from [41])**

The unique structural element that defines the amphiphysin-like subclass of the BAR domain containing family is a distinctive, amphipathic N-terminal helix. In free solution, the N-terminal amino acids appear to be unstructured. However upon binding to membrane, this segment of the protein appears to fold into an alpha helix, with the hydrophilic face interacting with the lipid head groups while the hydrophobic face inserts into the lipid hydrophobic layer [33, 157]. As noted above, insertion of an amphipathic helix of this type may act a wedge to generate membrane curvature (see Section Shallow insertions into the bilayer). In the membrane-bound structure of the N-BAR protein endophilin, the amphipathic helices are in close proximity to one another and potentially interact [169]. These observations have led to the hypothesis that interactions between the N-terminal helices are important to stabilize the oligomeric form of N-BAR proteins on the membrane [169, 170]. By contrast, endophilin mutants in which the N-terminal helix was deleted could still bind to and tubulate liposomes though they also displayed a decrease in affinity for membrane [32, 171]. These observations led to a competing hypothesis where the amphipathic helices are suggested to recruit the N-BAR proteins to the membrane, but have little impact on the ability of these proteins to generate membrane curvature. Even so, significant evidence shows that the result, amphipathic helices are important for the function of the N-BAR proteins *in vivo*. For example deletion of these helices in RVS161/167p reduced the endocytic uptake of an extracellular dye [172].

In addition to causing curvature, N-BAR proteins have also been observed to induce membrane fission. In early studies fly amphiphysin, and rat (*Rattus norvegicus*) endophilin were shown to generate a mixture of tubules and vesicles when incubated with large unilamellar vesicles (LUVs). At the same time in the presence of high concentrations of either amphiphysin or endophilin only vesicles are produced [32, 157]. RVS161/167p is also capable of generating both tubules and vesicles when incubated with liposomes created with a lipid composition similar to that of the yeast plasma membrane [172]. It has been suggested that even though the proteins can in principle, generate vesicles, their rigid structures normally prevents this [40]. The observation of fission at high concentration has been suggested to be an artifact of protein packing defects [159, 173]. Even so, substantial membrane fission activity has been reported with some N-BAR proteins. For example, incubation of phosphorylated endophilin with large unilamellar vesicles results in many small vesicles based on transmission electron microscopy (TEM imaging, while only tubules were observed with the unphosphorylated protein [42]. Likewise, the incorporation of PI(4,5)$P_2$ into a model bilayer induces Bin1 isoform 10 to produce large numbers of small vesicles, while in the absence of PI(4,5)$P_2$, only tubulation is observed [174]. It is apparent N-BAR proteins are capable of membrane fission, but what distinguishes or controls the difference between simple curvature generation and fission remains unclear.

### Possible mechanisms of membrane fission by either AMPH or RME-1

Taken all together, the data outlined above suggest two likely models of membrane fission at the basolateral recycling endosome. First, RME-1, as a dynamin family member, could act as the central fission machinery. In this model, AMPH-1 would bind to the membrane first, and would act to recruit RME-

1 to the basolateral recycling endosome, consistent with the localization of dynamin-1 by amphiphysin to the plasma membrane during CME. RME-1 would then undergo a conformational change upon the hydrolysis of ATP, which would provide the mechanical force for fission [150, 151]. Consistent with these ideas, EHD1 causes fission on membrane tubules (Figure I.15A) [154]. In the second model, it is AMPH-1 that serves as the core fission machinery, with the N-terminal amphipathic helices playing a critical role (Figure I.15B). Consistent with this model previous work, as outlined above, has shown that N-BAR proteins are capable of membrane fission *in vitro* [42] [40, 174]. In this model RME-1 would act as a regulator of AMPH-1 an activity similar to how the 1-EHD is proposed to regulate dynamin-1 [155]. A central goal of the work presented in this dissertation is to put these two models of regulated membrane fission to a test (Chapter IV).

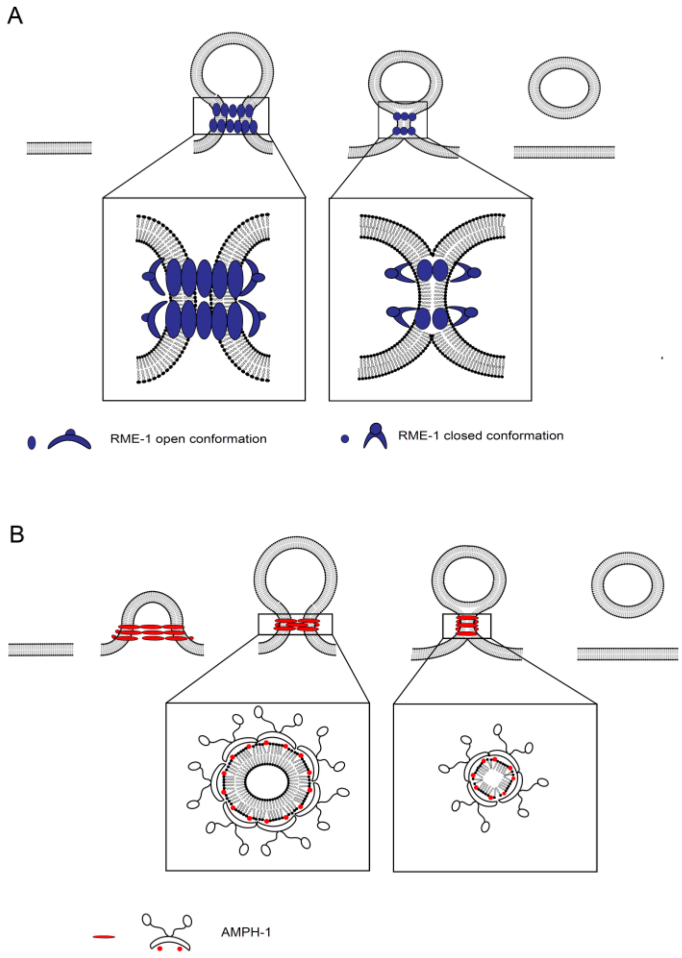

**Figure I.15 Models for the mechanisms of membrane fission at the basolateral recycling endosome. (A) RME-1 binds the lipid bilayer and generates curvature. Upon ATP hydrolysis it undergoes a conformational change which results in membrane fission. (B) AMPH-1 binds to the lipid bilayer, and creates high curvature. The amphipathic helix insertion causes constriction and fission.**

### Methods to measure membrane fission

The proteins responsible for membrane fission were initially characterized *in vivo*. To gain a detailed understanding of the mechanism of fission requires the development of precision *in vitro* assays [71, 143, 175]. One of the most commonly employed methods; negative stain transmission electron microscopy [176] is simple and permits direct observations of the consequences of proteins interacting with model membranes. TEM has provided key insights into the functional role of fission-associated proteins, importantly demonstrating tubulation activity by the N-BAR proteins and the fission activity of dynamin-1 [167] [82]. However, TEM provides little quantitative information. As an alternative sedimentation-based assays have been used. In this type of assay, model membranes labeled with a fluorescent lipid, are incubated with the protein of interest. Starting liposomes and fission products are separated by their different sedimentation behavior. Typically, the supernatant from a centrifugation run is examined for fluorescence in relative to a control without protein. While this approach is more quantitative, it provides no information on the population distribution of fission products, and cannot be used reliably to follow reaction rates.

More recently, significantly more powerful and flexible methods for examining fission have been developed. Numerous approaches involving the pulling of membrane tubules from giant unilamellar vesicles (GUVs), either by optical traps or micromanipulators has been described [26, 92, 177-180]. While these assays can provide valuable insight certain aspects of protein-tubule interactions into some proteins interaction with membrane tubules there are sever limitations to these methods. The small number of events observed in the tubule-based assays results in poor coverage of the product distributions, and limited ability to probe the kinetics of the membrane fission reaction. A different single particle approach that uses tethered liposomes, can quantitatively measure size of the products, but cannot quantify the species concentration distributions of fission products [181]. In order to develop a more detailed and mechanistic understanding of membrane fission, a new type of single particle assay is needed. A second goal of this dissertation is the development of a novel approach to quantitatively study of membrane fission reactions (Chapter III).

## Dissertation overview

The main research objective described in this dissertation is to identify the minimal machinery required for membrane fission at the recycling endosome of *C. elegans*. Chapter II covers methods that are used though out the subsequent chapters. In Chapter III, a new method to measure membrane fission is validated, Burst Analysis Spectroscopy (BAS). Chapter IV uses BAS to measure the fission activity of two key proteins required for membrane fission at the recycling endosome of *C. elegans*, Amphiphysin-1 (AMPH-1) and Receptor Mediated Endocytosis-1 (RME-1).

Chapter III uses the well characterized fission protein N-terminal domain of epsin, the ENTH domain, to validate a single particle fluorescent based method known as Burst Analysis Spectroscopy (BAS). Previous observations have shown the ENTH domain is a potent fission agent which causes membrane fission through the insertion of an amphipathic helix into the membrane [40]. Using the ENTH domain we were able to validate BAS as a method to measure membrane fission. Furthermore, we also were able to see fission by epsin, a previously uncharacterized function.

In Chapter IV, BAS is used to identify AMPH-1 as a fission agent. The fission activity of AMPH-1 is enhanced in the presence of GTP, a surprising result as AMPH-1 does not have a known GTP-binding domain. The fission activity of AMPH-1 is mediated through the amphipathic helices. Additionally, the *S. cerevisiae* homolog of AMPH-1 Reduced Viability upon Starvation 161/167 (RVS161/167p) also has GTP-stimulated membrane fission activity. These results suggest GTP-stimulated membrane fission may be a common function of amphiphysin proteins. Finally, RME-1 is shown to regulate the fission activity of AMPH-1.

# CHAPTER II

# METHODS

## Purification of the ENTH domain of epsin

The ENTH domain of Epsin was expressed and purified as previously described [39]. The coding sequence of the epsin ENTH domain (residues 1–164) from *Rattus norvegicus* was obtained from Addgene and was sub-cloned into the pPROEX HTb vector for expression in *E. coli* BL21. In brief, clarified lysates were run on a Ni-NTA column equilibrated with column buffer (20 mM Tris pH 8.0, 500 mM NaCl, 20 mM imidazole, 5 mM β-mercaptoethanol) and eluted with a step gradient of the same buffer, plus 500 mM imidazole. ENTH-domain containing fractions were pooled and dialyzed against column buffer with 0.4 μM $His_6$-TEV protease. $His_6$-TEV and the $His_6$-tag were separated from the untagged protein using the nickel affinity column. Untagged ENTH domain from the flow-through was further purified by ion exchange chromatography on a Source S column equilibrated in Source S Buffer A (20mM Tris pH 7.4, 2 mM DTT) and eluted with a linear gradient of Source S Buffer B (20 mM Tris pH 7.4, 2 M NaCl, 2 mM DTT). Purified ENTH was stored at -80°C, in 20 mM Tris pH 7.4, 150 mM KCl, 2 mM DTT.

**Liposome preparation**

Liposomes were prepared as previously described with modifications [145]. Experiments using the Folch fraction of brain total lipid extract, mixed Folch extract from Avanti Polar Lipids (cat. 131101), and Folch extract from Millipore Sigma (cat. B1502), at a 1:1 ratio with 5% brain extract phosphatidylinositol (4,5) bisphosphate (PI(4,5)$P_2$) (Avanti cat. 840046), and 0.3% acyl-chain, Ω-carbon labeled Top-Fluor phospatidylethanolamine (TopFluor PE) (Avant, cat. 810282C). Brain extract phosphatidylserine (PS) (Avanti, cat. 840032) was mixed with either 0.3% Top-Fluor PE, for single color BAS experiments or 0.06% Vybrant DiD (Invitrogen, cat. V22887) for MC-BAS experiments. The complex mixture of lipids, mixed 70% brain extract PS, 10% 18:0-20:4 phosphatidylcholine (PC) (Avanti cat. 850469), 10% egg extract phosphatidic acid (PA) (Avanti, cat. 840101), 5% brain extract PE (Avanti cat. 840022), 5% brain extract PI(4,5)$P_2$ and 0.3% Top-Fluor PE.

Lipids were first dried as previously described [145]. The lipids dried were then resuspended in argon sparged liposome extrusion buffer (50 mM Hepes pH 7.4, 150 mM NaCl) to a final concentration of 1 mg/ml for Folch extract membranes. For all other experiments, the lipids were resuspended to 1 mM in extrusion buffer containing 25 mM KCl. To hydrate the lipids evenly, the suspension underwent 10 rounds of freezing in liquid nitrogen followed by thawing, in hot water at temperatures between 52-60°C. Unilamellar Liposomes were extruded to 200 nm in an Avanti Mini-extruder by 11 rounds of passing the liposome suspension through a Whatman Nuclepore track-etched polycarbonate filter with a pore size of 200 nm. The liposomes were then passed 10 times through a high-pressure Lipex manifold extruder (Transferra, Canada) using Whatman Nuclepore track-etched polycarbonate filter with a pore size of 200 nm. The liposome suspension was centrifuged at 20,000 x g for 30 min at 21°C to remove small contaminating liposomes. The supernatant was removed, and the pellet was gently resuspended in liposome extrusion buffer. The sedimentation step was used for experiments in Chapter IV.

For experiments using liposomes smaller than 200 nm, the same protocol to make 200 nm liposomes was initially followed. After resuspension of the 200 nm liposomes, the liposome solution was further extruded in an Avanti Mini-extruder by 11 rounds of passing the liposome suspension through a Whatman Nuclepore track-etched polycarbonate filter with pore sizes of 30, 50, or 100 nm. Liposomes extruded to a diameter of 1 μm where hydrated as previously described and extruded in an Avanti Mini-extruder by eleven rounds of passing the liposome suspension through a Whatman Nuclepore track-etched polycarbonate filter with a pore size of 1 μm. The liposome suspension was centrifuged as described for the 200 nm liposomes.

### Single particle detection platform

The single particle detection platform was custom built and configured as descried in detail elsewhere [182]. Briefly, the single particle detection system is constructed around a Nikon Eclipse Ti-U inverted microscope, with a 60x/1.4NA CFI Plan Fluor oil immersion objective. The base of the microscope is coupled to a 3-channel fiber combiner (PSK-000843; Gould Technologies), which couples two diode lasers (488 nm and 642 nm; Omicron) and one diode-pumped solid laser (561nm; Lasos). The combined output is directed into the sample objective with a custom, triple-window dichroic filter (Chroma). The microscope is fitted with a 2-axis stepper motor sample stage (Optiscan II; Prior), which allows movement of the stage. The data is recorded with three independent detector channels, which are configured with an optimized band-pass filter set for wavelength selection and low noise, single photon counting avalanche photodiode unit (SPCM-AQRH-15; Excelitas). Either a multichannel hardware correlator (correlator.com) or a high speed Transistor-Transistor-Logic counting board (NI9402; National Instruments), is used to collect and time stamp photon pulses. Control of the laser power, stage, as well as the collection of the data is done in LabView (National Instruments) (Figure II.1).

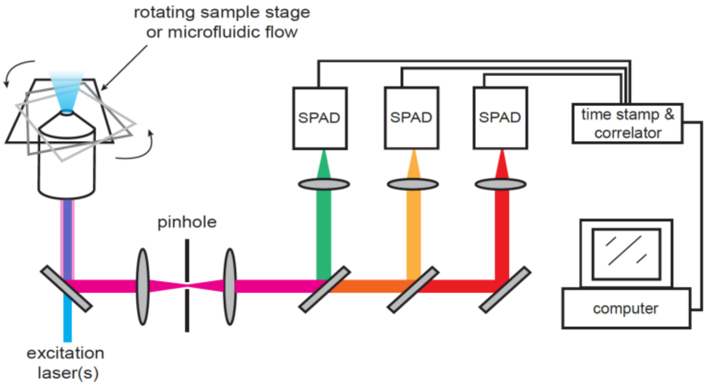

**Figure II.1 Single Particle Detection Platform. Schematic of the single particle detection platform. Burst measurements were taken using a confocal microscope with a rotating stage. Fluorescent particles are excited with one or more co-aligned lasers, and detected in independent detector channels with single photon counting avalanche photodiodes (SPADs). Photon pulses are recorded and time stamped in LabView.**

### Processing of raw intensity data

The raw fluorescent data is collected and time stamped by the single particle detection platform and assembled as a single data in LabView (National Instruments). All data from a single experiment contained at least 3 minutes of data per reaction. All data was processed using a suite of custom Matlab programs. In all cases, background correction of raw photon history data sets was accomplished by first measure the room mean square (rms) inter-burst baseline level for the data set. This value was multiplied by a factor of five and subtracted from the entire photon history data record. A threshold of five times this baseline level was then used as the minimum discriminator for subsequent fluorescent burst detection.

**Burst analysis spectroscopy**

Burst Analysis Spectroscopy (BAS) allows for the measurement of the size distribution of low concentration of fluorescent particles in free solution. Unlike other single particle methods, BAS does not rely on diffusion of these particles into the excitation volume. Rather BAS uses advective flow which allows these particles to transverse the excitation volume [182]. The stage of the confocal microscope is rotated, at a linear velocity of 500 microns/sec, achieving an adjective transport rate much faster than diffusion of large (> 5 nm) particles [182]. The probability of the objects traversing the excitation volume along different paths can be modeled to determine the size and concentration of fluorescently labeled objects in the reaction.

The raw fluorescence data is collected and time stamped by the single particle detection platform, resulting in fluorescent intensity versus time (Figure II.2A). The signal from a single particle crossing the excitation volume is called a burst (Figure II.2A inset). As each particle transverses the excitation volume, the signal intensity will increase as the particle enters the excitation volume and a decrease as the particle leaves it, with the highest intensity at the central plane where the laser intensity is highest [182]. The burst intensity is dependent on both the total signal from the fluorescent particle and where the particle crosses the beam. In a single uniformly bright population, it would be expected that the burst intensity from an object crossing the beam at the area of highest excitation intensity would produce a larger burst than an object crossing the beam at an area of low excitation intensity (Figure II.2B). With knowledge of the optical point spread function (psf) the probability of particles crossing different regions of the excitation volume can be predicted

The detected bursts are initially binned and plotted as a cumulative histogram, using log (burst amplitude) versus log (number). A logarithmic scale is used because there is a higher probability of objects crossing the excitation volume at areas of low excitation intensity. Importantly, the burst amplitude range is limited to approximately 100-fold due to incomplete knowledge of the psf [182]. In a single uniform population, the cumulative histogram for a Gaussian-Lorentzian excitation volume is equivalent to a power law of known index, which refer to as the microscope characteristic function this can then be used to describe the individual populations in a corrected histogram (Figure II.2C-D) [182].

In a heterogeneous sample, assuming all objects cross the excitation volume randomly, the largest burst could only come from the brightest object crossing the excitation volume in its center. The average number of objects of the same brightness going through the excitation volume at various points can then be estimated from the known characteristic function, and these events would be effectively removed from the overall burst data set. After the removal of the first population, the next largest burst would be from the second largest object crossing the excitation volume at the center (Figure 2E). The average number of objects can likewise be obtained using the characteristic functions and removed from further analysis. Operationally, this process can be visualized as the fitting a linear combination of weighted power law curves to the overall cumulative histogram of raw burst data. The resulting weighting factors are directly proportional to the underlying species concentrations and can be used to construct a corrected histogram that describes the underlying intensity distributions of the sample (Figure II.2F). If the relationship between brightness and size is known, the corrected histogram gives a direct measure of size versus object number. Using known geometry of the confocal volume, the observed concentration of each species can then be calculated as follows.

$$\mathrm{C} = \frac{\mathrm{Md_v}}{\mathrm{TvAV}}$$

Where M is the total number of burst events in the sample, $d_v$ is the diameter of the excitation volume (1.1 μm), T is time, v is the flow rate of the sample (0.5 mm/sec), A is Avogadro's number, and V is the volume of the excitation volume (1.8 $\mu m^3$).

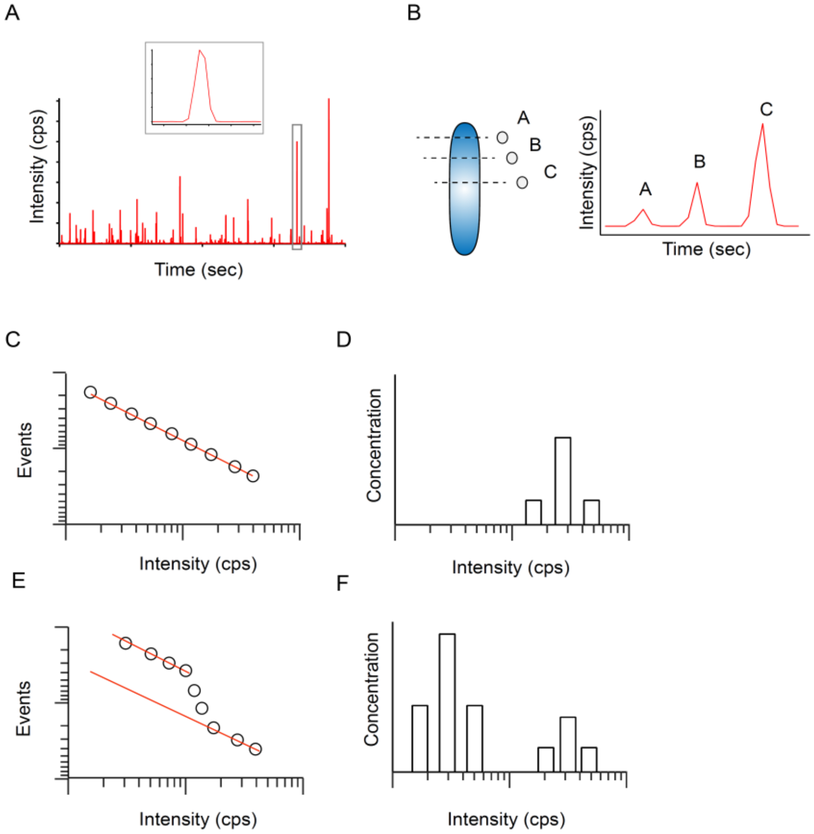

**Figure II.2. Single Particle Analysis. (A) Fluorescent burst data, with a single burst event shown in the inset. A schematic of the Gaussian-Lorentzian excitation profile. (B) A uniform population of objects transverse the excitation volume through areas of different excitation intensity resulting in various sized bursts intensities. (C) A simulated cumulative histogram of a uniform population of fluorescent objects fit to a power law (red). (D) The corrected histogram from a single uniform population of fluorescent objects. (E) A simulated cumulative histogram from a population of fluorescent objects with two unique populations fit to two power laws (red). (F) The corrected histogram from a heterogeneous population, containing two subpopulations of fluorescent objects.**

**Concatenated BAS**

Concatenated BAS or cBAS is performed as described [39, 183]. An important limitation of standard BAS is that the particle intensity range cannot exceed 100-fold. Another important constraint is that no particle species being analyzed can exceed single particle concentrations (>50 pM for the confocal geometry used here). As fission reactions can generate high concentrations of small products that are well outside the 100-fold intensity standard BAS cannot accurately measure the full population-resolved kinetics of a fission reaction (Figure II.3A). cBAS was developed to overcome these limitations. By diluting a reaction, the brightest objects are reduced, and dim objects at high concentration found in the baseline of the raw data, are resolved. The dilution factor is not a set value for all reactions but is chosen based on the ability to remove large objects and resolve small dim objects. The cumulative histogram from the diluted sample must have significant intensity overlap with the undiluted sample.

After initial processing to remove the background fluorescence, data from diluted and undiluted samples are combined to make a cumulative histogram (Figure II.3B). To concatenate the data a best-fit scale factor is determined for the overlap region by weighted least squares regression. The diluted data is multiplied by this factor creating a cumulative histogram with three regions, (1) the corrected diluted region, (2) the overlap region and (3) the undiluted region

(Figure II. 3C). This corrected, or “stitched” cumulative histogram can then be used to create the corrected histogram as described for standard BAS.

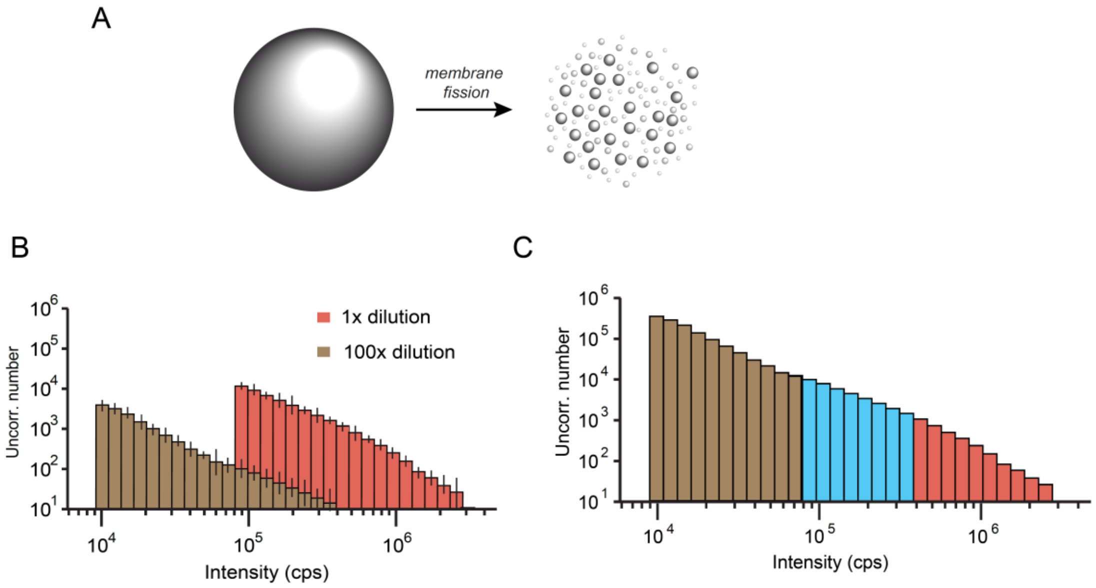

**Figure II.3. Concatenated BAS. (A) A schematic of the membrane fission reaction, one large liposome becomes many small vesicles. (B) Simulated cumulative histograms of the reaction diluted (brown) and undiluted (pink). The corrected cumulative histogram, with the corrected dilution region (brown), the overlap region (blue), and the undiluted reaction (pink).**

## Multicolor BAS

Multicolor BAS or MC-BAS is a multi-channel extension of BAS that can simultaneously determine both size and stoichiometry distributions [183]. MC-BAS utilizes two fluorescently labeled objects, excited at two different wavelengths, to measure the binding of a protein or peptide to a liposome. MC-BAS uses the same single particle detection platform as single color BAS, but uses at least two co-aligned lasers to excite the sample with at least two SPADs to record the bursts in each channel (Figure II.4A). Bursts are categorized as either coincident or non-coincident. Non-coincident bursts are those that are found only in one channel, can be analyzed as described for standard BAS. For a given stoichiometry, the ratios of the burst intensities are approximately independent of where the complex crosses the excitation volume (Figure II.4B). Coincident bursts are sorted by the ratio of the intensities. After sorting, the events within a ratio bin are analyzed as described for standard BAS. The corrected burst histograms are plotted in a heat map, with intensities plotted on a logarithmic scale for both x and y axes and the concentration of objects are proportional to color intensity (Figure II.4C). For these two-dimensional, log-log MC-BAS plots, regions of fixed stoichiometry follow the positive diagonal of the plots.

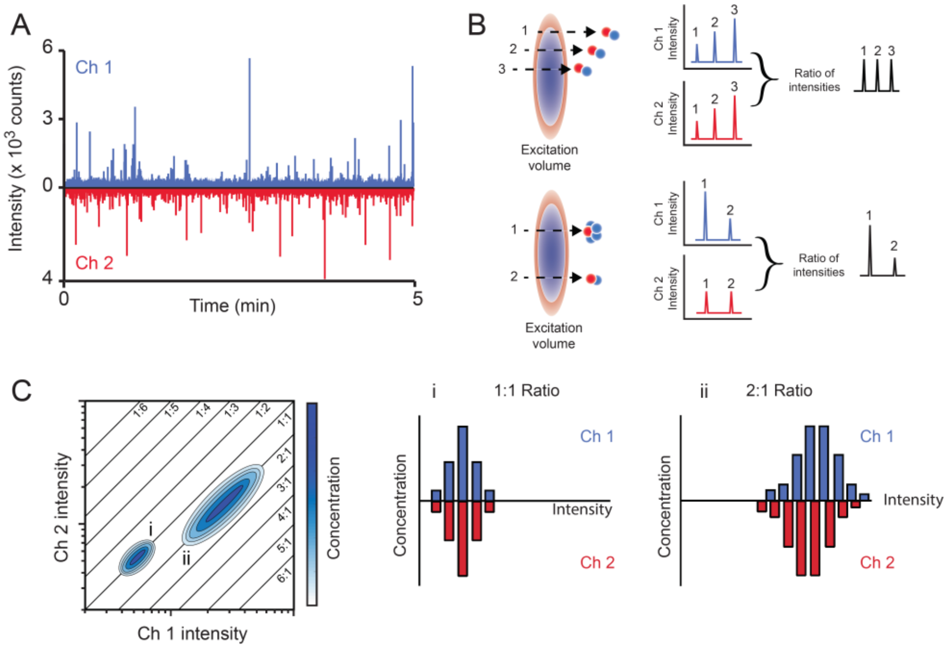

**Figure II.4. Multicolor BAS. (A) The raw fluorescent bursts of two different fluorescently labeled objects. Schematic of a Gaussian-Lorentzian excitation volume, with objects excited by two different wavelengths transversing the excitation volume. (B) Simulated bursts based on the crossing trajectory, and number of fluorescent molecules, and the ratios if intensities of the simulated bursts. Corrected histograms simulating a 1:1 binding (i), and a 2:1 binding (ii) of objects in channel 1:channel 2, which are plotted on the heat map.**

### Coverslip blocking protocol

The approach used to passivate the surface of coverslips and prevent sample sticking is essentially the same as previously described, with some modifications [182]. Round boro silicate glass coverslips were obtained from Ted Pella Inc. (cat. 26021). Coverslips were washed with Helmanex III (Helma Corp), for 45 minutes at room temperature. The coverslips were then extensively rinsed, by incubating the coverslips in water for at least 5 minutes after which the water was exchanged; this was repeated for a total of 9 exchanges, with three rounds in tap, distilled then high quality MilliQ water. Coverslips were then blocked for 4 hours with 10 mg/ml bovine serum albumin, BSA (Sigma cat. 3059) in blocking buffer (50 mM sodium phosphate pH 7.0, 200 mM KCl) at room temperature. Each coverslip was rinsed under tap water, distilled water, and MilliQ water to remove excess BSA. Coverslips were dried under a stream of nitrogen and stored for up to one month after blocking, at room temperature.

### Membrane fission assay using BAS

All BAS fission measurements were conducted using BSA blocked coverslips, which are secured into custom made sample holder. Coverslip assemblies were rotated at 0.5 mm per second. Typical sample volumes were between 10-15 μl per reaction, which were covered with a humidity-maintaining cap to prevent evaporation. Data was collected for 3 or 5 minutes per sample, at 0.5 microseconds per data bin. For cBAS data 8 minutes of data was taken for each reaction.

# CHAPTER III

# SINGLE PARTICLE BURST ANALYSIS OF EPSIN INDUCED MEMBRANE FISSION*

## Summary

Vital cellular processes, from cell growth to synaptic transmission, rely on membrane-bounded carriers and vesicles to transport molecular cargo to and from specific intracellular compartments throughout the cell. Compartment-specific proteins are required for the final step, membrane fission, which releases the transport carrier from the intracellular compartment. The role of fission proteins, especially at intracellular locations and in non-neuronal cells, while informed by the dynamin-1 paradigm, remains to be resolved. In this study, we introduce a highly sensitive approach for the identification and analysis of membrane fission machinery, called burst analysis spectroscopy (BAS). BAS is a single particle, free-solution approach, well suited for quantitative measurements of membrane dynamics. Here, we use BAS to analyze membrane fission induced by the potent, fission-active ENTH domain of epsin. Using this method, we

---

* Reproduced with permission from Brooks A., et al (2015) PLoS One 10(3). Copyright 2015. For the original publication: LK provided reagents, performed and analyzed data in Figure III.4 and contributed to the writing of the manuscript.

obtained temperature-dependent, time-resolved measurements of liposome size and concentration changes, even at sub-micromolar concentration of the epsin ENTH domain. We also uncovered, at 37°C, fission activity for the full-length epsin protein, supporting the argument that the membrane-fission activity observed with the ENTH domain represents a native function of the full-length epsin protein.

## Introduction

The parting and merging of lipid bilayers, as occur in vesicle budding (membrane fission) and in the delivery of vesicle contents to a target compartment (membrane fusion), are irreversible events. In order to impart specificity to the timing and integrity of each of these membrane remodeling events in the cell, proteins specialized to catalyze fission and fusion have evolved, as have regulatory factors, thus preventing indiscriminant events that would lead to intracellular disorganization [18, 184, 185].

While much progress has been made in the characterization of membrane fusion proteins [186, 187], an understanding of the mechanism of membrane fission remains limited [18, 54]. In part, this is due to the technical constraints of current methodologies. Bulk biochemical methods (such as sedimentation; [38, 40], tend to be inefficient, slow and provide only an estimate of the average observable activity of a complex system. While imaging methods can, in principle, circumvent this problem, to date these studies have either required intact cells, where detailed biochemical analysis of a system is not possible [188-191], are constrained by small event numbers [192], suffer from limited knowledge of population distributions and sampling bias, or are affected by surface perturbations of tethered objects [40, 85]. Here we develop an alternative approach to the study of membrane fission, in which we apply a single particle fluorescence technique called Burst Analysis Spectroscopy (BAS); [182]. BAS permits analysis of the dynamics of complex particle distributions in free solution, including populations of liposomes undergoing fission. As a test of the utility of this approach for studying membrane fission, we have applied BAS to the study of changes in size and concentration of liposomes over time, when mixed with the simple, fission-potent, epsin N-terminal homology domain [40].

Epsin is a 94 kDa protein, identified in screens for binding partners of α-adaptin and Eps15, both clathrin coat associated proteins involved in clathrin-mediated endocytosis in neurons [193, 194]. Epsin is generally believed to function in cargo selection and bud site nucleation, through direct interactions with Eps15, the clathrin adaptor protein, AP-2, endocytic cargo and with clathrin, itself (reviewed in ref.[195]). At the amino terminus of epsin is the highly conserved, ~140 amino acid ENTH domain shared with other endocytic proteins, including AP180/CALM [196]. This domain contains an N-terminal amphiphathic helix (the $H_0$ helix), which is known to insert into the outer-leaflet of membranes in a PtdIns(4,5)$P_2$-dependent fashion [34].

Membrane insertion of the $H_0$ helix is thought to facilitate membrane curvature and tubulation, prior to fission.

Recently, it was suggested that insertion of the ENTH $H_0$ helix into a lipid bilayer could directly facilitate fission [40]. This work reported potent fission activity when liposomes were mixed with the isolated ENTH domain, though full-length epsin did not appear to possess fission activity. Recently, the conclusions derived from those results have been called into question: the observed ENTH-domain activity was suggested to be an artifact of a non-native protein domain at high concentration interacting non-specifically with liposomes to generate small vesicles and/or micelles [38].

Here we have reexamined liposome membrane fission mediated by the ENTH-domain and full-length epsin protein with BAS. We find that the rate of membrane fission by the ENTH domain is sensitive to both temperature and protein concentration, and that fission activity can be observed at a sub-micromolar protein concentration, comparable to studies of dynamin-2 [38]. By exploiting the inherent sensitivity of BAS, we also observed measurable membrane fission activity for full-length epsin, albeit attenuated when compared to the ENTH domain. These observations not only support the argument that membrane fission is a function of full-length epsin, but also demonstrate that BAS offers a flexible and highly sensitive approach to the study of membrane dynamics.

## Experimental procedures

*Abbreviations*—BAS, Burst Analysis Spectroscopy; TIRF, total internal reflection; ENTH, epsin N-terminal homology; IPTG, isopropyl thiogalactose; DTT, dithiothreitol; FCS, fluorescence correlation spectroscopy; PtdEth, phosphatidylethanolamine; PtdChl, phosphatidylcholine; PtdIns, phosphatidylinositol; P, phosphate.

### *Protein expression and purification*

The coding sequence of the epsin ENTH domain (residues 1–164) from *Rattus norvegicus* was obtained from Addgene and was sub-cloned into the pPROEX HTb vector [197] for expression in *E. coli* BL21. In brief, clarified lysates were run on a Ni-NTA column equilibrated with column buffer (20 mM Tris pH 8.0, 500 mM NaCl, 20 mM imidazole, 5 mM β-mercaptoethanol) and eluted with a step gradient of the same buffer, plus 500 mM imidazole. ENTH-domain containing fractions were pooled and dialyzed against column buffer with 0.4 μM $\text{His}_6$-TEV protease. $\text{His}_6$-TEV and the $\text{His}_6$ tag were separated from the untagged protein using the nickel affinity column. Untagged ENTH domain from the flow-through was further purified by ion exchange chromatography on a Source S column equilibrated in Source S Buffer A (20 mM Tris pH 7.4, 2 mM DTT) and eluted with a linear gradient of Source S Buffer B (20 mM Tris pH 7.4, 2 M NaCl, 2 mM DTT). Purified ENTH was stored at -80°C, in 20 mM Tris pH 7.4, 150 mM KCl, 2 mM DTT.

The coding sequence of full-length rat epsin was obtained from Addgene (pCDNA3.1-Epsin1; plasmid 22225) and was sub-cloned into the pEX-N-$His_6$-GST vector (Origene) for expression in *E. coli* BL21(DE3). Purification of full length epsin followed the same affinity chromatography and proteolytic cleavage protocol used for the ENTH domain, followed by further purification by ion exchange with a high-resolution Mono Q column equilibrated and washed with Buffer A (20 mM Tris pH 7.4, 2 mM DTT) and eluted on a linear gradient with Buffer B (20 mM Tris pH 7.4, 2 mM DTT, 2 M NaCl).

*Liposome preparation*

Liposomes were prepared as previously described, with minor modifications [40]. Briefly, brain lipid Folch extracts from Avanti (cat. 131101P) and Sigma (cat. B-1502) were mixed 1:1, with 5% PtdIns(4,5)$P_2$ (Avanti, cat. 840046C) and 0.03% acyl-chain, O-carbon labeled TopFluor-PtdEth (Avanti, cat. 810282C). Lipids were dried under a stream of dry argon, vacuum desiccated to remove residual solvents, re-suspended, with freezing and thawing, to 1 mg/ml in liposome buffer (20 mM HEPES pH 7.4, 150 mM NaCl) and then extruded through polycarbonate filters with the indicated diameters with 11 passes in a mini extruder (Avanti), followed by 10 passes through a high-pressure manifold extruder (Northern Lipids), and used within 6 hr. Liposomes used at later times no longer respond to addition of ENTH domain or epsin, presumably due to loss of liposome binding upon PtdIns(4,5)$P_2$ hydrolysis.

### *Liposome fission assay by BAS*

Liposomes diluted to 0.01 mg/mL in liposome buffer were mixed with ENTH domain, or full-length epsin, at the concentrations indicated, and 10 μL of each sample was spotted onto a BSA-blocked glass coverslip held in a custom cassette. The coverslip cassette was clamped to a high-precision, computer controlled, 2-axis translation stage connected to a customized microscope system, and data were collected as previously described [182, 198]. Efficient fission of large (~ 200 nm) liposomes into small (20–30 nm) liposomes should result in a large (100 to 200-fold) increase in object concentration, read out as fluorescent bursts with amplitudes proportional to individual object sizes. From a starting sample of 50–100 pM large liposomes, this increase in object number will violate the single-particle concentration limit (< 500 pM) required for BAS. Additionally, due to limited knowledge of the instrument point spread function, an individual BAS measurement can only quantitatively probe an approximately 100-fold range in object intensity for a single, uniformly labeled species [182]. The fission of large liposomes into much smaller ones leads to a highly inverted population dominated by smaller particles. In this case, the resolving power of BAS deteriorates for the low intensity events, due to the high species concentrations that no longer permit single particle detection. Therefore, to accurately examine liposome populations produced during fission, we developed an enhanced measurement protocol that permits BAS histograms to be constructed over an arbitrarily large range of object sizes. In brief, standard BAS data are collected on a series of systematic dilutions of each reaction sample, followed by analytical reconstruction of the overall population distribution through simultaneous fitting of the object cumulative distributions across the dilution series. Our standard BAS analysis fitting routines [182] have been modified to accommodate this expanded data analysis strategy. The fitting and programmatic details will be published elsewhere.

### *Heat maps*

Plots representing the spread of liposome products as a function of time or concentration are shown in some cases as “heat maps”: a stack of rows, one experiment per row, with increasing brightness corresponding to an increased fractional intensity of each bin (where a bin represents a group of burst events of a given size). To convert the number of burst events in each bin to fractional intensity, we normalized the object intensities as follows:

$$\frac{I_i C_i}{\sum_{i=1}^{n} I_n C_n}$$

where $I_i$ is the intensity of each bin, $C_i$ is the concentration of objects in each bin, and the denominator represents the total fluorescence of all bins (the sum of intensity in a row) for a given sample.

## Results

### *BAS is sensitive to changes in liposome size and concentration*

In order to calibrate our BAS measurements of membrane fission, we first examined a series of liposome standards created with different diameters. Liposomes were extruded to 200 nm, 100 nm, and 50 nm and then examined by BAS. Single-particle burst data for these samples display the expected dependence of burst size on liposome size (Figure III.1A). The fluorescence intensity of these membrane labeled liposomes is expected to be proportional to their surface area; thus, the mean intensity of the 200 nm versus 100 nm, as well as the 100 nm versus the 50 nm liposomes should differ by ~ 4-fold and the 200 nm and 50 nm are expected to differ by ~ 16-fold. As shown in Figure III.1B, the BAS histograms of each liposome sample display distributions with mean intensity differences consistent with the expected values. Additionally, the dispersion in liposome sizes measured by BAS is consistent with the expected variation for liposomes created by extrusion, specified as ± 25% CV (coefficient of variation; Northern Lipids specifications). As shown in Figure. III.1B, the observed size variation in liposomes appears to be between 35–50% CV, based on Monte Carlo simulations of particle distributions in which the particle brightness is assumed to be proportional to surface area. While the observed liposome variation is somewhat larger than expected, several factors likely broaden the observed intensity distribution, including a small fraction of multi-lamellar objects [199] and the discreet distribution of dye molecules between objects of the same absolute size. As a complementary measurement, we examined each liposome sample by FCS (Figure III.1C). FCS provides information on hydrodynamic radius based on measurement of the average diffusion time of fluorescent objects as they diffuse in and out of the excitation beam. However, diffusion time increases linearly with particle radius and so is not as sensitive a measure of liposome size as fluorescence intensity, which increases with the square of the radius. Additionally, FCS is dependent on particle surface hydrophobicity so that the hydrodynamic radius can be converted to an effective size only with knowledge of this surface-solvent interaction. Therefore, we use FCS here primarily as an indicator of a difference in average population hydrodynamic radius. Consistent with the BAS measurements, the mean diffusion time for each liposome sample decreases as the extrusion filter pore diameter decreases (Figure III.1C).

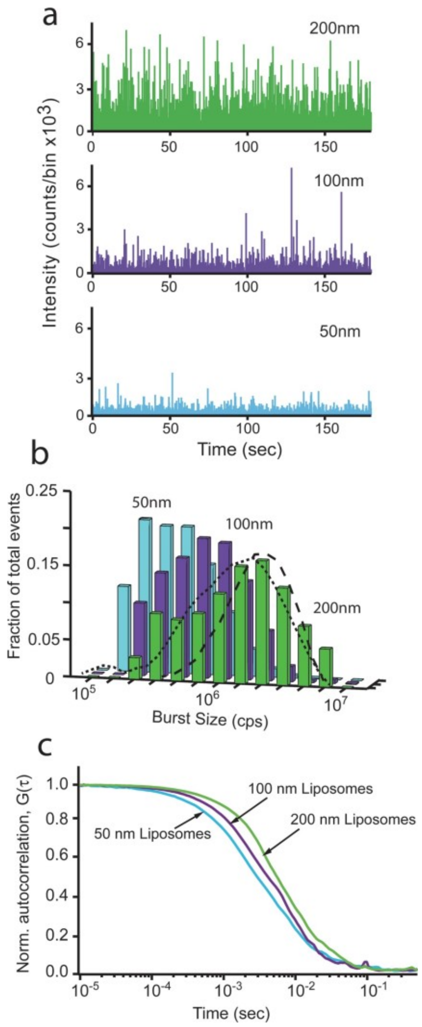

**Figure III.1 BAS assay distinguishes liposomes of different sizes. The size distribution of 200 nm, 100 nm and 50 nm fluorescent liposomes was examined by FCS and BAS. (a) Fluorescent burst data of TopFluor-labeled Folch liposomes extruded to 200 nm (*red*), 100 nm (*purple*) and 50 nm (*cyan*). (b) BAS histograms generated from the burst data in (a). Fraction of total events is the concentration of each bin divided by the total concentration, for each sample. Dashed lines show theoretical diameter distributions (35% CV, *dash*; 50% CV, *dot*) derived from Monte Carlo simulated intensity data in which fluorescence brightness was set proportional to particle surface area. The resulting simulated intensity distributions were analyzed with BAS analysis code. (c) FCS profiles of 200 nm, 100 nm, and 50 nm liposomes. The data shown is representative of two experimental replicates.**

### *Membrane fission activity of the epsin ENTH domain*

We next examined the ability of BAS to detect products of ENTH domain-mediated fission. Samples of large liposomes (either 400 nm or 200 nm) were mixed with purified ENTH domain and then examined by BAS after 40 min incubation at 37°C. We anticipated fission to be detectable as a shift from a small number of large fluorescence bursts to a larger number (high concentration) of much smaller bursts. As shown in Figure III.2 A-D, the expected changes are observed upon addition of the ENTH domain to either 400 nm, or 200 nm liposomes. Importantly, the total fluorescence intensity of the sample before and after ENTH addition changed by no more than 10–20% (Figure III.3), confirming that the disappearance of the large bursts was not caused by a loss of the starting liposomes, but rather by their conversion into a high concentration of smaller objects.

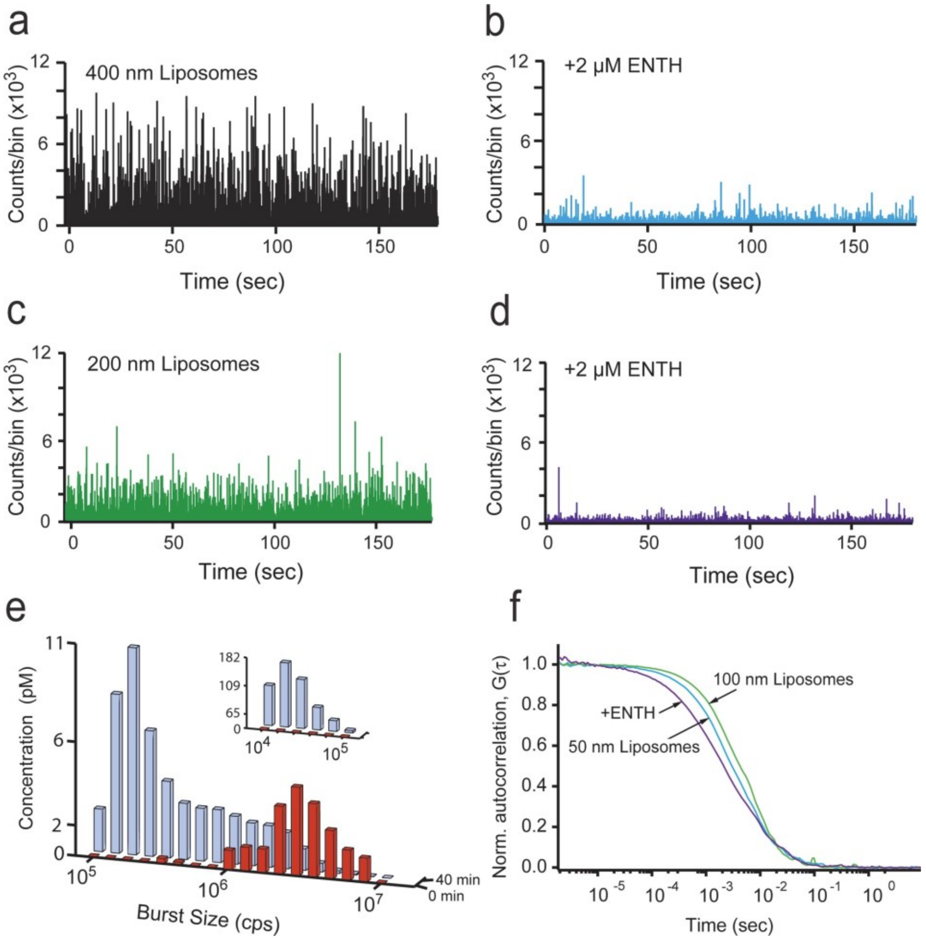

**Figure III.2 BAS analysis of liposomes vesiculated by the ENTH domain of epsin.Fluorescent burst data for 400 nm-diameter, TopFluor-labeled, (5%) PtdInsP(4,5)$P_2$ Folch liposomes incubated at 37°C for 40 min before (a) and after addition of 2 µM ENTH (b). Fluorescent burst data for 200 nm-diameter liposomes incubated at 37°C for 40 min before (c) and after addition of 2 µM ENTH (d). (e) BAS histograms generated from starting 200 nm liposomes before (*red*) and after addition of ENTH (*blue*; insets indicate resolution of small particles in a 10-fold dilution of the same reaction). (f) FCS profiles of liposomes extruded to 100 nm (*red*), 50 nm (*cyan*) and the end products (*purple*) of the fission reaction of 200 nm liposomes from (d). The data shown is representative of three experimental replicates.**

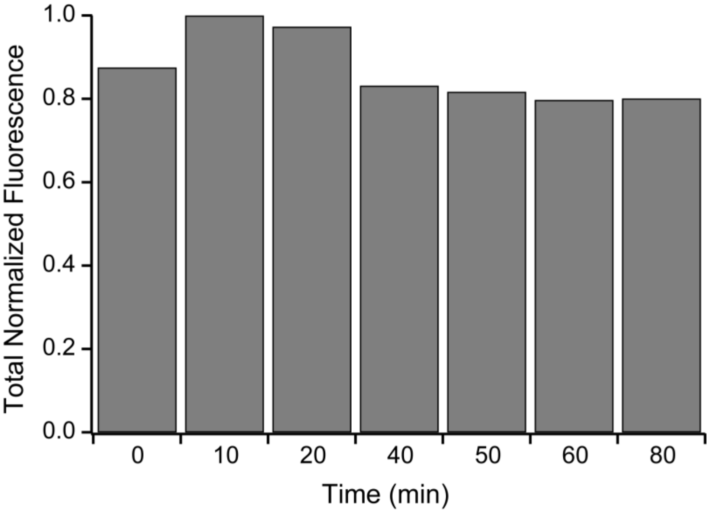

**Figure III.3 Liposome fission by ENTH is not accompanied by loss of fluorescent material.The total fluorescent signal for each time point during ENTH-mediated fission at 37°C (Figure 3C) is shown. In each case, the integrated signal was normalized to the maximal total signal observed during the experiment. The data shown is representative of three experimental replicates.**

The extent of fission of the 200 nm liposomes was quantified by BAS analysis of the raw burst data. The resulting BAS histograms display a dramatic shift from a low concentration of large liposomes to an increased concentration of small ones (Figure III.2E). The smallest products of the fission process (Figure III.2E, inset) increase by over 100-fold relative to the staring concentration of 200 nm liposomes, consistent with the number of small liposomes expected from efficient fission of the starting 200 nm liposomes into ~ 20 nm products. A similar scaling argument predicts that the mean burst size of a 20 nm product liposome should be ~ 100-fold smaller than the mean burst size of a starting 200 nm liposome, assuming that segregation of the fluorescent label is not biased by the process of fission. As shown in Figure III.2E, the relative difference in mean burst size for the staring and product liposomes is consistent with the product liposomes being ~ 20 nm in size. The product liposome distribution is most consistent with an approximately 30% CV (20 nm ± 6 nm), based on comparison of the intensity variation in the smallest product liposomes with simulated particle populations created at different size variations (10–50% CV; see Figure III.1B for an example). Examination of samples by FCS is also consistent with efficient membrane fission. Liposomes mixed with the ENTH domain show a dramatic shift in average diffusion time to values substantially less than that observed for 50 nm liposomes (Figure III.2F). However, similar experiments in which the ENTH domain was replaced with a non-specific protein (bovine serum albumin; BSA) displayed no detectable fission activity (Figure III.4), indicating that the observed shift in liposome size requires a potent, fission-active protein. Taken together, these observations are consistent with the generation of ~ 20 nm vesicles by the ENTH domain, as previously observed by electron microscopy [40].

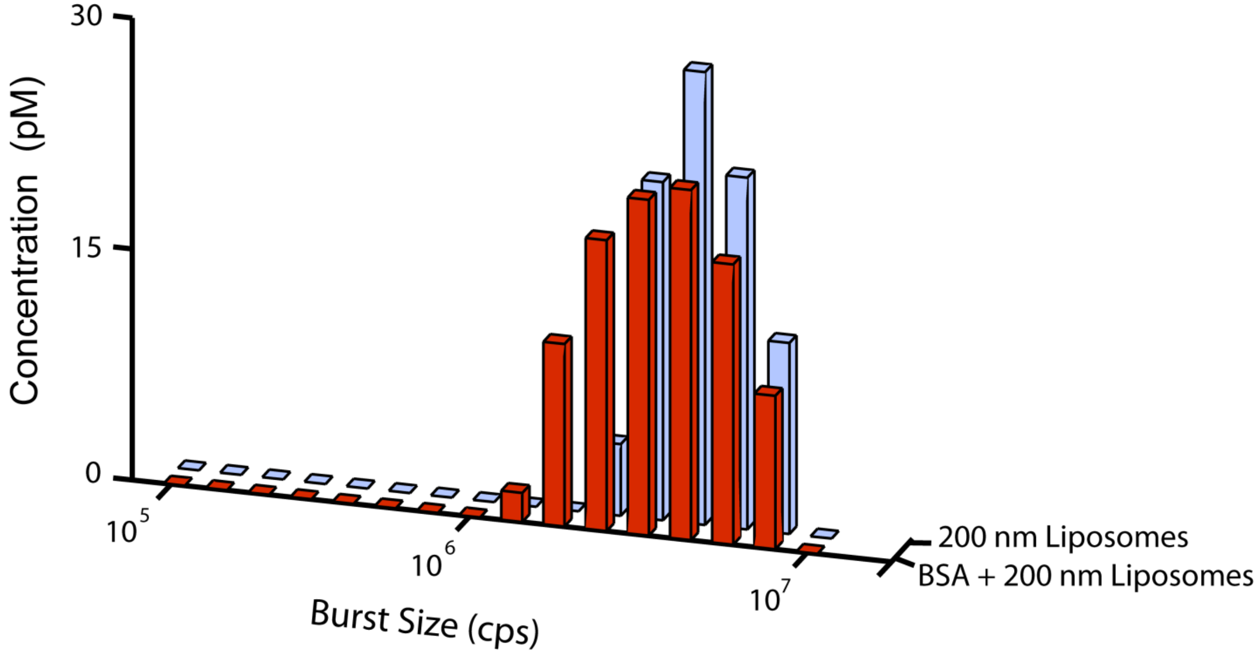

**Figure III.4 Liposome size distribution is not altered by a non-fission active protein. A BAS histogram of 200 nm-diameter, TopFluor-labeled, (5%) PtdInsP(4,5)$P_2$ Folch liposomes (*light blue*) remains relatively unchanged, following a 60 min incubation at 37°C in the presence of 10 μM BSA (*red*). The data shown is representative of duplicate experiments.**

### *The ENTH domain acts on the timescale of minutes*

The sensitivity of BAS permits changes in the liposome population as a function of time to be mapped with far greater accuracy than achieved previously. After 20 min at 23°C, a significant shift in the vesicle population size distribution is observed; however, some large vesicles remain (Figure III.5A). By 60 min, the largest vesicles are observed rarely, and the disappearance of large vesicles is concurrent with the appearance of smaller ones, over the 100 min time course. The fission activity of the ENTH domain is enhanced at 37°C (Figure III.5C), with the largest vesicles observed rarely at 20 min. By 80 minutes, at 37°C, the reaction appears to be complete, matching the 100 min time point at 23°C. In order to more fully illustrate the changes in liposome populations as a function of time, we normalized the fractional intensity of each BAS intensity bin and re-plotted the data as a heat map (see methods; Figure III.5B, III.5D). While the large, starting liposomes at time zero form a bright peak on the right end of the plot, at later time points, the fractional fluorescence is distributed between small and medium products, eventually populating a bright peak of small liposomes at the top (left), plus a lower concentration of broadly distributed, medium liposome sizes. Whether these intermediate-sized liposomes are static end products or the result of additional liposome dynamics is unknown, but they persist regardless of protein concentration or time. Interestingly, the rate at which the largest liposome population disappears does not appear to be detectably different at 23°C and 37°C. This observation is likely due to the small fractional change in intensity that occurs when 20 nm liposomes split from the much larger 200 nm liposome objects. The resulting 1–2% change in fluorescence intensity is not detectable in this assay, given the difference in the rate of fission at the two temperatures. However, the smallest products reach their maximum concentration at ~ 30 min at 37°C and ~ 60 min at 23°C, indicating a ~ 2-fold increased rate at 37°C.

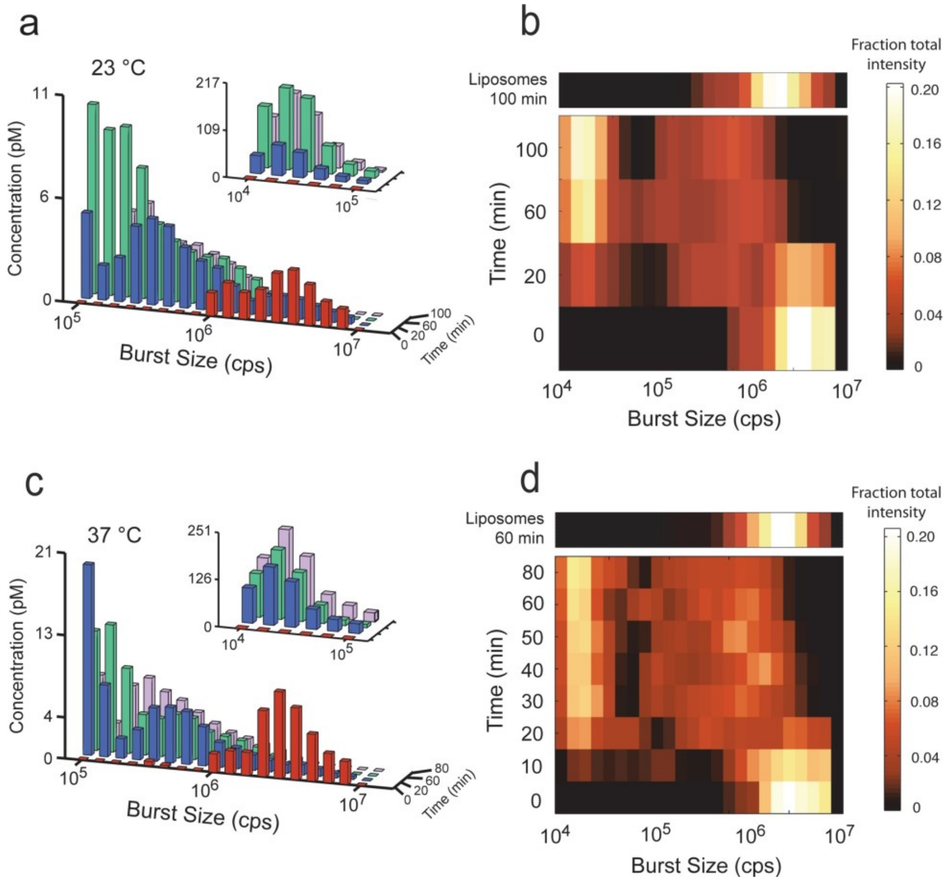

**Figure III.5. Kinetics of liposome fission are temperature dependent. (a) Histograms of BAS analyzed 200 nm-diameter, TopFluor-labeled, (5%) PtdInsP(4,5) P2 Folch liposomes (red) and products of ENTH incubation at 23°C for 20 (*blue*), 60 (*red*), and 100 min (*purple*) after addition of 2 µM ENTH. At each time point, an aliquot was removed and placed on ice, and measurements were started within 1–2 min. Inset indicates resolution of small particles in a 10-fold dilution of each reaction. (b) Heat map representation of the fractional intensity for each reaction shown in (a). (c) BAS histograms generated from starting liposomes (red) and products of ENTH incubation at 37°C for 20 (blue), 60 (red), and 80 min (purple) after addition of 2 µM ENTH. (d) Heat-map representation of the fractional intensity for each reaction shown in (c). Additional time points are shown, for increased resolution. The effect of incubating liposomes in the absence of the ENTH domain for 60 min at 37°C or 100 min at 23°C is shown as an additional row, above the respective heat maps. The data shown for the experiments conducted at 23°C is representative of four experimental replicates. The data shown for experiments conducted at 37°C is representative of three experimental replicates.**

### *Fission activity of the ENTH domain is dose-dependent*

Next, we looked for a dose-dependent change in fission activity of the ENTH domain. In order to maximize the sensitivity of observable changes in the liposome size-distribution, we chose an early time point in the fission reaction (20 min at 37°C) and focused on the disappearance of large liposomes and appearance of intermediate-sized products (without the dilutions required to resolve small products). Using this approach, we were able to measure fission activity at concentrations as low as 500 nM ENTH domain (Figure III.6A, 6B). At this early time point, the fission activity increases as a function of protein concentration, up to 10 μM (Figure III.6A, III.6B).

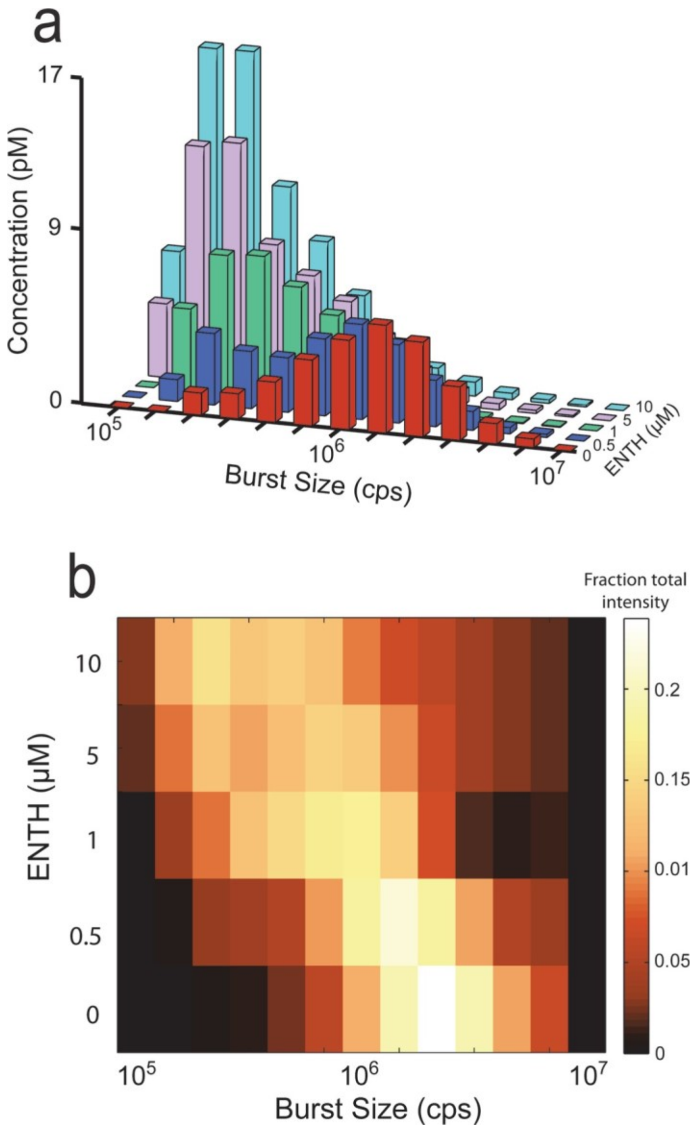

**Figure III.6. Dose dependence of ENTH-mediated vesiculation. (a) BAS histograms of 200 nm-diameter, TopFluor-labeled, (5%) PtdInsP(4,5)P$_2$ Folch liposomes before (*red*) and after incubation at 37°C for 20 min with 500 nM (*blue*), 1 μM (*red*) , 5μM (*purple*), and 10 μM (*cyan*) ENTH. (b) Heat-map representation of the fractional intensity for each reaction shown in (a). The data shown is representative of three experimental replicates.**

### *Fission activity of full-length epsin*

While the results of these and previous studies [40] indicate potent membrane fission activity for the epsin ENTH domain, it remained possible that the activity we observed is an artifact of the truncation and not a function of the full-length epsin protein. We reasoned that if epsin has latent membrane fission activity, then we might uncover that activity using the high sensitivity of BAS and conditions that maximize fission activity for the ENTH domain. Using this approach, we observed dose-dependent liposome fission activity at epsin concentrations as low as 1 μM, albeit with significantly slower rates than observed for the ENTH domain (Figure III.7A, III.7B). To compensate for the slower rates, the dose-dependence of epsin activity was measured at a 40 min time point and compared to the earlier, 20 min time point, used for the ENTH domain (Figure III.6). Despite the kinetic differences, the distribution of liposome products is remarkably similar and converges to the same size end products, after a 90 minute incubation. These results suggest that both the ENTH domain and the full-length epsin protein employ the same membrane-fission mechanism (Figure III.7C).

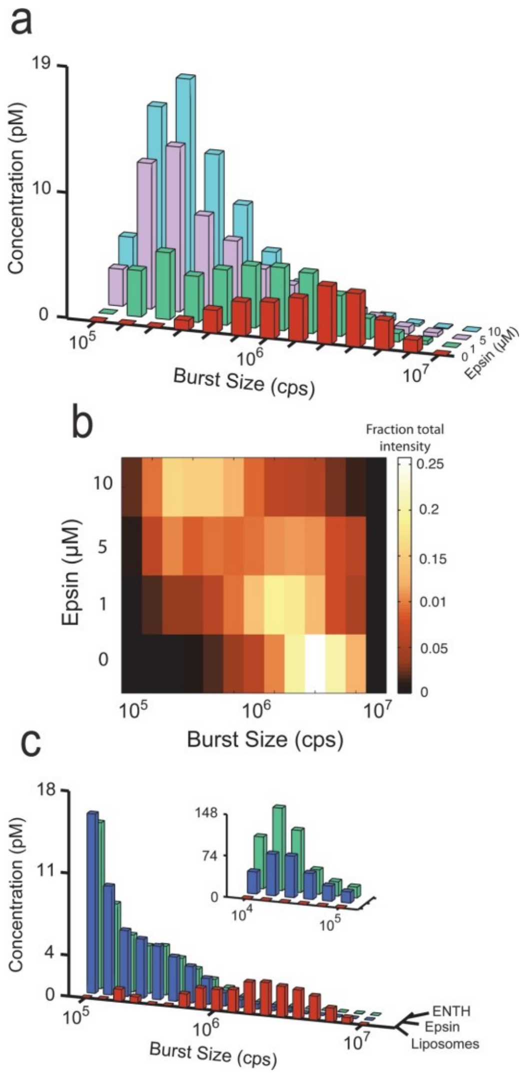

**Figure III.7 Full-length epsin has vesicle fission activity. (a) BAS histograms of 200 nm-diameter, TopFluor-labeled, (5%) PtdInsP(4,5)$P_2$ Folch liposomes before (*red*) and after incubation at 37°C for 40 min with 1 µM (*red*) , 5 µM (*purple*), and 10 µM (*blue*) full-length epsin. (b) Heat-map representation of the fractional intensity for each reaction shown in (a). (c) Comparison of ENTH and epsin activity. BAS histograms of starting liposomes (*red*), and liposomes incubated at 37°C for 90 min with 2 µM ENTH (*blue*) or full-length epsin (*red*) . The data shown is representative of three experimental replicates.**

## Discussion

Using BAS, we observed time-resolved liposome membrane fission in free solution, induced by the potent epsin ENTH domain. These results agree with those of a previous study, which showed, using living cells and an *in vitro* sedimentation assay, that epsin, in particular the ENTH domain, is necessary and sufficient for endocytic vesicle membrane fission [40]. Recently, concerns were raised regarding the physiological significance of the fission activity observed in that study, specifically citing the small size of the starting liposomes (200 nm diameter), the high protein concentration (10 µM), and the likelihood that many of the products, rather than vesicular in nature, were micellar [38]. The high sensitivity of BAS allowed us to address these concerns: (i) fission activity was observed at sub-micromolar protein concentration, (ii) fission activity does not depend on the curvature of starting liposomes, as those of 400 nm diameter worked as well as smaller ones and (iii) the products are consistent with 20 nm vesicles and not micelles, as observed previously [40].

In addition, the high sensitivity of BAS allowed us to uncover attenuated membrane fission activity in experiments with the full-length epsin protein. Attenuation may suggest an inhibited conformation for full-length epsin, as has been suggested for syndapin, another protein involved in formation of vesicles at the recycling endosome [200]. Intermolecular interactions have also been observed to cause auto-inhibition, in the case of endophilin A1, a curvature-inducing endocytic protein that also contains an N-terminal amphipathic helix [201].

Although epsin is required for clathrin-mediated endocytosis from early to late stages of endocytic vesicle formation [191], it has been classified as an adaptor protein. Like the well-characterized adaptins, epsin was shown to act at an early step, recruiting other adaptins and cargo [195], in addition to binding to the clathrin coat. However, unlike the classic adaptins, little epsin is found in clathrin-coated vesicles [194, 202], raising questions regarding its role solely as an adaptor protein. Furthermore, epsin can rescue a block in the release of endocytic vesicles in dynamin-depleted cells [40], arguing for a late role in vesicle fission. These results, in addition to the liposome fission activity of the epsin ENTH domain, led those authors to conclude that epsin is also required for fission of clathrin-coated endocytic vesicles. Furthermore, an analogy was made to the early and late requirement for the amphipathic-helix containing proteins, Arf1p and Sar1p, in the formation of COPI coated vesicles at the Golgi apparatus and COPII coated vesicles at the endoplasmic reticulum, respectively [147, 203]. BAS has the ability to resolve membrane fission reactions over a concentration range that is more physiologically significant and on a sub-second timescale. Yet, the fastest fission reactions we observed, at high protein concentration and 37°C, proceeded on the minute, to tens of minutes timescale. This suggests that other factors are required to increase the fission activity to physiologically significant rates, on the order of seconds, to tens of seconds [191]. Notably, the results of recent studies indicated a reciprocal requirement for the amphipathic-helix containing amphiphysin and partner protein, dynamin, in order to stimulate membrane fission [38, 204]. Our results using BAS reopen the question of how membrane fission is induced, not only in endocytosis, but also, how transport carriers and vesicles are released at other locations in the cell, where dynamin does not appear to play a role. Our findings also raise others questions: how is epsin regulated, and what stimulates epsin-induced membrane fission? Moreover, our findings indicate that BAS offers a highly sensitive approach to follow single particle dynamics of a membrane fission reaction in free-solution, for identification of membrane fission agents and characterization of the mechanism of membrane fission regulation.

# CHAPTER IV

# AMPH-1 MEDIATES MEMBRANE FISSION AT THE BASOLATERAL RECYCLING ENDOSOME

## Summary

Endocytic recycling is the process by which endocytosed cargoes, such as membrane bound proteins and lipids, are returned to the plasma membrane. At the tubular recycling endosome, material is sorted from non-recycled material prior to its return to the plasma membrane in transport carriers. The release of these transport carriers requires a membrane separation process known as membrane fission. The mechanism of membrane fission at the tubular recycling endosome is poorly understood. At the basolateral tubular recycling endosome of *C. elegans,* two key proteins are required for membrane fission: receptor mediated endocytosis 1 (RME-1) and amphiphysin 1 (AMPH-1). Here we use Burst Analysis Spectroscopy (BAS), a free-solution, single particle fluorescence-based technique, to identify the minimal fission machinery of the recycling endosome. We identify AMPH-1, an N-BAR protein, as the key mediator of membrane fission. Surprisingly, the fission activity of AMPH-1 is stimulated by GTP. An unexpected result as AMPH-1 does not have a canonical nucleotide binding motif. Furthermore we show that the GTP-stimulated membrane fission activity may be a general feature of amphiphysin family of N-BAR proteins, as

the *S. cerevisiae* amphiphysin homolog RVS161/167p also possesses GTP stimulated membrane fission activity. Finally we identify RME-1 as a negative regulator of the AMPH-1 mediated membrane fission activity. The data presented here supports a model in which the worm and yeast N-BAR proteins function as a core membrane fission machine, using the insertion of their amphipathic helices into the bilayer to induce membrane fission.

## Introduction

Endocytic recycling is the process of returning membrane-bound proteins and lipids back to the plasma membrane, and is critical in regulating cell homeostasis [17, 205]. Endocytosed membrane-bound proteins and lipids (cargo) can be transported to tubular recycling endosomes (TRE) before returning to the plasma membrane. TRE are long-lived organelles that accumulate cargo like transporters, such as glucose transporter 4 (GLUT4), and cell signaling proteins such as TGFβ proteins [135] [206]. At the TRE, cargo is sorted and membrane enclosed transport carriers are released through a process known as membrane fission. Due to the importance of the cell signaling and transport proteins that are trafficked to the TRE, dysregulation of membrane trafficking, particularly membrane fission, can lead to a wide range of devastating diseases such as diabetes, cancer and neurological disorders [207, 208]. The mechanism by which membrane fission occurs at the TRE is illdefined, however key proteins that mediate this reaction have been identified [143, 145, 148].

The best understood membrane fission reaction is catalyzed by dynamin-1 during clathrin mediated endocytosis at the synapse. Dynamin-1 is a large GTPase that localizes to the plasma membrane during the late-stages of clathrin coated pit (CCP) formation where it forms helical oligomers. Dynamin-1 undergoes a conformational change upon GTP hydrolysis that catalyzes membrane fission and releases a clathrin coated vesicle into the cytoplasm of the cell [88, 121]. *In vitro* dynamin-1 is able to cause membrane fission on low tension membrane reservoirs in the absence of an accessory protein [192].

The ubiquitously expressed isoform dynamin-2 can also catalyze membrane fission *in vitro* but requires amphiphysin to generate membrane curvature [38, 209]. Amphiphysin is an N-BAR protein that contain an N-terminal amphipathic helix and a structurally conserved BAR domain that dimerizes to form a highly curved crescent or “banana-like” structure [32]. N-BAR proteins generate curvature through an insertion of the amphipathic helix into the lipid bilayer, and the scaffolding activity of the BAR domain [18, 23, 30, 32, 157]. These proteins localize to the plasma membrane during the late stages of CCP formation, prior to dynamin-1 or dynamin-2, to generate and stabilize areas of high curvature [121].

In *C. elegans,* two key proteins have been identified in the regulation of membrane fission at the basolateral recycling endosome: Receptor Mediated

Endocytosis 1 (RME-1) and amphiphysin 1 (AMPH-1). RME-1, a member of the dynamin superfamily, is enriched in polarized epithelial cells and localizes to basolateral recycling endosomes [143]. The intestine of *rme*-1 mutant worms display the phenotype associated with a block in basolateral recycling [144]. AMPH-1, an N-BAR protein, also localizes to the basolateral recycling endosome and *amph-1* knockdowns have a similar but weaker phenotype than the *rme-1* mutant phenotype [145]. The Eps15 homology (EH) domain of RME-1 binds to conserved Asn-Pro-Phe motifs on the linker region of AMPH-1 [145]. This interaction is important for the localization of RME-1 to the basolateral recycling endosome [145]. These observations provide evidence that AMPH-1 and RME-1 function together at the basolateral recycling endosome and may be the minimal machinery required for membrane fission.

Previous work on members of the dynamin superfamily, and the N-BAR family suggests a likely model of membrane fission at the basolateral recycling endosome. RME-1, as a dynamin family member, could act as the central fission machinery. If RME-1 is the central fission machinery then it could mediate membrane fission alone, like dynamin-1 or require AMPH-1, like dynamin-2 [38]. Alternatively, AMPH-1 could serve as the core fission machinery, with the N-terminal amphipathic helices playing a critical role. The shallow insertions of amphipathic helices of small globular proteins, such as the ENTH domain of epsin, are observed to cause membrane fission *in vitro* [40]. A single particle fluorescence-based method known as Burst Analysis Spectroscopy (BAS) will be used to test these models *in vitro*. Previously, this method was used to measure the fission activity of the ENTH domain of epsin [39].

## Methods

### *Purification of AMPH-1*

Amphiphysin 1 (AMPH-1) from *C. elegans*, was expressed and purified as previously described with modifications [145]. Briefly, AMPH-1, AMPH-1 L9Q and AMPH-1-eGFP were expressed as GST fusion proteins in the *E. coli* strain Rosetta (DE3) which is resistant to T5 phage, or T5$^R$. *E. coli* cells were grown an $OD_{600}$ of 0.4-0.5, and induced with 0.4 mM isopropyl β -D-1-thiogalactopyranoside (IPTG). Cells induced overnight at 18°C and lysed using a Microfluidizer (Microfluidics Corporation; Newton MA) in lysis buffer (50 mM Tris pH 7.4, 300 mM NaCl, 1 mM $MgCl_2$, 0.5 mM ethylenediaminetetraacetic acid (EDTA), 20% (w/v) sucrose, 2 mM dithiothreitol (DTT), and 1 mM phenylmethanesulfonyl fluoride (PMSF). Clarified lysate was loaded onto a glutathione column, equilibrated with buffer A (50 mM Tris pH 7.4, 300 mM NaCl, 1 mM $MgCl_2$, 2 mM DTT). The protein was eluted off the column, after extensive washing with buffer A, using a single step of buffer B (buffer A supplemented with 10 mM glutathione). Purified protein was cleaved with 225 µM Precission protease for 18 hours in buffer A. The dialyzed protein was run over another glutathione affinity column to remove the protease, the GST-tag, and GST-AMPH-1. AMPH-1 was exchanged into storage buffer (25 mM Tris pH 7.4, 150 mM KCl, 1 mM $MgCl_2$, 2 mM DTT), concentrated, flash frozen and stored at -80°C. Protein aggregates were removed prior to the running of biochemical experiments at 300,000xg for 30 minutes at 4°C. Final protein concentration for AMPH-1, AMPH-1 L9Q and AMPH-1-eGFP were measured after centrifugation. AMPH-1 and AMPH-1 L9Q concentration was measured in Edelhoch buffer at 280 nm. AMPH-1-eGFP concentration was measured in a Bradford Assay using AMPH-1 as a standard. All concentrations of the protein are the dimer formation. This protocol was also used to purify the "Mock" protein where GST was expressed using the plasmid pGEX-N-His-GST.

*Purification of RME-1*

Receptor mediated endocytosis 1 (RME-1) from *C. elegans* was expressed and purified as previously described with minor modifications [146]. The coding sequences of *rme-1* isoform d, a kind gift from Dr. Barth Grant, was sub-cloned into pET21a, containing an N-terminal MBP fusion tag, and a tobacco etch virus [210] recognition site. RME-1 was expressed as a fusion protein in the *E. coli* strain OverExpress C43(DE3) $T5^R$, a kind gift from Dr. Karthik Chamakura and Dr. Ryland Young. *E. coli* cells were grown to an $OD_{600}$ of 0.5-0.6, at which time protein expression was induced with 0.4 mM IPTG. Protein was induced overnight at 18°C. Cells pellets were resuspended in lysis buffer (50 mM Tris pH 7.4, 300 mM NaCl, 1 mM $MgCl_2$, 1 mM $CaCl_2$, 20 mM imidazole, 20% (w/w) sucrose, 5 mM β-mercaptoethanol (β-ME), and 1 mM PMSF. Cells were lysed using a Microfluidizer (Microfluidics Corporation; Newton MA). $His_6$-MBP-RME-1 was separated from contaminating E. coli proteins on a Ni-NTA affinity column as described [146]. The eluted protein was loaded onto an amylose column, pre-equilibrated with amlyose column buffer A (50mM Tris pH 7.4, 300 mM NaCl, 1 mM $MgCl_2$, 5 mM β-ME), and eluted off using a single step with amylose buffer B (amylose buffer A plus 10 mM maltose). The protein was dialyzed in the lysis buffer without sucrose or PMSF, with 0.1 μM $His_6$-TEV protease and allowed to cleave for 18 hours. The untagged RME-1 was removed from the protease, $His_6$-MBP, and uncleaved protein using a Ni-NTA column, equilibrated in dialysis buffer. Cleaved RME-1 was further purified using a Superdex 200 16/60 column equilibrated in gel filtration buffer (25mM Tris pH 7.4, 150 mM KCl, 1 mM $MgCl_2$, 2 mM DTT). RME-1 was concentrated and trehalose was added to the purified protein to a final concentration of 100 mM prior to flash freezing. RME-1 was stored at -80°C. RME-1 concentration is expressed as the dimer.

*Purification of RVS161/167p*

The coding sequences of Reduced Variability upon Starvation 161p, and 167p from *S. cerevisiae*, were cloned from yeast genomic DNA into a pET-Duet 1 vector. RVS161p was cloned into the multiple cloning site 1, with an N-terminal $His_6$-GST-TEV recognition site, and RVS167p was cloned into the multiple cloning site 2 with an N-terminal $His_6$-MBP-TEV recognition site.RVS161/167p was expressed together as fusion proteins in the *E. coli* strain BL21 (DE3) $T5^R$. *E. coli* cells were grown to an absorbance of 0.5-0.6, and induced with 0.5 mM IPTG. Protein expression was induced for 16-18 hours at 18°C. Cell pellets were resuspended in lysis buffer (50 mM Tris pH 7.4, 300 mM NaCl, 1 mM $MgCl_2$, 1 mM $CaCl_2$, 20% (w/v) sucrose, 5 mM β-ME, and 2 mM PMSF). Cells were lysed using a Microfluidizer (Microfluidics Corporation; Newton MA) and clarified lysate was loaded onto a Ni-NTA column, equilibrated with nickel buffer A (50 mM Tris pH 7.4, 300 mM NaCl, 20 mM imidazole, 1 mM $MgCl_2$, 1 mM $CaCl_2$, 5 mM β-ME). The protein was eluted off the column using a step gradient using nickel buffer B (nickel buffer A with a final concentration of 500 mM imidazole). The protein was dialyzed in nickel buffer A, with 0.5 µM $His_6$-TEV protease for 18 hours. The purified RVS161/167p was removed from The $His_6$-TEV protease and the $His_6$-MBP and $His_6$-GST using a nickel affinity column, equilibrated in dialysis buffer. The RVS161/167p that was found in the flow through of the nickel affinity column was exchanged into Mono Q buffer A (50 mM Tris pH 7.4, 20 mM NaCl, 1 mM $MgCl_2$, 2 mM DTT). RVS161/167p was loaded onto a MonoQ column was equilibrated with Mono Q buffer A, and eluted off of the column using a linear gradient of MonoQ buffer B (50 mM Tris pH 7.4, 1 M NaCl, 1 mM $MgCl_2$, 2 mM DTT). Purified RVS161/167p was concentrated, flash frozen and stored at -80°C. RVS161/167p concentration is expressed as the dimer.

*Purification of the ENTH domain of epsin*

The ENTH domain of epsin was purified as previously described [39].

*Liposome preparation*

Liposomes were prepared as previously described with minor modifications [39]. Brain extract phosphatidylserine (PS) (Avanti, cat. 840032) was mixed with either 0.3% Top-Fluor PE, for BAS experiments or 0.06% Vybrant DiD (Invitrogen, cat. V22887) for MC-BAS experiments. Product analysis experiments used brain extract PS with 0.6% TopFluor-PE. The complex mixture of lipids, mixed 70% brain extract PS, 10% 18:0-20:4 phosphatidylcholine (PC) (Avanti cat. 850469), 10% egg extract phosphatidic acid (PA) (Avanti, cat. 840101), 5% brain extract PE (Avanti cat. 840022), 5% brain extract PI(4,5)$P_2$ and 0.3% Top-Fluor PE.

Lipids were first dried as previously described [145]. The lipids dried were then resuspended in argon sparged liposome extrusion buffer (50 mM Hepes pH 7.4, 150 mM NaCl) to a final concentration of 1 mg/ml for Folch extract membranes. For all other experiments, the lipids were resuspended to 1 mM in extrusion buffer containing 25 mM KCl. To hydrate the lipids evenly, the suspension underwent 10 rounds of freezing in liquid nitrogen followed by thawing, in hot water at temperatures between 52-60°C. Unilamellar Liposomes were extruded to 200 nm in an Avanti Mini-extruder by 11 rounds of passing the liposome suspension through a Whatman Nuclepore track-etched polycarbonate filter with a pore size of 200 nm. The liposomes were then passed 10 times through a high-pressure Lipex manifold extruder (Transferra, Canada) using Whatman Nuclepore track-etched polycarbonate filter with a pore size of 200 nm. The liposome suspension was centrifuged at 20,000 x g for 30 min at 21°C to remove small contaminating liposomes. The supernatant was removed, and the pellet was gently resuspended in liposome extrusion buffer.

For experiments using liposomes smaller than 200 nm, the same protocol to make 200 nm liposomes was initially followed. After resuspension of the 200 nm liposomes, the liposome solution was further extruded in an Avanti Mini-extruder by 11 rounds of passing the liposome suspension through a Whatman Nuclepore track-etched polycarbonate filter with pore sizes of 30, 50, or 100 nm. Liposomes extruded to a diameter of 1 μm where hydrated as previously described and extruded in an Avanti Mini-extruder by eleven rounds of passing the liposome suspension through a Whatman Nuclepore track-etched polycarbonate filter with a pore size of 1 μm. The liposome suspension was centrifuged as described for the 200 nm liposomes.

### *Membrane fission measured by burst analysis spectroscopy*

Membrane fission assays were performed as previously described with modifications [39]. AMPH-1 and RME-1 reactions were performed in reaction buffer (20 mM Hepes pH 7.4, 200 mM KCl, 0.5 mM $MgCl_2$, and 2 mM DTT). The standard protein concentration of all experiments was 1 μM AMPH-1 or RME-1, and the standard nucleotide concentration for all experiments was 0.5 mM unless otherwise stated. Protein was briefly incubated with bnucleotide prior to the addition of 200 nm TopFluor-PE labeled liposomes, which were added to the reaction at a final concentration of 40-50 pM. Liposomes used in these assays were either 100:0.3 PS:TopFluor-PE, or 70:10:10:5:5:0.3 PS:PC:PA:PE:PI(4,5)$P_2$:TopFluor-PE. All reactions were incubated at 23°C for at least 30 minutes unless otherwise stated. RVS161/167p reactions were performed in liposome extrusion buffer supplemented with 0.5 mM $MgCl_2$, and 2 mM DTT. The fission reaction was measured after 10 minute incubations of 200 nM RVS161/167p, 0.5 mM of GTP, and 60 pM of 200 nm TopFluor-PE labeled PS liposomes, unless otherwise stated. The ENTH domain of Epsin was incubated with liposomes for 1 hour at 23°C in 50 mM Hepes pH 7.4, 150 mM NaCl, 25 mM KCl, 0.5 mM $MgCl_2$, and 2 mM DTT.

After incubation of AMPH-1, RME-1 and RVS161/167p with liposomes, 10 μ L of each sample was spotted onto a BSA-blocked glass coverslip held in a custom cassette. The coverslip cassette was clamped to a high-precision, computer controlled, 2-axis translation stage connected to a customized microscope system, and data were collected as previously described [182]. To accurately obtain concentrations for medium to small liposomes formed during the fission assay, a variation in the standard BAS protocol, which is optimized for samples with large size and concentration differences was employed [39, 183]. In brief, standard BAS data are collected on a series of systematic dilutions of each reaction sample, followed by analytical reconstruction of the overall population. For each experimental run, 3 to 5 minutes of data was collected for the undiluted reaction, and 8 minutes of data was collected for the diluted data. All experiments were repeated in triplicate.

*Membrane binding assay measured by MC-BAS*

Single particle, two-color BAS membrane binding assays were conducted similarly to membrane fission with modifications. Using the AMPH-1 reaction buffer, 120 nM AMPH-1-eGFP was incubated with and without 0.5 mM nucleotide. Vybrant DiD labeled liposomes were added to a final concentration of 40 pM to the reaction. The reactions were spotted onto a BSA-blocked coverslip without incubation. For all binding experiments, dual excitation was employed with 50 μW input power for both 488 and 642 nm lasers. For each experimental run, 3 minutes of data was collected a minimum of 4 times. The data analysis has been described elsewhere [182, 183].

*Membrane fission and membrane tubulation by TEM.*

Briefly, 3 μM AMPH-1 or 3 μM RME-1 were incubated with 120 pM 200 nm PS liposomes with and without 0.5 mM nucleotide for 30 minutes at 23°C. These conditions are the same protein to lipid ratios used in the BAS fission experiments. For the analysis of the products generated by AMPH-1 with GTP, the reaction was incubated for 2 hours at 23°C. For the tubulation assay, 3 μM

AMPH-1 was incubated in the presence or absence of 0.5 mM GTP with 120 pM 1 µm PS liposomes. The reaction was incubated for 30 minutes prior to staining. For RVS161/167p fission assays, 200 nM RVS161/167p was incubated with 50 pM of 200 nm PS liposomes with 0.5 mM GTP. Reactions were incubated for 10 minutes to capture an early time point in the fission reaction or 30 minutes to capture the endpoint prior to staining. All samples were spotted on formvar carbon coated 400 mesh copper grids, and stained with 2% uranyl acetate. Electron microscopy was performed using a JEOL 1200EX transmission microscope at 100kV.

## Results

### *AMPH-1, not RME-1, induces membrane fission.*

In order to test the roles of AMPH-1 and RME-1 in membrane fission, we used Burst Analysis Spectroscopy (BAS) [178]. The fluorescence burst amplitude of a liposome that incorporates a dye-labeled lipid is directly related to the size of the liposome through its surface area [39]. For our *in vitro* membrane fission assay, we used purified AMPH-1 and RME-1 proteins with 200 nm diameter phosphatidylserine (PS) liposomes labeled with the fluorescent lipid, TopFluor-phosphatidylethanolamine (TopFluor-PE). Inconsistent with fission activity, liposomes incubated with 1 µM RME-1 and ATP for 30 minutes results in a clear qualitative increase in average burst intensities, with an overall decrease in the number of bursts, relative to liposomes alone (Figure IV.1A, B).

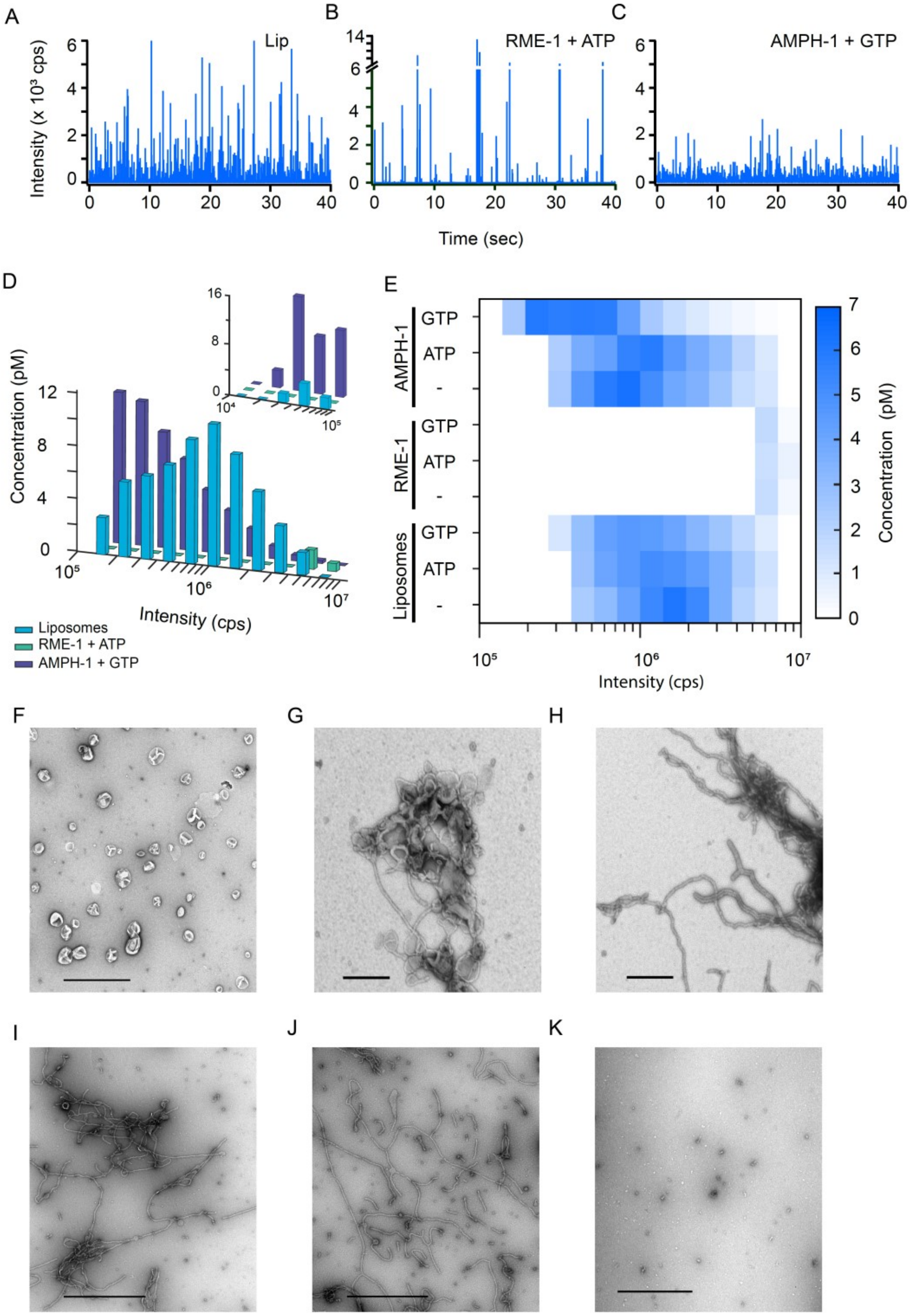

**Figure IV.1. AMPH-1, but not RME-1, induces membrane fission. (continued on next the page)**

**(A-C) 200 nm PS liposomes labeled with 0.3% TopFluor-PE are detected as fluorescent bursts, after incubation for 30 min at 23 °C in the absence (A), or presence of protein and nucleotide. Fewer, higher intensity bursts are observed, upon addition of 1 µM RME-1 and 0.5 mM ATP (B), whereas an increased abundance of bursts of lower intensity are observed upon addition of 1 µM AMPH-1 and 0.5 mM GTP (C). (D) Analysis of fluorescent burst data is plotted as histograms for starting liposomes (light blue), liposomes incubated in the presence of 1 µM RME-1 and 0.5 mM ATP (green) and 1 µM AMPH-1 with 0.5 mM GTP (purple). Inset shows the large increase in the concentration of small fission products. (E) Analysis of fluorescent burst data using the same conditions as (D) is plotted as a heat map which includes liposome and nucleotide controls. (F-K) Using the same incubation conditions, liposomes are detected by negative-stain electron microscopy in the absence of protein (F), with 1 µM RME-1 (G) with 1 µM RME-1 and 0.5 mM ATP (H), with 1 µM AMPH-1 (I), with 1 µM AMPH-1 with 0.5mM GTP (J) and with 1 µM AMPH-1 and 0.5 mM GTP in the absence of liposomes (K). Scale bar is 0.5 µm for RME-1 images (G-H) otherwise scale bar is 1 µm. Abbreviation: Lip, Liposomes.**

Upon analysis, the liposomes in the presence of 1 µM RME-1 display a dramatic increase in apparent size (green; Figure IV.1D, E) [182]. This result is suggestive of liposome clustering or flocculation and a disappearance of the initial of 200 nm liposome population. The fission activity of RME-1 was also measured in the presence of GTP, as a control because RME-1 is a member of the large G-protein dynamin superfamily. Clustering or flocculation of the starting liposomes is also observed with RME-1 in the presence of GTP (Figure IV.1E). However, at 25 nM RME-1 an increase in the size of the liposomes is apparent in the presence of ATP, but not with GTP or in the absence of nucleotide, consistent with the flocculation activity depending on RME-1 binding to ATP (Figure IV.2).

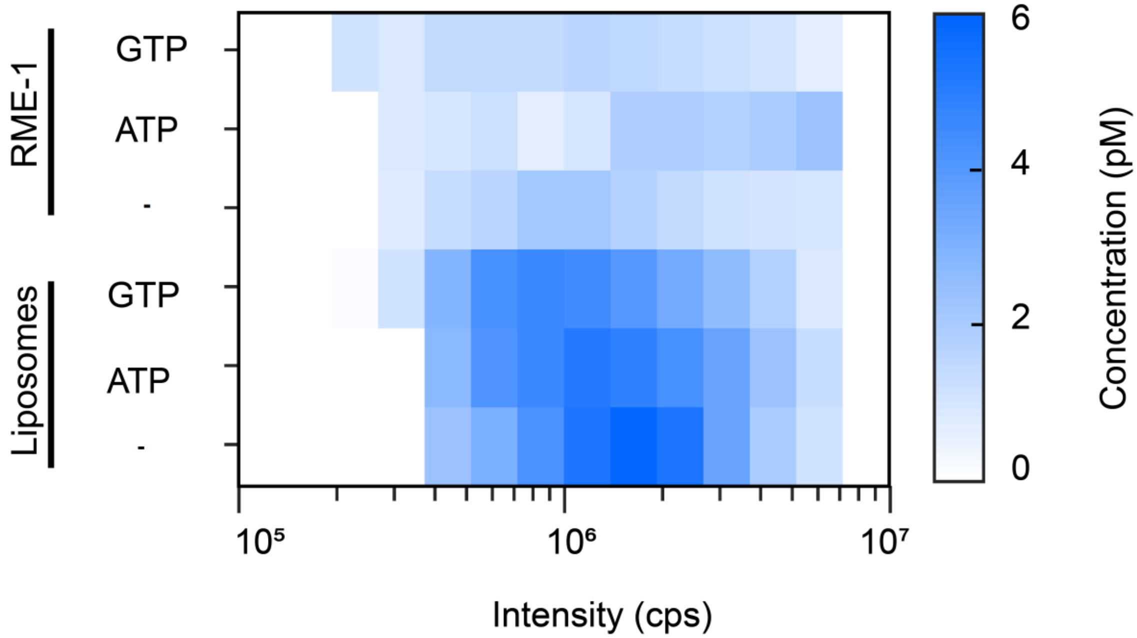

**Figure IV.2 The flocculation of liposomes induced by RME-1 depends on ATP. BAS histograms of the reaction of liposomes incubated for 30 minutes with 25 nM RME-1 in the absence and presence of 0.5 mM ATP, and 0.5 mM GTP.**

Surprisingly however, fission activity was observed in the presence of AMPH-1 with GTP after 30 minute incubation, as evident from an overall decrease in burst size (Figure IV.1A, C). Upon analysis, the liposomes in the presence of 1 μM AMPH-1 and GTP displays a dramatic decrease in size, as well as a large increase in the concentration of small liposome products (purple; Figure IV.1 D, E). The decrease in the overall size of the starting liposomes is not observed in the absence of nucleotide nor in the presence of ATP. This result is consistent with AMPH-1 acting as a GTP-stimulated membrane fission protein [39]. The GTP enhancement occurs at concentrations of AMPH-1 as low as 100 nM and as high as 5 μM (Figure IV.3). This unexpected enhancement is not due to a co-purifying contaminant, as a mock preparation shows little change in the distribution of liposomes when incubated with GTP (Figure IV.4). The GTP stimulated fission activity of AMPH-1 is also observed on liposomes of a more complex composition, which is similar to that found at the recycling endosome (Figure IV.5).

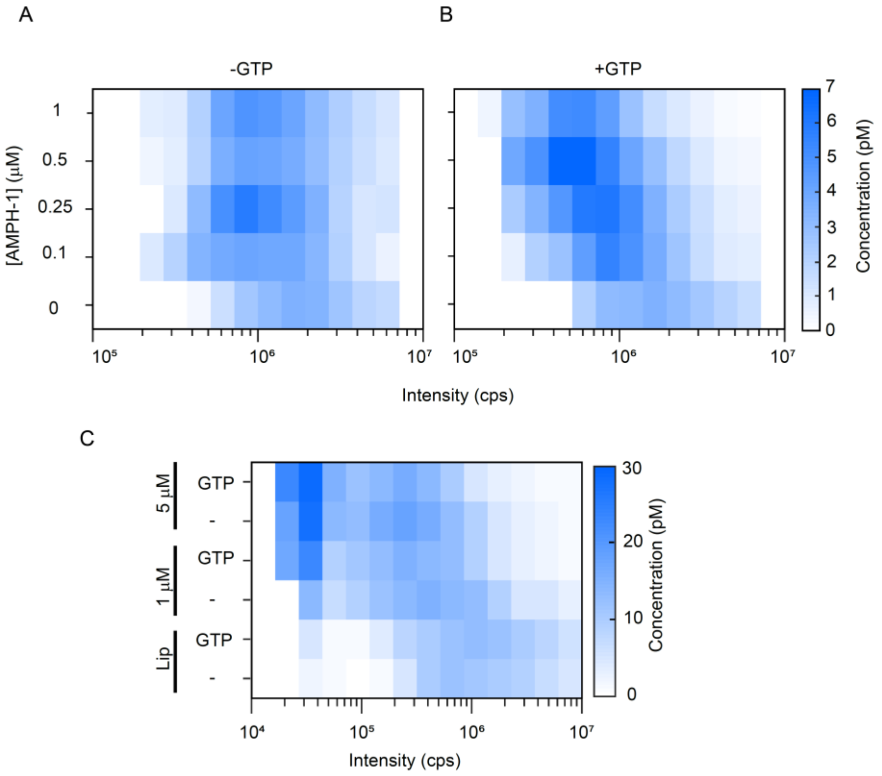

**Figure IV.3 GTP stimulated membrane fission of AMPH-1 is concentration dependent. (A-B) BAS histograms of PS liposomes incubated with varying concentrations of AMPH-1 for 30 minutes in the absence (A) or presence of 0.5 mM GTP(B). (C) Membrane fission is observed at 1 μM and 5 μM AMPH-1 after incubation for 30 minutes. At both concentrations of protein, GTP stimulates the fission activity of AMPH-1.**

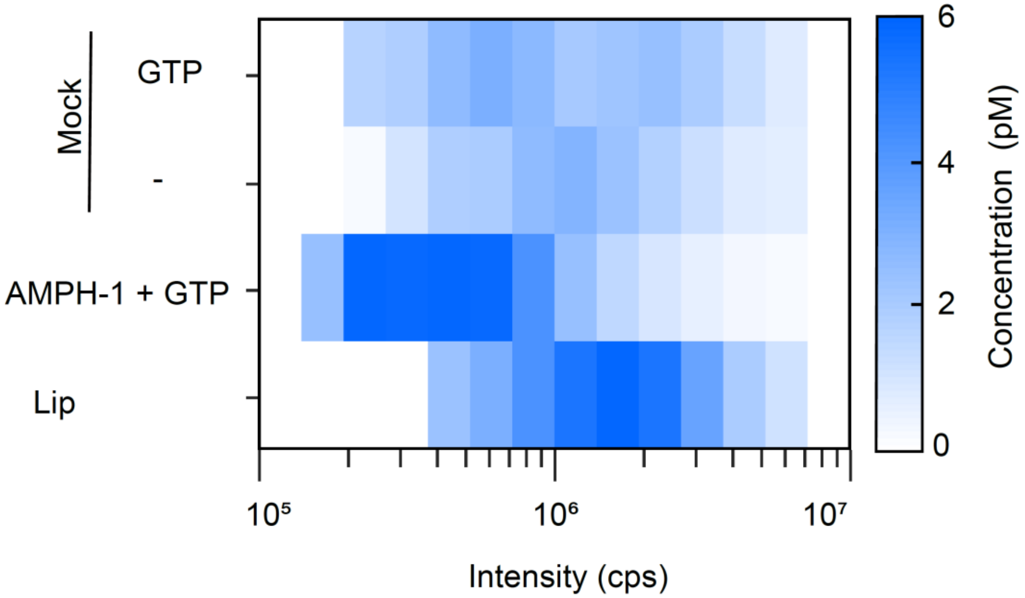

**Figure IV.4 A mock purification of AMPH-1 displays no detectable fission activity. BAS histograms represented as heat maps of 200 nm PS liposomes incubated for 30 minutes with 1 µM AMPH-1 and 0.5 mM GTP, or similar volumes of the mock purification in the presence and absence of GTP.**

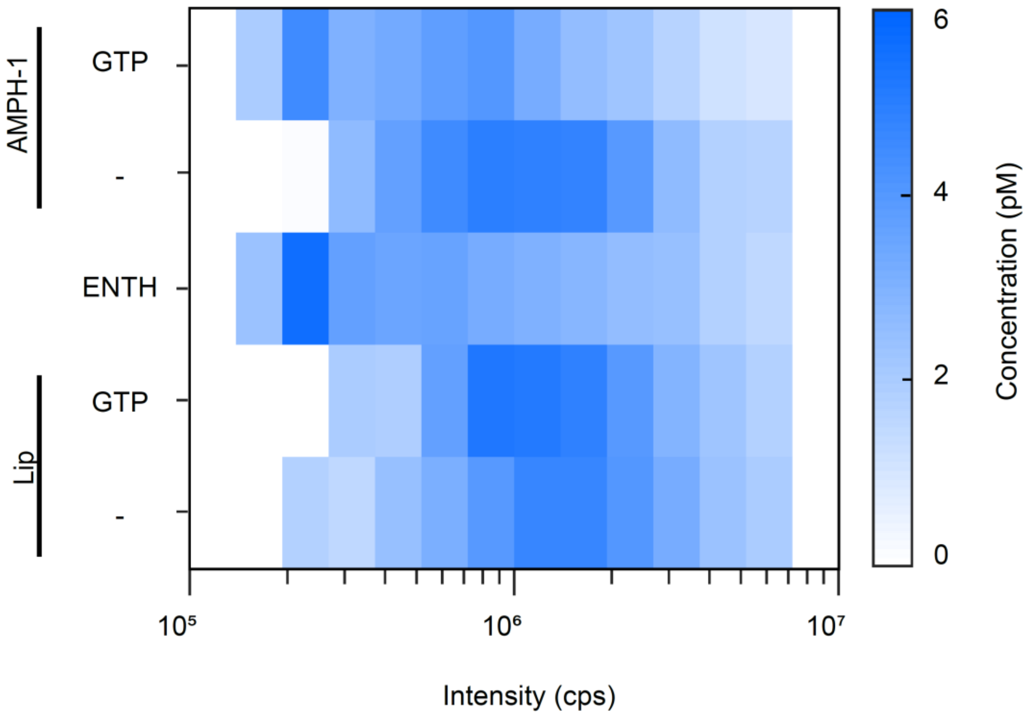

**Figure IV.5 AMPH-1 displays GTP-stimulated fission activity on liposomes created from a complex lipid mixture. BAS histograms of 200 nm 10:70:10:5:5:0.3 PC:PS:PA:PE:PI(4,5)P2:TopFluor PE liposomes incubated with either 1 µM ENTH domain of epsin or 1µM AMPH-1 for 1 hour in the absence or presence of 0.5 mM GTP.**

Negative stain electron microscopy images confirm our BAS observations. A mixture of clusters and tubular structures are observed in the RME-1 reactions with and without ATP (Fig IV.1G, H). The overall morphology of the tubular structures in the RME-1 reaction is similar to those previously observed [145]. When AMPH-1 alone is mixed with liposomes, extensive tubulation is observed. The overall morphology of these tubules is similar to those reported previously (Figure IV.1 I; IV.6 A-D) [145]. Strikingly, when GTP is added along with AMPH-1, high concentrations of both short tubules and small roughly spherical objects consistent with small vesicles are observed (Figure IV.1 J; Figure IV.6 E-H). At the same time, some larger tubules remain visible in the presence of GTP, suggesting that fission is incomplete. At the same time, in the absence of GTP, some smaller tubules and vesicles are observed indicating that AMPH-1 can support a low level of fission in the absence of GTP.

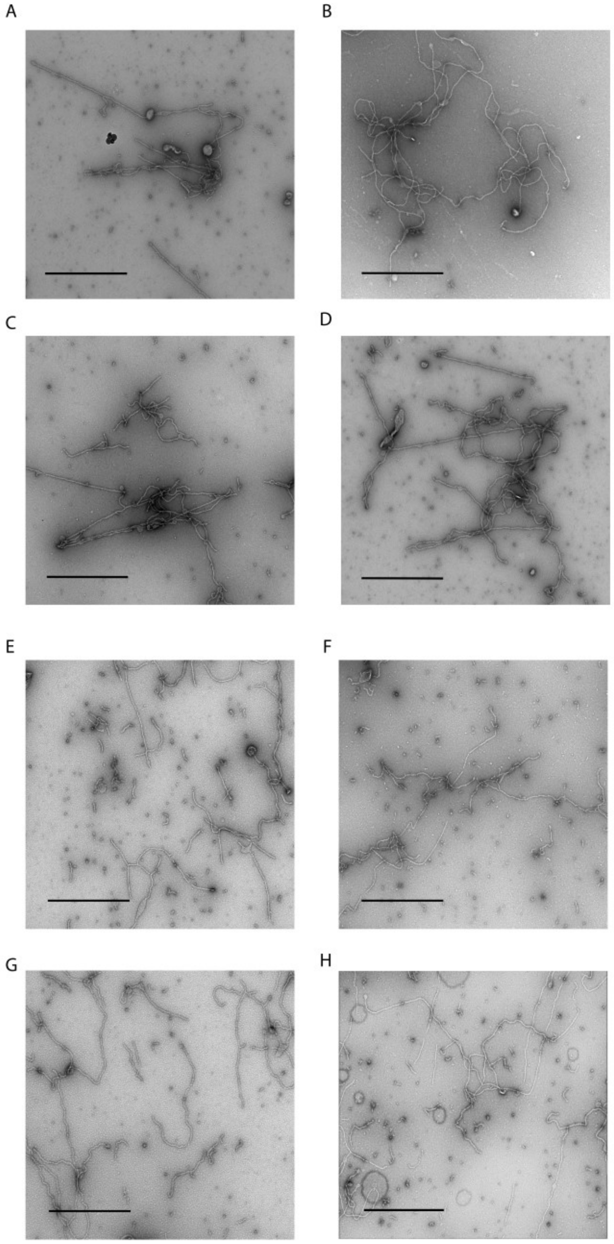

**Figure IV.6 Membrane tubulation and fission activity of AMPH-1. (A-H) Electron micrographs of negatively stained 200 nm PS liposomes after a 30 minute incubation at 23°C with 1 μM AMPH-1 in the absence (A-D) and presence of 0.5 mM GTP (E-H). Scale bar is 1 μm.**

### *Analysis of the GTP-stimulated membrane fission activity of AMPH-1*

While AMPH-1 alone can induce a low level of membrane fission, GTP dramatically stimulates this fission activity (Figure IV.7 A-B). Aggressive fission of the starting 200 nm liposomes by AMPH-1 and GTP results in concentrations of small product liposomes and tubules that are too high for standard BAS. Consequently, we employed an enhanced version of BAS in which data is acquired from a series of systematic dilutions to reconstruct the overall particle distribution [39] [183]. The overall particle distributions show a large increase in the small product vesicles, which are generated continuously when AMPH-1 is incubated with GTP.

In order to characterize the affect AMPH-1 has on the liposome distribution over ninety minutes, the data was binned into subcategories: small, medium and large. The smallest 5 bins were considered “small”, the next 5 bins were considered “medium”, and the final 6 bins were considered “large”. The rate of small product formation or the loss of the medium and large starting liposomes are shown with AMPH-1 (purple) and the AMPH-1 in the presence of GTP (blue) (Figure IV.7 C-E). With this course binning approach, the rate of small product formation can be estimated by fitting the rate of the small product formation. The GTP-stimulated AMPH-1 fission causes a single event every 37 seconds based on this rate. Although the rate of membrane fission at the recycling endosome is not known, the rate of fission by AMPH-1 is about 4 times slower than the rate of fission mediated by the synaptic dynamin-1 [88].

Suggesting that the rate of fission mediated by AMPH-1 is well within a physiologically relevant time scale.

We next sought to determine the size of the limit fission products generated by AMPH-1 in the presence of GTP. The fission reaction of 1 µM AMPH-1 with 0.5 mM GTP was incubated for 2 hours at 23°C, using 50 pM PS liposomes with 0.6% TopFluor-PE. After incubation, the reaction was examined by BAS relative to a set of liposomes standards that were created by extrusion of the same starting lipid sample to a range of known sizes between 30-200 nm (Figure IV.7 F). The endpoint fission products display a heterogeneous size distribution that appears to peak between 20-30 nm, along with a substantial tail that extends on the high side to at least 50 nm. Because of the limited detector dynamin range of the BAS microscope and the large (~100x) difference in surface area between the starting 200 nm liposomes and the much smaller fission products, concentrations of the TopFluor-PE that yield optimal brightness for the fission product vesicles and tubules could not be employed without risking damage to the detectors. Consequently, the low effective brightness of the smallest fission products limits our ability to accurately specify their size distribution by BAS. At a minimum, however, this endpoint BAS analysis sets an upper limit on the size of the smallest fission products. As an independent and complementary measurement, we also examined the endpoint fission products by Fluorescence Correlation Spectroscopy (FCS). Similarly, FCS analysis of the endpoint fission products is consistent with a heterogeneous population of vesicles that range between 30 nm and 100 nm in diameter (Figure IV.7 G).

To further confirm these results, negative stain transmission electron microscopy (TEM) images were taken of the products of this reaction. Detailed analysis of these TEM images demonstrates that the starting 200 nm liposomes have been converted to a much larger number of smaller vesicles and tubules. The bulk of the fission products have an apparent size of ~30 nm, though there is a significant representation of larger objects and tubules with sizes extending up to 50-100 nm (Figure IV.7H-J). The product vesicles and tubules are consistent with the size of transport carriers observed in *C. elegans*, as these carriers range from 28.5 nm to 100 nm in diameter [211].

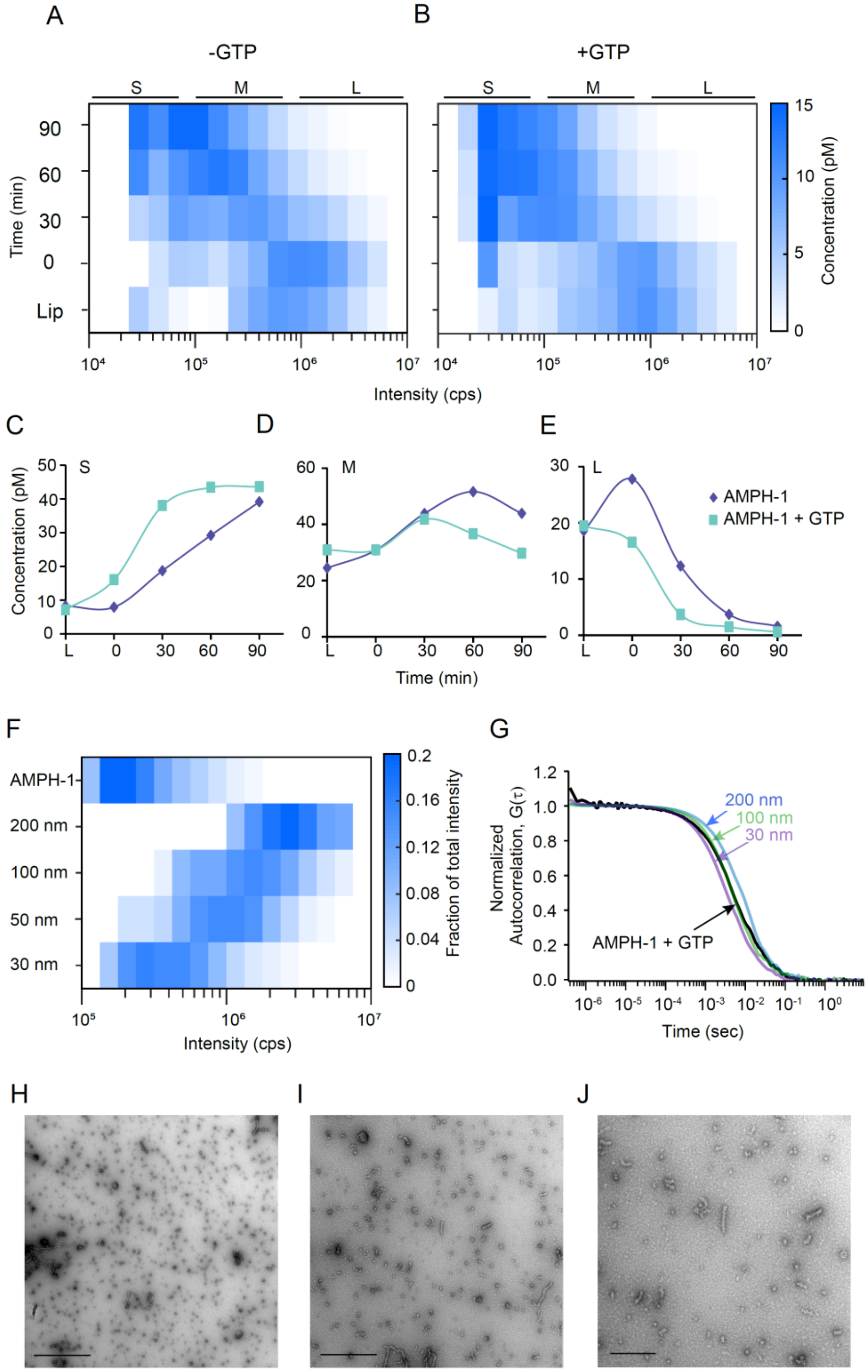

**Figure IV.7. Analysis of GTP-stimulated membrane fission activity of AMPH-1.**
**(continued on the next page)**

**(A-B) BAS distributions of liposomes with 1 µM AMPH-1 incubated for the time indicated in the absence (A), or presence (B) of 0.5 mM GTP. (C-E) The BAS data was segmented into three distinct size bins small, medium and large based on the intensity of the liposomes. The rate of small product formation (C) or the loss of the medium size liposomes (D) and large starting liposomes (E) are shown for the reactions with 1 µM AMPH-1 in the absence (purple diamonds) or presence of 0.5 mM GTP (blue squares). (G-K) Analysis of limit products derived from fission of 200 nm PS liposomes labeled with 0.6% TopFluor-PE, 1 µM AMPH-1 and 0.5 mM GTP after incubation for 2 hours at 23°C using BAS(G) and FCS (H) using liposomes extruded to 30, 50, 100, and 200 nm as standards. Micrographs of negative stain liposomes after 2 hour incubation with 1 µM AMPH-1 and 0.5 mM GTP (I-K). Scale bar is 1 µm (I), 0.5 µm (J), and 0.2 µm (K). Abbrviation: Lip, Liposomes; S, small; M, medium; L, large.**

*The role of GTP hydrolysis in membrane fission by AMPH-1.*

In order to address the role of GTP in stimulated fission by AMPH-1, we took three approaches. We first measured the fission activity of AMPH-1 in the presence of various concentrations of GTP, to test whether AMPH-1 could cause fission at physiologic concentrations of GTP (Figure IV. 8A). The AMPH-1 reaction with 62.5 µM GTP, shows a subtle change in the distribution compared to the protein alone. However, the AMPH-1 reaction at 125 µM GTP shows a significant change in both the size and the concentration of liposomes. The distributions of membrane fission at 250 µM, and 500 µM GTP do not appear to be significantly different than the liposome distribution at 125 µM GTP. Therefore, the AMPH-1 fission an apparent half maximal activity at requires 125 µM GTP, well within the range of GTP found in living cells [212].

Next we tested whether GTP hydrolysis is necessary for fission by AMPH-1 using guanine nucleotide analogs. The fission activity of 1 μM AMPH-1 was measured using GTP, GDP, GTPγS, a slowly hydrolysable analog of GTP, and GMP-PNP, a non-hydrolyzable analog of GTP, and the results were compared to fission with protein alone (Figure IV.8B). Incubation of the liposomes with the guanine nucleotides in the absence of AMPH-1 shows little change in the distribution of the liposomes (Figure IV.9); therefore, the changes in peak distributions are not a result of incubation of the liposomes with nucleotides. Interestingly, incubation with GMP-PNP appears to inhibit even the basal fission activity of AMPH-1, while the other nucleotides enhance fission activity. These findings are consistent with a functional GTP hydrolytic cycle linked to membrane fission. Because GDP also causes fission, it is unlikely that AMPH-1 uses the energy from GTP hydrolysis to induce large scale conformational change similar that observed with dynamin [88]. Rather, it is more likely that the hydrolysis of GTP to GDP acts as a switch that allows the GDP-bound AMPH-1 to populate a fission active conformation.

Negative stain TEM was employed to examine at the morphologies of tubules formed by AMPH-1 in the presence and absence of GTP. Liposomes were extruded to 1 μm and processed quickly to observe the tubulation activity of AMPH-1 in order to reduce the amount of starting liposomes converted to small products. In the absence of GTP, AMPH-1 generated tubules that were non-uniform (Figure IV.8C). In contrast, tubules formed by AMPH-1 in the presence of GTP are uniform, and narrower than those formed in the absence of nucleotide (Figure IV.8D). Membrane fission is also observed using these larger liposomes in the presence of GTP but not in the absence.  These observations are, in principle consistent with two models of GTP-stimulated fission: (1) conformational change of AMPH-1 in the presence of GTP and (2) with guanine nucleotide affecting the binding of AMPH-1 to the membrane.

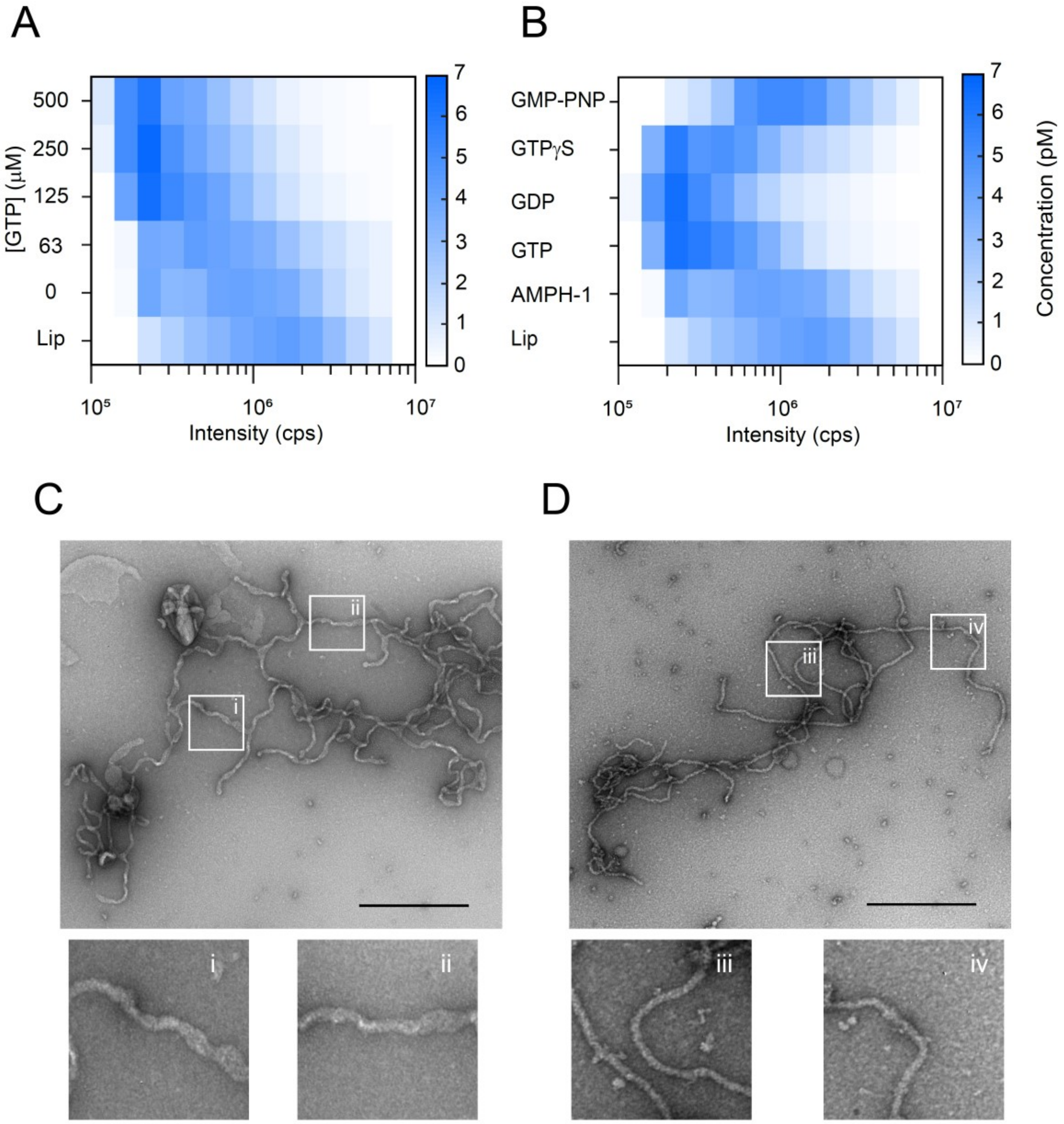

**Figure IV.8 The effect of GTP on AMPH-1 mediated fission, and tubular morphologies. (A-B) BAS histograms of 1 µM AMPH-1 and 200 nm PS liposomes incubated for 30 minutes in the absence, or presence of varying concentrations of GTP as indicated (A). BAS histograms of 200 nm liposomes incubated with 1 µM AMPH-1 for 30 minutes in the absence, or presence of 0.5 mM GTP, GDP, GTPγS, or GMP-PNP (B). (C-D) Electron micrographs of negatively stained 1 µm PS liposomes with 3 µM AMPH-1 in the absence (C) and presence of 0.5 mM GTP (D). Scale bar is 1 µm. Abbreviation: Lip, Liposomes.**

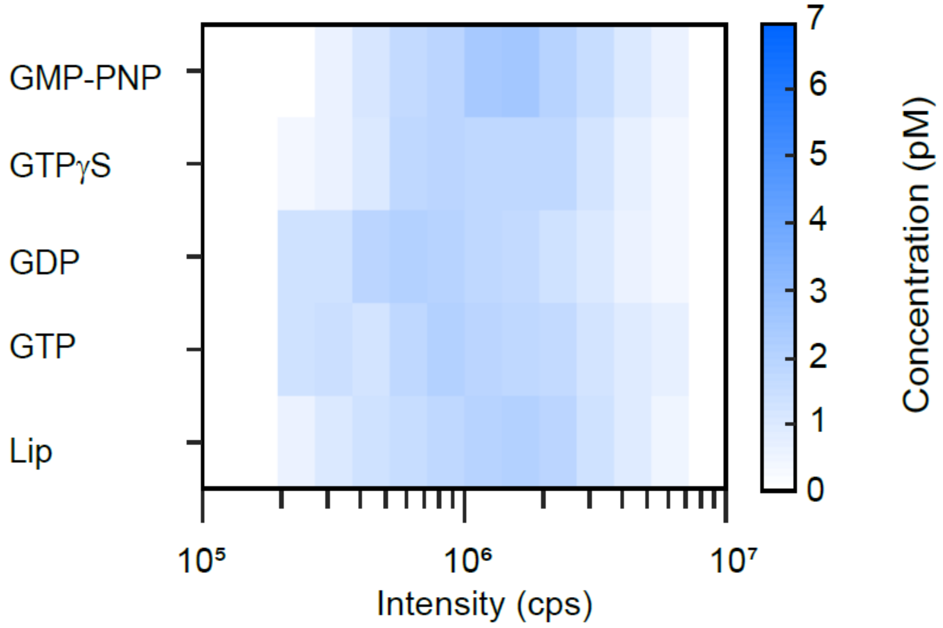

**Figure IV.9 PS liposome size distributions are unaffected by the presence of guanine nucleotides. BAS histograms of 200 nm PS liposomes incubated in the absence, or presence of 0.5 mM GTP, GDP, GTPγS, or GMP-PNP.**

*The binding of AMPH-1 to liposomes was measured using multi-color-BAS*

In order to determine whether the nucleotide state affects the ability of AMPH-1 to bind to liposomes, we performed a multi-color BAS (MC-BAS) experiment [183]. In this experiment, liposomes are labeled with Vybrant DiD and AMPH-1 is labelled with eGFP (Figure IV.10A). In an MC-BAS experiment, two co-aligned lasers are used to excite eGFP, and Vybrant DiD, and correlated burst are measured using single a pair of photon counting avalanche photodiodes. Raw data of 120 nM AMPH-1 incubated with 0.06% Vybrant DiD labeled PS liposomes shows primarily coincident bursts, and few non-coincident bursts (Figure 4B). Coincident bursts from samples of AMPH-1-eGFP incubated with PS liposomes, and with and without nucleotide were analyzed and plotted as a heat map (Figure IV.10C-E, IV.11A-C). The diagonal on the plot is related to the protein:lipid stoichiometry of the liposomes bound to AMPH-1. Importantly, binding extent and distribution remains unchanged, regardless of the absence or presence of nucleotides. This observation strongly suggests that nucleotide does not affect the binding of AMPH-1 to liposomes. Therefore it is more likely that the enhanced membrane fission activity in the presence of GTP is due to nucleotide-induced conformational change.

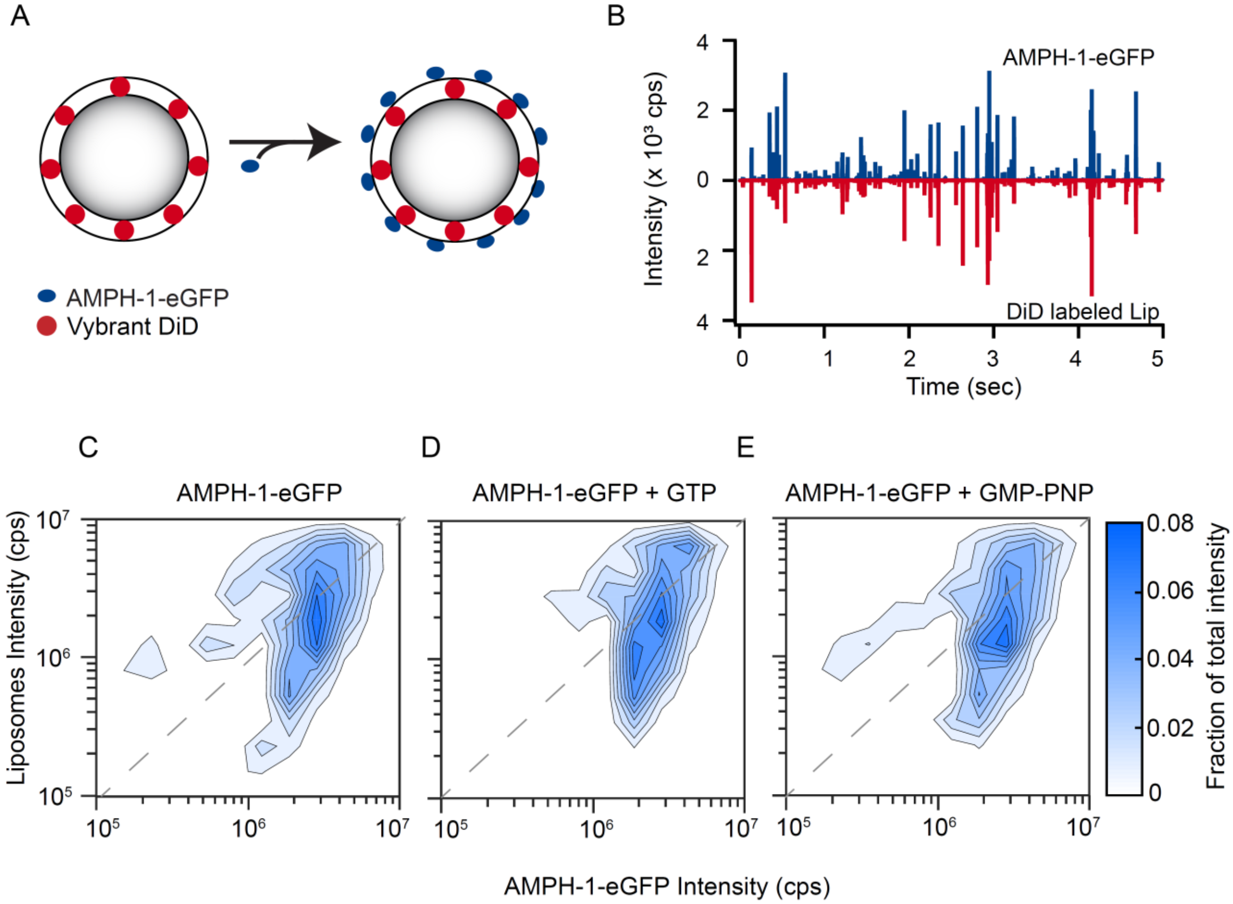

**Figure IV.10 The binding of AMPH-1 to liposomes was measured by Multi-color-BAS. (A) Schematic of the MC-BAS experiment where AMPH-1-eGFP binds to Vybrant DiD labeled liposomes. (B) Fluorescent bursts of AMPH-1-eGFP and 200 nm PS liposomes labeled with 0.06% Vybrant DiD. (C-E) 2D MC-BAS contour plot showing the binding distribution of 120 nM of AMPH-1 eGFP to Vybrant DiD labeled liposomes in the absence (C), or presence of 0.5 mM GTP (D) or 0.5 mM GMP-PNP (E). Abbreviation: Lip, Liposome.**

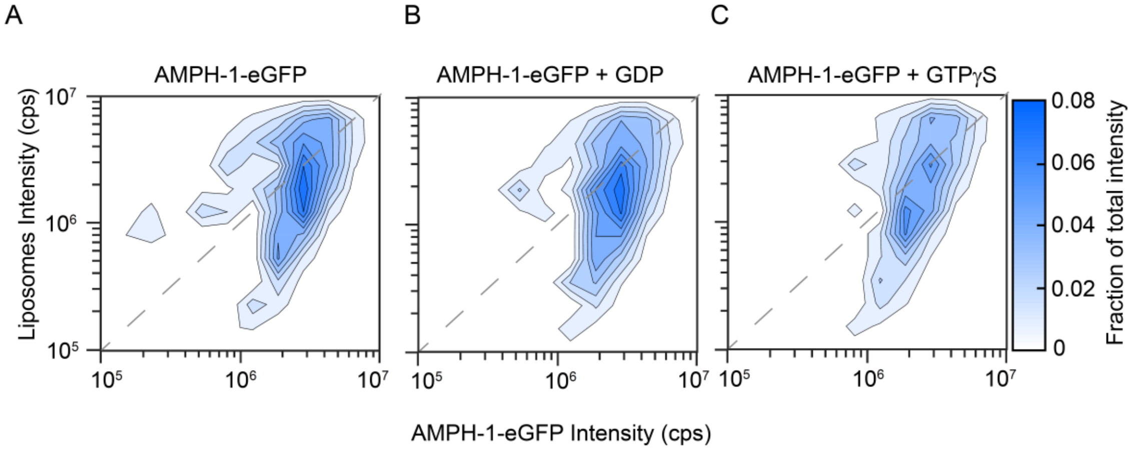

**Figure IV.11 AMPH-1 binding to PS liposomes is independent of guanine nucleotide. (A-C) 2D MC-BAS contour plot showing the binding distribution of 120 nM of AMPH-1 eGFP to Vybrant DiD labeled liposomes in the absence (A), or presence of 0.5 mM GDP (B) or with 0.5 mM GTPγS (C).**

*Efficient membrane fission by AMPH-1 requires the amphipathic helices*

In order to test the role of the amphipathic helix in membrane fission, a leucine on the hydrophobic face of the helix was mutated to a glutamine (Figure IV.12A). A similar mutation was made in the amphipathic helix of the ENTH domain of epsin, which affected the fission activity of the ENTH domain, but did not affect the binding of the protein to the liposomes [34]. The fission activity of 1 μM AMPH-1 and AMPH-1 L9Q was measured in the presence of 0.5 mM GTP on 200 nm PS liposomes. AMPH-1 L9Q incubated with GTP has decreased membrane fission activity compared to the AMPH-1 wild type protein under the same conditions (Figure IV.12B). In order to exclude the possibility that this change in activity was due to a change in the affinity of the mutant protein for the liposomes an MC-BAS experiment was performed. The coincident burst from the reaction of 120 nM AMPH-1-eGFP or AMPH-1-eGFP L9Q incubated with 0.06% Vybrant DiD labeled liposomes and 0.5 mM GTP were analyzed and plotted as a 2D contour map (Figure IV.12 C-D). The extent and distribution of liposome binding by both proteins is very similar, showing that this mutation does not significantly alter the binding activity of the protein. Therefore the N-terminal amphipathic helix of AMPH-1 is essential for efficient membrane fission.

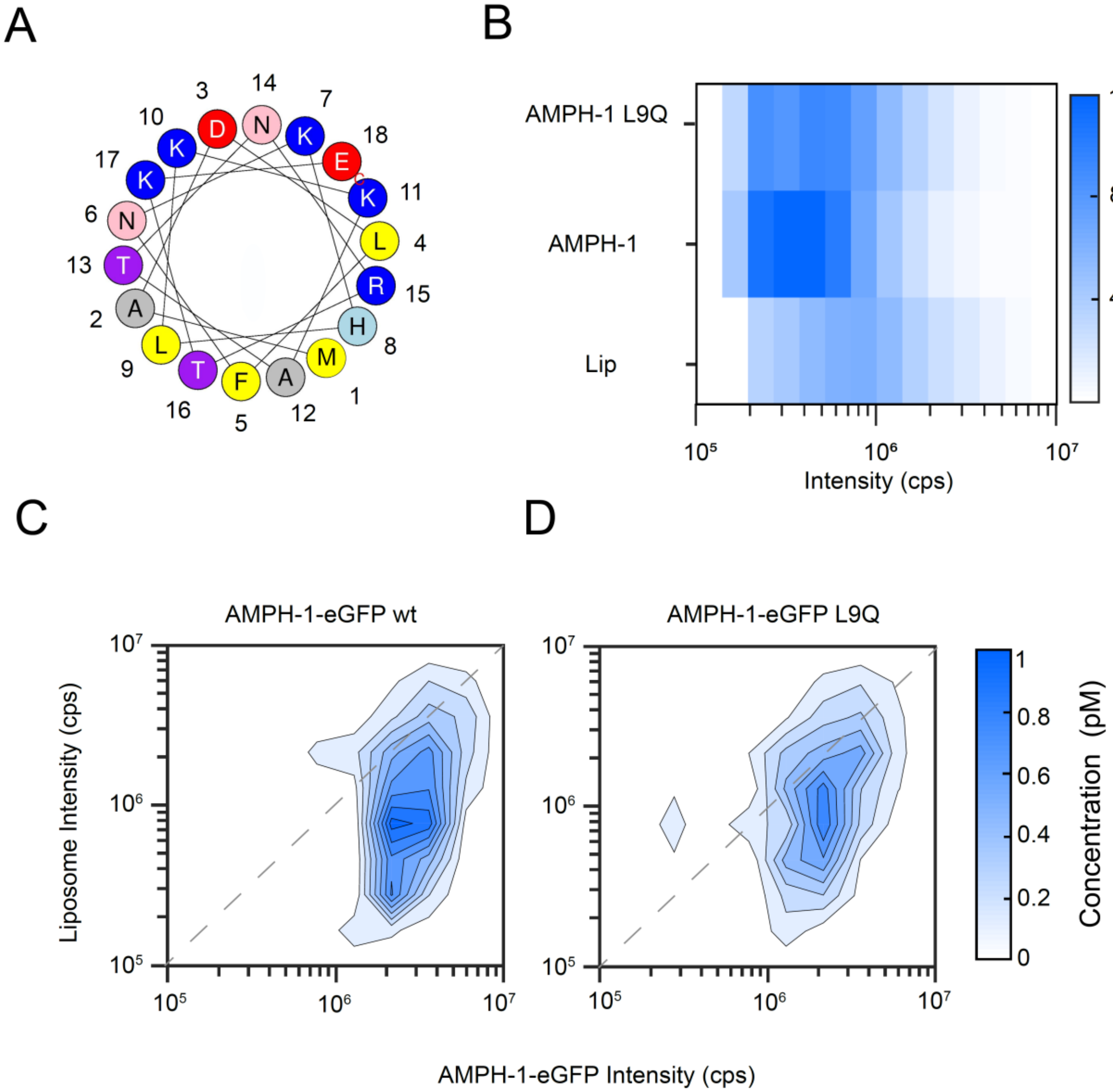

**Figure IV.12 Efficient membrane fission mediated by AMPH-1 requires the N-terminal amphipathic helices. (A) Helical wheel diagram of the amphipathic helix of AMPH-1. (B) BAS historgrams of the reaction of liposomes incubated with 0.5 mM GTP in the absence of AMPH-1, with 1 μM AMPH-1 or with 1 μM AMPH-1 L9Q. (C-D) 2D MC-BAS contour plot showing the binding distribution of 120 nM AMPH-1-eGFP (C) or AMPH-1-eGFP L9Q (D) to liposomes labeled with 0.06% Vybrant DiD in the presence of 0.5 mM GTP. Abbreviation: Lip, Liposome**

### *GTP-stimulated fission activity of S. cerevisiae RVS161/167*

We next asked whether GTP stimulated membrane fission by AMPH-1 is a general feature of this family of proteins. We therefore examined the fission activity of the distantly related *S. cerevisiae* amphiphysin homolog RVS161/167p. Using TopFluor-PE labeled PS liposomes, 0.2 μM RVS161/167p showed membrane fission activity after a 10 minute incubation at 20°C (Figure IV.13A). Like AMPH-1, this activity is greatly stimulated with GTP (Figure IV.13A). Negative stain TEM images confirm the BAS observations (Figure IV.13 B). While even 0.2 μM RVS161/167p can induce membrane fission alone, addition of GTP dramatically accelerates the fission reaction, resulting in a fission event every 10 seconds on average, a physiologically relevant rate (Figure IV.13 C) [213] . In order to test whether this fission activity is specific to GTP, 0.2 μM RVS161/167p was incubated with 0.5 mM ATP, GMP-PNP or GDP for 10 minutes at 20°C. Consistent with the results with AMPH-1, RVS161/167p does not show stimulated fission activity in the presence of ATP, and the activity appears to be inhibited by GMP-PNP (Figure IV.13 D).

We next sought to analyze the products of the RVS161/167p fission reaction. The membrane fission reaction was incubated with 0.2 μM RVS161/167p and 0.5 mM GTP for 40 minutes, after which BAS and FCS data were acquired (Figure IV.13 E-F). The endpoint fission products display a heterogeneous size distribution that appears to peak between 20-30 nm based on calibrated BAS measurements. Similarly, FCS observations are consistent with fission products similar to 15-30 nm diameter liposomes. Thus, like AMPH-1, RVS161/167p also possesses a potent GTP-stimulated membrane fission activity.

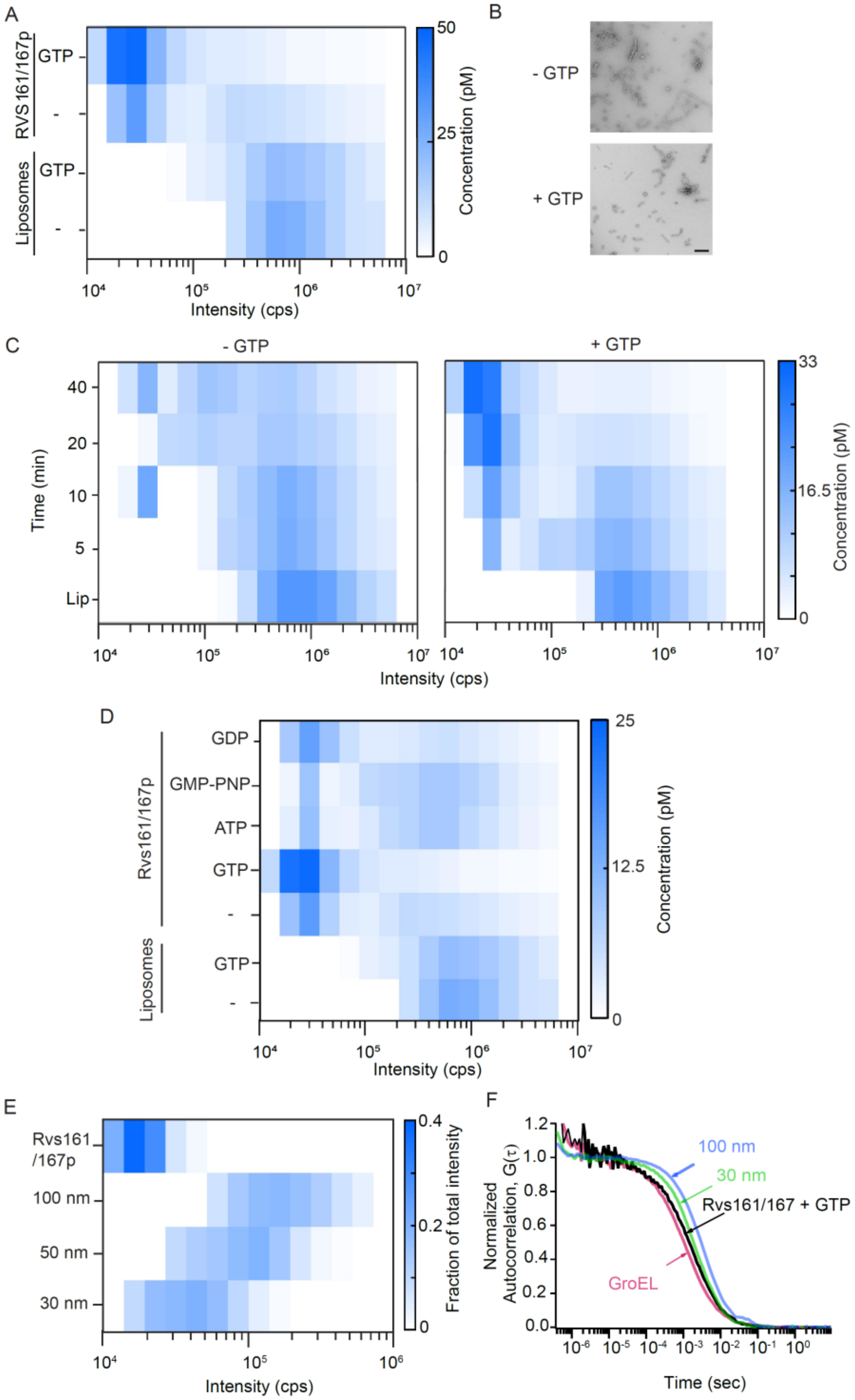

**Figure IV.13 The yeast amphiphysin homolog RVS161/167p also possesses aggressive, GTP-stimulated membrane fission activity. (continued on the next page)**

**(A) Observation of RVS161/167 fission by BAS. PS liposomes with 0.3% TopFluor-PE were incubated with 200 nM RVS161/167p for 10 minutes at 20°C in the presence and absence of GTP. (B) Micrographs of PS liposomes incubated with 200 nM RVS161/167p in the presence and absence of GTP. (C-D) BAS histograms of 200 nM RVS161/167p incubated for the time indicated in the absence (C), or presence of 0.5 mM GTP (D). (E) The fission activity of 200 nM RVS161/167p in the absence, or presence of 0.5 mM GTP, ATP, GMP-PNP or GDP (E). (F-G) Analysis of limit products derived from fission of 200 nm PS liposomes labeled with 0.6% TopFluor-PE, 200 nM RVS161/167p and 0.5 mM GTP after incubation for 40 minutes at 20°C using BAS(G) and FCS (H) using liposomes extruded to 30, 50, 100, and 200 nm as standards**

### *RME-1 regulates the GTP-stimulated AMPH-1 mediated membrane fission*

RME-1 is essential for membrane fission at the recycling endosome [143]. However, we have shown that RME-1 cannot cause fission alone (Figure IV.1). In order to examine the role of RME-1 we performed an order of addition experiment. In these experiments RME-1 with ATP and AMPH-1 with GTP were incubated briefly at room temperature, prior to mixing the proteins with liposomes. All reactions were done with 0.25 mM of each nucleotide, and 1 µM of each protein. Three conditions were examined: (1) AMPH-1 incubated with the liposomes prior to the addition of RME-1, (2) AMPH-1 and RME-1 incubated prior to the addition of the liposomes, and (3) RME-1 incubated with liposomes prior to the addition of AMPH-1. After mixing was complete all reactions were incubated at 23°C, for 30 minutes (Figure IV.14A). AMPH-1 was incubated with 0.25 mM ATP plus 0.25 mM GTP as a control. Under all conditions, the AMPH-

1 mediated fission activity was inhibited by the addition of RME-1, consistent with RME-1 acting as a negative regulator of AMPH-1. In order to confirm this conclusion, the molar ratio of RME-1 to AMPH-1 was decreased. If RME-1 does act as a negative regulator of AMPH-1 lower concentrations of RME-1 should release AMPH-1 fission activity. The fission activity of 1 μM AMPH-1 with 0.25 mM ATP, and 0.25 mM GTP was measured in the presence of varying concentrations of RME-1 (Figure IV.14B). The fission activity of AMPH-1 was inhibited at equimolar concentrations of AMPH-1 and RME-1. However, as the concentration of RME-1 is decreased in relation to the AMPH-1 concentration, the fission activity begins to increase, though it does not reach the activity of AMPH-1 alone with nucleotide in the concertation range explored in this experiment. These results are consistent with RME-1 acting as a negative regulator of AMPH-1 mediated membrane fission activity.

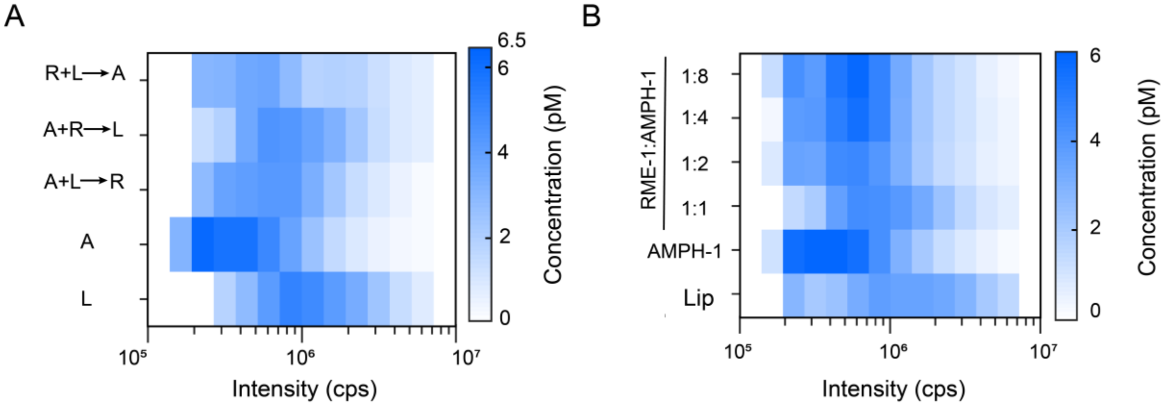

**Figure IV.14 RME-1 regulates AMPH-1 mediated membrane fission. (A) BAS histograms of the reaction of 200 nm PS liposomes with 1 µM AMPH-1 with 0.25 mM GTP, and 1 µM RME-1 with 0.25mM ATP. Reactions were performed as indicated, with the protein and liposomes (before the arrow) incubated for 1 minute at room temperature prior to the addition of the final component (after the arrow). After the addition of the final assay component the reactions were incubated for 30 minutes at 23 °C. AMPH-1 and liposomes were incubated for 30 minutes with 0.25 mM GTP, and 0.25 mM ATP. (B) BAS histograms of liposomes and 1 µM AMPH-1 incubated with various concentrations of RME-1 as indicated in the presence of 0.25 mM GTP and 0.25 mM ATP. Abbreviations: A, AMPH-1; R, RME-1; L, Liposomes.**

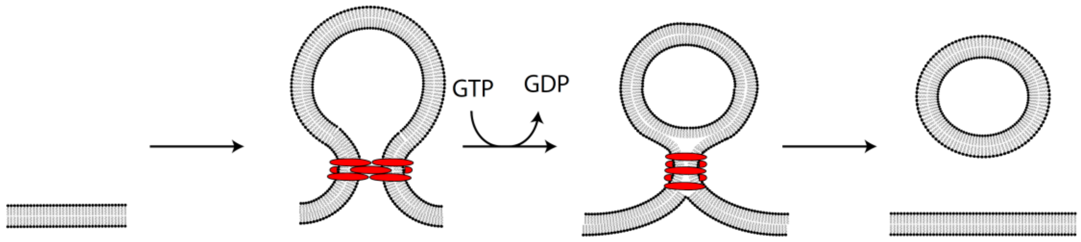

**Figure IV.15 Model of AMPH-1 mediated membrane fission. AMPH-1 binds to membranes to generate and stabilize membrane curvature. Membrane fission is stimulated when AMPH-1 is bound to GDP.**

## Discussion

RME-1 and AMPH-1 are key regulators of membrane fission at the basolateral recycling endosome. In this study we show that RME-1 is not the minimal fission machinery like dynamin-1, nor does RME-1 cause membrane fission with AMPH-1 as was seen with dynamin-2 [38]. These observations are in contrast to recent findings with the mammalian EHD1 on supported membrane tubules (SMrT) [154]. This study found the probability of fission by EHD1 increased as the diameter of SMrTs decrease [154]. It is likely that either AMPH-1 cannot form tubules of the narrow diameter required for RME-1 mediated membrane fission activity or RME-1 does not have EHD1–like fission activity. By contrast, we show that AMPH-1 possesses very efficient membrane fission activity, which is dramatically stimulated by GTP (Figure IV.15). Importantly, the evolutionarily diverged and heterodimeric yeast amphiphysin homolog RVS161/167 also displays aggressive GTP-stimulated membrane fission activity. We show that the amphipathic helices of AMPH-1 are required for fission as mutations in the hydrophobic face of the amphipathic helices diminish the membrane fission activity. Significantly, MC-BAS experiments demonstrate this effect is not caused by a change in the affinity of the protein for the liposomes compared to wild-type AMPH-1. These results are consistent with previous observations that the ENTH domain of epsin and N-BAR proteins are able to cause membrane fission through the insertions of its amphipathic helix into the lipid bilayer [34, 39, 40]. The RME-1 inhibition of AMPH-1 mediated membrane fission activity is consistent with it acting as a negative regulator, a function that has been previously suggested for RME-1 homologs [153, 155].

Membrane fission has been extensively studied and the diversity of membrane fission mechanisms has increased over the past two decades [37, 214]. Potential mechanisms include line tension, friction driven scission, and the localization of actin pulling to the membrane in order to generate pulling forces[126] [215]. N-BAR proteins have been proposed create lipid “fences”, recruit the cytoskeleton and act to generate and stabilize membrane curvature [37, 127] [18] [168]. In general, the N-BAR proteins have been assigned roles as regulatory proteins in most fission models. While this study does not address these other potential roles of AMPH-1, and therefore it is possible that these mechanisms also play a role, this study strongly suggests AMPH-1 is not simply a regulatory or accessory factor.

This study can also exclude the protein crowding model [60]. N-BAR mediated membrane fission has been proposed to occur through a protein crowding at the membrane [64, 159]. The results presented in this study are inconsistent with this model. If AMPH-1 caused fission by simply crowding the membrane then nucleotide would likely have no effect on the fission activity, given that binding is not affected by nucleotide. Furthermore, the amphipathic helix mutant displays reduced membrane fission activity though it shows no significant difference in the amount of protein bound to the liposomes. Therefore we can conclude that the AMPH-1 mediated membrane fission is most likely not a consequence of protein crowding.

The observation that evolutionarily divergent N-BAR proteins are able to cause membrane fission in a GTP-stimulated manner argues strongly that this is likely a general feature of the amphiphysins. Amphiphysin could, therefore, play an active role in clathrin mediated endocytosis. This result is relevant to membrane fission mediated by dynamin-2, the ubiquitously non-neuronal isoform of this protein. Previous work has shown that amphiphysin stimulates the fission activity of dynamin-2 [216]. Based on the work presented here, it is likely that amphiphysin plays an active role in dynamin-2 mediated membrane fission.

The results presented in this study show GTP-stimulated membrane fission activity of AMPH-1. However the results from this study do not address the mechanism by which GTP stimulates the membrane fission activity of AMPH-1. Furthermore, we identify RME-1 as a regulator of AMPH-1 GTP-stimulated membrane fission, but the mechanism by which this regulation occurs remains to be established. It is possible that the regulation observed by RME-1 acts to restrict the tubulation activity of AMPH-1 as previously observed [155]. Future work will focus on these two proteins and the functional roles proposed in this paper to further the understanding of membrane fission at the basolateral recycling endosome.

# CHAPTER V

# CONCLUSIONS AND FUTURE DIRECTIONS

## Conclusions

The purpose of this study was to identify the minimal machinery needed for membrane fission at the basolateral recycling endosome (BRE) of *C. elegans*. Receptor Mediated Endocytosis 1 (RME-1) and amphiphysin 1 (AMPH-1) were identified to be key regulators of membrane trafficking from the BRE to the plasma membrane in the intestine of adult worms [143] [145]. RME-1 is an EH domain containing protein and a member of the dynamin superfamily. Members of the dynamin superfamily undergo conformational changes which are linked to membrane fission and fusion [217]. AMPH-1 is an N-BAR protein which is a subgroup of the structurally conserved BAR domain superfamily that possesses an N-terminal amphipathic helix. Proteins in the BAR domain superfamily generate and stabilize membrane curvature. Based on previous studies with other members of these two protein superfamilies, two models of membrane fission were proposed. In the first model RME-1 alone is proposed to act a fission machine similar to dynamin-1/2. In this model, AMPH-1 acts as an accessory factor needed to target RME-1 and help induce membrane curvature [38]. In the second model AMPH-1 directly acts as the core fission machinery through the insertion of its amphipathic helices into the membrane [40, 42]. A principal goal of the work described here was to put these models to the test.

### *RME-1 does not mediate membrane fission*

Results from this study do not support a role for RME-1 as the central machinery for membrane fission at the BRE. Rather, RME-1 appears to cause 200 nm phosphatidylserine (PS) liposomes to clump, or flocculate, as observed by BAS and negative stain TEM [176] images. The flocculation activity of RME-1 appears to be independent of nucleotide but tubules are observed in EM images when RME-1 is incubated in the presence of ATP. This function is not unique to RME-1, as flocculation activity has been described for the mammalian Eps15 homology domain containing protein 2 (EHD2) [146, 218]. These results suggest that RME-1 can bind to membranes in the absence of ATP, as previously observed, and causes flocculation through an uncharacterized mechanism [146, 218]. Like the EHD proteins, RME-1 in the ATP bound form likely makes nucleotide-dependent contacts between dimers that form helical oligomers, or rings, around membrane tubules, however this has not been shown for RME-1 [145, 146, 150]. While RME-1 does not cause membrane fission, it may play a role in the stabilization of membrane curvature based on these observations.

The work described here also shows that RME-1 does not cause membrane fission in the presence of AMPH-1. This observation suggests that the lack of membrane fission by RME-1 alone is not a consequence of insufficient membrane curvature [38]. Recently, the RME-1 homolog EHD1 was shown to cause membrane fission on lipid tubules with diameters less than 20 nm [154]. The results from our single particle, free solution study are not, however consistent with these results. It is possible that the tubules formed by AMPH-1 are not narrow enough to facilitate the membrane fission activity of RME-1, though this explanation is not consistent with *in vivo* observations [145]. It is also possible that RME-1 is not able to cause membrane fission despite the high amount of sequence homology with EHD1. Previous observations made with mammalian EHD1 and EHD3 suggest that these proteins have significantly different functions at the tubular recycling endosome despite their high sequence identity (86%) [148]. In the presence of AMPH-1, RME-1 does not cause liposome flocculation. The flocculation activity observed with EHD2 was mitigated by using vesicles smaller than 50 nm in diameter, which is consistent with the diameter of the tubules formed by AMPH-1 [218]. RME-1 requires a membrane tubule of a specific diameter in order to form correct between the dimers and oligomerize correctly on a membrane bilayer.

### *AMPH-1 as the mediator of membrane fission*

The results reported here strongly support a model in which AMPH-1 acts as a core fission machinery. More significantly, this work suggests that N-BAR proteins like AMPH-1 are unappreciated GTP utilizing proteins which can act as molecular switches. The *S. cerevisiae* N-BAR proteins RVS161/167p also catalyzes membrane fission in the presence of GTP. Amphipathic helices are required for the fission activity of AMPH-1, because mutations in the hydrophobic face of the amphipathic helices diminish membrane fission activity. Multi-Color BAS experiments show this effect is not due to a change in the affinity of the protein for the liposomes relative to wild-type AMPH-1. These observations are consistent with previous work showing the ENTH domain of epsin is able to cause membrane fission through the insertions of its amphipathic helix into the lipid bilayer [39] [40]. These observations support a model in which AMPH-1 acts as a fission machine, at least in part, through GTP-dependent regulation of its amphipathic helices.

The fission activity observed with N-BAR proteins has previously been attributed to the high protein concentrations used *in vitro*, resulting in high local protein concentrations at the membrane that cause a molecular crowding-induced membrane disruption [159]. However our results are inconsistent with a simple protein crowding mechanism [64]. The enhanced membrane fission activity of AMPH-1 in the presence of GTP cannot be explained by a crowding mechanism unless nucleotide affects the binding of AMPH-1 to the membrane. The results of the MC-BAS experiments show guanine nucleotides do not affect the amount of AMPH-1 bound to the lipid bilayers (Figure IV.4, IV.14). Furthermore, if fission activity was due to a protein crowding effect, then the AMPH-1 and AMPH-1 L9Q would have similar membrane fission activity, as the binding of the proteins to the liposomes is not significantly different (Figure IV.5). However, a decrease in membrane fission activity is observed with the mutant protein compared to the wild type. Based on the results of this study, the GTP-stimulated fission activity of AMPH-1 cannot be attributed to a non-specific protein crowding effect.

This study does not address whether other proposed biophysical mechanisms might also contribute to membrane fission by AMPH-1. These models include the line tension model, membrane fission mediated by actin pulling forces, or friction-driven scission. The nature of the single particle BAS fission assay precludes drawing any conclusions about the contributions of line tension. However, prior work has shown the *S. cerevisiae* N-BAR proteins RVS161/167p are able to stabilize phosphatidylinositol 4,5 bisphosphate (PI(4,5)$P_2$) microdomains and generate a phase boundary during clathrin mediated endocytosis (CME) [127, 219]. This boundary coupled with actin pulling forces is proposed to mediate membrane fission at the plasma membrane of yeast. PI(4,5)$P_2$ is an important lipid also found in the membrane of the BRE [220]. Like RVS161/167p, AMPH-1 may create microdomains of PI(4,5)$P_2$ resulting in phase boundaries at the BRE. The phase boundary could be coupled to actin pulling forces to cause membrane fission [221]. It is likely that if this mechanism is relevant *in vivo* it must work in some fashion with the GTP stimulated activity characterized in this work described here.

### *GTP stimulation of AMPH-1 activity*

The finding that AMPH-1 has GTP stimulated membrane fission activity is unprecedented. Membrane fission mediated by N-BAR proteins has often been attributed to the high concentrations of protein used *in vitro*, a model that is not consistent with our results [40, 64, 159]. Several other studies have observed membrane fission activity by N-BAR proteins that are also not consistent with a simple protein crowding effect. From these studies and the data obtained in this study, three models can be proposed to explain how GTP stimulates AMPH-1 mediated membrane fission.

In the first model the binding of GTP to AMPH-1 could release an autoinhibited state of the protein, allowing this active form of the protein to bind to lipid bilayers. This autoinibitory mechanism of membrane binding has been observed with numerous members of the BAR superfamily including the N-BAR proteins Bin 1 and endophilin, the F-BAR protein syndapin and the BAR protein PICK1 [174] [193, 200, 204, 222-224] . In this mechanism intramolecular interactions between the SH3 or PDZ domain and the BAR domain inhibit membrane tubulation activity. This autoregulation is not through an interaction with SH3 or PDZ domains consensus sequences but rather is mediated through electrostatic interactions between the SH3 or PDZ domain and the BAR domain [174] [200] [222]. Activation of the BAR proteins is mediated by a partner protein which contain the consensus sequence for the SH3 (poly-proline) or PDZ (ϕ-G-ϕ where ϕ is a hydrophobic amino acid) domains [225] [226]. Upon activation the

BAR proteins are able to bind and tubulate liposomes. Our results are not consistent with a model in which the SH3 domains of AMPH-1 prevent the protein from binding to the membrane until GTP is bound, because membrane binding and tubulation is observed in the absence of GTP.

In the second model, GTP acts to trigger a conformational switch that would prevent the BAR domain of AMPH-1 from directly binding to the lipid bilayer. The binding of the BAR domain to the liposomes membrane has been proposed restrict the fission activity of N-BAR proteins [40].

Based on the data from this study neither model explains how GTP stimulates the fission activity of AMPH-1. However, it is possible the GTP stimulation of AMPH-1 mediated membrane fission contains elements of both models. Data presented here shows AMPH-1 does not bind to guanine nucleotides in free solution (see Appendix A). This observation suggests the GTP binding site is only accessible when AMPH-1 is oligomerized on a lipid bilayer. The data also shows the membrane fission activity of AMPH-1 is enhanced in the presence of GDP and inhibited with GMP-PNP. This result suggests that AMPH-1 is able to adopt a specific conformation in the GDP-bound form that is able to cause membrane fission. This observation may link the fission activity of AMPH-1 to the hydrolysis of GTP. Finally, the difference in the tubular morphologies formed by AMPH-1 with and without GTP on 1 μm phosphatidylserine liposomes is suggestive of a large-scale conformational change in the presence of GTP.

### *Regulation of AMPH-1 membrane fission activity by RME-1*

The results from this study most strongly support a model of RME-1 function in which this protein acts to regulate or control membrane fission by AMPH-1. The membrane fission activity of AMPH-1 is significantly decreased in the presence of equimolar ratios of RME-1 (Figure IV.14A). As the molar ratio of RME-1 to AMPH-1 decreases the membrane fission activity increases, consistent with RME-1 regulating AMPH-1 mediated membrane fission (Figure IV.14B). Other members of the EH domain family have also been shown to regulate membrane fission [153, 155]. The lamprey EH domain protein (1-EHD) was shown to regulated dynamin-1 mediated membrane fission [155]. Furthermore 1-EHD could also inhibit the tubulation activity of dynamin-1, a state which is not able to mediate membrane fission. Therefore 1-EHD was proposed to act as a "ruler" to prevent the excessive tubulation activity of dynamin-1. Consistent with this model, previous *in vitro* work has shown that tubules formed with RME-1 and AMPH-1 are significantly shorter than those formed with either protein alone [145]. These experiments were done in the presence of ATP$\gamma$S, and it is currently unknown if these results will be consistent when the proteins are incubated with GTP or a GTP analog.

### *Implications for AMPH-1 homologs*

Observations made in this dissertation show that the amphiphysin homologs from *C. elegans* (AMPH-1) and *S. cerevisiae* (RVS161/167p) have membrane fission activity which is stimulated by GTP. This observation is unprecedented, as neither protein has a canonical GTP-binding domain. AMPH-1 and RVS161/167p are structurally homologous proteins, with little sequence identity (~22%). The conserved membrane fission activity of the two proteins may indicate that other amphiphysin homologs also have GTP-stimulated membrane fission activity. In mammals, amphiphysin localizes to the plasma membrane during clathrin mediated endocytosis (CME) [121]. Amphiphysin generates high membrane curvature, and recruits dynamin to the site of membrane fission. Dynamin-1, the neuronal isoform of dynamin, undergoes a conformational change upon GTP hydrolysis which catalyzes membrane fission [88]. Membrane fission mediated by dynamin-1 has been observed in vitro, in the absence of any other proteins[192]. However, the ubiquitiously expressed isoform of dynamin, dynamin-2, requires amphiphysin in order to cause membrane fission [38]. Amphiphysin also decreases the GTP hydrolysis activity of dynamin-2 [38]. Based on the previous results with dynamin-1 the increase in membrane fission with a decrease in GTP hydrolysis are contradictory. However, these results can be explained in two possible models; (1) amphiphysin causes the fission or (2) amphiphysin plays a very active role in fission with dynamin-2. The results outlined in this dissertation, along with previous observations with dynamin-2, potentially shift the paradigm of membrane fission mediated by only dynamin to one that is dependent on amphiphysin as the fission machinery.

## Future Directions

### *Determining how GTP stimulates membrane fission by AMPH-1*

The data presented in this work is the first step in understanding the mechanism of membrane fission at the basolateral recycling endosome of *C. elegans*. In order to fully understand the role of GTP in AMPH-1 mediated fission, however, the conformational changes associated with guanine nucleotide binding should be explored in greater depth. Although our results are not consistent with a role for the AMPH-1 SH3 domain in modulating binding to a membrane, however it is possible that the SH3 domain impacts the ability of AMPH-1 to adopt its fission activity conformation. Two different approaches could be used to test a model in which the SH3 domain regulates the fission activity of AMPH-1. The first approach involves removal of the SH3 domain of AMPH-1 and measure the fission activity of the ΔSH3 protein compared to the wild-type AMPH-1. The second approach would be to measure the fission activity of AMPH-1 in the presence of a poly-proline peptide that can bind directly to the SH3 domain [207]. If the SH3 domain does bind to another site in the AMPH-1 dimer and thus inhibit activity, fission should increase in the absence of the SH3 domain or the presence a poly-proline consensus sequence. Furthermore if the role of GTP is to release this SH3-based auto-inhibition, then the ΔSH3 variant or the addition of the poly-proline peptide should display GTP-independent and aggressive fission activity.

An alternative model for the role of GTP is similar to other mechano-chemical systems, GTP binding and hydrolysis causes a large scale conformational change in AMPH-1 that is directly linked to the fission. Structural information is required in order to test for and understand a conformation-based model. Because the AMPH-1 dimer does not appear to bind GTP in free solution, therefore, it is likely that the membrane-bound form of the protein binds to nucleotide. The most likely route to developing structural information about this state would, therefore, most likely involve electron microscopy, either TEM or cryoelectron microscopy (cryo-EM). The structure of membrane bound endophilin and amphiphysin were solved previously and can be used to inform experiments with AMPH-1 going forward [169]. If a structural model can be developed at sufficiently high resolution, it is hoped that the GTP binding site of the protein can be identified. Subsequently, mutations can be made in *amph-1* to further probe the mechanism of GTP-stimulated membrane fission activity of AMPH-1.

### *"Leakiness" of AMPH-1 mediated membrane fission*

It is likely that physiologically relevant membrane fission uses a conserved mechanism in which the lumen of the organelle does not leak into the cytoplasm. We have validated a single particle leakage assay based on MC-BAS that can measure loss of a fluorescent lumenal dye from a liposome undergoing fission. This assay can be used to assess whether membrane fission mediated by AMPH-1 occurs through a conserved or non-conserved mechanism. If AMPH-1 causes membrane fission through a non-conserved mechanism, then an appealing model is that the role of RME-1 may be to control this fission reaction in a way that enforces lumenal conservation.

*Elucidating the how RME-1 regulates the fission activity of AMPH-1*

The results from this study strong support a model in which RME-1 acts to regulate of AMPH-1 fission activity. Previous work has shown that RME-1 homologs regulate the membrane fission activity of caveolea and dynamin by restricting the tubulation activity of fission proteins [153] [155]. These shorter tubules are proposed to prevent long, fission-inactive tubules from forming. Previous observations have shown that RME-1 and AMPH-1 form short tubules in the presence of ATPγS [145].

To obtain further insight into the mechanism of regulated membrane fission at the BRE, the role of the nucleotide hydrolysis cycle of RME-1 and AMPH-1 must be elucidated. As RME-1 binds to ATP and AMPH-1 binds to GTP it is possible that the binding interaction of the two proteins is regulated by the nucleotide hydrolysis cycle. In order to address the role of nucleotides in the binding of RME-1 to AMPH-1, two different approaches can be taken. The first is to measure the binding of AMPH-1 and RME-1 in solution. The binding of RME-1 and AMPH-1 can be measured using biolayer interferometry (BLI), (data not shown). Preliminary BLI results show that ATPγS-bound RME-1 cannot bind to AMPH-1; however the binding of ATPγS-bound RME-1 to AMPH-1 is observed in the presence of GMP-PNP. These results are suggestive of a role of nucleotide binding and possibly hydrolysis in the binding interaction of AMPH-1 and RME-1. To test whether nucleotide impacts the localization of AMPH-1 and RME-1 to liposomes, MC-BAS experiments could be performed with fluorescently labeled protein. These two approaches can then be used in combination to measure the role of nucleotide in the binding of AMPH-1 to RME-1 and their localization to a liposome.

An ATP hydrolysis cycle has been proposed to play an important role in the release of the mammalian EHD proteins from membranes, but it unknown whether this function is conserved in RME-1 [150, 151]. MC-BAS experiments could be performed using fluorescently labeled RME-1 to assess the role of nucleotide hydrolysis in membrane binding and dissociation. These experiments should focus on three RME-1 mutants: RME-1 T88A (cannot bind to ATP), RME-1 T110A (cannot hydrolyze ATP), and RME-1 I173Q (has enhanced ATP hydrolysis activity). Similar mutants were originally characterize in EHD2 [146]. Using these variants, and ATP analogs it should be possible to understand the functional role of ATP hydrolysis in the membrane binding activity of RME-1. Importantly, these point mutants have already been made in the pET21a-MBP vector used for the expression of RME-1.

While many models can be proposed to explain how RME-1 regulates AMPH-1, two models would appear most likely based on the results outlined here. First, RME-1 could restrict the oligomerization of AMPH-1 on membrane in much the same way as proposed for the RME-1 homolog 1-EHD [155]. If correct we would anticipate that upon RME-1 release from the membrane, AMPH-1 could initiate membrane fission. This model could be examined using TEM and BAS. EM can be used to determine the length of the tubule formed by AMPH-1 and RME-1. If RME-1 acts as a ruler, shorter tubules will be observed with the two proteins in the presence of guanine and adensosine nucleotide analogs [145]. Subsequently, MC-BAS experiments with AMPH-1 and RME-1 or the RME-1 ATP hydrolysis mutants will be used to measure the binding of AMPH-1 and RME-1 to liposomes. It is expected that as RME-1 dissociates from the liposomes, AMPH-1 can initiate fission. It is possible that dissociation of an mRuby2 labeled RME-1 from a liposome cannot be reliably measured if the protein re-binds to the liposomes. As an alternative, pulse-chase experiments, where RME-1-mRuby2 is allowed to bind to the liposomes first, and unlabeled RME-1 added subsequently could be used. If RME-1 releases from the membrane it would be expected that the coincidence of RME-1 and liposomes would decrease as the unlabeled protein replaces the fluorescent protein on the membrane. Finally, the structure of the protein complexes on liposomes would give further insight into the mechanism in which RME-1 restricts the oligomerization of AMPH-1. Structural studies could be approached using by cryo-EM and single particle reconstruction.

In an alternative model, the binding of the EH domain of RME-1 to the linker region of AMPH-1 could block AMPH-1 from adopting a fission active conformation. To test this model, MC-BAS will be performed using fluorescently labeled AMPH-1 and RME-1. For these experiments, an AMPH-1 mutant that cannot bind to RME-1 will be employed (AMPH-1 F306A F363A) [145]. These MC-BAS experiments could then be used to determine whether RME-1 binds to the liposomes in the presence of the AMPH-1 mutant. If there is no change in the ability of RME-1 to bind to the liposomes, then standard BAS could be used to determine the fission activity of RME-1 and AMPH-1 F306A F363A. If the membrane fission activity is the same in the presence and absence of RME-1 it is likely that the the binding of the EH domain to the linker region of AMPH-1 regulates its membrane fission activity. To gain further understanding into this mechanism, cryo-EM could be used to determine the structure of the two proteins simultaneously bound to liposomes. These results coupled with the structure of AMPH-1 oligomerized on a liposome could give key insight into the active and inactive forms of AMPH-1.

# REFERENCES

1. Palade, G., *Intracellular Aspects of the Process of Protein Synthesis.* Science, 1975.

2. Wu, L.G., et al., *Exocytosis and endocytosis: modes, functions, and coupling mechanisms.* Annu Rev Physiol, 2014. **76**: p. 301-31.

3. Doherty, G.J. and H.T. McMahon, *Mechanisms of endocytosis.* Annu Rev Biochem, 2009. **78**: p. 857-902.

4. Watanabe, S. and E. Boucrot, *Fast and ultrafast endocytosis.* Curr Opin Cell Biol, 2017. **47**: p. 64-71.

5. Olkkonen, V.M. and E. Ikonen, *Genetic defects of intracellular-membrane transport.* N Engl J Med, 2000. **343**(15): p. 1095-104.

6. Gomez-Navarro, N. and E.A. Miller, *COP-coated vesicles.* Curr Biol, 2016. **26**(2): p. R54-R57.

7. Swanton, E. and N.J. Bulleid, *Protein folding and translocation across the endoplasmic reticulum membrane.* Mol Membr Biol, 2003. **20**(2): p. 99-104.

8. Appenzeller-Herzog, C. and H.P. Hauri, *The ER-Golgi intermediate compartment (ERGIC): in search of its identity and function.* J Cell Sci, 2006. **119**(Pt 11): p. 2173-83.

9. Chidgey, M.A., *Protein targeting to dense-core secretory granules.* Bioessays, 1993. **15**(5): p. 317-21.

10. Howell, G.J., et al., *Cell Biology of Membrane Trafficking in Human Disease.* 2006. **252**: p. 1-69.

11. Ponnambalam, S. and S.A. Baldwin, *Constitutive protein secretion from the trans-Golgi network to the plasma membrane.* Mol Membr Biol, 2003. **20**(2): p. 129-39.

12. Naesens, M., et al., *Bartter's and Gitelman's syndromes: from gene to clinic.* Nephron Physiol, 2004. **96**(3): p. p65-78.

13. Thuenauer, R., et al., *Four-dimensional live imaging of apical biosynthetic trafficking reveals a post-Golgi sorting role of apical endosomal intermediates.* Proc Natl Acad Sci U S A, 2014. **111**(11): p. 4127-32.

14. Traub, L.M. and J.S. Bonifacino, *Cargo recognition in clathrin-mediated endocytosis.* Cold Spring Harb Perspect Biol, 2013. **5**(11): p. a016790.

15. Maxfield, F.R., *Role of endosomes and lysosomes in human disease.* Cold Spring Harb Perspect Biol, 2014. **6**(5): p. a016931.

16. Schoneberg, J., et al., *Reverse-topology membrane scission by the ESCRT proteins.* Nat Rev Mol Cell Biol, 2017. **18**(1): p. 5-17.

17. Grant, B.D. and J.G. Donaldson, *Pathways and mechanisms of endocytic recycling.* Nat Rev Mol Cell Biol, 2009. **10**(9): p. 597-608.

18. Daumke, O., A. Roux, and V. Haucke, *BAR domain scaffolds in dynamin-mediated membrane fission.* Cell, 2014. **156**(5): p. 882-92.

19. Chernomordik, L.V. and M.M. Kozlov, *Protein-lipid interplay in fusion and fission of biological membranes.* Annu Rev Biochem, 2003. **72**: p. 175-207.

20. Billcliff, P.G. and M. Lowe, *Inositol lipid phosphatases in membrane trafficking and human disease.* Biochem J, 2014. **461**(2): p. 159-75.

21. Helfrich, W., *Elastic properties of lipid bilayers: theory and possible experiments.* Z Naturforsch C, 1973. **28**(11): p. 693-703.

22. Zimmerberg, J. and M.M. Kozlov, *How proteins produce cellular membrane curvature.* Nat Rev Mol Cell Biol, 2006. **7**(1): p. 9-19.

23. Kozlov, M.M., et al., *Mechanisms shaping cell membranes.* Curr Opin Cell Biol, 2014. **29**: p. 53-60.

24. Frolov, V.A. and J. Zimmerberg, *Cooperative elastic stresses, the hydrophobic effect, and lipid tilt in membrane remodeling.* FEBS Lett, 2010. **584**(9): p. 1824-9.

25. Chappie, J.S. and F. Dyda, *Building a fission machine--structural insights into dynamin assembly and activation.* J Cell Sci, 2013. **126**(Pt 13): p. 2773-84.

26. Bashkirov, P.V., et al., *GTPase cycle of dynamin is coupled to membrane squeeze and release, leading to spontaneous fission.* Cell, 2008. **135**(7): p. 1276-86.

27. Mattila, J.P., et al., *A hemi-fission intermediate links two mechanistically distinct stages of membrane fission.* Nature, 2015. **524**(7563): p. 109-113.

28. Manni, M.M., J. Derganc, and A. Copic, *Crowd-Sourcing of Membrane Fission: How crowding of non-specialized membrane-bound proteins contributes to cellular membrane fission.* Bioessays, 2017. **39**(12).

29. Frolov, V.A., et al., *Geometry of membrane fission.* Chem Phys Lipids, 2015. **185**: p. 129-40.

30. McMahon, H.T. and E. Boucrot, *Membrane curvature at a glance.* J Cell Sci, 2015. **128**(6): p. 1065-70.

31. Simunovic, M., et al., *When Physics Takes Over: BAR Proteins and Membrane Curvature.* Trends Cell Biol, 2015. **25**(12): p. 780-92.

32. Peter, B.J., et al., *BAR domains as sensors of membrane curvature: the amphiphysin BAR structure.* Science, 2004. **303**(5657): p. 495-9.

33. Drin, G. and B. Antonny, *Amphipathic helices and membrane curvature.* FEBS Lett, 2010. **584**(9): p. 1840-7.

34. Ford, M.G., et al., *Curvature of clathrin-coated pits driven by epsin.* Nature, 2002. **419**(6905): p. 361-6.

35. Lee, A., et al., *Dominant-negative inhibition of receptor-mediated endocytosis by a dynamin-1 mutant with a defective pleckstrin homology domain.* Curr Biol, 1999. **9**(5): p. 261-4.

36. Ramachandran, R., et al., *Membrane Insertion of the Pleckstrin Homology Domain Variable Loop 1 Is Critical for Dynamin-catalyzed Vesicle Scission.* Mol Biol Cell, 2009. **20**: p. 4630-4639.

37. Renard, H.F., L. Johannes, and P. Morsomme, *Increasing Diversity of Biological Membrane Fission Mechanisms.* Trends Cell Biol, 2018. **28**(4): p. 274-286.

38. Neumann, S. and S.L. Schmid, *Dual role of BAR domain-containing proteins in regulating vesicle release catalyzed by the GTPase, dynamin-2.* J Biol Chem, 2013. **288**(35): p. 25119-28.

39. Brooks, A., et al., *Single particle fluorescence burst analysis of epsin induced membrane fission.* PLoS One, 2015. **10**(3): p. e0119563.

40. Boucrot, E., et al., *Membrane fission is promoted by insertion of amphipathic helices and is restricted by crescent BAR domains.* Cell, 2012. **149**(1): p. 124-36.

41. Isas, J.M., et al., *Tubulation by amphiphysin requires concentration-dependent switching from wedging to scaffolding.* Structure, 2015. **23**(5): p. 873-81.

42. Ambroso, M.R., H.B. G., and L. R., *Endophilin A1 induces different membrane shapes using a conformational switch that is regulated by phosphorylation.* Proc Natl Acad Sci U S A, 2014. **111**(19): p. 6982-6987.

43. Lee, M.C., et al., *Sar1p N-terminal helix initiates membrane curvature and completes the fission of a COPII vesicle.* Cell, 2005. **122**(4): p. 605-17.

44. Bielli, A., et al., *Regulation of Sar1 NH2 terminus by GTP binding and hydrolysis promotes membrane deformation to control COPII vesicle fission.* J Cell Biol, 2005. **171**(6): p. 919-24.

45. Li, S.C. and P.M. Kane, *The yeast lysosome-like vacuole: endpoint and crossroads.* Biochim Biophys Acta, 2009. **1793**(4): p. 650-63.

46. Gopaldass, N., et al., *Membrane scission driven by the PROPPIN Atg18.* EMBO J, 2017. **36**(22): p. 3274-3291.

47. Rossman, J.S., et al., *Influenza virus M2 protein mediates ESCRT-independent membrane scission.* Cell, 2010. **142**(6): p. 902-13.

48. Martyna, A., et al., *Membrane remodeling by the M2 amphipathic helix drives influenza virus membrane scission.* Sci Rep, 2017. **7**: p. 44695.

49. Mukherjee, S. and F.R. Maxfield, *Role of membrane organization and membrane domains in endocytic lipid trafficking.* Traffic, 2000. **1**(3): p. 203-11.

50. Harayama, T. and H. Riezman, *Understanding the diversity of membrane lipid composition.* Nat Rev Mol Cell Biol, 2018. **19**(5): p. 281-296.

51. Brown, D.A. and E. London, *Functions of lipid rafts in biological membranes.* Annu Rev Cell Dev Biol, 1998. **14**: p. 111-36.

52. Lenz, M., S. Morlot, and A. Roux, *Mechanical requirements for membrane fission: common facts from various examples.* FEBS Lett, 2009. **583**(23): p. 3839-46.

53. Johannes, L., C. Wunder, and P. Bassereau, *Bending "on the rocks"--a cocktail of biophysical modules to build endocytic pathways.* Cold Spring Harb Perspect Biol, 2014. **6**(1).

54. Hurley, J.H., et al., *Membrane budding.* Cell, 2010. **143**(6): p. 875-87.

55. Lipowsky, R., *Domain-induced budding of fluid membranes.* Biophys J, 1993. **64**(4): p. 1133-8.

56. Baumgart, T., S.T. Hess, and W.W. Webb, *Imaging coexisting fluid domains in biomembrane models coupling curvature and line tension.* Nature, 2003. **425**(6960): p. 821-4.

57. Allain, J.M., et al., *Fission of a multiphase membrane tube.* Phys Rev Lett, 2004. **93**(15): p. 158104.

58. Roux, A., et al., *Role of curvature and phase transition in lipid sorting and fission of membrane tubules.* EMBO J, 2005. **24**(8): p. 1537-45.

59. Ewers, H. and A. Helenius, *Lipid-mediated endocytosis.* Cold Spring Harb Perspect Biol, 2011. **3**(8): p. a004721.

60. Stachowiak, J.C., et al., *Membrane bending by protein-protein crowding.* Nat Cell Biol, 2012. **14**(9): p. 944-9.

61. Busch, D.J., et al., *Intrinsically disordered proteins drive membrane curvature.* Nat Commun, 2015. **6**: p. 7875.

62. Zeno, W.F., et al., *Synergy between intrinsically disordered domains and structured proteins amplifies membrane curvature sensing.* Nat Commun, 2018. **9**(1): p. 4152.

63. Snead, W.T., et al., *Membrane fission by protein crowding.* Proc Natl Acad Sci U S A, 2017. **114**(16): p. E3258-E3267.

64. Snead, W.T., et al., *BAR scaffolds drive membrane fission by crowding disordered domains.* J Cell Biol, 2019. **218**(2): p. 664-682.

65. Guigas, G. and M. Weiss, *Effects of protein crowding on membrane systems.* Biochim Biophys Acta, 2016. **1858**(10): p. 2441-2450.

66. Shpetner, H.S. and R.B. Vallee, *Identification of dynamin, a novel mechanochemical enzyme that mediates interactions between microtubules.* Cell, 1989. **59**(3): p. 421-32.

67. Obar, R.A., et al., *Molecular cloning of the microtubule-associated mechanochemical enzyme dynamin reveals homology with a new family of GTP-binding proteins.* Nature, 1990. **347**(6290): p. 256-61.

68. Scaife, R. and R.L. Margolis, *Biochemical and immunochemical analysis of rat brain dynamin interaction with microtubules and organelles in vivo and in vitro.* J Cell Biol, 1990. **111**(6 Pt 2): p. 3023-33.

69. van der Bliek, A.M. and E.M. Meyerowitz, *Dynamin-like protein encoded by the Drosophila shibire gene associated with vesicular traffic.* Nature, 1991. **351**(6325): p. 411-4.

70. Chen, M.S., et al., *Multiple forms of dynamin are encoded by shibire, a Drosophila gene involved in endocytosis.* Nature, 1991. **351**(6327): p. 583-6.

71. Grigliatti, T.A., et al., *Temperature-sensitive mutations in Drosophila melanogaster. XIV. A selection of immobile adults.* Mol Gen Genet, 1973. **120**(2): p. 107-14.

72. Kosaka, T. and K. Ikeda, *Reversible blockage of membrane retrieval and endocytosis in the garland cell of the temperature-sensitive mutant of Drosophila melanogaster, shibirets1.* J Cell Biol, 1983. **97**(2): p. 499-507.

73. van der Bliek, A.M., et al., *Mutations in human dynamin block an intermediate stage in coated vesicle formation.* J Cell Biol, 1993. **122**(3): p. 553-63.

74. Damke, H., et al., *Induction of mutant dynamin specifically blocks endocytic coated vesicle formation.* J Cell Biol, 1994. **127**(4): p. 915-34.

75. Shpetner, H.S., J.S. Herskovits, and R.B. Vallee, *A binding site for SH3 domains targets dynamin to coated pits.* J Biol Chem, 1996. **271**(1): p. 13-6.

76. David, C., et al., *A role of amphiphysin in synaptic vesicle endocytosis suggested by its binding to dynamin in nerve terminals.* Proc Natl Acad Sci U S A, 1996. **93**(1): p. 331-5.

77. Wigge, P., Y. Vallis, and H.T. McMahon, *Inhibition of receptor-mediated endocytosis by the amphiphysin SH3 domain.* Curr Biol, 1997. **7**(8): p. 554-60.

78. McMahon, H.T., P. Wigge, and C. Smith, *Clathrin interacts specifically with amphiphysin and is displaced by dynamin1.* FEBS Letters, 1997. **413**(2): p. 319-322.

79. Shupliakov, O., et al., *Synaptic vesicle endocytosis impaired by disruption of dynamin-SH3 domain interactions.* Science, 1997. **276**(5310): p. 259-63.

80. Tuma, P.L. and C.A. Collins, *Dynamin forms polymeric complexes in the presence of lipid vesicles. Characterization of chemically cross-linked dynamin molecules.* J Biol Chem, 1995. **270**(44): p. 26707-14.

81. Stowell, M.H., et al., *Nucleotide-dependent conformational changes in dynamin: evidence for a mechanochemical molecular spring.* Nat Cell Biol, 1999. **1**(1): p. 27-32.

82. Sweitzer, S.M. and J.E. Hinshaw, *Dynamin undergoes a GTP-dependent conformational change causing vesiculation.* Cell, 1998. **93**(6): p. 1021-9.

83. Chen, Y.J., et al., *The stalk region of dynamin drives the constriction of dynamin tubes.* Nat Struct Mol Biol, 2004. **11**(6): p. 574-5.

84. Mears, J.A., P. Ray, and J.E. Hinshaw, *A corkscrew model for dynamin constriction.* Structure, 2007. **15**(10): p. 1190-202.

85. Roux, A., et al., *GTP-dependent twisting of dynamin implicates constriction and tension in membrane fission.* Nature, 2006. **441**(7092): p. 528-31.

86. Zhang, P. and J.E. Hinshaw, *Three-dimensional reconstruction of dynamin in the constricted state.* Nat Cell Biol, 2001. **3**(10): p. 922-6.

87. Danino, D., K.H. Moon, and J.E. Hinshaw, *Rapid constriction of lipid bilayers by the mechanochemical enzyme dynamin.* J Struct Biol, 2004. **147**(3): p. 259-67.

88. Antonny, B., et al., *Membrane fission by dynamin: what we know and what we need to know.* EMBO J, 2016. **35**(21): p. 2270-2284.

89. Cocucci, E., R. Gaudin, and T. Kirchhausen, *Dynamin recruitment and membrane scission at the neck of a clathrin-coated pit.* Mol Biol Cell, 2014. **25**(22): p. 3595-609.

90. Chappie, J.S., et al., *A pseudoatomic model of the dynamin polymer identifies a hydrolysis-dependent powerstroke.* Cell, 2011. **147**(1): p. 209-22.

91. Sundborger, A.C., et al., *A dynamin mutant defines a superconstricted prefission state.* Cell Rep, 2014. **8**(3): p. 734-42.

92. Shnyrova, A.V., et al., *Geometric catalysis of membrane fission driven by flexible dynamin rings.* Science, 2013. **339**(6126): p. 1433-6.

93. Copic, A., et al., *ER cargo properties specify a requirement for COPII coat rigidity mediated by Sec13p.* Science, 2012. **335**(6074): p. 1359-62.

94. Faini, M., et al., *Vesicle coats: structure, function, and general principles of assembly.* Trends Cell Biol, 2013. **23**(6): p. 279-88.

95. Raiborg, C., et al., *FYVE and coiled-coil domains determine the specific localisation of Hrs to early endosomes.* J Cell Sci, 2001. **114**(Pt 12): p. 2255-63.

96. Wollert, T. and J.H. Hurley, *Molecular mechanism of multivesicular body biogenesis by ESCRT complexes.* Nature, 2010. **464**(7290): p. 864-9.

97. Chiaruttini, N., et al., *Relaxation of Loaded ESCRT-III Spiral Springs Drives Membrane Deformation.* Cell, 2015. **163**(4): p. 866-79.

98. Babst, M., et al., *Endosomal transport function in yeast requires a novel AAA-type ATPase, Vps4p.* EMBO J, 1997. **16**(8): p. 1820-31.

99. Monroe, N. and C.P. Hill, *Meiotic Clade AAA ATPases: Protein Polymer Disassembly Machines.* J Mol Biol, 2016. **428**(9 Pt B): p. 1897-911.

100. Schoneberg, J., et al., *ATP-dependent force generation and membrane scission by ESCRT-III and Vps4.* Science, 2018. **362**(6421): p. 1423-1428.

101. Babst, M., et al., *Escrt-III: an endosome-associated heterooligomeric protein complex required for mvb sorting.* Dev Cell, 2002. **3**(2): p. 271-82.

102. Babst, M., et al., *Endosome-associated complex, ESCRT-II, recruits transport machinery for protein sorting at the multivesicular body.* Developmental Cell, 2002. **3**(2): p. 283-289.

103. Katzmann, D.J., M. Babst, and S.D. Emr, *Ubiquitin-dependent sorting into the multivesicular body pathway requires the function of a conserved endosomal protein sorting complex, ESCRT-I.* Cell, 2001. **106**(2): p. 145-155.

104. Garrus, J.E., et al., *Tsg101 and the vacuolar protein sorting pathway are essential for HIV-1 budding.* Cell, 2001. **107**(1): p. 55-65.

105. Licata, J.M., et al., *Overlapping Motifs (PTAP and PPEY) within the Ebola Virus VP40 Protein Function Independently as Late Budding Domains: Involvement of Host Proteins TSG101 and VPS-4.* Journal of Virology, 2003. **77**(3): p. 1812-1819.

106. Martin-Serrano, J., T. Zang, and P.D. Bieniasz, *Role of ESCRT-I in Retroviral Budding.* Journal of Virology, 2003. **77**(8): p. 4794-4804.

107. Radulovic, M. and H. Stenmark, *ESCRTs in membrane sealing.* Biochem Soc Trans, 2018. **46**(4): p. 773-778.

108. Farsad, K. and P.D. Camilli, *Mechanisms of membrane deformation.* Current Opinion in Cell Biology, 2003. **15**(4): p. 372-381.

109. de Figueiredo, P., et al., *Phospholipase A2 antagonists inhibit constitutive retrograde membrane traffic to the endoplasmic reticulum.* Traffic, 2000. **1**(6): p. 504-11.

110. De Figueiredo, P., et al., *Evidence that phospholipase A2 activity is required for Golgi complex and trans Golgi network membrane tubulation.* Proc Natl Acad Sci U S A, 1998. **95**(15): p. 8642-8647.

111. Fujiwara, T., et al., *Brefeldin A causes disassembly of the Golgi complex and accumulation of secretory proteins in the endoplasmic reticulum.* J Biol Chem, 1988. **263**(34): p. 18545-52.

112. Pfanner, N., et al., *Fatty Acyl-Coenzyme-a Is Required for Budding of Transport Vesicles from Golgi Cisternae.* Cell, 1989. **59**(1): p. 95-102.

113. Weigert, R., et al., *CtBP/BARS induces fission of Golgi membranes by acylating lysophosphatidic acid.* Nature, 1999. **402**(6760): p. 429-33.

114. Pagliuso, A., et al., *Golgi membrane fission requires the CtBP1-S/BARS-induced activation of lysophosphatidic acid acyltransferase delta.* Nat Commun, 2016. **7**: p. 12148.

115. Schmidt, J.A. and W.J. Brown, *Lysophosphatidic acid acyltransferase 3 regulates Golgi complex structure and function.* J Cell Biol, 2009. **186**(2): p. 211-8.

116. Valente, C., A. Luini, and D. Corda, *Components of the CtBP1/BARS-dependent fission machinery.* Histochem Cell Biol, 2013. **140**(4): p. 407-21.

117. Carlsson, A.E., *Membrane bending by actin polymerization.* Curr Opin Cell Biol, 2017. **50**: p. 1-7.

118. Svitkina, T., *The Actin Cytoskeleton and Actin-Based Motility.* Cold Spring Harb Perspect Biol, 2018. **10**(1).

119. Mattila, P.K. and P. Lappalainen, *Filopodia: molecular architecture and cellular functions.* Nat Rev Mol Cell Biol, 2008. **9**(6): p. 446-54.

120. Leduc, C., et al., *Mechanism of membrane nanotube formation by molecular motors.* Biochim Biophys Acta, 2010. **1798**(7): p. 1418-26.

121. Kaksonen, M. and A. Roux, *Mechanisms of clathrin-mediated endocytosis.* Nat Rev Mol Cell Biol, 2018.

122. Hinze, C. and E. Boucrot, *Local actin polymerization during endocytic carrier formation.* Biochem Soc Trans, 2018. **46**(3): p. 565-576.

123. Valente, C., R. Polishchuk, and M.A. De Matteis, *Rab6 and myosin II at the cutting edge of membrane fission.* Nat Cell Biol, 2010. **12**(7): p. 635-8.

124. Boulant, S., et al., *Actin dynamics counteract membrane tension during clathrin-mediated endocytosis.* Nat Cell Biol, 2011. **13**(9): p. 1124-31.

125. Kaksonen, M., Y. Sun, and D.G. Drubin, *A pathway for association of receptors, adaptors, and actin during endocytic internalization.* Cell, 2003. **115**(4): p. 475-87.

126. Simunovic, M., et al., *Friction Mediates Scission of Tubular Membranes Scaffolded by BAR Proteins.* Cell, 2017. **170**(1): p. 172-184 e11.

127. Zhao, H., et al., *Membrane-sculpting BAR domains generate stable lipid microdomains.* Cell Rep, 2013. **4**(6): p. 1213-23.

128. Gautreau, A., K. Oguievetskaia, and C. Ungermann, *Function and regulation of the endosomal fusion and fission machineries.* Cold Spring Harb Perspect Biol, 2014. **6**(3).

129. Ghosh, R.N., *Evidence for nonvectorial, retrograde transferrin trafficking in the early endosomes of HEp2 cells.* The Journal of Cell Biology, 1995. **128**(4): p. 549-561.

130. Knight, A., et al., *Membrane-Protein Trafficking through the Common Apical Endosome Compartment of Polarized Caco-2 Cells.* Molecular Biology of the Cell, 1995. **6**(5): p. 597-610.

131. Sheff, D.R., et al., *The Receptor Recycling Pathway Contains Two Distinct Populations of Early Endosomes with Different Sorting Functions.* The Journal of Cell Biology, 1999. **145**(1): p. 123-139.

132. Goldenring, J.R., *Recycling endosomes.* Curr Opin Cell Biol, 2015. **35**: p. 117-22.

133. Roberts, R.C., et al., *Mistargeting of SH3TC2 away from the recycling endosome causes Charcot-Marie-Tooth disease type 4C.* Hum Mol Genet, 2010. **19**(6): p. 1009-18.

134. Li, X. and M. DiFiglia, *The recycling endosome and its role in neurological disorders.* Prog Neurobiol, 2012. **97**(2): p. 127-41.

135. Gleason, R.J., et al., *BMP signaling requires retromer-dependent recycling of the type I receptor.* Proc Natl Acad Sci U S A, 2014. **111**(7): p. 2578-83.

136. Wakefield, L.M. and C.S. Hill, *Beyond TGFbeta: roles of other TGFbeta superfamily members in cancer.* Nat Rev Cancer, 2013. **13**(5): p. 328-41.

137. Keiser, M., et al., *Altered folding, turnover, and polarized sorting act in concert to define a novel pathomechanism of congenital sucrase-isomaltase deficiency.* J Biol Chem, 2006. **281**(20): p. 14393-9.

138. Kravtsov, D., et al., *Myosin 5b loss of function leads to defects in polarized signaling: implication for microvillus inclusion disease pathogenesis and treatment.* Am J Physiol Gastrointest Liver Physiol, 2014. **307**(10): p. G992-G1001.

139. Koivisto, U.M., A.L. Hubbard, and R. Mellman, *A novel cellular phenotype for familial hypercholesterolemia due to a defect in polarized targeting of LDL receptor.* Cell, 2001. **105**(5): p. 575-585.

140. Sato, K., et al., *C. elegans as a model for membrane traffic.* WormBook, 2014: p. 1-47.

141. Marsh, E.W., *Oligomerized transferrin receptors are selectively retained by a lumenal sorting signal in a long-lived endocytic recycling compartment.* The Journal of Cell Biology, 1995. **129**(6): p. 1509-1522.

142. Grant, B. and D. Hirsh, *Receptor-mediated endocytosis in the Caenorhabditis elegans oocyte.* Mol Biol Cell, 1999. **10**(12): p. 4311-26.

143. Grant, B., et al., *Evidence that RME-1, a conserved C-elegans EH-domain protein, functions in endocytic recycling.* Nature Cell Biology, 2001. **3**(6): p. 573-579.

144. Chen, C.C., et al., *RAB-10 is required for endocytic recycling in the Caenorhabditis elegans intestine.* Mol Biol Cell, 2006. **17**(3): p. 1286-97.

145. Pant, S., et al., *AMPH-1/Amphiphysin/Bin1 functions with RME-1/Ehd1 in endocytic recycling.* Nat Cell Biol, 2009. **11**(12): p. 1399-410.

146. Daumke, O., et al., *Architectural and mechanistic insights into an EHD ATPase involved in membrane remodelling.* Nature, 2007. **449**(7164): p. 923-7.

147. Lee, D.W., et al., *ATP binding regulates oligomerization and endosome association of RME-1 family proteins.* J Biol Chem, 2005. **280**(17): p. 17213-20.

148. Cai, B., et al., *Differential roles of C-terminal Eps15 homology domain proteins as vesiculators and tubulators of recycling endosomes.* J Biol Chem, 2013. **288**(42): p. 30172-80.

149. Bahl, K., et al., *EHD3 Protein Is Required for Tubular Recycling Endosome Stabilization, and an Asparagine-Glutamic Acid Residue Pair within Its Eps15 Homology (EH) Domain Dictates Its Selective Binding to NPF Peptides.* J Biol Chem, 2016. **291**(26): p. 13465-78.

150. Melo, A.A., et al., *Structural insights into the activation mechanism of dynamin-like EHD ATPases.* Proc Natl Acad Sci U S A, 2017. **114**(22): p. 5629-5634.

151. Hoernke, M., et al., *EHD2 restrains dynamics of caveolae by an ATP-dependent, membrane-bound, open conformation.* Proc Natl Acad Sci U S A, 2017. **114**(22): p. E4360-E4369.

152. Sharma, M., N. Naslavsky, and S. Caplan, *A role for EHD4 in the regulation of early endosomal transport.* Traffic, 2008. **9**(6): p. 995-1018.

153. Moren, B., et al., *EHD2 regulates caveolar dynamics via ATP-driven targeting and oligomerization.* Mol Biol Cell, 2012. **23**(7): p. 1316-29.

154. Deo, R., et al., *ATP-dependent membrane remodeling links EHD1 functions to endocytic recycling.* Nat Commun, 2018. **9**(1): p. 5187.

155. Jakobsson, J., et al., *Regulation of synaptic vesicle budding and dynamin function by an EHD ATPase.* J Neurosci, 2011. **31**(39): p. 13972-80.

156. Posey, A.D., Jr., et al., *EHD1 mediates vesicle trafficking required for normal muscle growth and transverse tubule development.* Dev Biol, 2014. **387**(2): p. 179-90.

157. Gallop, J.L., et al., *Mechanism of endophilin N-BAR domain-mediated membrane curvature.* EMBO J, 2006. **25**(12): p. 2898-910.

158. Renard, H.F., et al., *Endophilin-A2 functions in membrane scission in clathrin-independent endocytosis.* Nature, 2015. **517**(7535): p. 493-6.

159. Simunovic, M., et al., *Physical basis of some membrane shaping mechanisms.* Philos Trans A Math Phys Eng Sci, 2016. **374**(2072).

160. Kaksonen, M., C.P. Toret, and D.G. Drubin, *A modular design for the clathrin- and actin-mediated endocytosis machinery.* Cell, 2005. **123**(2): p. 305-20.

161. Lee, E., et al., *Amphiphysin 2 (Bin1) and T-tubule biogenesis in muscle.* Science, 2002. **297**(5584): p. 1193-6.

162. Karbowski, M., S.Y. Jeong, and R.J. Youle, *Endophilin B1 is required for the maintenance of mitochondrial morphology.* J Cell Biol, 2004. **166**(7): p. 1027-39.

163. Takahashi, Y., C.L. Meyerkord, and H.G. Wang, *Bif-1/endophilin B1: a candidate for crescent driving force in autophagy.* Cell Death Differ, 2009. **16**(7): p. 947-55.

164. Lichte, B., et al., *Amphiphysin, a novel protein associated with synaptic vesicles.* EMBO J, 1992. **11**(7): p. 2521-30.

165. McPherson, P.S., et al., *A presynaptic inositol-5-phosphatase.* Nature, 1996. **379**(6563): p. 353-7.

166. Sivadon, P., et al., *Actin cytoskeleton and budding pattern are altered in the yeast rvs161 mutant: the Rvs161 protein shares common domains*

*with the brain protein amphiphysin.* Mol Gen Genet, 1995. **246**(4): p. 485-95.

167. Takei, K., *Functional partnership between amphiphysin and dynamin.* Nat Cell Biol, 1999. **1**: p. 33-39.

168. Salzer, U., J. Kostan, and K. Djinovic-Carugo, *Deciphering the BAR code of membrane modulators.* Cell Mol Life Sci, 2017. **74**(13): p. 2413-2438.

169. Mim, C., et al., *Structural basis of membrane bending by the N-BAR protein endophilin.* Cell, 2012. **149**(1): p. 137-45.

170. Adam, J., N. Basnet, and N. Mizuno, *Structural insights into the cooperative remodeling of membranes by amphiphysin/BIN1.* Sci Rep, 2015. **5**: p. 15452.

171. Chen, Z., et al., *The N-Terminal Amphipathic Helix of Endophilin Does Not Contribute to Its Molecular Curvature Generation Capacity.* J Am Chem Soc, 2016. **138**(44): p. 14616-14622.

172. Youn, J.Y., et al., *Dissecting BAR domain function in the yeast Amphiphysins Rvs161 and Rvs167 during endocytosis.* Mol Biol Cell, 2010. **21**(17): p. 3054-69.

173. Boucrot, E., et al., *Endophilin marks and controls a clathrin-independent endocytic pathway.* Nature, 2015. **517**(7535): p. 460-5.

174. Wu, T. and T. Baumgart, *BIN1 membrane curvature sensing and generation show autoinhibition regulated by downstream ligands and PI(4,5)P2.* Biochemistry, 2014. **53**(46): p. 7297-309.

175. Ramaswami, M., K.S. Krishnan, and R.B. Kelly, *Intermediates in synaptic vesicle recycling revealed by optical imaging of Drosophila neuromuscular junctions.* Neuron, 1994. **13**(2): p. 363-75.

176. Rotem-Yehudar, R., E. Galperin, and M. Horowitz, *Association of insulin-like growth factor 1 receptor with EHD1 and SNAP29.* J Biol Chem, 2001. **276**(35): p. 33054-60.

177. Frolov, V.A., et al., *Shape bistability of a membrane neck: a toggle switch to control vesicle content release.* Proc Natl Acad Sci U S A, 2003. **100**(15): p. 8698-703.

178. Pucadyil, T.J., *A novel fluorescence microscopic approach to quantitatively analyse protein-induced membrane remodelling.* Journal of Biosciences, 2018. **43**(3): p. 431-435.

179. Roux, A., et al., *Membrane curvature controls dynamin polymerization.* Proc Natl Acad Sci U S A, 2010. **107**(9): p. 4141-6.

180. Morlot, S., et al., *Membrane shape at the edge of the dynamin helix sets location and duration of the fission reaction.* Cell, 2012. **151**(3): p. 619-29.

181. Snead, W.T. and J.C. Stachowiak, *A Tethered Vesicle Assay for High-Throughput Quantification of Membrane Fission.* Methods Enzymol, 2018. **611**: p. 559-582.

182. Puchalla, J., et al., *Burst analysis spectroscopy: a versatile single-particle approach for studying distributions of protein aggregates and fluorescent assemblies.* Proc Natl Acad Sci U S A, 2008. **105**(38): p. 14400-5.

183. Shoup, D., et al., *Development and Applications of Extended Range and Multi-dimensional Burst Analysis Spectroscopy.* in preperation, 2019.

184. Carr, C.M. and J. Rizo, *At the junction of SNARE and SM protein function.* Curr Opin Cell Biol, 2010. **22**(4): p. 488-95.

185. Campelo, F. and V. Malhotra, *Membrane fission: the biogenesis of transport carriers.* Annu Rev Biochem, 2012. **81**: p. 407-27.

186. Chernomordik, L.V. and M.M. Kozlov, *Mechanics of membrane fusion.* Nat Struct Mol Biol, 2008. **15**(7): p. 675-83.

187. Wickner, W. and R. Schekman, *Membrane fusion.* Nat Struct Mol Biol, 2008. **15**(7): p. 658-64.

188. Loerke, D., et al., *Cargo and dynamin regulate clathrin-coated pit maturation.* PLoS Biol, 2009. **7**(3): p. e57.

189. Merrifield, C.J., D. Perrais, and D. Zenisek, *Coupling between clathrin-coated-pit invagination, cortactin recruitment, and membrane scission observed in live cells.* Cell, 2005. **121**(4): p. 593-606.

190. Massol, R.H., et al., *A burst of auxilin recruitment determines the onset of clathrin-coated vesicle uncoating.* Proc Natl Acad Sci U S A, 2006. **103**(27): p. 10265-10270.

191. Taylor, M.J., D. Perrais, and C.J. Merrifield, *A high precision survey of the molecular dynamics of mammalian clathrin-mediated endocytosis.* PLoS Biol, 2011. **9**(3): p. e1000604.

192. Pucadyil, T.J. and S.L. Schmid, *Real-time visualization of dynamin-catalyzed membrane fission and vesicle release.* Cell, 2008. **135**(7): p. 1263-75.

193. Wang, Q., et al., *Molecular mechanism of membrane constriction and tubulation mediated by the F-BAR protein Pacsin/Syndapin.* Proc Natl Acad Sci U S A, 2009. **106**(31): p. 12700-5.

194. Chen, H., et al., *Epsin is an EH-domain-binding protein implicated in clathrin-mediated endocytosis.* Nature, 1998. **394**: p. 793-797.

195. Legendre-Guillemin, V., et al., *ENTH/ANTH proteins and clathrin-mediated membrane budding.* J Cell Sci, 2004. **117**(Pt 1): p. 9-18.

196. Simpson, F., et al., *SH3-domain-containing proteins function at distinct steps in clathrin-coated vesicle formation.* Nat Cell Biol, 1999. **1**(2): p. 119-24.

197. Shorter, J. and S. Lindquist, *Hsp104, Hsp70 and Hsp40 interplay regulates formation, growth and elimination of Sup35 prions.* EMBO J, 2008. **27**(20): p. 2712-24.

198. Krantz, K.C., et al., *Clathrin coat disassembly by the yeast Hsc70/Ssa1p and auxilin/Swa2p proteins observed by single-particle burst analysis spectroscopy.* J Biol Chem, 2013. **288**(37): p. 26721-30.

199. Hope, M.J., K.F. Wong, and P.R. Cullis, *Freeze-fracture of lipids and model membrane systems.* J Electron Microsc Tech, 1989. **13**(4): p. 277-87.

200. Rao, Y., et al., *Molecular basis for SH3 domain regulation of F-BAR-mediated membrane deformation.* Proc Natl Acad Sci U S A, 2010. **107**(18): p. 8213-8.

201. Chen, Z., et al., *Intradimer/Intermolecular interactions suggest autoinhibition mechanism in endophilin A1.* J Am Chem Soc, 2014. **136**(12): p. 4557-64.

202. Mills, I.G., et al., *EpsinR: an AP1/clathrin interacting protein involved in vesicle trafficking.* J Cell Biol, 2003. **160**(2): p. 213-22.

203. Beck, R., et al., *Coatomer and dimeric ADP ribosylation factor 1 promote distinct steps in membrane scission.* J Cell Biol, 2011. **194**(5): p. 765-77.

204. Meinecke, M., et al., *Cooperative recruitment of dynamin and BIN/amphiphysin/Rvs (BAR) domain-containing proteins leads to GTP-dependent membrane scission.* J Biol Chem, 2013. **288**(9): p. 6651-61.

205. Maxfield, F.R. and T.E. McGraw, *Endocytic recycling.* Nat Rev Mol Cell Biol, 2004. **5**(2): p. 121-32.

206. Huang, S. and M.P. Czech, *The GLUT4 glucose transporter.* Cell Metab, 2007. **5**(4): p. 237-52.

207. Xin, X., et al., *SH3 interactome conserves general function over specific form.* Mol Syst Biol, 2013. **9**: p. 652.

208. Puertollano, R., *Endocytic Trafficking and Human Diseases.* Endosomes, 2006.

209. Liu, Y.W., et al., *Differential curvature sensing and generating activities of dynamin isoforms provide opportunities for tissue-specific regulation.* Proc Natl Acad Sci U S A, 2011. **108**(26): p. E234-42.

210. Mizuno, N., et al., *Multiple modes of endophilin-mediated conversion of lipid vesicles into coated tubes: implications for synaptic endocytosis.* J Biol Chem, 2010. **285**(30): p. 23351-8.

211. Watanabe, S., et al., *Ultrafast endocytosis at Caenorhabditis elegans neuromuscular junctions.* Elife, 2013. **2**: p. e00723.

212. Traut, T.W., *Physiological concentrations of purines and pyrimidines.* Mol Cell Biochem, 1994. **140**(1): p. 1-22.

213. Picco, A., et al., *Visualizing the functional architecture of the endocytic machinery.* Elife, 2015. **4**.

214. Snead, W.T. and J.C. Stachowiak, *Structure Versus Stochasticity-The Role of Molecular Crowding and Intrinsic Disorder in Membrane Fission.* J Mol Biol, 2018. **430**(16): p. 2293-2308.

215. Liu, J., et al., *Endocytic vesicle scission by lipid phase boundary forces.* Proc Natl Acad Sci U S A, 2006. **103**(27): p. 10277-82.

216. Neumann, S., T.J. Pucadyil, and S.L. Schmid, *Analyzing membrane remodeling and fission using supported bilayers with excess membrane reservoir.* Nat Protoc, 2013. **8**(1): p. 213-22.

217. Ferguson, S.M. and P. De Camilli, *Dynamin, a membrane-remodelling GTPase.* Nat Rev Mol Cell Biol, 2012. **13**(2): p. 75-88.

218. Shah, C., et al., *Structural insights into membrane interaction and caveolar targeting of dynamin-like EHD2.* Structure, 2014. **22**(3): p. 409-20.

219. Liu, J., et al., *The mechanochemistry of endocytosis.* PLoS Biol, 2009. **7**(9): p. e1000204.

220. Shi, A. and B.D. Grant, *Interactions between Rab and Arf GTPases regulate endosomal phosphatidylinositol-4,5-bisphosphate during endocytic recycling.* Small GTPases, 2013. **4**(2): p. 106-9.

221. Shi, A., et al., *A novel requirement for C. elegans Alix/ALX-1 in RME-1-mediated membrane transport.* Curr Biol, 2007. **17**(22): p. 1913-24.

222. Karlsen, M.L., et al., *Structure of Dimeric and Tetrameric Complexes of the BAR Domain Protein PICK1 Determined by Small-Angle X-Ray Scattering.* Structure, 2015. **23**(7): p. 1258-1270.

223. Wang, Q., et al., *Structure and plasticity of Endophilin and Sorting Nexin 9.* Structure, 2008. **16**(10): p. 1574-87.

224. Vazquez, F.X., V.M. Unger, and G.A. Voth, *Autoinhibition of endophilin in solution via interdomain interactions.* Biophys J, 2013. **104**(2): p. 396-403.

225. McPherson, P.S., *Regulatory role of SH3 domain-mediated protein-protein interactions in synaptic vesicle endocytosis.* Cell Signal, 1999. **11**(4): p. 229-38.

226. Lee, H.J. and J.J. Zheng, *PDZ domains and their binding partners: structure, specificity, and modification.* Cell Communication and Signaling, 2010. **8**.

227. Madan, D., Z. Lin, and H.S. Rye, *Triggering protein folding within the GroEL-GroES complex.* J Biol Chem, 2008. **283**(46): p. 32003-13.

228. Niesen, F.H., H. Berglund, and M. Vedadi, *The use of differential scanning fluorimetry to detect ligand interactions that promote protein stability.* Nat Protoc, 2007. **2**(9): p. 2212-21.

229. Brock, D.J., et al., *Efficient cell delivery mediated by lipid-specific endosomal escape of supercharged branched peptides.* Traffic, 2018. **19**(6): p. 421-435.

230. Brooks, H., B. Lebleu, and E. Vives, *Tat peptide-mediated cellular delivery: back to basics.* Adv Drug Deliv Rev, 2005. **57**(4): p. 559-77.

231. Samal, S.K., et al., *Cationic polymers and their therapeutic potential.* Chem Soc Rev, 2012. **41**(21): p. 7147-94.

232. Zelphati, O., et al., *Intracellular delivery of proteins with a new lipid-mediated delivery system.* J Biol Chem, 2001. **276**(37): p. 35103-10.

233. Kay, M.A., J.C. Glorioso, and L. Naldini, *Viral vectors for gene therapy: the art of turning infectious agents into vehicles of therapeutics.* Nature Medicine, 2001. **7**: p. 33.

234. Fotin-Mleczek, M., R. Fischer, and R. Brock, *Endocytosis and Cationic Cell-Penetrating Peptides - A Merger of Concepts and Methods.* Current Pharmaceutical Design, 2005. **11**(28): p. 3613-3628.

235. Kez, C., et al., *Endocytosis, Intracellular Traffic and Fate of Cell Penetrating Peptide Based Conjugates and Nanoparticles.* Current Pharmaceutical Design, 2013. **19**(16): p. 2878-2894.

236. S., C. and H. L., *Structure and Function of Lipid-DNA Complexes for Gene Delivery.* Annual Review of Biophysics and Biomolecular Structure, 2000. **29**(1): p. 27-47.

237. Lee, Y.-J., A. Erazo-Oliveras, and J.-P. Pellois, *Delivery of Macromolecules into Live Cells by Simple Co-incubation with a Peptide.* ChemBioChem, 2010. **11**(3): p. 325-330.

238. Erazo-Oliveras, A., et al., *Protein delivery into live cells by incubation with an endosomolytic agent.* Nature Methods, 2014. **11**: p. 861.

239. Cronican, J.J., et al., *A class of human proteins that deliver functional proteins into mammalian cells in vitro and in vivo.* Chem Biol, 2011. **18**(7): p. 833-8.

240. McNaughton, B.R., et al., *Mammalian cell penetration, siRNA transfection, and DNA transfection by supercharged proteins.* Proc Natl Acad Sci U S A, 2009. **106**(15): p. 6111-6.

241. Lawrence, M.S., K.J. Phillips, and D.R. Liu, *Supercharging Proteins Can Impart Unusual Resilience.* Journal of the American Chemical Society, 2007. **129**(33): p. 10110-10112.

242. Cronican, J.J., et al., *Potent Delivery of Functional Proteins into Mammalian Cells in Vitro and in Vivo Using a Supercharged Protein.* ACS Chemical Biology, 2010. **5**(8): p. 747-752.

243. Freire, J.M., et al., *Intracellular Nucleic Acid Delivery by the Supercharged Dengue Virus Capsid Protein.* PLOS ONE, 2013. **8**(12): p. e81450.

244. Freire, J.M., et al., *Mining viral proteins for antimicrobial and cell-penetrating drug delivery peptides.* Bioinformatics, 2015. **31**(14): p. 2252-2256.

245. Freire, J.M., et al., *Rethinking the capsid proteins of enveloped viruses: multifunctionality from genome packaging to genome transfection.* FEBS J, 2015. **282**(12): p. 2267-78.

246. Sung, M., G.M. Poon, and J. Gariepy, *The importance of valency in enhancing the import and cell routing potential of protein transduction domain-containing molecules.* Biochim Biophys Acta, 2006. **1758**(3): p. 355-63.

247. Lönn, P., et al., *Enhancing Endosomal Escape for Intracellular Delivery of Macromolecular Biologic Therapeutics.* Scientific Reports, 2016. **6**: p. 32301.

248. Erazo-Oliveras, A., et al., *The Late Endosome and Its Lipid BMP Act as Gateways for Efficient Cytosolic Access of the Delivery Agent dfTAT and Its Macromolecular Cargos.* Cell Chemical Biology, 2016. **23**(5): p. 598-607.

249. Futaki, S., et al., *Translocation of Branched-Chain Arginine Peptides through Cell Membranes:  Flexibility in the Spatial Disposition of Positive Charges in Membrane-Permeable Peptides.* Biochemistry, 2002. **41**(25): p. 7925-7930.

250. Jeong, C., et al., *A branched TAT cell-penetrating peptide as a novel delivery carrier for the efficient gene transfection.* Biomaterials Research, 2016. **20**(1): p. 28.

251. Liu, Z., et al., *Macro-branched cell-penetrating peptide design for gene delivery.* Journal of Controlled Release, 2005. **102**(3): p. 699-710.

252. Backlund, C.M., et al., *Relating structure and internalization for ROMP-based protein mimics.* Biochimica et Biophysica Acta (BBA) - Biomembranes, 2016. **1858**(7, Part A): p. 1443-1450.

253. Fretz, Marjan M., et al., *Temperature-, concentration- and cholesterol-dependent translocation of L- and D-octa-arginine across the plasma and nuclear membrane of CD34 leukaemia cells.* Biochemical Journal, 2007. **403**(2): p. 335-342.

254. Najjar, K., et al., *An l- to d-Amino Acid Conversion in an Endosomolytic Analog of the Cell-penetrating Peptide TAT Influences Proteolytic Stability, Endocytic Uptake, and Endosomal Escape.* J Biol Chem, 2017. **292**(3): p. 847-861.

255. Peitz, M., et al., *Ability of the hydrophobic FGF and basic TAT peptides to promote cellular uptake of recombinant Cre recombinase: A tool for efficient genetic engineering of mammalian genomes.* Proceedings of the National Academy of Sciences, 2002. **99**(7): p. 4489-4494.

256. Sun, X., et al., *Development of SNAP-Tag Fluorogenic Probes for Wash-Free Fluorescence Imaging.* ChemBioChem, 2011. **12**(14): p. 2217-2226.

257. El-Sayed, A., S. Futaki, and H. Harashima, *Delivery of Macromolecules Using Arginine-Rich Cell-Penetrating Peptides: Ways to Overcome Endosomal Entrapment.* The AAPS Journal, 2009. **11**(1): p. 13-22.

258. Kobayashi, T., et al., *Late endosomal membranes rich in lysobisphosphatidic acid regulate cholesterol transport.* Nature Cell Biology, 1999. **1**: p. 113.

259. Kobayashi, T., et al., *Localization of Lysobisphosphatidic Acid-Rich Membrane Domains in Late Endosomes*, in *Biological Chemistry*. 2001. p. 483.

260. Araç, D., et al., *Close membrane-membrane proximity induced by Ca2+-dependent multivalent binding of synaptotagmin-1 to phospholipids.* Nature Structural &Amp; Molecular Biology, 2006. **13**: p. 209.

261. Kobayashi, T., et al., *Separation and characterization of late endosomal membrane domains.* J Biol Chem, 2002. **277**(35): p. 32157-64.

262. Rusnati, M., et al., *Interaction of HIV-1 Tat protein with heparin. Role of the backbone structure, sulfation, and size.* J Biol Chem, 1997. **272**(17): p. 11313-20.

263. Tyagi, M., et al., *Internalization of HIV-1 tat requires cell surface heparan sulfate proteoglycans.* J Biol Chem, 2001. **276**(5): p. 3254-61.

264. Argyris, E.G., et al., *The perlecan heparan sulfate proteoglycan mediates cellular uptake of HIV-1 Tat through a pathway responsible for biological activity.* Virology, 2004. **330**(2): p. 481-6.

# APPENDIX A

# THE BINDING OF GTP TO AMPH-1

## Introduction

AMPH-1 does not have a characterized nucleotide binding domain but it appears to have membrane fission activity that is stimulated by GTP. Based on this observation it would be expected that AMPH-1 would bind and possibly hydrolyze GTP.

## Experimental procedures

### *Protein preparation*

Amphiphysin 1 (AMPH-1) from *C. elegans* was expressed and purified as previously described with modifications (Chapter 4). Briefly, expression and cell lysis were performed as described. Clarified lysate was loaded onto a glutathione column, equilibrated with buffer A (50 mM Tris pH 7.4, 300 mM NaCl, 25 mM KCl, 1 mM $MgCl_2$, 2 mM DTT, 1 mM ATP). The column was extensively washed with at least 330 ml of buffer A. The protein was eluted off the column using a single step of buffer B (50 mM Tris pH 7.4, 300 mM NaCl, 1 mM $MgCl_2$, 2 mM DTT, 10 mM glutathione). The protein preparation was continued as described. For GST-AMPH-1, the protocol above was followed but the GST tag was not cleaved with Precission protease.

*GTPase assay*

GTP hydrolysis experiments were performed as previously described with modifications [227]. Briefly, 10 μ M AMPH-1 (dimer) was incubated with 500 μM GTP and 2.5 μCi of GTP [γ-$^{32}$P] (PerkinElmer) in reaction buffer (50 mM Hepes pH 7.4, 200 mM KCl, 0.5 mM $MgCl_2$, and 2 mM DTT). Reactions were incubated at room temperature with and without 2.5 mM 200 nm phosphatidylserine liposomes. Reactions were stopped in 4 M Formic acid. Free phosphate was separated from GTP using thin layer chromatography (TLC) and quantified by PhosphorImager analysis (Typhoon FLA 700; GE Healthcare) using ImageQuantTL software.

*Protease protection*

Protease protection experiments were performed using 5 μ M AMPH-1 (dimer) and 2 mM GTP, GDP, or GMP-PNP in reaction buffer (50 mM Hepes pH 7.4, 200 mM KCl, 2 mM $MgCl_2$, and 2 mM DTT). After 1 minute of incubation either 250 pg/ml proteinase K or 150 pg/ml trypsin was added to the reaction. Reactions were quenched at various time points by 10 mM phenylmethylsulfonyl fluoride (PMSF). Reactions were run on a 10% SDS-PAGE gel and bands were resolved using a coomassie blue based stain. Gels were imaged (Fotodyne gel imager) and the protein bands were quantified (ImageJ).

### *Differential scanning Fluorimetry (DSF)*

DSF was performed as previously described with modifications [228]. Briefly, 1, 2.5 or 5 μM AMPH-1 (dimer) were incubated with 1 mM GTP, GDP, GMP-PNP, GTPγS, or ATP in reaction buffer (20 mM Hepes pH 7.4, 200 mM KCl, 1 mM $MgCl_2$, and 2 mM DTT). Sypro orange (Invitrogen S6650) was added to the protein for a final concentration of 2.5X. A temperature scan was run from 25°C to 95°C with an increase of 0.5°C per min in a CFX96 Real Time PCR (BioRad). Data was analyzed using Precission Melt Analysis software.

### *Quenching of the intrinsic tryptophan fluorescence of AMPH-1*

Intrinsic fluorescence measurements were performed on a PTI fluorometer at 23°C. The excitation wavelength was set at 295 nm and the emission spectra were taken from 310 to 400 nm with a slit width of 4 nm. Spectra was taken of 110 nM of AMPH-1 with concentration of GMP-PNP and AMP-PNP ranging from 0.6 to 60 μM in reaction buffer (50 mM Hepes pH 7.4, 200 mM KCl, 2 mM $MgCl_2$, and 2 mM DTT). Spectra of 400 nM of N-acetyl-tryptophanamide (NATA) were taken under the same experimental conditions as the GMP-PNP titration with AMPH-1 to correct for the inner filter effect of GMP-PNP. The integrated signal from each spectrum was quantified between 330-350 nm for the AMPH-1 reactions, and 345-365 for the NATA reactions. The change in fluorescence between the AMPH-1 without nucleotide ($F_0$) and with nucleotide (F) is calculated by 1-$F/F_0$. The change in fluorescence signal at each nucleotide concentration was fit to a single site binding equation:

$$F(L) = \frac{n * L}{K_d + L} + C$$

where n is the number of binding sites, L is the ligand concentration, $K_d$ is the dissociation constant and C is a constant. Error was calculated by

$$\frac{dQ}{Q} = \sqrt{\left(\frac{dF}{F}\right)^2 + \left(\frac{dF_0}{F_0}\right)^2}$$

where dQ, dF and $dF_0$ are the standard deviations at the different nucleotide concentrations.

*Biolayer interferometry*

BLI experiments were performed on an Octet RED96 instrument (FortéBio). Anti-GST antibody-coated sensor tips (FortéBio cat 18-5096) were wetted in reaction buffer (50 mM Hepes pH 7.4, 200 mM KCl, 2 mM $MgCl_2$, 2 mM DTT) prior to the exposure to the GST-AMPH-1. The sensor tips were loaded with 125 nM GST-AMPH-1 or 125 nM GST, and then transferred into reaction buffer to removed nonspecifically bound protein. The loaded tips were reacted with either GMP-PNP or GDP at various concentrations ranging from 0.03 mM to 1 mM. For all experiments using GMP-PNP the reaction buffer was supplemented with 0.05% Tween-20. Binding was measured for 5 minutes, followed by a 5 minute dissociation period in reaction buffer. Sensors were washed in 10 mM glucine pH 1.9 between experiments.  The resulting binding curves were processed using the FortéBio Octet data analysis software.

### *Isothermal titration calorimetry*

ITC experiments were performed using a MicroCal iTC200 instrument (Malvern Paralytical).  Briefly, 2 mM GMP-PNP was titrated into 50 µM AMPH-1 (dimer) or reaction buffer (50 mM Hepes pH 7.4, 200 mM KCl, 5 mM MgCl2, 2 mM DTT) at 25°C.  The GMP-PNP stock solution was added to AMPH-1 using a total of 9 injections.  The first injection was 0.2 µl and each subsequent injection was 4 µl.  The reaction was allowed to equilibrate for 2.5 minutes between injections.

## Results

### *GTP hydrolysis assay*

The GTPase activity of AMPH-1 was measured using a standard phosphate release assay.  The GTP hydrolysis activity was measured with 10 µM AMPH-1 dimer, and 0.5 mM GTP. In order to see if the GTP hydrolysis rate is affected by a membrane bilayer, the activity of AMPH-1 was measured in the presence and absence of 200 nm phosphatidylserine (PS) liposomes. The spontaneous hydrolysis rate of GTP was also measure as a control.  The reactions were run at room temperature with a total of 8 time points taken over 60 minutes.  The rate of GTP hydrolysis by AMPH-1 is 0.014 mM $P_i$/mM AMPH-

1/min and the addition of liposomes to the reaction did not further stimulate the rate 0.017 mM $P_i$/mM AMPH-1/min (Figure A.1). The spontaneous rate of GTP hydrolysis is 0.006 mM $P_i$/ min, about 2 to 3 fold lower than the reactions with AMPH-1.

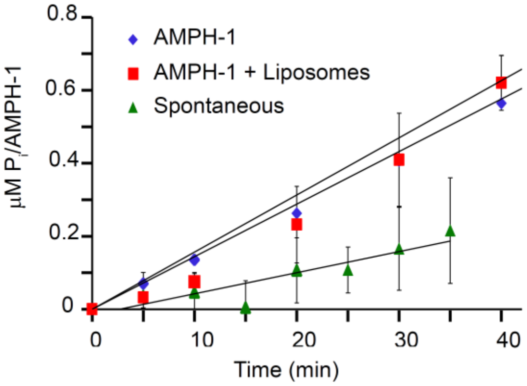

**Figure A.1 GTP hydrolysis active of AMPH-1. The GTP hydrolysis activity of 10 µM AMPH-1 with 0.5 mM GTP, with and without 2.5 mM 200 nm PS liposomes. Spontaneous GTP hydrolysis was measured as a control.**

*GTP binding assays*

To test whether AMPH-1 bound to GTP in free solution five assays were run. The first assay was a protease protection assay in which 5 µM AMPH-1 was incubated with 2 mM guanine nucleotide. The AMPH-1 digested with either 250 pM/ml proteinase K or 150 pM/ml trypsin. The reaction was incubated at room temperature and at total of nine time points over 20 minutes. The protein bands on a SDS-PAGE gel were compared, with no novel bands appearing in the reactions with nucleotide. The band which corresponded to the starting protein was quantified using densitometry. No difference is observed in the rate of the digestion of the starting material (Figure A.2).

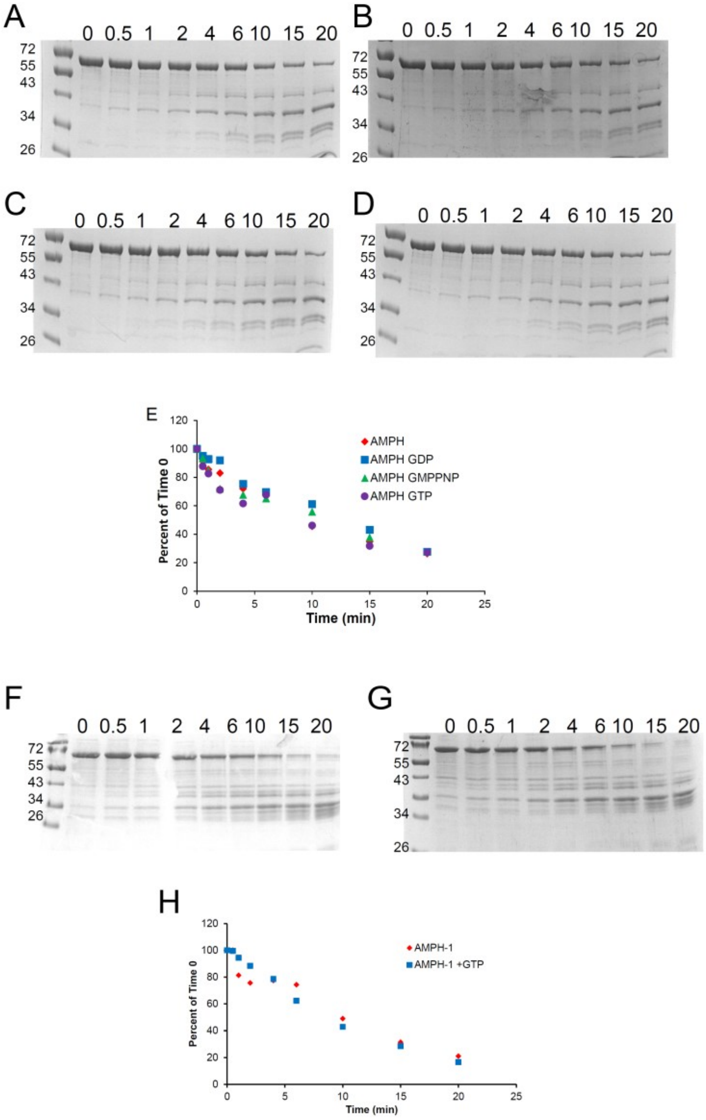

**Figure A.2 Limited protease digestion to measure the binding of guanine nucleotides to AMPH-1. (A-D) Coomassie stained gels of the digestion of 5 μM AMPH-1 by proteinase K without nucleotide (A), with GTP (B), with GDP (C) and with GMP-PNP (D). (E) Quantitation of the protein band that corresponds to full length AMPH-1 as it is digested by proteinase K. (F-G) Coomassie stained gels of the digestion of 5 μM AMPH-1 by trypsin in the absence (F) and presence of GTP (G). (H) Quantitation of the protein band that corresponds to full length AMPH-1 as it is digested by trypsin. Each digestion was repeated at least 3 times with similar results.**

Differential scanning fluorimetry was used to measure the binding of AMPH-1 to guanine nucleotides. Three concentrations of AMPH-1 (1, 2.5 and 5 μM) were incubated with 1 mM GTP, GDP, GMP-PNP, GTPγS, or ATP. Thermostability was measured by Sypro Orange binding to the denatured protein over a temperature range between 25°C to 95°C (Figure A.3). No change in the melting temperature of AMPH-1 is observed in the presence of nucleotide.

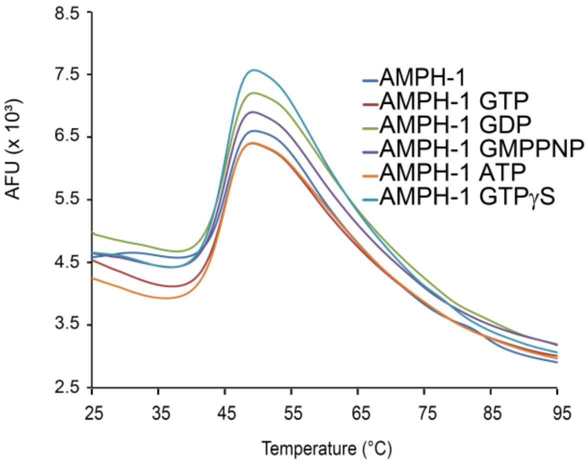

| | $T_m$ (°C) |
|---|---|
| AMPH-1 | 58.0 |
| AMPH-1 GTP | 58.5 |
| AMPH-1 GDP | 59.3 |
| AMPH-1 GMP-PNP | 58.5 |
| AMPH-1 GTPγS | 58.2 |
| AMPH-1 ATP | 57.3 |

**Figure A.3 The binding of guanine nucleotide to AMPH-1 measured by differential scanning fluorimetry. The thermal stability of 2.5 μM AMPH-1 was measured in the absence of nucleotide, or with 1 mM GTP, GDP, GMP-PNP, ATP, and GTPγS using Sypro Orange.**

The intrinsic fluorescence of tryptophans found in AMPH-1 was used to measure the binding of the protein to GMP-PNP and AMP-PNP. Spectra were taken of the interaction of 110 nM AMPH-1 to varying concentrations of GMP-PNP and AMP-PNP, and the change in fluorescence was calculated from the intergrated fluorescent intensities. The titration of GMP-PNP was also corrected for the inner filter effect of guanine nucleotides. The data from the GMP-PNP and AMP-PNP titrations were fit to a single binding site and both proteins have the same $K_d$. The tryptophan quench observed in this experiment is likely due to a non-specific binding of nucleotide to protein (Figure A.4).

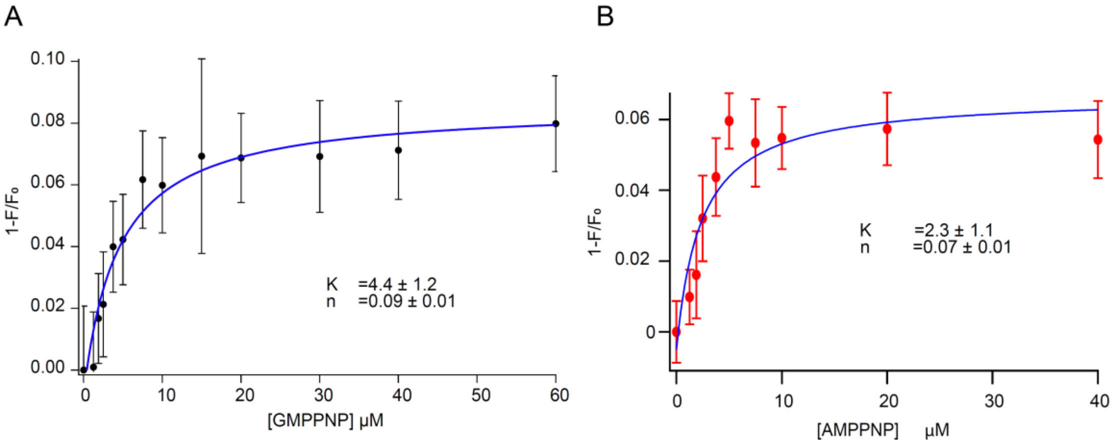

**Figure A.4 Tryptophan quenching of AMPH-1 to measure the binding of GMP-PNP, and AMP-PNP to AMPH-1.(A-B) The change in the tryptophan fluorescence of 125 nM AMPH-1 was measured with various concentrations of GMP-PNP (A) or AMP-PNP (B)**

The binding of GDP and GMP-PNP to AMPH-1 was measured using biolayer interferometry. Anti-GST biosensor tips were loaded with 125 nM GST-AMPH-1. The tips were then dipped into reaction buffer containing up to 1 mM GMP-PNP or GDP. For each experiment, a tip was loaded with GST and dipped into GMP-PNP or GDP as a control to measure non-specific binding. The assay was optimized, however there were two problems (1) the nucleotide showed non-specific binding to the GST-loaded biosensor and (2) if a difference between the control and the protein was observed the signal was low (Figure A.5).

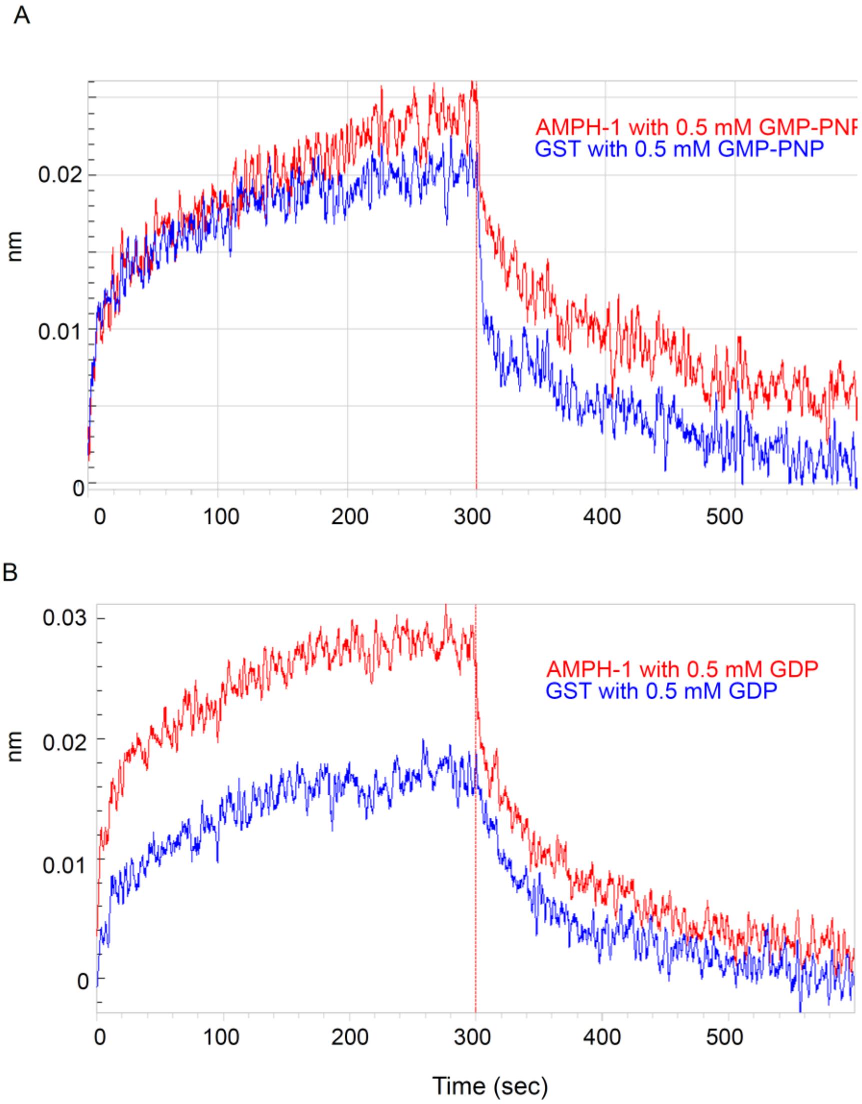

**Figure A.5 The binding of guanine nucleotide to AMPH-1 measured by biolayer interferometry. (A-B) BLI was used to measure the binding of 125 nM AMPH-1 or 125 nM GST to 0.5 mM GMP-PNP (A) or GDP (B).**

Finally ITC was used to measure the binding of GMP-PNP to AMPH-1. The heat of binding 2 mM GMP-PNP to 50 µM AMPH-1 was measured at 23°C. GMP-PNP was also titrated into assay buffer as a control. No binding was observed (Figure A.6).

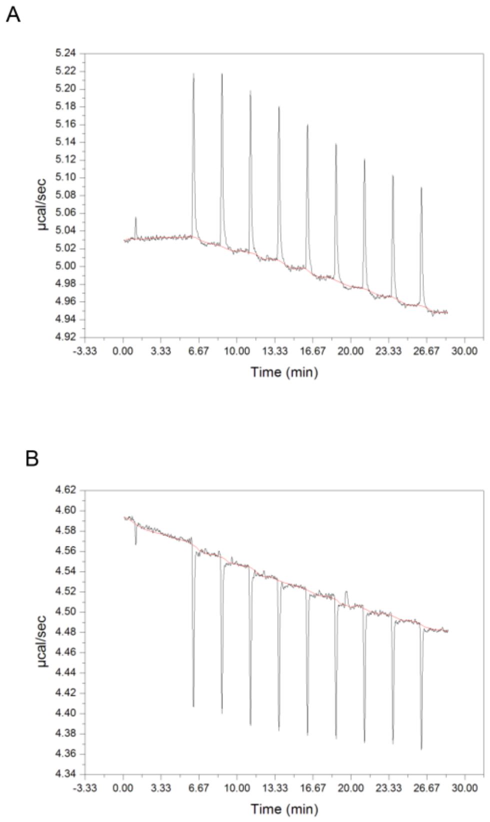

**Figure A.6 The binding of GMP-PNP to AMPH-1 measured by ITC. (A-B) A stock solution of 2 mM GMP-PNP was titrated into reaction buffer (A) or 50 µM AMPH-1 (B)**

## Discussion

Numerous assays were tried to measure the binding of GTP or a GTP analog to AMPH-1. There could be several reasons why each individual assay failed, however all the data taken together suggests that AMPH-1 does not bind to GTP in solution.

# APPENDIX B

# VALIDATION OF A SINGLE PARTICLE LEAKAGE ASSAY

## Introduction

Biologically relevant membrane fission is proposed to go through a conserved mechanism, which prevents the leaking of luminal content into the cytoplasm [23]. The current method to measure whether the reaction is conserved or “leaky” relies on a sedimentation-based assay [229]. In this type of assay, the protein of interest is incubated with liposomes that contain a fluorescent molecule. Intact liposomes are removed from solution by sedimentation. The supernatant from a centrifuge run is examined for fluorescence relative to the control reaction without protein. If more fluorescence is observed in the supernatant in the presence of the protein than the control, then the fission reaction can be considered non-conservative. While this approach is adequate to assess the leakiness of the membrane fission reaction, it cannot be used to follow the kinetics of the fission reaction nor does this method provide any information about the population distribution of fission products. In principle a single particle leakage assay can be done using MC-BAS. The ENTH domain of epsin is used to validate this assay.

## Experimental procedure

### *Liposome preparation*

Folch fraction of total brain lipid extract was prepared as previously described with modifications [39]. Alexa 647 caboxylate (Molecular Probes cat. A33084) was made up in dimethyl fumarate to a final concentration of 7.7 mM. The lipids were resuspended in argon sparged liposome extrusion buffer (50 mM Hepes pH 7.4, 150 mM NaCl, 770 μM Alexa 647 caboxylate) to a final concentration of 1 mg/ml. To hydrate the lipids evenly, the suspension underwent 15 rounds of freezing in liquid nitrogen and thawing in hot water at temperatures between 52-60°C. The liposomes were passed 11 times through an Avanti Mini-extruder using a Whatman Nuclepore track-etched polycarbonate filter with a pore size of 200 nm. The liposomes were then passed 10 times through a high-pressure Lipex manifold extruder (Transferra, Canada) using Whatman Nuclepore track-etched polycarbonate filter with a pore size of 200 nm. A sample of the 200 nm liposomes was taken to extrude to 30 nm to use as a standard. Unencapsulated Alexa 647 carboxylate was removed using a PD-10 column (GE Healthcare 17-0851-01), and 1 ml fractions were taken. The third fraction contained the liposomes without free Alexa 647 carboxylate.

*“Leakiness” of membrane fission measured by Burst Analysis Spectroscopy*

The ENTH reaction was performed using 2 μM ENTH and the rest of the reaction volume was made up of undiluted liposomes. Reactions were run in real time, and 10 μL of each sample was spotted onto a BSA-blocked glass coverslip held in a custom cassette. The coverslip cassette was clamped to a high-precision, computer controlled, 2-axis translation stage connected to a customized microscope system, and data were collected as previously described [182]. All reactions were analyzed as previously described [183].

## Results

### *Membrane fission by the ENTH is not conserved*

In order to test whether ENTH used a conserved or non-conserved mechanism of fission a single particle leakage assay was used. If the ENTH domain caused conserved membrane fission then the lumenal dye would be expected to remain in the product liposomes however if it caused non-conserved fission then the lumenal dye would be expected to leak out of the liposomes (Figure B.1A). Liposomes loaded with Alexa 647 carboxylate were incubated with 2 μM of the ENTH domain, and read in real-time. Data from the beginning of the reaction show the signal from the Top-Fluor PE incorporated into the bilayer of the liposomes and the lumenal dye are coincident (Figure B.1B-C). After incubation for 26 minutes the raw intensities show a loss of large bursts and an increase in smaller bursts in the liposome channel consistent with membrane fission. An increase in the baseline of the lumenal channel is observed and result is consistent with leakage of the dye out of the liposomes. A loss of coincidence is also observed in the MC-BAS data (Figure B.1D-E). After 40 minutes, almost all lumenal dye is has leaked out of the liposomes, as observed by the increase in the baseline of the raw data and loss of almost all coincident events (Figure B.1F-G).

### Conclusion

The result of this experiment shows that the ENTH domain of epsin does not cause membrane fission through a conserved mechanism. More importantly, these data act to validate that MC-BAS can be used to measure if the membrane fission reaction is conserved or non-conserved.

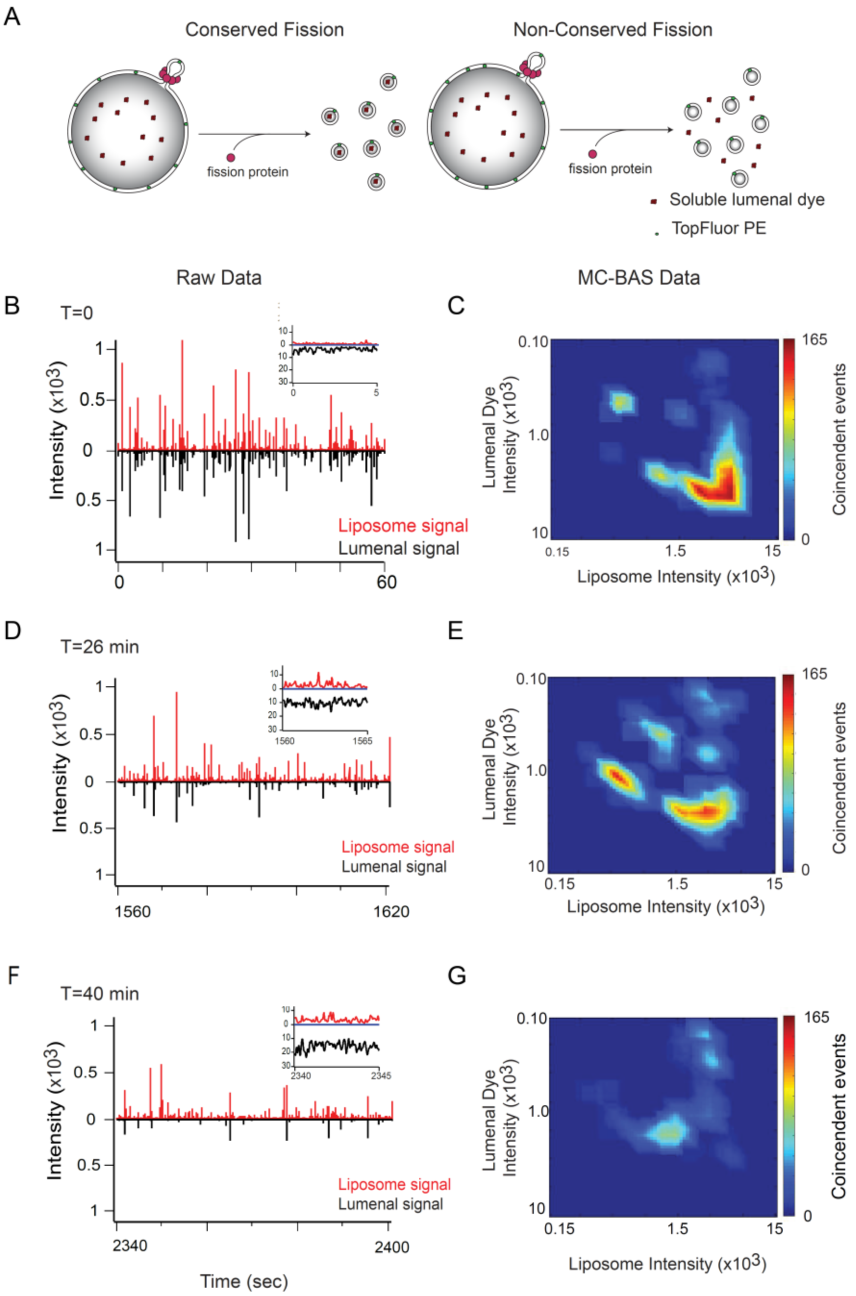

**Figure B.1 The ENTH domain of Epsin does not cause membrane fission through a conserved mechanism. Schematic of lumenal dye location in conserved and non-conserved membrane fission (A). Raw signal from the TopFluor PE in the bilayer of the liposomes (red), and Alexa 647 carboxylate in the lumen of the liposomes (black) at the beginning of the reaction (B), after 26 (D) and 40 minutes (F). MC-BAS data from the beginning of the reaction (C), after 26 (E) and 40 minutes (G).**

# APPENDIX C

# EFFICIENT CELL DELIVERY MEDIATED BY LIPID-SPECIFIC ENDOSOMAL ESCAPE OF SUPERCHARGED BRANCHED PEPTIDES*

## Summary

Various densely charged polycationic species, whether of biological or synthetic origin, can penetrate human cells, albeit with variable efficiencies. The molecular underpinnings involved in such transport remain unclear. Herein, we assemble 1, 2 or 3 copies of the HIV peptide TAT on a synthetic scaffold to generate branched cell-permeable prototypes with increasing charge density. We establish that increasing TAT copies dramatically increases the cell penetration efficiency of the peptides while simultaneously enabling the efficient cytosolic delivery of macromolecular cargos. Cellular entry involves the leaky fusion of late endosomal membranes enriched with the anionic lipid BMP. Derivatives with multiple TAT branches induce the leak- age of BMP-containing lipid bilayers, liposomal flocculation, fusion and an increase in lamellarity.

* Reproduced with permission from Brock D., et al (2018) Traffic 19(6):421-435. Copyright 2018 Wiley Publications. For the original publication: LK contributed to the experimental design as well as the generation and processing of data from BAS experiments.

In contrast, while the monomeric counterpart 1TAT binds to the same extent and causes liposomal flocculation, 1TAT does not cause leakage, induce fusion or a significant increase in lamellarity. Overall, these results indicate that an increase in charge density of these branched structures leads to the emergence of lipid specific membrane-disrupting and cell-penetrating activities.

## Introduction

Reagents that can deliver exogenously administered macromolecules into live cells are useful in applications ranging from basic cell biology, ex vivo cell manipulations for biotechnological purposes or in vivo therapeutic strategies. Crossing cellular membranes to gain access to the cell interior is, however, a significant challenge and, whether it is because of low efficiencies or toxicity, the search for ideal delivery agents remains a research focus. A general class of delivery agents consists of polycationic molecules. It includes lipid particles, polymers, artificial or viral proteins and cell-penetrating peptides (CPPs) [230-233]. For many decades, polycationic molecules have been recognized for their propensity for cellular internalization by endocytosis. It is thought that electrostatic interactions between polycationic species and anionic cell-surface glycosaminoglycans are important for this process [234, 235]. However, while advantageous as a first step of cellular entry, endocytic uptake itself does not lead to successful delivery. In fact, endosomal entrapment is typically useless in most applications, as macromolecular cargos shuttled in endocytic organelles cannot reach intended targets that may be localized in other parts of the cell. Notably, polycationic species, in some cases, appear to also be able to escape from endosomes, thereby releasing their cargo into to the cytosolic space of cells. For instance, this is the case for cationic, lipid-based DNA transfection reagents or for CPP-mediated delivery of enzymes [236-239]. While the percentage of molecules that escape is relatively low (often estimated to be less than 1% of what remains trapped inside endosomes), intracellular activities can nonetheless be detected.

Recently, a number of studies have highlighted how increasing the charge density of polycationic delivery agents to a relatively high degree may help increase their endosomal escape activities. An example is supercharged green fluorescent protein (GFP), a GFP mutant obtained by replacing anionic residues of wild-type superfolder GFP with cationic amino acids. While GFP has a charge of −7 at pH 7, supercharged GFP has an overall charge of +48 [240, 241]. When fused to other proteins, supercharged GFP is capable of escaping endosomes and delivering a variety of cargos [242]. Remarkably, cell-permeable supercharged proteins also appear to occur in nature. Viral capsid proteins seem especially prone to “supercharging.” This is the case of proteins of flaviviruses, including DENV C (+42 charge, +1.97/kDa, Dengue virus) or YFC (+52 charge, +2.30/kDa, Yellow fever virus) and WNV (+46 charge, +1.74/kDa, West Nile virus) [243-245]. These proteins, which are involved in the entry of viruses into host cells at endosomal sites, can also be used as delivery agents for exogenous cargos. The notion of supercharging molecules for increased membrane permeation may be expanded to CPPs. For instance, CPPs incorporated into multimeric proteins have shown better delivery outcomes than their monomeric counterparts [246]. Similarly, increasing the number of protein transduction fusion tags incorporated recombinantly at the N-terminus of a protein can improve the cell penetration of the macromolecule [247]. In our laboratory, we have recently observed that dimerization of the prototypical CPP TAT (GRKKRRQRRR, residues 48-57 form HIV-1 Trans-Activator of Transcription) could lead to a reagent, dfTAT (dimeric fluorescent TAT), with dramatically increased endosomal escape activity [238]. In particular, dfTAT is capable of causing the endosomal release and cytosolic egress of more than 90% of material initially trapped inside endosomes. Because of this improved activity, dfTAT can deliver relatively high concentrations of small molecules, peptides and proteins in a simple coincubation assay. More specifically, dfTAT and its cargo do not need to interact: they simply need to be endocytosed together and, by making endosomes leaky, dfTAT mediates the cytosolic release of the cargo. Mechanistically, dfTAT escapes specifically from late endosomes, which are organelles where the cationic CPP encounters the anionic lipid BMP[248]. dfTAT is in turn capable of causing the leaky fusion of late endosomal BMP-rich membranes.

One promising approach toward the generation of supercharged cell-penetrating agents is by the branching of polycationic moieties of a molecular scaffold. When exploited in solid phase peptide synthesis (SPPS), this technique allows one to greatly increase the cationic content of potential cell-penetrating agents with relative ease when compared with linear peptide synthesis. One early example utilized branched-chain arginine-rich peptides to study plasma membrane translocation [249]. In more recent work, branched polycationic peptides have even been successfully employed as gene transfection tools as well [250, 251]. Herein, we were interested in elucidating how multimerization of the TAT peptide leads to an enhanced endosomal escape activity. To address this question, we generated branched structures that present a variable number of copies of the peptide on a common scaffold. The cell penetration activities of the constructs were evaluated in cell cultures and their propensities to disrupt membranes were characterized in vitro. We establish that multivalent display of the TAT peptide leads to dramatic increases in endosomal leakage, cytosolic escape and overall delivery efficiencies. These improved performances result from BMP-specific activities that are present in the branched species but not in the monomeric parent compound. They include a glue-like behavior that promotes lipid bilayer contact and the ability to induce the leaky fusion of BMP-containing bilayers.

## Experimental procedures

### *Peptide design, synthesis and characterization*

Peptides were synthesized on Rink amide MBHA resin (Novabiochem). The amino acids used in synthesis were Fmoc-Lys(Mtt)-OH, Fmoc-Gly-OH, Fmoc-Arg(Pbf )-OH, Fmoc-Gln(Trt)-OH and Fmoc-Lys(Boc)-OH (Novabiochem) (0.78 mmol). Reactions were performed in a glass vessel at room temperature while streaming dry $N_2$ for effective mixing. Deprotection of Fmoc was accomplished by incubation of the peptide-bound resin with a mixture of piperidine in dimethylformamide (DMF) (Fisher Scientific) (20%, 15 mL). Two deprotections were performed for 5 and 15 minutes, respectively, washing with DMF in between deprotections. Coupling reactions of the amino acids to synthesize the peptide scaffold were performed for 4 hours with streaming dry $N_2$ at room temperature using a solution containing the Fmoc-protected amino acid (4 mmol), HCTU (Novabiochem) (3.9 mmol) and di-isopropylethylamine (DIEA) (Sigma-Aldrich) (10 mmol) dissolved in DMF. In between coupling reactions, the resin was washed extensively with DMF (Fisher Scientific). Once synthesized, peptide scaffolds were labeled using a mixture of 5(6)-TAMRA (Novabiochem), HCTU and DIEA (3, 2.9 and 7.5 eq., respectively) in DMF that was allowed to react overnight at room temperature under dry $N_2$. For the non-fluorescent variants, nf2TAT and nf3TAT, the scaffold's N-terminus was rendered relatively inert via standard acetic anhydride-mediated acetylation. After the peptide scaffolds were labeled with TMR or acetylated, Mtt deprotection was carried out using a solution of 1% trifluoroacetic acid (TFA) (Fisher Scientific) and 2% tri-isopropylsilane (TIS) (Sigma-Aldrich) in dichloromethane (DCM), and, in between deprotections, the resin was washed with DCM, DMF and methanol. For the synthesis of 1TAT, 2TAT and 3TAT, equivalents of coupling solutions were adjusted to Fmoc-protected amino acid (3, 6 and 9 mmol, respectively), HCTU (2.9, 5.8 and 8.7 mmol, respectively) and DIEA (7.5, 15 and 22.5 mmol, respectively) in DMF and allowed to react while streaming dry $N_2$ overnight for each coupling. Upon completion of each peptide, the N-terminal Fmoc was deprotected and the resin was washed with DCM and dried in vacuo. For cleavage of peptide from the resin, a solution containing 2.5% $H_2O$, 2.5% TIS and 95% TFA was added to the resin and allowed to react for 3 hours at room temperature to achieve cleavage as well as deprotection of the side chain of each amino acid. Upon completion of the cleavage, crude peptide products were allowed to precipitate in cold, anhydrous diethyl ether (Fisher Scientific). Precipitants were then resuspended in $H_2O$ and lyophilized. Dried peptide products were then resuspended in 0.1% TFA in $H_2O$ and then analyzed and purified by reverse-phase HPLC. rpHPLC analysis was performed on an Agilent 1200 series instrument with an analytical Biobasic-18 C18 column (Thermo Scientific) (5 µm particle size, 4.6 × 250 mm). The flow rate was 2 mL/ min, and absorbance at $\lambda = 214, 556$ nm was measured using a diode array detector (Agilent). Preparative HPLC was performed on an Ultimate 3000 preparative HPLC (Thermo Scientific) with a preparative Biobasic-18 C18 column (Thermo

Scientific) (10 µm particle size, 21.2 × 250 mm). The flow rate was 20 mL/min, and absorbance at 214 and 556 nm was measured using a diode array detector (Thermo Scientific). For all analytical and preparative runs, linear gradients using 0.1% aqueous TFA (solvent A) and 90% acetonitrile, 9.9% $H_2O$ and 0.1% TFA (solvent B). Correct peptide products were confirmed via MALDI-TOF using a Shimadzu/Kratos instrument (AXIMA-CFR). The expected mass for 1TAT was 2447.90 Da; 1TAT observed mass was [M-H$^+$/H$^+$] = 2448.55 Da. The expected mass for 2TAT was 3784.53 Da; 2TAT observed mass was [M-H$^+$/ H$^+$] = 3784.53 Da. The expected mass for 3TAT was 5121.16 Da; 3TAT observed mass was [M-H$^+$/H$^+$] = 5121.83 Da. For the fluorescent peptides, concentration was determined using Beer's law over the absorbance of TMR. For the non-fluorescent peptides, back-calculation of the concentration was made possible by utilizing amino acid analysis (Protein Chemistry Lab, TAMU).|

*Cell penetration and delivery experiments*

Cells were seeded and grown to 100% confluency after 24 hours. Prior to treatment, cells were washed twice with Leibovitz's L-15 medium (L-15) (Fisher Scientific). Cells were then either incubated with peptide or coincubated with peptide and cargo, 4 µM TAT-Cre or 50 µM SNAP-Surface 488 (NEB), at specified concentrations at 37$^{\text{o}}$ C for 30 minutes. Immediately following incubation, cells were washed twice with L-15 containing heparan (1 mg/mL) and once with L-15. To assess cytotoxicity, cells were treated with 2.5 µM SYTOX

Blue or SYTOX Green 1 hour post-treatment. SYTOX dyes are cell-impermeable and are only capable of staining nucleic acids if a cell has a compromised plasma membrane. Fluorescence microscopy was performed using an inverted microscope (Olympus IX-81) with both×20 and ×100 objectives as well as a heated stage (37$^{o}$ C) and images were taken using a Rolera-MGI Plus back-illuminated electron-multiplying CCD camera (Qimaging). Filters used in fluorescence imaging included DAPI (λex/λem = 300-388, 425-488 nm), CFP (λex/ λem = 420-450, 450-600 nm), FITC (λex/λem = 450-490, 500-550 nm) and RFP (λex/λem = 535-580, 570-670 nm) filter cubes (Chroma Technology).

Cytosolic penetration and delivery of cargo was determined, qualitatively, by ×100 imaging and quantitatively by ×20 imaging. Cells scored for penetration or delivery of cargo (nuclear or cytosolic fluorescence distribution) were counted using Slidebook and ImageJ software. Cells were not counted for penetration if they displayed SYTOX staining. The percentage of cells with successful penetration or delivery of cargo was determined by dividing scored cells by total cells. The total number of cells was determined by Hoechst 33 342 stain (5 μM) for penetration, cells that transiently expressed EGFP using the control plasmid gWiz for TAT-Cre or cells stained with SNAP-Cell Fluorescein (5 μM) for SNAP-Surface 488. In each experiment, more than 1000 cells were counted to assess penetration and delivery efficiency, as well as cytotoxicity. Fluorescent images acquired using the ×100 objective were subjected to deconvolution using the

Slidebook software. Each experiment was performed in triplicate. It is important to note that in each cell assay, individual wells were used for each condition as prolonged or repeated exposure of light to the TMR-labeled peptides can lead to the artifact of photolysis, extensively covered in the following publications.

To measure the whole cell lysate for peptide uptake, cells were grown and treated as before with each peptide at varying concentrations. Post-treatment, cells were harvested by treatment with 0.5% trypsin in PBS for 3 minutes followed by suspension and dilution in L-15 medium. Cells were pelleted by centrifugation at 1500*g* × 10 minutes, resuspended in L-15 and then treated with 2× lysis buffer (50 mM Tris, pH 7.4, 2 mM EDTA, 1× HALT protease inhibitors (Thermo Scientific) and 20% Triton X-100) and vortexed to complete lysis. The cell lysates were then transferred to a 96-well plate where 3TAT fluorescence was measured using the green channel (Em = 525; Ex = 580-640 nm) of a GloMax-Multi+ detection system plate reader (Promega). Triplicate experiments were performed and measured on the same day to avoid fluctuation in fluorescence read out.

To measure colocalization of 1TAT or DEAC-k5 with LysoTracker Green (Thermo), cells were grown to 100% confluency and then treated with 9 μM 1TAT for 30 minutes or 25 μM DEAC-k5 for 1 hour. Cells were washed as before then treated with 500 nM LysoTracker Green at 0, 1 or 3 hours after DEAC-k5 treatment. Cells were imaged at ×100 magnification using fluorescence microscopy to produce representative images of colocalization.

Finally, colocalization was determined using the colocalization function of the software ImageJ. Pearson's colocalization coefficient, R, and Manders' colocalization coefficient, M1, were reported to effectively determine the degree of colocalization.

*Expression and purification of TAT-Cre*

The gene for TAT-Cre from pTriEx-HTNC (Addgene) was cloned into the vector pTXB1 and transformed into *Escherichia coli* BL21 (DE3) cells (Agilent Technologies) using a standard heat shock method. LB media containing 100 µg/mL of ampicillin was inoculated with colonies containing the plasmid and allowed to grow shaking at $37^{o}$ C overnight. Cultures were then used to inoculate 1 L of LB containing ampicillin and allowed to grow until $OD_{600}$ = 0.6. Cultures were then induced with 1 mM IPTG (Fisher Scientific) and grown, shaking, at $37^{o}$ C for 3 hours. *Escherichia coli* cells were then pelleted by centrifugation using a J2-21 (Beckman) centrifuge and a JA-10 rotor at 4000 RPM x 30 minutes at $4^{o}$ C. Cell pellets were then resuspended in buffer containing 20 mM $NaH_2PO_4$, 500 mM NaCl and 20 mM Imidazole and then cells were lysed by sonication for a total sonication time of8 minutes. Cell debris was removed from the whole-cell lysate by centrifugation using a JA-20 rotor at 17000 RPM x 45 minutes at $4^{o}$ C. TAT-Cre was then purified using metal-affinity chromatography (HisTrap HP) (GE Healthcare).

### *Transfection*

For experiments requiring transfections, cells were first grown to 80% confluency and then treated with transfection solutions. For TAT-Cre delivery, HeLa cells were transfected with the plasmid pCALNL (Addgene) using Lipofectamine 2000 (Thermo). For SNAP-Surface 488 (NEB) delivery, FuGene HD (Promega) was used to transfect HeLa cells with the plasmid pSNAP-H2B (NEB). In both conditions, cells were incubated with transfection solutions for 12 (Lipofectamine 2000) or 18 hours (FuGene HD) followed by a 12 or 6 hours recovery, respectively, in DMEM supplemented with 10% FBS prior to treatment.

### *Delivery of preloaded endosomal cargo*

For this experiment, cells were grown to 100% confluency and then treated with 50 µM DEAC-k5 in L-15 for 1 hour. Cells were then washed twice in L-15 and then incubated with L-15 ± 200 nM bafilomycin (Sigma-Aldrich). Following this incubation, cells were washed and finally treated with 3TAT as before (± 200 nM bafilomycin). Ten minutes prior to imaging, cells were treated with 2.5 µM SYTOX Green to visualize and exclude dead cells.

### *Liposome preparation*

Liposomes were prepared using the following lipids: 1,2-di-(9Z-octadecenoyl)-sn-glycero-3-phosphocholine (DOPC), 1,2-di-(9Z-octadecenoyl)-sn-glycero-3-phosphoethanolamine (DOPE), sn-(3-oleoyl-2-hydr oxy)-glycerol-1-

phospho-sn-1′-(3′-oleoyl-2′-hydroxy)-glycerol (S,S) (BMP) and cholesterol (ovine wool) (Chol) (Avanti Polar Lipids). For BAS experiments, liposomes were doped with 0.03% DiD (Vybrant).

Lipids dissolved in chloroform, at aforementioned ratios, were transferred to a clean glass vial and dried overnight in vacuo. Lipid cakes were hydrated in LUV buffer (10 mM $NaHPO_3$, 100 mM NaCl, pH 7.4) which contained 60 mM calcein if used in leakage assays. The hydrated lipid cake underwent multiple freeze thaw cycles and the generated MLVs were extruded to 100 nm LUVs using a 0.1 µm membrane (Whatman). For BAS experiments, liposomes were further extruded using a manifold extruder (Northern Lipids) and a 0.05 µm membrane (Whatman). Liposomes loaded with calcein were purified from free calcein using Sephadex G50 resin (Fisher Scientific).

*Leakage assays*

LUVs (250 µM total lipid) loaded with calcein were mixed with varying concentrations of peptide (1-25 µM) in LUV Buffer (10 mM $NaH_2PO_4$, 100 mM NaCl, pH 5.5 [LE] or 7.4 [EE/PM]). Peptides were allowed to react with LUVs for 1 hour at room temperature, rocking in the dark. A supernatant was obtained by centrifugation at 15000*g* × 2 minutes and then the supernatant was applied to an illustra NAP-10 column (GE Healthcare Life Science) to isolate free calcein. Free calcein was pooled and the fluorescence intensity was measured using the blue channel (Ex = 490 nm, Em = 520-560 nm) of a GloMax-Multi+ detection plate reader. To normalize leakage results, a positive control was conducted by treating LUVs with 0.2% Triton X-100. Where indicated, lipid composition of LUVs varied. For leakage experiments involving antibodies, LUVs were first treated with 250 μg/mL of anti-BMP or anti-IgG for 30 minutes, room temperature, followed by direct addition of peptide to the reaction mixture. Extent of liposomal leakage was determined as before.[19]

*BAS experiments*

BAS measurements are taken with a custom-built, multichannel confocal microscope, as previously described. (32,33) Built on a research quality, vibrationally isolated 40  × 80  optical table, the system is constructed around a Nikon Eclipse Ti-U inverted microscope base with a 60×/1.4NA CFI Plan Fluor oil-immersion objective. The microscope base is outfitted with a precision, 2-axis stepper motor sample stage (Optiscan II; Prior) and a custom-designed confocal optical bench with 3 independent detection channels. Each detection channel is configured with an optimized band-pass filter set for wavelength selection and a low-noise, single photon counting APD unit (SPCM-AQRH-15; Excelitas). Photon pulses are collected and time stamped with either a multichannel hardware correlator (correlator.com) or high-speed TTL counting board (NI9402; National Instruments). Sample excitation is provided by a diode laser (642 nm; Omicron) and a diode-pumped solid-state laser (561 nm; Lasos). The free-space beams of each laser are each coupled to a 3-channel fiber combiner (PSK-000843; Gould Technologies) and the combined output is directed into the sample objective with a custom, triple-window dichroic filter (Chroma). Each laser is addressable from the integrated control and data acquisition software, custom developed using LabView (National Instruments).

Liposomes, diluted to 2.5 μM in LUV Buffer pH 5.5, were mixed with 1TAT, 2TAT or 3TAT (1-12.5 nM). Each sample was spotted onto a BSA-blocked glass coverslip held in a custom cassette. The coverslip cassette was clamped to a high-precision, computer controlled, 2-axis translation stage connected to a customized microscope system. For all experiments, dual excitation was employed with 50 μW input power (measured at the back of the objective) for both 488 and 561 nm lasers. For each experimental run, 5 minutes of fluorescence burst data was recorded and each experiment was repeated a minimum of 3 times. The TMR/DiD was calculated from the raw burst that were coincident in both channels.

### *Cryo-EM and image processing*

L.E. LUVs treated with 1TAT, L.E. LUVs treated with 3TAT and PG LUVs treated with 3TAT were frozen in vitreous ice on a Quantfoil R2/1 holey carbon grid with an FEI Vitrobot, respectively. Cryo-EM images were acquired on a K2 Summit Direct-detection camera (Gatan) in the electron-counting mode using a TECNAI F20 cryo-electron microscope (FEI) operated at 200 kV. A nominal magnification of ×19 000 or ×7800 was used, giving a pixel size of 1.87 Å/pixel or 4.8 Å/pixel, respectively.

## Results

Several new CPP constructs were synthesized. These compounds are named 1TAT, 2TAT and 3TAT in relation of the number of TAT copies attached to a common scaffold (Figure C.1A). This scaffold consists of the peptide KGKGKG, where the amino side-chains of the lysine residues are connected to either the C-terminus of a TAT peptide or to an acetyl capping group. The N-terminus of the scaffold is labeled with carboxy-tetramethylrhodamine (TMR), a red fluorophore used herein for peptide quantification and fluorescent microscopy tracking of the peptide behavior in cells. The peptides were synthesized by solid-phase peptide synthesis, purified by high-performance liquid chromatography (HPLC) and analyzed by mass spectrometry (Figures C.2 and C.3).

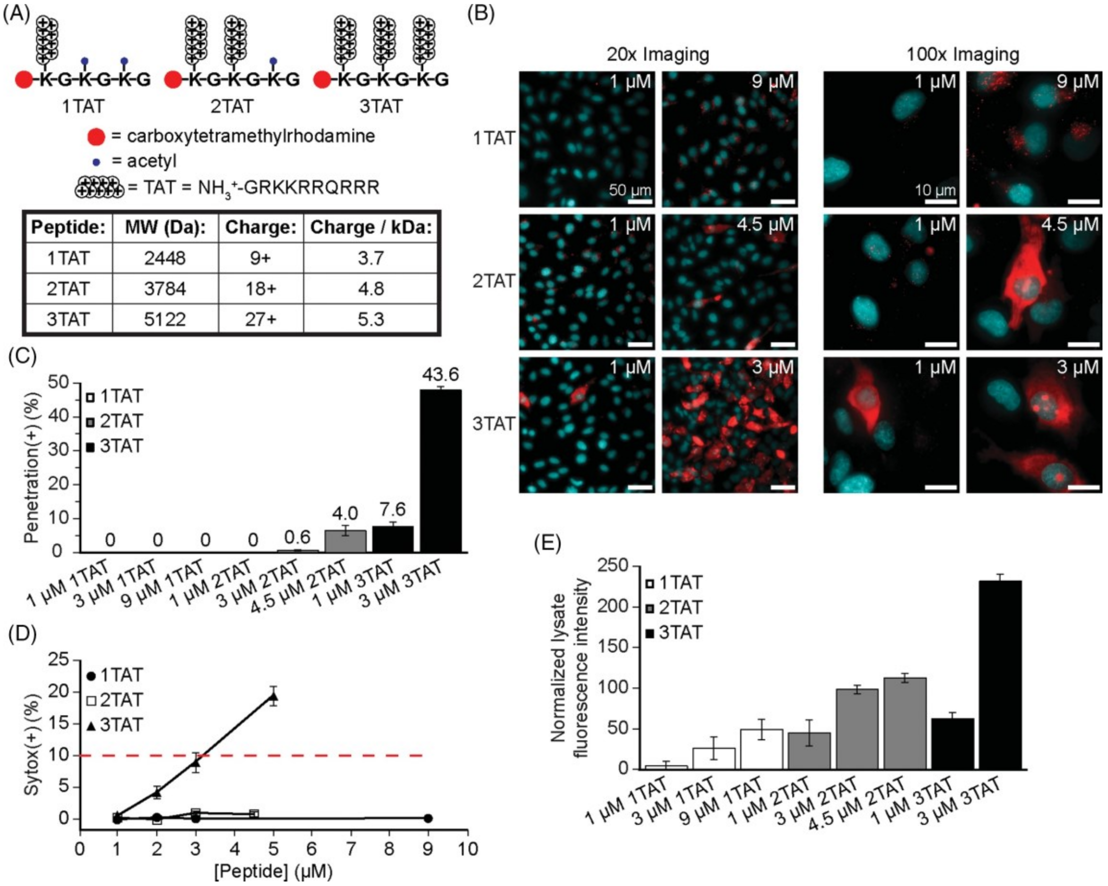

| Peptide: | MW (Da): | Charge: | Charge / kDa: |
|---|---|---|---|
| 1TAT | 2448 | 9+ | 3.7 |
| 2TAT | 3784 | 18+ | 4.8 |
| 3TAT | 5122 | 27+ | 5.3 |

**Figure C.1 Representative scheme of the peptide constructs 1TAT, 2TAT and 3TAT. (A) The constructs consist of a KGKGKG scaffold labeled with the TAT peptide or an acetyl capping group on the side chain of the lysine residues. Additionally, the scaffold is labeled with the fluorophore carboxy-tetramethylrhodamine (TMR) at its N-terminus. The molecular weight and expected charge of each construct at pH 7 and below are represented. (B) 2TAT and 3TAT reach the cytosol and nucleoli of cells but 1TAT does not. Fluorescence microscopy images of cells treated with each peptide for 30 minutes at indicated concentrations, washed, and stained with SYTOX green and the nuclear stain Hoechst 33 342. Cells were imaged 1 hour after incubation with peptides. Images are overlay of images pseudocolored red for TMR, blue for Hoechst 33 342 and green for SYTOX green (only present if cells have a disrupted plasma membrane). (Scale bars: ×20: 50 μm, ×100: 10 μm). (C) The cell penetration activity of 3TAT is superior to that of 2TAT and 1TAT. Quantitative evaluation of the percentage of cells positive for penetration (ie, showing nucleolar staining while excluding SYTOX green) after incubation for 30 minutes (1 hour wait) at the concentrations indicated.** **(continued on the next page)**

**The data represented correspond to the mean of biological triplicates (>500 cells counted per experiment). (D) Evaluation of the toxicity of the peptides by a SYTOX green exclusion assay. Cells were treated as in (B) and (C). The number of cells displaying a nucleus stained by SYTOX green was counted. The data represented correspond to the mean of biological triplicates (>500 cells counted per experiment). The red dashed line indicates a threshold toxicity at which, in our hands, cell penetration cannot be reliably quantified because of high levels of fluorescently stained cellular debris. (E) Evaluation of the levels of peptide uptake in cells by quantification of the TMR fluorescence intensity of cell lysates. Cells were treated as in (B) and (C). Cells were washed, trypsinized and homogenized. The fluorescence of the cell lysate was measured and normalized to the number of cells in each sample, assessed by flow cytometry. The data reported corresponds to the mean of technical triplicates**

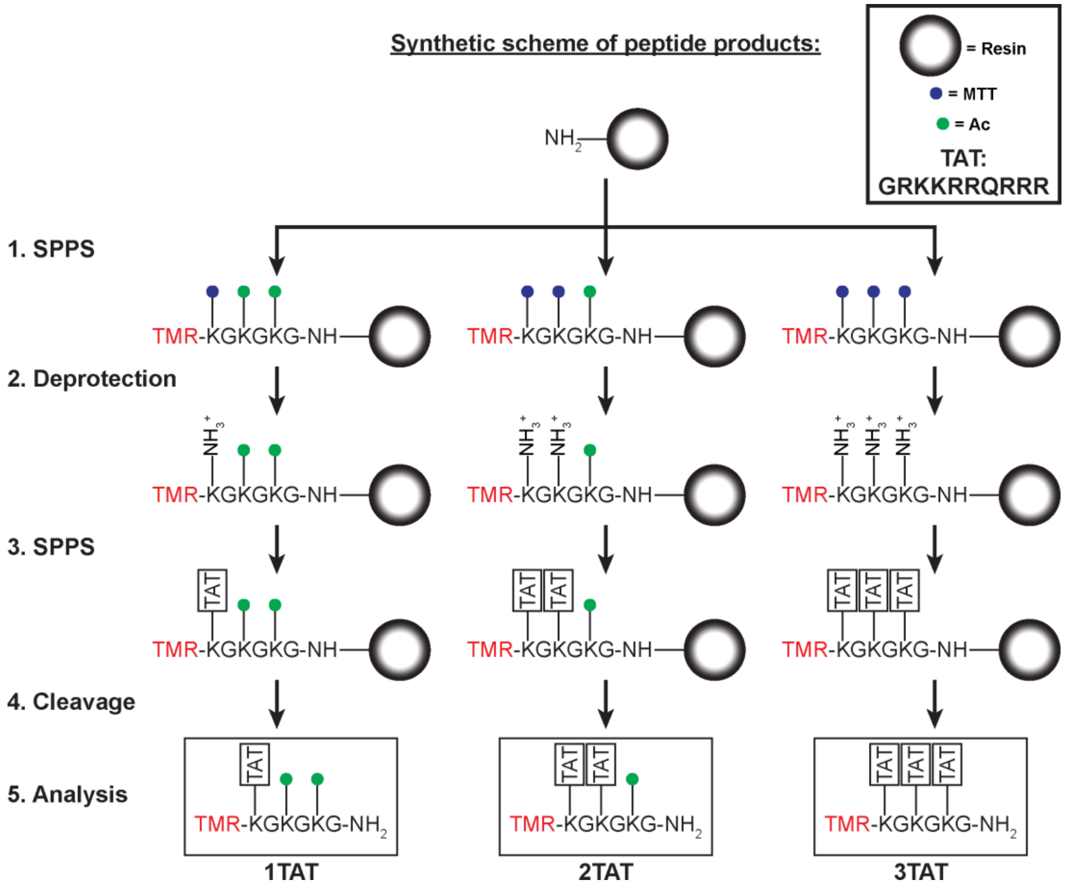

**Figure C.2 Synthetic route used for the generation of the peptides 1TAT, 2TAT, 3TAT. Scaffold peptides are first synthesized via solid phase peptide synthesis (SPPS) using standard Fmoc-chemistry. Lysine residues containing cleavable (MTT) or non-cleavable (Ac) protecting groups on the ε-N are introduced at different positions in the scaffold sequence. Following Fmoc removal, the N-terminus of the scaffold peptide is capped with the fluorophore TMR. Next, MTT groups are selectively cleaved under 1% TFA. The TAT peptide branches are then assembled off the ε-N of each deprotected lysine residues. Completed products are cleaved from the solid support by treatment with 95% TFA.**

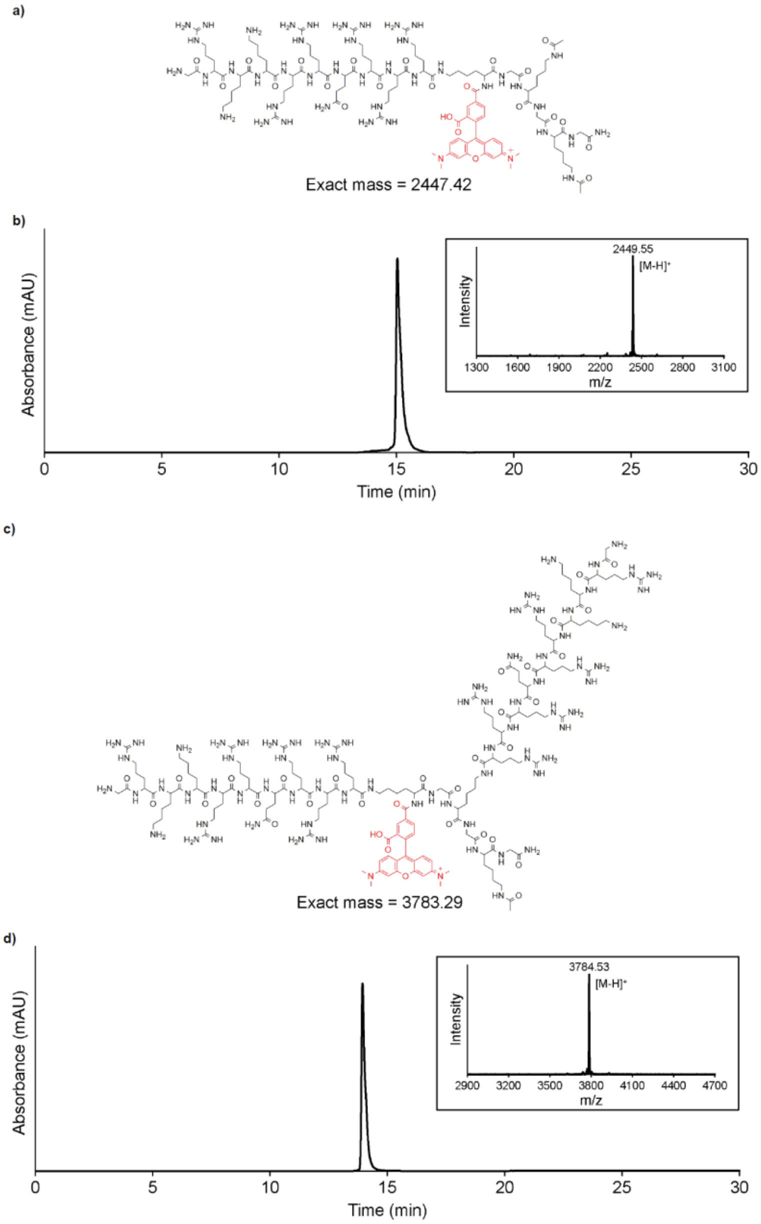
a)
Exact mass = 2447.42
b)
Absorbance (mAU)
0
5
10
15
20
25
30
Time (min)
2449.55
[M-H]+
Intensity
1300
1600
1900
2200
2500
2800
3100
m/z
c)
Exact mass = 3783.29
d)
Absorbance (mAU)
0
5
10
15
20
25
30
Time (min)
3784.53
[M-H]+
Intensity
2900
3200
3500
3800
4100
4400
4700
m/z

e)

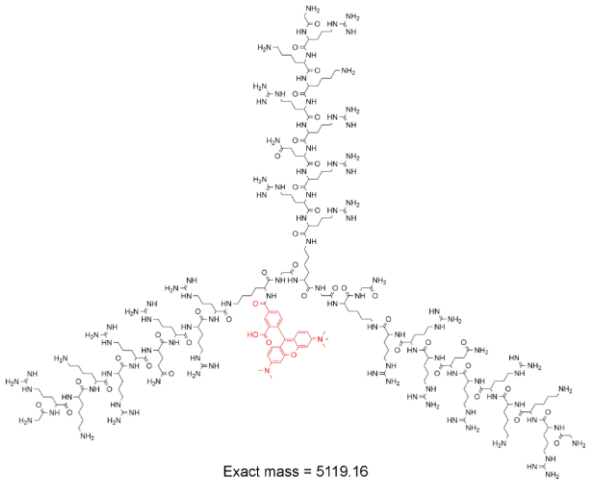

Exact mass = 5119.16

f)

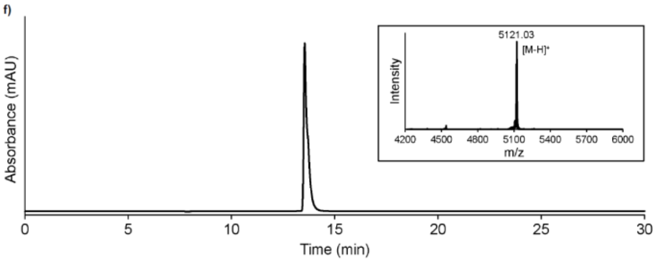

g)

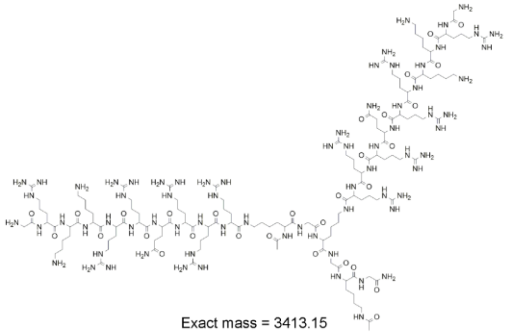

Exact mass = 3413.15

h)

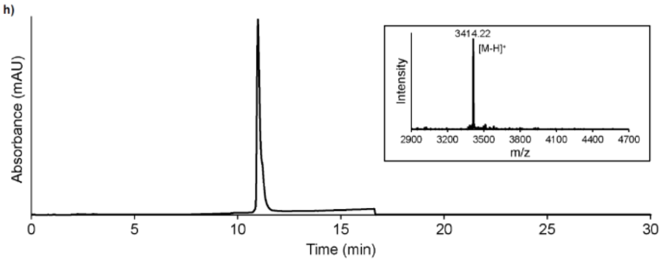

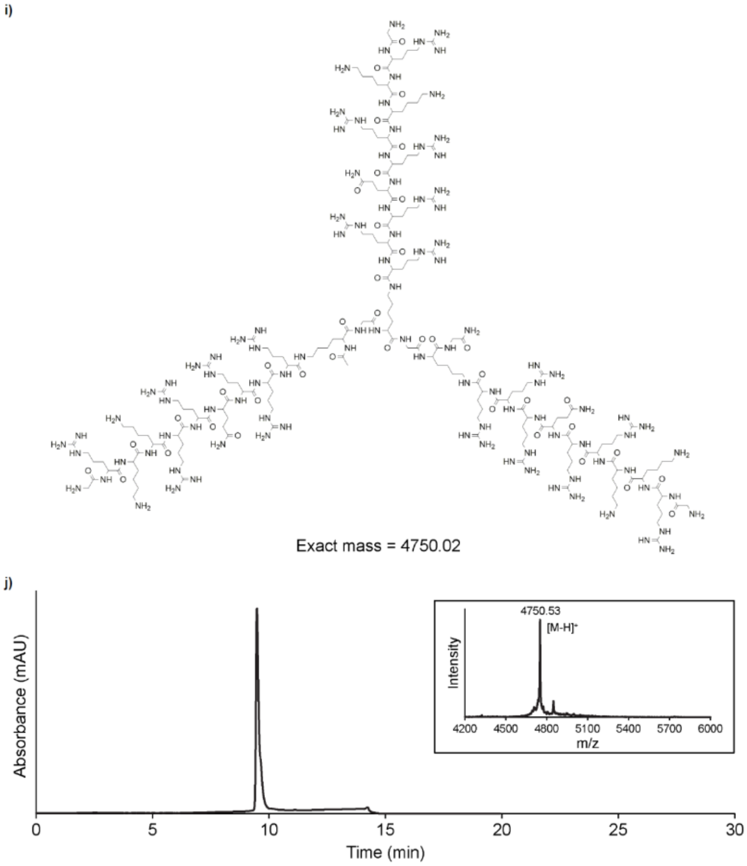

**Figure C.3 Characterization of 1TAT, 2TAT and 3TAT. (a) Structure of 1TAT. (b) rpHPLC analysis and MALDI-TOF MS spectrum of purified 1TAT (retention time (rt): 15.04 min, 0-73% solvent B in 0-30 min) (1TAT, expected mass = 2447.42, observed mass: (M-H+)/H+ = 2449.55). (c) Structure of 2TAT. (d) rpHPLC analysis and MALDI-TOF MS spectrum of purified 2TAT (retention time (rt): 13.94 min, 0-73% solvent B in 0-30 min) (2TAT, expected mass = 3783.29, observed mass: (M-H+)/H+ = 3784.53). (e) Structure of 3TAT. (f) rpHPLC analysis and MALDI-TOF MS spectrum of purified 3TAT (retention time (rt): 13.54 min, 0-73% solvent B in 0-30 min) (3TAT, expected mass = 5119.16, observed mass: (M-H+)/H+ = 5121.03). (g) Structure of nf2TAT. (h) rpHPLC analysis and MALDI-TOF MS spectrum of purified nf2TAT (retention time (rt): 9.25 min, 0-30% solvent B in 0-30 min) (nf2TAT, expected mass = 3413.15, observed mass: (M-H+)/H+ = 3414.22). (i) Structure of nf3TAT. (j) rpHPLC analysis and MALDI-TOF MS spectrum of purified nf3TAT (retention time (rt): 9.52 min, 0- 30% solvent B in 0-30 min) (nf3TAT, expected mass = 4750.02, observed mass: (M-H+)/H+ = 4750.53).**

In order to first test the peptide reagents, cells were treated with 1TAT, 2TAT and 3TAT for 30 minutes, a time that is, in our experience, convenient for delivery protocols in cell cultures. Under this condition, 1TAT, 2TAT and 3TAT displayed 2 distinct cellular localizations. In the case of 1TAT, a punctate distribution was observed at all concentrations tested (1, 3, 9 μM; Figure C.1B). Colocalization of the red puncta with LysoTracker Green, a marker of acidic-organelles such as late endosomes and lysosomes, indicated that 1TAT is trapped in the lumen of endocytic organelles (Figure C.4), as previously reported for similar peptides [252]. In the case of 2TAT and 3TAT, a similar punctate distribution was observed at low concentration (1 μM).

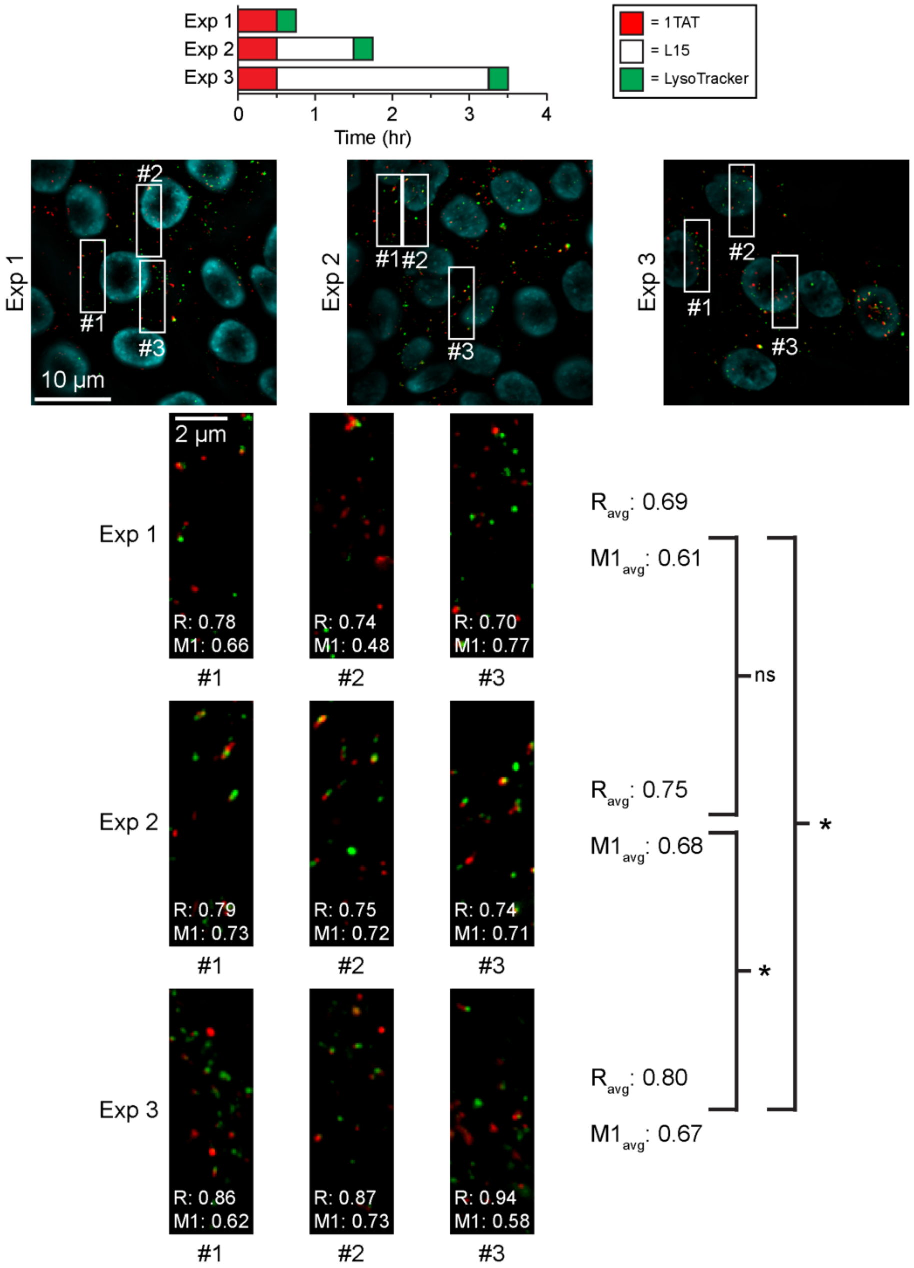

**Figure C.4 1TAT colocalizes inside cells with LysoTracker Green.** Cells were incubated with 1TAT (3 µM) for 30 min at 37°C and washed thereafter. Next, cells were incubated in L-15 medium for indicated times (exp 1 = 0 hr, exp 2 = 0.75 hr, exp 3 = 2.75 hr) and then stained with LysoTracker Green (500 nM), a marker of acidified endocytic organelles, as well as Hoechst 33342 (5 µM) for nuclear visualization. Representative fluorescence microscopy images taken under 100x magnification were taken for 1TAT (pseudocolored red), LysoTracker (continued on the next page)

**Green (pseudocolored green) and an overlay of 1TAT, LysoTracker green and Hoechst 33342 (pseudocolored blue). Colocalization analysis was performed over zoomed- in sections of 1TAT and LysoTracker images of each condition. Pearson's R and Manders' M1 coefficients are reported to represent the extent of colocalization. A student's t-test was performed between the $R_{avg}$ of each condition. Scale bars: 100x images: 10 µm, zoomed images: 2 µm. NS, $p>0.05$; *, $p<0.05$. These data suggest that the accumulation of 1TAT in lysotracker-stained organelles, late endosomes and lysosomes, increases overtime.**

However, as the incubation concentration is increased, a population of cells displaying a diffuse cytoplasmic staining can be observed (Figure C.1B). The red fluorescence of these cells also includes a distinct nucleolar staining, a feature previously observed for other cationic peptides [238, 253, 254]. In this particular instance, nucleolar staining serves to demonstrate that the fluorescence signal detected is, at least in part, intracellular (as opposed to originating from surface binding). Notably, the percentage of cells showing cytoplasmic/nucleolar staining was low in the case of 2TAT (less than 10% at an incubation concentration of 4.5 µM). In contrast, approximately 50% of the cells showed cytosolic penetration by 3TAT. The cells counted in this assay exclude SYTOX Green positive cells, indicating that the cells do not have a compromised plasma membrane. However, it should be noted that less than 10% of cells become positive to SYTOX Green when exposed to 3 µM 3TAT, indicating that the peptide is modestly toxic at this concentration. Importantly, 3TAT was significantly more toxic at 5 μM (Figure C.1D). This increased toxicity, which gives rise to peptide-stained cellular debris during imaging, made quantifying cell penetration difficult. Achieving delivery while killing cells is also counterproductive. For these reasons, in the context of our mechanistic studies, 3TAT was not tested at a concentration higher than 3 μM (longer incubation times were, however, tested to characterize the cytotoxicity of the peptides more fully, Figure C.5). Overall, this concentration alone was sufficient to exemplify that 3TAT is significantly more active than 1TAT and 2TAT. This is apparent when the peptides are compared at equal incubation concentrations, or at concentrations that lead to similar overall TAT content (ie, 9 μM 1TAT vs 4.5 μM 2TAT vs 3 μM 3TAT). In particular, 3 μM 3TAT is internalized by cells at a higher level than 1TAT or 2TAT, at all concentrations tested. This indicates that 3TAT enters cells, being either trapped inside endosomes or diffused in the cytoplasm, in a larger amount than the analogs with fewer peptide copies. This in turn may suggest that this higher propensity for uptake is correlated to its ability to enter the cytosolic space of cells. However, it should be noted that, under conditions where 3TAT is internalized to a lower extent than 2TAT (ie, 4.5 μM 2TAT vs 1 μM 3TAT), 3TAT displays more cytosolic penetration than 2TAT.

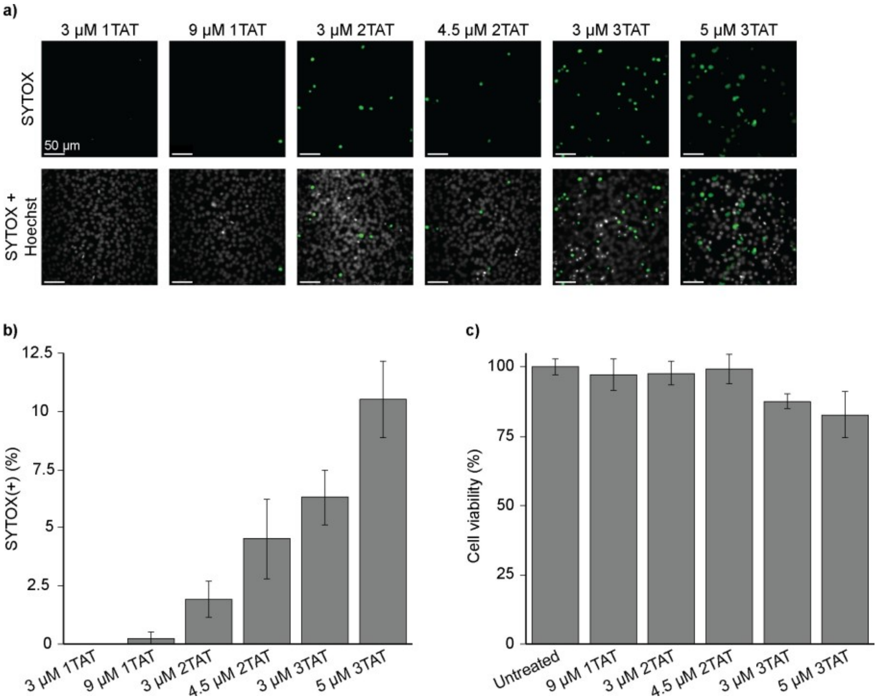

**Figure C.5 Cytotoxicity upon 24h exposure of HeLa cells to 1TAT, 2TAT, and 3TAT. (a) Representative fluorescence microscopy images of a SYTOX exclusion assay over HeLa cells treated with each peptide for 24 hr. HeLa cells were incubated with the peptides at the listed concentrations for 24 hr. Post-treatment, cells were washed and stained with SYTOX Green and Hoechst 33342, as before. Fluorescence microscopy was performed over the cells under each condition and representative images were taken at 20x magnification. (Scale bars: 20x: 50 µm). (b) Evaluation of the toxicity of the peptides by a SYTOX Green exclusion assay. Cells were treated as in a. The number of cells displaying a nucleus stained by SYTOX Green were counted. The data represented correspond to the mean of technical triplicates (>500 cells counted per experiment). (c) Evaluation of the viability of cells treated with the peptides by an MTT viability assay. Cells were treated as in a and b. Post-treatment, cell viability was assessed using a standard MTT viability assay. Each condition was replicated (n=7) and represented as the normalized mean ± standard deviation.**

**These data suggest that the majority cytotoxic effect conferred by addition of the peptides occurs initially, that is, within the first 30 min of addition. Little to no additional deleterious effects were observed upon prolonged exposure of the cells to the peptides.**

The usefulness of these peptides is not found in whether they penetrate cells per se, but instead in whether they can mediate the cytosolic delivery of other molecules. In order to address how 1TAT, 2TAT and 3TAT compare in this respect, we chose 2 cargoes, the enzyme Cre recombinase and the cell-impermeable small molecule SNAP-Surface 488. The cytosolic delivery of Cre recombinase, and the subsequent accumulation of the enzyme in the cell nucleus, can be quantified by the expression of an enhanced GFP (EGFP) reporter incorporated in a Cre-Lox recombination system (Figure C.6 A) [255]. Similarly, the cytosolic delivery of SNAP-Surface 488 in cells expressing SNAP-H2B, a histone fusion, results in cells displaying fluorescent nuclei (Figure C.6 B) [238, 256]. In principle, the successful delivery of only a few Cre recombinase molecules is sufficient to induce GFP expression. In In contrast, micromolar intracellular concentrations of molecules are required for microscopy detection of SNAP-Surface (based on calibration experiments performed in-house). We, therefore, envisioned that these 2 assays span a range of detection sensitivities that may reveal differences between the CPPs tested. As shown in Figure C.6 A, the percentage of cells positive for GFP expression was small when Cre recombinase was incubated with 1TAT (~10%, 3 μM 1TAT, 4 μM Cre recombinase; Cre recombinase used is expressed as a TAT fusion to promote endocytic uptake and the protein itself displays some cell-permeation activity, ~5%). In comparison, incubating Cre recombinase with 2TAT and 3TAT led to more than 50% of GFP positive cells. Interestingly, the delivery activities of 2TAT and 3TAT were relatively equivalent, indicating that both compounds are capable of delivering enough enzyme to initiate expression of the EGFP reporter (however, the amount of enzyme actually delivered could, in principle, vary). In contrast, 3TAT was dramatically more effective at inducing the delivery of SNAP-Surface 488 to the nucleus of cells than 1TAT or 2TAT. These results closely match the results obtained with the peptides in Figure 1 and indicate that 3TAT is able to induce the cytosolic of delivery of a significantly higher amount of SNAP-Surface 488 than 1TAT and 2TAT. Overall, these data indicate that 1TAT is ineffective, that 2TAT is active enough to mediate the delivery of few molecules, and that 3TAT, in contrast, can deliver larger quantities.

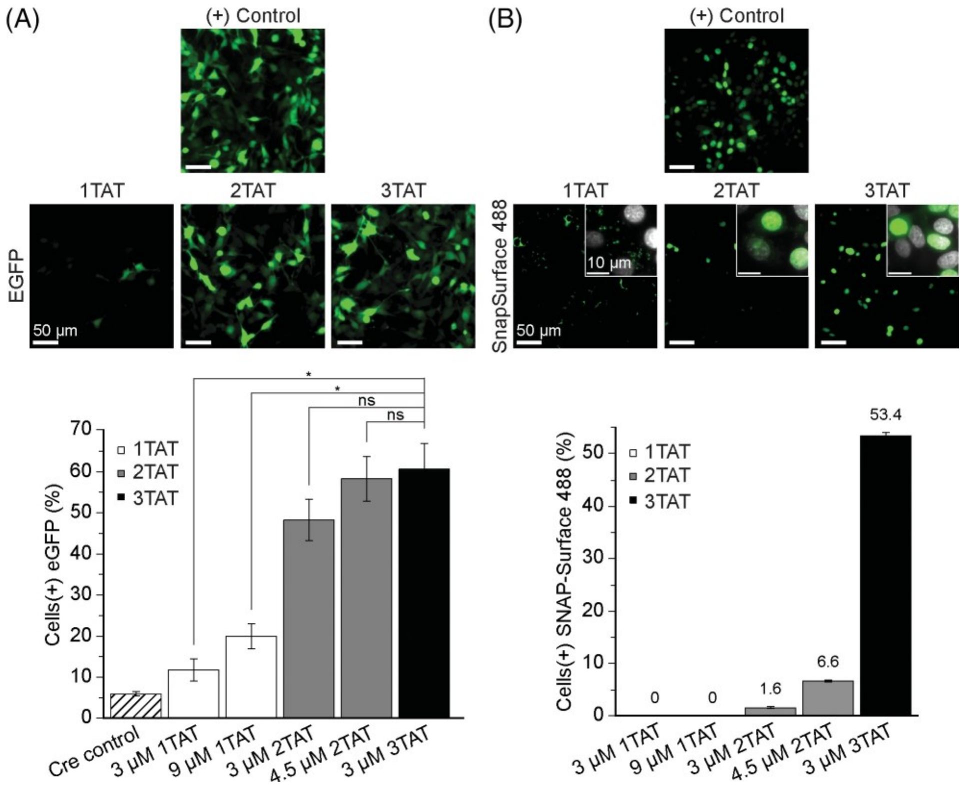

**Figure C.6 (A) 2TAT and 3TAT deliver the enzyme TAT-Cre into cells. Cells transfected with a plasmid containing EGFP downstream of an LSL cassette were coincubated with TAT-Cre (4 µM) and peptide at indicated concentrations for 30 minutes. Because successful cellular entry of TAT-Cre results in EGFP expression, the number of cells positive for EGFP fluorescence was counted 24 hours after each peptide/TAT-Cre incubations. Fluorescence microscopy images, pseudocolored green for EGFP, are representative examples of the cells 24 hours after enzyme delivery (scale bars: ×20: 50 µm, ×100: 10 µm). The data reported corresponds to the normalized mean of biological triplicates (>500 cells per experiment). NS, *P* > .05; **P* < .05. (B) 3TAT delivers the cell-impermeable green fluorophore SNAP-Surface 488 into the cytosolic space of cells. Cells transfected with a plasmid coding for histone H2B-SNAP$_f$ were coincubated with SNAP-Surface 488 (50 µM) and peptide at indicated concentrations for 30 minutes. Cells were then washed, and stained with Hoechst 33 342. Upon entry into cells, SNAP-Surface 488 is retained in the nucleus of cells by reaction with H2B-SNAP. Successful delivery was, therefore, assessed by counting the number of cells displaying a green nucleus. Fluorescence microscopy images, pseudocolored green for SNAP-Surface 488 and colored white for Hoechst 33 342, are (continued on the next page)**

**representative examples of the cells 1 hour after incubation (scale bars: ×20: 50 μm, ×100: 10 μm). The data reported corresponds to the normalized mean of biological triplicates (>500 cells per experiment) contrast, micromolar intracellular concentrations of molecules are required for microscopy detection of SNAP-Surface (based on calibration experiments performed in-house). We, therefore, envisioned that these 2 assays span a range of detection sensitivities that may reveal differences between the CPPs tested. As shown in Figure 2A, the percentage of cells positive for GFP expression was small when Cre recombinase was incubated with 1TAT (~10%, 3 μM 1TAT, 4 μM Cre recombinase; Cre recombinase used is expressed as a TAT fusion to promote endocytic uptake and the protein itself displays some cell-permeation activity, ~5%). In comparison, incubating Cre recombinase with 2TAT and 3TAT led to more than 50% of GFP positive cells. Interestingly, the delivery activities of 2TAT and 3TAT were relatively equivalent, indicating that both compounds are capable of delivering enough enzyme to initiate expression of the EGFP reporter (however, the amount of enzyme actually delivered could, in principle, vary). In contrast, 3TAT was dramatically more effective at inducing the delivery of SNAP-Surface 488 to the nucleus of cells than 1TAT or 2TAT. These results closely match the results obtained with the peptides in Figure 1 and indicate that 3TAT is able to induce the cytosolic of delivery of a significantly higher amount of SNAP-Surface 488 than 1TAT and 2TAT. Overall, these data indicate that 1TAT is ineffective, that 2TAT is active enough to mediate the delivery of few molecules, and that 3TAT, in contrast, can deliver larger quantities.**

### *Cell penetration involves endosomal escape*

We have previously demonstrated that dfTAT delivers macromolecular cargos by causing endosomal leakage. In order to test whether 3TAT has a similar activity, the intracellular localization of the peptide was first monitored in a pulse-chase experiment (Figure C.7A). Cells were incubated with 3 μM 3TAT for 5 minutes, washed and examined by fluorescence microscopy. At early time points, cells displayed a punctate distribution consistent with endosomal entrapment. At later time points, this distribution change to a cytosolic and nucleolar staining. Because the peptide is not present extracellularly during the post-treatment period, these data, therefore, suggest that the peptide, initially trapped inside endosomes, is subsequently able to escape from endosomes and reach a cytosolic destination. To ensure cells under each condition assayed were exposed to the same amount of internalized peptide, uptake measurements were performed, as before, at the indicated time points. These measurements indicate that the relative amount of peptide taken up by the cells was relatively equivalent across the 2 conditions.

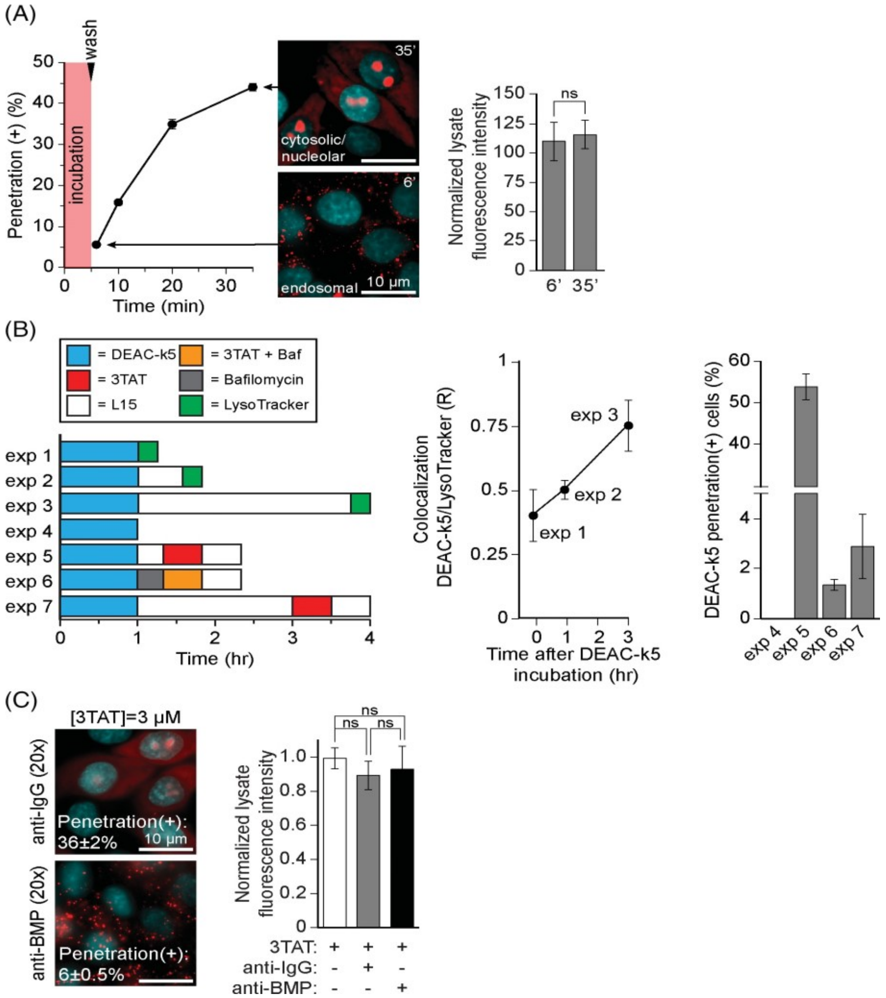

**Figure C.7 3TAT enters the cytosol of cells after endocytic uptake.(A) Cells were incubated with 3TAT (3 μM) for 5 minutes, washed, and then imaged by fluorescence microscopy at different time points to determine the extent of cell penetration. The number of cells displaying nucleolar staining (ie, penetration positive) was counted as previously described. The fluorescence microscopy images represented, pseudocolored red for TMR, highlight that cells first display a punctate distribution consistent endosomal entrapment at first and that nucleolar staining appear subsequently. The data reported corresponds to the mean of biological triplicates (>500 cells per experiment). Total peptide uptake at the 6 and 35 minutes time points was determined by lysing cells and measuring the bulk lysate for TMR fluorescence. The fluorescence of the cell lysate was measured and normalized to the number of cells in each sample, assessed by flow cytometry. The data reported corresponds to the mean of technical triplicates. NS, *P* > .05. (B) 3TAT releases a cargo entrapped inside endocytic vesicles into the cytosol of cells. First, experiments were (continued on the next page)**

**performed to determine the lysosomal accumulation of DEAC-k5 as a function of time after incubation. In experiments 1 to 3, cells were incubated with the blue fluorescent peptide DEAC-k5 (25 µM) for 1 hour. Cells were then washed, and incubated in L15 medium for the indicated time periods (exp 1 = 0 hours, exp 2 = 0.75 hours and exp 3 = 2.75 hours). Following L15 incubation, cells were treated with LysoTracker green (500 nM) for 15 minutes prior to imaging by fluorescence microscopy. Colocalization analysis was performed over representative images taken of DEAC-k5 and LysoTracker green taken under ×100 magnification. From this analysis, Pearson's R value is reported to represent the extent of colocalization. For experiments 4 to 7, cells were treated with DEAC-k5 for 1 hour, as before. For experiments 2 and 3, cells were washed, incubated with L-15 ± bafilomycin (200 nM) for 20 minutes, and then treated with 3TAT (3 µM) ± bafilomycin for 30 minutes. For experiment 4, following DEAC-k5 incubation, cells were washed and incubated with L15 for 2 hours. Cells were then treated with 3TAT (3 µM) for 30 minutes. Following a 30 minutes wait for experiments 2 to 4, fluorescence microscopy images were taken at ×20 and ×100 magnification to quantify DEAC-k5 delivery. Cells were scored, as before, for successful DEAC-k5 penetration if nucleoli staining was observed (biological triplicates, >500 cells per experiment). Prior to 3TAT treatment, DEAC-k5 displays a punctate distribution consistent with endosomal entrapment. After treatment with 3TAT, DEAC-k5 redistributes throughout the cell (nucleolar staining, presumably attributable to the polycationic nature of the peptide, can be observed). This effect is blocked by bafilomycin, an inhibitor of endosomal acidification and trafficking. However, whenever DEAC-k5 is accumulated predominantly in the lysosome, cell delivery of the molecular cargo is abolished. (C) Preincubation with an anti-BMP mAb inhibits 3TAT cytosolic penetration but not endocytic uptake. Cells were preincubated with anti-BMP or the control antibody, anti-IgG (50 µg/mL), for 1 hour, washed, and then treated with 3TAT (3 µM) for 30 minutes. Cell penetration was then visualized and quantified by fluorescence microscopy as previously described. The percentage of penetration positive cells reported is the mean of biological triplicates (>500 cells per experiment). Fluorescence images are pseudocolored red for 3TAT (scale bars: ×20: 50 µm, ×100: 10 µm). Total peptide uptake was determined by lysing cells and measuring the bulk lysate for TMR fluorescence. The fluorescence of the cell lysate was measured and normalized to the number of cells in each sample and to the level of uptake observed for 3TAT alone, assessed by flow cytometry. Each condition was normalized to cells treated with 3TAT (3 µM) for 30 minutes. The data reported corresponds to the mean of technical triplicates. NS, *P* > .05**

In order to further assess how 3TAT enters cells and mediates the delivery of cargos, we next tested whether the peptide could cause the release of material preloaded inside endosomes. Cells were preincubated with DEAC-k5, a peptide labeled with a blue fluorescent coumarin and containing cationic D-lysine residues that confer protease-resistance and that facilitate endocytic uptake [254, 257]. Cells were washed, treated with or without 3TAT and imaged by fluorescence microscopy (Figure C.7B; Figure C.8). Cells incubated with DEAC-k5 for 1 hour displayed punctate fluorescence signal (Figure C.7B). The blue fluorescent puncta colocalized with LysoTracker Green, consistent with endosomal accumulation of DEAC-k5 (Figure C.7B; Figure C.9). Upon addition of 3TAT, the blue fluorescence was redistributed throughout the cell cytosol. In addition, like 3TAT, DEAC-k5 showed a distinct nucleolar staining, confirming that the signal detected is intracellular. The cytosolic penetration of both 3TAT and DEAC-k5 was inhibited by addition of bafilomycin (cells are treated after DEAC-k5 loading), suggesting that blocking endosomal acidification prevents endosomal escape. Cytosolic delivery of DEAC-k5 was also abolished when addition of 3TAT was delayed by 2 hours, a time frame that allows accumulation of DEAC-k5 in lysosomes [248]. Together, these data indicate that 3TAT is capable of reaching endosomes preloaded with DEAC-k5 and of causing a membrane leakage that results in the release of both peptides. When the time window between DEAC-k5 and 3TAT is short, endocytic organelles containing 3TAT presumably fuse with endocytic organelles containing DEAC-k5, leading to content mixing. When the time window is longer, DEAC-k5 reaches organelles further downstream in the endocytic pathway (ie, lysosomes), away from sites of 3TAT-mediated escape.

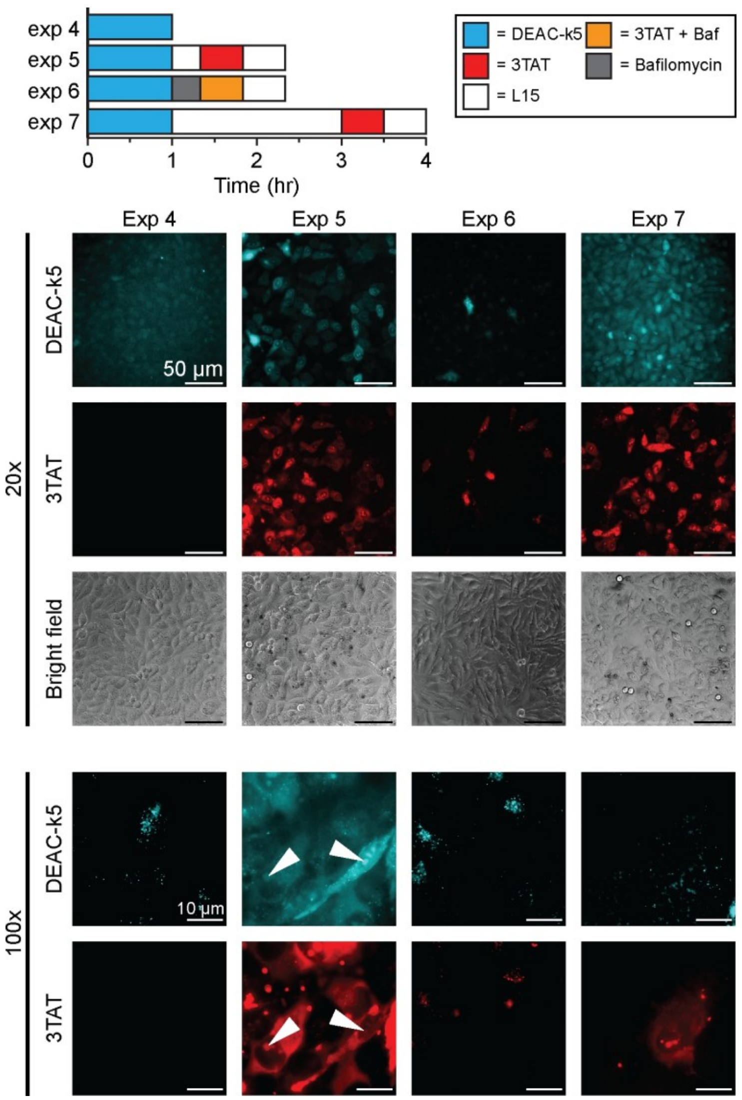

**Figure C.8 Representative fluorescence microscopy images of 3TAT-mediated DEAC-k5 cellular delivery under different conditions.**

**Cells were treated as described in the main text Figure 3b. Fluorescence microscopy images, at 20x and 100x magnification, were taken over treated cells. Images are reported over the cells (bright field), DEAC-k5 (pseudocolored blue), and 3TAT (pseudocolored red). In experiments 4 and 7, the DEAC-k5 channel contrast of 20x magnification images was adjusted in an attempt to show the minimal level of staining of cells with the peptide. In the 100x magnification images of experiment 5, white arrows are superimposed to highlight the nucleoli-staining characteristic shared by both DEAC-k5 and 3TAT. Scale bars: 20x: 50 µm, 100x: 10 µm**

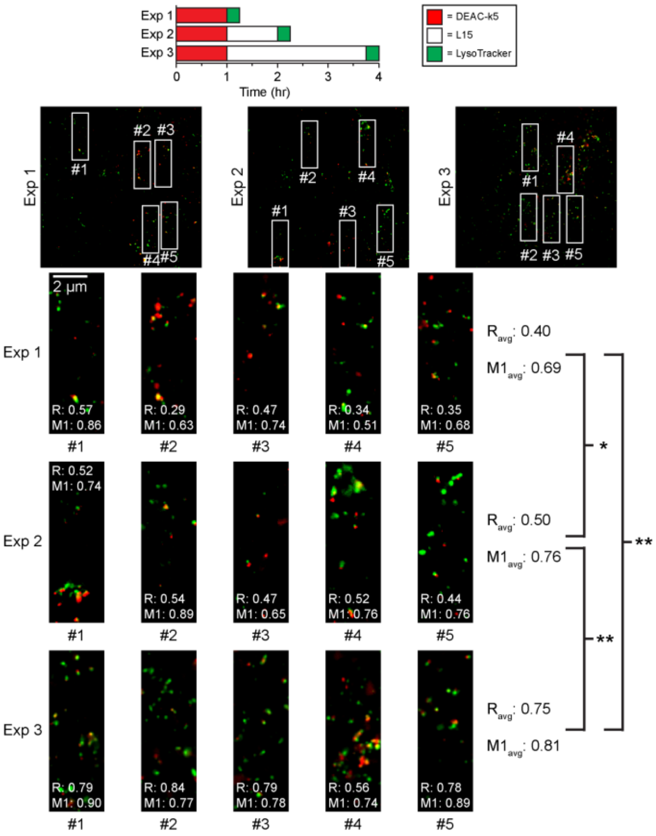

**Figure C. 9 DEAC-k5 colocalizes with LysoTracker Green. Cells were incubated with DEAC-k5 (25 μM) for 1 hr at 37°C and washed thereafter. Next, cells were incubated in L-15 medium for indicated times (exp 1 = 0 hr, exp 2 = 0.75 hr, exp 3= 2.75 hr) and then stained with LysoTracker Green (500 nM) as well as Hoechst 33342 (5 μM) for nuclear visualization. Representative fluorescence microscopy images taken under 100x magnification were taken for DEAC-k5 (pseudocolored red), LysoTracker Green (pseudocolored green) and an overlay of DEAC-k5, LysoTracker green and Hoechst 33342 (pseudocolored blue). Colocalization analysis was performed over zoomed-in sections of DEAC-k5 and LysoTracker images of each condition. Pearson's R and Manders' M1 coefficients are reported to represent the extent of colocalization. A student's t-test was performed between the $R_{avg}$ of each condition. DEAC-k5 was pseudocolored red in the images provided to enhance the contrast between the peptide and LysoTracker Green (as opposed to comparing blue and green). Scale bars: 100x images: 10 μm, zoomed images: 2 μm. NS, $p>0.05$; *, $p<0.05$; **, $p<0.01$.**

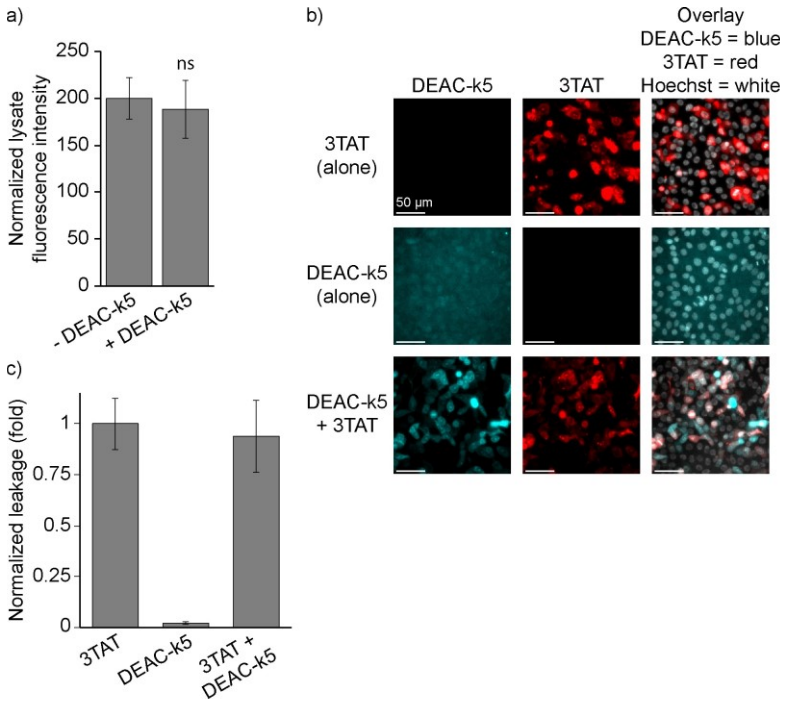

**Figure C.10 DEAC-k5 does not affect cell penetration or endosomolytic activities of 3TAT. (a) DEAC-k5 does not affect cellular uptake of 3TAT. Cells were treated with 3 µM 3TAT ± DEAC-k5 (25 µM) for 30 min, 37C. Following treatment, cells were washed, trypsinized, and lysed as described previously. Cellular uptake of 3TAT was determined by measuring the red fluorescence of the cell lysates. The data represented correspond to the mean of technical triplicates (>500 cells counted per experiment) with corresponding standard deviation. NS, p>0.05. (b) DEAC-k5 does not affect endosomal escape of 3TAT. Cells were treated with 3 µM 3TAT and/or DEAC-k5 (25 µM) for 30 min, 37C. Following treatment, cells were washed and then stained with Hoechst 33342 (2.5 µM) 30 min later. Representative fluorescence microscopy images at 20x magnification were taken of DEAC-k5 (pseudocolored blue), 3TAT (pseudocolored red) and Hoechst 33342 (pseudocolored white). (Scale bars: 20x: 50 µm). (c) DEAC-k5 does not affect membrane lysis of liposomes treated with 3TAT. LE LUVs (250 µM total lipid) were treated with 3TAT (5 µM), DEAC-k5 (25 µM), or both peptides for 1 hr. The release of calcein from LUVs was then quantified. The data reported is the mean of technical triplicates and the corresponding standard deviation. Means were normalized to the leakage induced by 3TAT alone.These data suggest that the accumulation of DEAC-k5 in lysotracker-stained organelles, late endosomes and lysosomes, increases overtime.**

Previous reports on dfTAT have established that endosomal escape involves the disruption of the membrane of late endosomes [248]. In particular, dfTAT mediates its membrane-disrupting activity by interacting with the anionic lipid BMP in late endosomes. Because lipid bilayers of both late endosomes and lysosomes contain BMP, 3TAT may have the capacity to disrupt either of these organelles. To determine the major route of endosomal escape, a delivery assay of preloaded lysosomal cargo was performed (Figure 7B, exp 4). Cells first incubated with DEAC-k5 were then treated with 3TAT following a 2 hours wait to ensure that a majority of the endocytosed cargo was sequestered to the lysosome (a time frame in which one would expect this to happen). This experiment displayed very poor delivery of DEAC-k5 (<3%). Furthermore, whenever cells were treated shortly after the DEAC-k5 delivery, cells displayed a substantial amount of DEAC-k5 delivery (54%). Taken together, these data suggest that cargo must not be sequestered to the lysosome for successful delivery.

Notably, anti-BMP, a monoclonal antibody raised against BMP, can prevent the fusion of late endosomal membranes (late endosomes are organelles that contain vesicles in their lumen) and thereby block the endosomal escape of dfTAT [248]. In order to establish whether 3TAT would respond to a similar treatment, cells were preincubated with anti-BMP or with the control antibody anti-IgG, a monoclonal antibody that does not recognize BMP as an epitope. Cells were then incubated with 3TAT and imaged. As shown in Figure

7 C, anti-IgG did not prevent 3TAT from reaching the cytosol and nucleoli of cells. In contrast, anti-BMP inhibited cytosolic penetration, most of the cells displaying instead a punctate distribution of the peptide. Importantly, neither antibodies led to a significant reduction in peptide uptake, as measured by the total fluorescence of cell lysates. This indicates that the peptide is capable of accumulating inside endosomes but becomes unable to escape endosomes when anti-BMP is present.

### *In vitro characterization of 1TAT, 2TAT and 3TAT*

To test whether the involvement of late endosomes and BMP could be corroborated *in vitro*, lipid bilayer leakage assays were performed. Large unilamellar vesicles (LUVs) were prepared with membrane composition mimicking that of the plasma membrane or early endosomes (P.M./E.E. LUV: 65:15:20 PC:PE:Chol) or that of late endosomes (L.E. LUV: 77:19:4 BMP:PC:PE). The lipid composition for early and late endosomes is adapted from studies performed by Gruenberg et al [258]. It should be noted that in this and more recent studies, it was not possible to differentiate the lipid compositions between late endosomes and lysosomes. These LUVs were loaded with the green fluorophore calcein and membrane leakage upon treatment with peptides was evaluated by measuring calcein release [258]. When mixed at a peptide-to-lipid ratio (P:L) of 1:50, 3TAT was unable to induce leakage of P.M./E.E. LUVs. In contrast, 3TAT caused dramatic leakage of soluble lumenal dye from L.E. LUVs (Figure C.10A; ~40%, 100% leakage being obtained after treatment of LUVs with the detergent Triton X100). 3TAT did not induce leakage when BMP was substituted with its structural isomer PG. Because PG is negatively charged like BMP, this suggests that electrostatic interactions between the cationic peptide and an anionic lipid are not sufficient to induce leakage. This in turn implies that a relative specificity is involved in the interaction between 3TAT and BMP. Furthermore, addition of 250 µg/mL of anti-BMP was sufficient to inhibit 3TAT-mediated leakage. In this assay, the amount of peptide added exceeds that anti-BMP by a factor of $3 \times 10^6$ (5 µM vs $1.7 \times 10^{-6}$ µM). As previously reported, anti-BMP does not block peptide binding to the lipid membrane. Instead, it inhibits contact between BMP-containing liposomes [258] [259]. Notably, preincubation with anti-IgG had no effect on the leakage. Together, these results mirror those obtained in cellulo and further validate the involvement of the late endosome and of its lipid BMP in the process of endosomal escape.

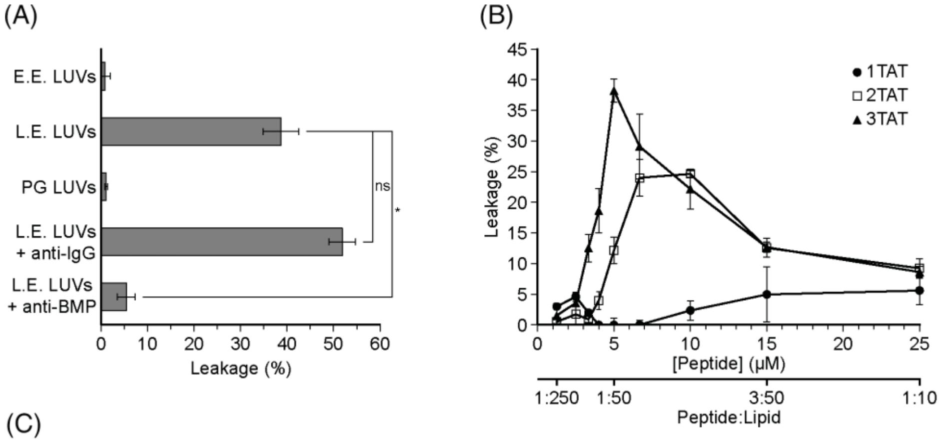

(C)

| P:L | 1:250 | | | 1:50 | | | 1:10 | | | 3:10 | 1.5:10 |
|---|---|---|---|---|---|---|---|---|---|---|---|
| Peptide | 1TAT | 2TAT | 3TAT | 1TAT | 2TAT | 3TAT | 1TAT | 2TAT | 3TAT | 1TAT | 2TAT |
| Zeta potential (mV) | -53.0 | -50.4 | -51.3 | N/A | N/A | N/A | N/A | N/A | +39.7 | +21.7 | +35.2 |
| Flocculation | No | No | Yes | Yes | Yes | Yes | Yes | Yes | No | No | No |

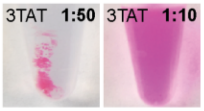

**Figure C.11 3TAT causes the leakage of LUVs with a lipid composition consistent with that of the late endosome.**

**(A) 3TAT causes the leakage of LUVs with a lipid composition consistent with that of the late endosome. (L.E. LUVs, 77:19:4 BMP: PC:PE) but does not disrupt LUVs with a lipid composition consistent with that the early endosome (E.E. LUVs, 65:15:20 PC:PE:Chol). LUVs (250 µM total lipid), preloaded with the green fluorophore calcein, were treated with 3TAT (5 µM) for 1 hour. Membrane leakage was assessed by measuring the release of calcein. The peptide activity is normalized against the leakage obtained after treatment of LUVs with 1% of the detergent Triton X-100. PG LUVs correspond to L.E. LUVs in which the lipid BMP is substituted to its isomer phosphatidyl glycerol (PG). The effects of the monoclonal antibodies anti-IgG and anti-BMP (250 µg/mL). The data represented correspond to the mean of triplicates. NS, *P* > .05; **P* < .05. (B) The leakage of L.E. LUVs induced by 2TAT or 3TAT displays a non-linear dose response. L.E. LUVs (250 µM total lipid) were treated with peptides at the indicated concentrations (peptide: Lipid ratios are also provided) for 1 hour. The release of calcein from LUVs was then quantified. The data reported is the mean of technical triplicates and the corresponding SD. (C) Table representing the zeta potential measurements and flocculation propensity of liposomal suspensions at different peptide: Lipid ratios. Flocculation was determined by visual examination of the sample after centrifugation (photographic examples of 2 conditions, P:L of 1:50 and 1:10 for 3TAT, are provided). Under conditions where substantial flocculation occurred, it was not possible to take zeta potential measurements as the number of particles in colloidal suspension was too low. Values in each experiment are represented as the mean percentage with resultant SD of triplicate experiments**

To establish how 1TAT, 2TAT and 3TAT differ in their membrane-disruption activities, L.E. liposomes were treated with the peptides and leakage was quantified (total lipid concentrations are kept constant). At low P:L, both 2TAT and 3TAT induced leakage, 3TAT being consistently more active than 2TAT. In contrast, 1TAT showed negligible membrane disruption. When increasing peptide concentration and P:L ratio, the leakage activity of both 2TAT and 3TAT reach a maximum but, instead of displaying a continual increase, the extent of induced leakage declines to levels comparable to 1TAT. Interestingly, we observed that the leakage activity of 2TAT and 3TAT appeared to be correlated with the turbidity of the liposomal suspensions. For instance, upon centrifugation, a pellet of liposomes coated with the red-colored 3TAT was obtained at a P:L ratio of 1:50, a condition leading to liposomal leakage (Figure C.10 A-C).

Because the liposomes do not form a pellet in the absence of peptide at the centrifugation speed used here (data not shown), this suggests that 3TAT can cause liposomes in suspension to flocculate and sediment. Remarkably, at a P:L ratio of 1:10, the liposomes did not form a noticeable pellet upon centrifugation. This behavior correlated with an inversion of charge on the surface of liposomes, as indicated by zeta potential measurements (Figure C.10 C). In particular, addition of increasing amounts of peptide changes the zeta potential of the particles from highly negative (zeta potential of −58.9 V for BMP-containing liposomes in the absence of peptide) to highly positive (eg,+39.7 V at 1:10 3TAT:L; zeta potential measurements were not possible when excessive flocculation takes place at intermediate P:L). Together, these results are consistent with the notion that as 3TAT coats the surface of liposomes, the negative charges of the lipids are neutralized. Liposomes may then flocculate either because of the absence of repulsive electrostatic forces, or because of the bridging action of the peptide itself. In contrast, as the amount of peptide partitioning on the surface of liposomes increases, particles become positively charged and repulsion is restored (our data also suggest that coating of the liposome surface with peptide happens faster than leakage does). Notably, similar behaviors were observed with 1TAT and 2TAT with the exceptions that higher P:L were necessary to abolish flocculation. In addition, it is worth noting that 3TAT induced flocculation even at low P:L and that overall, 2TAT can do what 3TAT does (ie, leakage, flocculation and liposomes charge inversion), albeit at higher concentrations. It is, however, clear that while 1TAT can also bind to liposomes and induce their flocculation, it fails to induce significant leakage. Overall, while contact between liposomes appears to be necessary for leakage, it may not be sufficient.

Considering both the in cellulo and *in vitro* results gathered thus far, it is surprising that such low activity is reported for 2TAT despite the very high activity we reported for the TAT-dimer, dfTAT. One notable difference between the 2 peptides is that 2TAT is labeled with only one fluorophore, while dfTAT is labeled with 2. To investigate whether the fluorophore plays a role in the membrane activity of 2TAT and 3TAT, non-fluorescent variants, nf2TAT and nf3TAT, were synthesized (Figure C.3 G-I). The non-fluorescent peptides were then assayed for cell penetration, cytotoxicity, delivery of macromolecules and membrane lytic activity of late endosomes (Figure C.11). Because these peptides do not contain a covalent fluorescent label, cell penetration was assayed by the ability of the non-fluorescent peptides to deliver the small molecular cargo DEAC-k5 or the enzyme TAT-Cre. In all assays, the trend observed for nf2TAT and nf3TAT across all the conditions assayed is similar to that of 2TAT and 3TAT. Namely, the peptide with 3 TAT branches is more active than the analog with only 2. Yet, the non-fluorescent analogs are overall less active than the fluorescent counterparts. In particular, nf3TAT requires higher concentrations than 3TAT to achieve similar cell delivery activities. The lytic activity of nf3TAT toward liposomes is also substantially less than that of 3TAT.

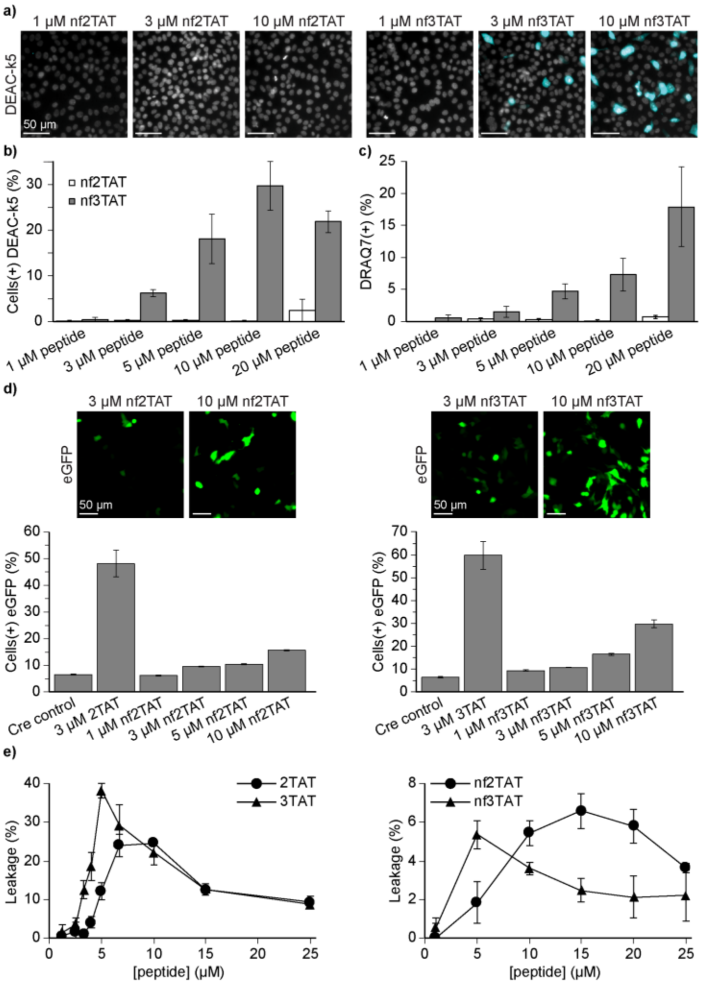

**Figure C.12 Non-fluorescent peptide-mediated delivery of DEAC-k5 into HeLa cells.(a) Non-fluorescent peptide-mediated delivery of DEAC-k5 into HeLa cells. DEAC-k5 delivered by nf2TAT and nf3TAT allows for the quantification of cell penetration efficiency. Representative fluorescence microscopy images of cells co-incubated with DEAC-k5 (25 µM) and each peptide at indicated concentrations for 30 min, washed, and stained with DRAQ7 (cell impermeable nucleic acid stain) and the nuclear stain Hoechst 33342. Cells were imaged 1 hr after incubation with peptides. Images are an overlay of DEAC-k5 (pseudocolored blue) and Hoechst 33342 (pseudocolored white). Scale bars: 20x: 50 µm. (b) The cell penetration activity of nf3TAT is superior to that of nf2TAT with a marked decrease from the activity of the fluorescent variant, 3TAT. Cells were treated as in a. Quantitative (continued on the next page)**

**evaluation of the percentage of cells positive for penetration/delivery of DEAC-k5 (i.e. showing nucleolar staining by DEAC-k5 while excluding DRAQ7(+) cells. The data reported represent the mean of biological triplicates with corresponding standard deviation (>500 cells counted per experiment). (c) At high concentrations, nf3TAT is toxic to cells but significantly less toxic than 3TAT. Evaluation of the toxicity of the peptides by a DRAQ7 exclusion assay. Cells were treated as in b and c. The number of cells displaying a nucleus stained by DRAQ7 were counted. The data reported represent the mean of biological triplicates (>500 cells counted per experiment). (d) nf2TAT and nf3TAT deliver the biologically active enzyme TAT-Cre into HeLa cells. Cells transfected with a plasmid containing EGFP downstream of an LSL cassette were co- incubated with TAT-Cre (4 µM) and each peptide at indicated concentrations for 30 min. Because successful cellular entry of TAT-Cre results in EGFP expression, the number of cells positive for EGFP fluorescence were counted 24 hr after each peptide/TAT-Cre incubations. Fluorescence microscopy images, pseudocolored green for EGFP, are representative examples of the cells 24 hr after enzyme delivery (scale bars: 20x: 50 µm, 100x: 10 µm). Quantification of cells positive for TAT-Cre delivery were scored and reported as the mean of biological triplicates (>500 cells per experiment) with corresponding standard deviation. (e) The leakage of LE LUVs induced by nf2TAT or nf3TAT displays a non-linear dose- dependent response. LE LUVs (250 µM total lipid) were treated with peptides at the indicated concentrations (peptide:lipid ratios are also provided) for 1 hr. The release of calcein from LUVs was then quantified. The data reported is the mean of technical triplicates and the corresponding standard deviation.**

In order to gain additional insights into the complex behavior of the peptides with L.E. LUVs, liposomal suspensions treated with 1TAT, 2TAT and 3TAT were analyzed by Burst Analysis Spectroscopy (BAS), a single particle technique that permits quantitative analysis of liposome size distributions in heterogeneous samples [178] [39]. In these assays, liposomes were doped with a membrane staining carbocyanine fluorescent dye, Vybrant DiD (0.03% of total lipid). Fluorescence bursts were first recorded from individual liposomes as they advectively flowed through the detection volume of a custom 2-channel confocal microscope at velocities much greater than the rate of particle diffusion. The underlying particle size distribution was reconstructed by BAS from the observed fluorescence burst amplitude distribution [182]. The resulting BAS size distributions from the DiD channel are then directly proportional to liposome membrane content, while the TMR amplitude distributions measure the amount of bound peptide. We examined samples representing P:L ratios in the range 1:2500 to 1:200. We envisioned that these conditions would be representative of the early steps in liposomal flocculation and possibly reveal how peptides and lipids interact as membrane leakage is initiated. As shown in Figure C.13 A, addition of peptides to liposomal suspension at these low P:L ratios induced a shift of the liposomes to much larger mean particle size for both 2TAT and 3TAT. This indicates that the particles detected contain a much greater level of lipid bilayer content as more peptide is added. By contrast, the shift in mean particle size upon the addition of 1TAT was far more modest. These results demonstrate that, while the binding of 1TAT does not dramatically alter the size distribution of the liposomes, the binding of 2TAT and 3TAT fundamentally restructures the liposome particles in suspension. In order to assess whether this restructuring can be linked to differences in peptide binding, the ratio of TMR signal to DiD signal was plotted for all correlated burst events (Figure C.13 B). At the lowest concentration of peptide tested (1 nM), the distribution of the TMR/DiD burst amplitude ratios are shifted to higher values for 2TAT and 3TAT vs 1TAT, indicating that the branched species may have a higher binding affinity for the liposomes than the monomeric peptide. In contrast, at 5 nM, the TMR/DiD ratio distribution is similar for all 3 peptides. This strongly suggests that, for the same number of peptide molecules bound, 1TAT does not cause an increase in membrane content per particle detected but that 2TAT and 3TAT do. Importantly, each molecule bound leads to 1, 2 or 3 TAT copies being present on the surface of the lipid bilayer for 1TAT, 2TAT and 3TAT, respectively. Therefore, we next examined how the behavior of the peptides compares when differences in absolute TAT content are taken into account. For this test, the binding of 1TAT at 12.5 nM (the maximal peptide concentration accessible in our BAS experiments without causing detector saturation) was evaluated. Under this condition, a large population of liposomal particles can be observed that contain levels of bound 1TAT peptide that exceeds by several-fold (>3-fold) the amount of 2TAT and 3TAT bound at 5 nM. Yet, the liposomes coated with this higher amount of 1TAT retain a smaller mean particle size than liposomes coated with substantially less 2TAT or 3TAT. These results, therefore, suggest that the differential impact of 1TAT vs 2TAT or 3TAT on the liposome size distributions are not a consequence of how much peptide is bound per se, but to differences in how the peptides interact with the membrane (Figure C.14).

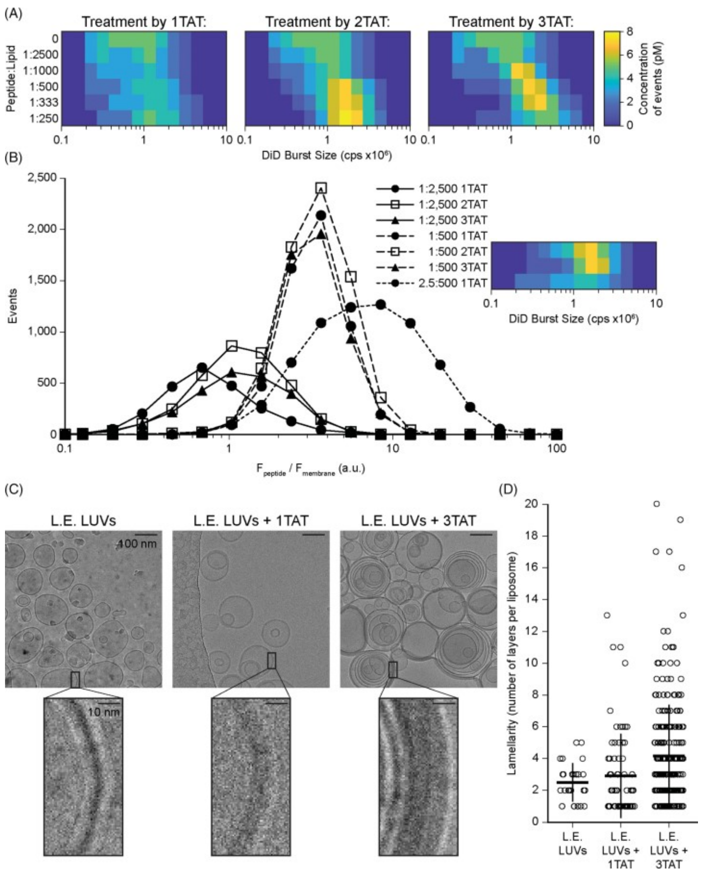

**Figure C.13 (A) 2TAT and 3TAT cause increases in the size and membrane content of L.E.**

**LUVs when 1TAT does not. L.E. LUVs doped with DiD (2.5 μM total lipid, 0.03% DiD) and treated with peptide at indicated concentrations were analyzed by the BAS [182]. Fluorescence bursts from individual DiD-labeled liposomes in each sample are detected and quantified. Each fluorescent event is binned based on its fluorescence intensity and the overall population is represented as a heat map [39]. The x-axis is a logarithmic scale of DiD fluorescence burst amplitude (which is directly proportional to liposome size) while the color of each bin is pseudo-colored blue to yellow and is proportional to the concentration of liposomes of a given size. The data represented is the compilation of triplicates. (B) Differences in binding affinity do not contribute to the lower membrane perturbing behavior of 1TAT when compared to 2TAT and 3TAT. Peptide binding to individual liposomes was assessed in 2 color BAS experiments by measuring the ratio of the fluorescence of the peptide (continued on the next page)**

**($F_{peptide}$, TMR signal) to the fluorescence of the membrane ($F_{membrane}$, DiD signal) obtained for each burst event detected during a BAS measurement. The data represented is the compilation of triplicates. (C) 3TAT causes the flocculation and fusion of L.E. LUVs and favors lipid bilayer contacts. L.E. LUVs (250 µM total lipid) were treated with 1TAT or 3TAT peptides (5 µM), sedimented and imaged by cryo-electron microscopy [260]. Untreated L.E. LUVs were imaged as a control. Insets represent zoomed in portions of images to highlight lipid bilayer contact or the lack there of. (D) Images of liposomes were quantified for lamellarity (number of lipid bilayers present in individual spherical liposomal structures). Each data point represents a liposomal structure observed from cryo-EM images (each experiment was duplicated and 5 images were acquired per sample)**

To further reveal the basis for the 3TAT-mediated flocculation and leakage, liposomal samples were analyzed by cryo-electron microscopy[260]. Liposomes were treated with peptides at a P:L ratio of 1:50, conditions that lead to maximal leakage for 3TAT. Untreated L.E. liposomes were on average bilamellar (Figure C.13 D). It is notable that BMP-containing liposomes have a propensity to spontaneously form multivesicular structures at acidic pH [261]. When treated with 1TAT, the lamellarity of the liposomes increased, albeit to a modest extent. In contrast, liposomes treated with 3TAT showed several clear differences. Consistent with both the observed propensity to sediment and increases in particle size observed by BAS, the liposomes were clustered (Figure C.13 C). The number of bilayers present per liposome was also significantly increased, with up to 20 layers observed in a single liposome (Figure C.13 D). Finally, multilamellar liposomes displayed thick external membranes. This apparent thickness is the result of several bilayers being in close proximity (Figure C.13 C). The vicinity between bilayers is particularly high. This is exemplified by the fact that, in the absence of peptide, a solvent layer is present between liposomes, even when liposomes are forced against one another (as illustrated by membrane distortion in Figure C.13 C). An interstitial solvent layer is, however, not visible when 3TAT is present. Together, these data demonstrate that 3TAT has the ability to bring lipid bilayers into close contact and reconfigure liposomes into complex multilamellar structures. However, 1TAT does not display these activities.

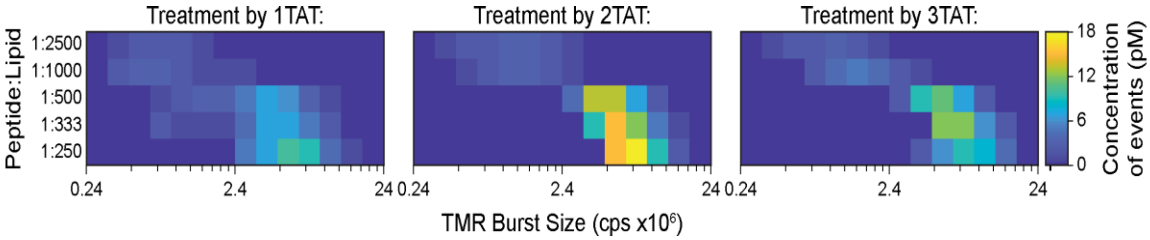

**Figure C.14 Quantification of peptides bound to L.E. LUVs by BAS.L.E. LUVs doped with DiD (2.5 µM total lipid, 0.03% DiD) and treated with peptide at indicated concentrations were analyzed by Burst Analysis Spectroscopy (BAS). Fluorescence bursts from individual TMR-labeled peptides coincident with fluorescence bursts of DiD-labeled liposomes in each sample were detected and quantified. Each fluorescent event is binned based on its fluorescence intensity and the overall population is represented as a heat map. The x-axis is a logarithmic scale of TMR fluorescence burst amplitude while the color of each bin is pseudo-colored blue to yellow and is proportional to the concentration of peptide bound to liposomes. The data represented is the compilation of triplicates.**

## Discussion

The cellular assays performed in this study demonstrate that the number of branches present in the peptide constructs dramatically impact cell penetration. For instance, the efficiency of endocytosis, endosomal escape, and cargo delivery is consistently greater for 3TAT than for 2TAT. The monomeric 1TAT, an analog of the prototypical and widely used HIV TAT peptide, is relatively poor in all activities and clearly outperformed by 3TAT. In particular, the relatively sensitive Cre recombinase assay illustrates how 1TAT can only deliver the enzyme in few cells. In turn, the SNAP-Surface assay and the monitoring of the cellular distribution of the peptide itself indicate that the delivery activity of 1TAT is too poor for microscopy detection. Notably, 1TAT and 2TAT are typically unable to produce the results obtained with 3TAT even when the concentration of the monomeric and dimeric constructs is increased to match the total amount of TAT species present in each condition. These results, therefore, highlight that covalently linking of several TAT copies produces effects that are not obtained when the same number of individual TAT peptides are present. In other words, raising the concentration of 1TAT can never reproduce what is achieved with 3TAT. One of the positive effects observed with peptide branching is a high propensity for endocytosis. In particular, the overall peptide internalization quantified in Figure 1E is a measure of endocytic uptake efficiency. This is because, although 3TAT distributes in the cytosol and nucleoli of cells, it needs to be first endocytosed to reach these localizations (the total amount of peptide present in the cell was, therefore, originally taken up by endocytosis first). As such, the endocytosis of 3TAT, 2TAT and 1TAT is proportional the peptide copy numbers, indicating that a multibranch display is favoring endocytosis-inducing interactions on the cell surface. This effect is potentially mediated by the clustering of heparan sulfate proteoglycans, known interaction partners of polycationic CPPs on the cell surface [262-264]. Moreover, the enhanced endocytic uptake of 3TAT may contribute to making this compound more prone than 2TAT or 1TAT at escaping endosomes. As a matter of fact, by being able to accumulate inside endosomes at higher levels than monomeric or dimeric counterparts, 3TAT may be able to reach a membrane-disruption concentration threshold more readily. Yet, the connection between endocytic uptake and endosomal escape may be more complicated. This is because 2TAT does not escape from endosomes as well as 3TAT, even when 2TAT is endocytosed at higher levels than 3TAT (eg, 4.5 µM 2TAT vs 1 µM 3TAT, Figure 1E). Instead, our results indicate that 3TAT is also more prone to induce membrane disruption and endosomal leakage than 2TAT and 1TAT.

The enhanced membrane-disruption efficacy of 3TAT is corroborated *in vitro*, with liposomes mimicking the lipid bilayers of late endosomes. It should be noted that late endosomes are organelles with a limiting membrane and multiple intralumenal vesicles with a size and composition consistent with the liposomes tested. These membrane highlighted in Figure C.13 C) also highlight that 3TAT must act as a bridging agent that keeps the bilayers glued to one another.

Induced membrane fusion is in itself not sufficient to explain the cell penetration activity of 3TAT. This is because fusion does not imply translocation across membranes. In other words, fusion of late endosomal vesicles does not equate to endosomal escape. It is, therefore, more probably that the leakage activity of 3TAT detected *in vitro* is more pertinent to the mechanism of endosomal escape and cytosolic entry. However, we envision that leakage and fusion are intimately related. In particular, leakage appears to decrease when liposomes cease to flocculate. Furthermore, leakage does not take place with 1TAT, a compound that also has a limited ability to induce multilamellarity and bilayer contact. The decline in leakage observed at high peptide to lipid ratios may also indicate that leakage requires liposomal contact. Indeed, liposomes do not sediment when leakage is low. Finally, anti-BMP, an antibody that can block the fusion of BMP-containing liposomes, can inhibit membrane leakage, *in vitro* and in cellulo [258, 259]. Overall, it would, therefore, seem that 3TAT, by coating the surface of liposomes, directly creates linkages between various lipid bilayers. This, in turn, causes membrane contact that overcomes liposomal repulsion and allows leakage to occur. When treated with a higher concentration of peptide, these 3TAT-bound liposomes possess a net positive charge restoring repulsion between individual liposomes resulting in no leakage.

While the compounds tested clearly highlight the influence of the number of branches present in the constructs, several questions remain open. For instance, 2TAT performed poorly in our assays in comparison to the previously reported reagent dfTAT, despite the fact that both reagents contain 2 TAT copies. Structural features, such as the number of fluorophores bound or the linker length between TAT branches may, therefore, play a role in membrane permeabilization. The contribution of the fluorophore in our constructs is highlighted herein by the decrease membrane-disruption activities observed for the non-fluorescent analogs. It is, therefore, possible that the fluorophore, when attached to 2TAT and 3TAT, interacts with lipid bilayers and enhances membrane destabilization. Notably, this contribution is not sufficient to cause substantial membrane leakage when the fluorophore is linked to a single copy of the peptide, as in 1TAT. Overall, these results, therefore, indicate that, while a threshold charge density is required to induce membrane leakage by the molecules reported, other parameters, such as perhaps the relative hydrophobicity of a fluorophore, can further enhance this activity. A detailed characterization of what these parameters may be will be the object of future studies.

Another question left open is the topic of toxicity, specifically when comparing 3TAT to dfTAT. While 3TAT displays a delivery efficiency and mode of cellular entry similar to dfTAT, 3TAT is relatively toxic while dfTAT is relatively innocuous (dfTAT-mediated delivery does not noticeably impact viability, proliferation rates or transcription). On one hand, disrupting cellular membranes to gain cytosolic access can obviously be damaging to cells. It may not, therefore, be surprising that 3TAT is toxic, though it remains remarkable that dfTAT is not. Notably, because of its disulfide linkage, dfTAT is reduced into TAT monomers upon entry into the cytosolic space [238, 254]. The membrane-disrupting activity of the reagent is, therefore, greatly reduced after delivery is achieved. In contrast, 3TAT, while presumably susceptible to partial proteolytic cleavage, should remain trimeric and membrane active after cytosolic entry. 3TAT could, therefore, kill cells by disrupting the membrane of various intracellular organelles, a scenario that will be examined in future studies. Finally, it should be noted that our study does not directly address whether the branching design of the multivalent CPPs tested is necessary for efficient cellular penetration. For instance, it is possible that a linear peptide containing 3TAT sequence back-to-back could reproduce some of the activities observed with 3TAT. Unfortunately, we could not test this possibility because, in our hands, the solid-phase peptide synthesis of linear constructs failed due to extremely poor coupling yields during the incorporation of residues of the second and third TAT segments. Such issue is well-known limitation of SPPS and, perhaps, this highlights a benefit of synthesizing branched structures containing shorter sequences. Overall, because of their synthetic accessibility and of their advantageous cell penetration properties, branched CPP structures may provide new opportunities in the delivery field.